

GRAIN GROWTH AND TEXTURE EVOLUTION IN THIN FILMS

by

Roland Carel

Submitted to the Department of Materials Science and Engineering in Partial Fulfillment
of the Requirements for the Degree of


Doctor of Philosophy

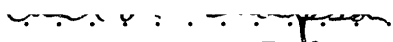
at the

Massachusetts Institute of Technology
September 1995

© 1995 Massachusetts Institute of Technology
All rights reserved

Signature of the Author . . .


Department of Materials Science and Engineering
August 11, 1995

Certified by . . .  . . .

Professor Carl V. Thompson
Thesis Supervisor

Accepted by . . .  . . .

Carl V. Thompson II

MASSACHUSETTS INSTITUTE
OF TECHNOLOGY

Professor of Electronic Materials
Chair, Departmental Committee on Graduate Students

NOV 07 1995

ARCHIVES

LIBRARIES

GRAIN GROWTH AND TEXTURE EVOLUTION IN THIN FILMS

by

Roland Carel

Submitted to the Department of Materials Science and Engineering on August 11, 1995, in partial fulfillment of the requirements for the degree of Doctor of Philosophy in Materials Science.

ABSTRACT

Microstructural and texture evolution during grain growth in polycrystalline thin films was investigated. Grain growth in thin films is a coarsening process driven by the reduction of grain boundary energy, surface energies, and strain energy density. Because crystal properties can be anisotropic, grain growth in thin films is an orientation selective process. Surface and interfacial energy minimization or reduction favors the growth of grains with low combined surface and interfacial free energy. For the films and substrates investigated in this thesis, surface and interfacial energy promotes the growth of (111)-textured grains. Thin films on thick substrates are usually subjected to a non-zero state of strain, arising from differential thermal expansion between the film and the substrate, from densification and from intrinsic strains. For elastically deformed fcc metal films, strain energy density promotes the growth of (001)-textured grains. In plastically deformed films, strain energy density can favor the growth of (011)-textured grains; this results from the orientation dependence of the yield stress of grains in thin films. (111) grains are predicted to maximize the yield stress, and (011) grains are predicted to have low yield stress. An analytic model for texture evolution during grain growth in thin films can be developed by equating the magnitudes of the orientation-dependent driving forces, for pairs of orientations. The analytic model can be used to generate texture maps that define which orientations are expected to grow preferentially as a function of the processing conditions, i.e., the deposition temperature, the grain growth temperature, and the film thickness. Experimental texture maps can be generated and used to test the validity of the analytic model.

Computer simulations of grain growth have been carried out using a front-tracking simulation method. Interfacial energy, elastic and plastic strain energy density, and grain growth stagnation are accounted for in the simulations. Materials parameters characteristic of Ag/(001)Ni were used. The main result of the simulations is to validate the analytic model for texture evolution during grain growth. The computer simulations also provide insights into the coupling between yielding and grain growth.

Grain growth experiments in Ag/(001)Ni/(001)Ag/(001)MgO, Ag/SiO₂/MgO, Ag/SiO₂/Si, Ni/SiO₂/Si, and Al/SiO₂/Si were carried out. Both the thickness and the thermal strain were systematically varied, and an experimental texture map was constructed for each system. The dependence of texture evolution on strain and thickness was found to be consistent with the trends predicted by the analytic model in all of these systems. While the texture map for Ag/(001)Ni was found in quantitative agreement with the model, with no adjustable parameters, no single set of fitting parameters was found for Ag/SiO₂/Si and for Ag/SiO₂/MgO. Possible origins of this discrepancy are discussed.

Additional experiments are proposed that could provide a better understanding of mechanical properties of thin films and of grain growth. Ultimately, texture and microstructural evolution during grain growth could be used to design effective processing so as to obtain desired microstructures. Grain growth could also be used in conjunction with a fully quantitative model to determine materials properties, for example interfacial energies.

Thesis Supervisor: Carl V. Thompson, Professor of Electronic Materials

Table of Contents

LIST OF FIGURES	8
LIST OF TABLES.....	17
ACKNOWLEDGMENTS	18
1 - REVIEW OF GRAIN GROWTH AND STRESS GENERATION IN THIN FILMS.....	19
1.1 - INTRODUCTION	19
1.2 - ORGANIZATION OF THIS THESIS.....	20
1.3 - FILM FORMATION AND INTRINSIC STRESS.....	21
<i>1.3.1 - Nucleation.....</i>	<i>22</i>
<i>1.3.2 - Island Formation.....</i>	<i>23</i>
<i>1.3.3 - Island Coalescence and Film Thickening.....</i>	<i>25</i>
<i>1.3.4 - Non-equilibrium growth</i>	<i>29</i>
<i>1.3.5 - Surface and interface stresses.....</i>	<i>30</i>
<i>1.3.6 - Epitaxial films and misfit dislocations</i>	<i>30</i>
<i>1.3.7 - Microstructure and stress state of as-deposited films</i>	<i>31</i>
1.4 - REVIEW OF GRAIN GROWTH	32
<i>1.4.1 - Phenomenology.....</i>	<i>32</i>
<i>1.4.2 - Grain growth as a quasi two-dimensional process</i>	<i>34</i>
<i>1.4.3 - Driving force for normal grain growth</i>	<i>35</i>
<i>1.4.4 - Grain boundary grooving</i>	<i>37</i>
<i>1.4.5 - Abnormal and secondary grain growth.....</i>	<i>41</i>
<i>1.4.6 - Macroscopic models of grain growth.....</i>	<i>44</i>
1.5 - GRAIN GROWTH AS A DENSIFICATION PROCESS.....	46

1.6 - SUMMARY	52
2 - ANALYTICAL MODEL FOR TEXTURE DEVELOPMENT DURING GRAIN GROWTH IN THIN FILMS	53
2.1 - INTRODUCTION.....	53
2.2 - STATE OF STRAIN AND STRESS OF A THIN FILM ON A SUBSTRATE.....	54
2.3 - ELASTIC ANISOTROPY.....	57
2.4 - YIELD STRESS OF A POLYCRYSTALLINE THIN FILM.....	64
2.4.1 - <i>Functional form for the yield stress of polycrystalline thin films</i>	65
2.4.2 - <i>Orientation and geometry dependent yield stress</i>	68
2.4.3 - <i>Coupling between yield stress and grain growth</i>	72
2.5 - SURFACE AND INTERFACE ENERGY	76
2.6 - DRIVING FORCES FOR GRAIN GROWTH	78
2.7 - ORIENTATION SELECTION DURING GRAIN GROWTH	81
2.8 - SUMMARY AND CONCLUSIONS	87
3 - COMPUTER SIMULATION OF GRAIN GROWTH IN THIN FILMS.....	89
3.1 - INTRODUCTION	89
3.2 - SIMULATION TECHNIQUES	89
3.2.1 - <i>Front tracking model</i>	90
3.2.2 - <i>Implementation of the strain energy density driving force</i>	92
3.3 - AG/Ni SYSTEM.....	93
3.3.1 - <i>Surface- and interface energy of the Ag/Ni system</i>	93
3.3.2 - <i>Mechanical properties of the Ag/Ni system</i>	95
3.4 - INITIAL CONDITION.....	97
3.5 - SIMULATION RESULTS	100

3.5.1 - Strain energy alone	100
3.5.2 - Surface and interface energy alone	107
3.5.3 - Combined effects of strain energy and surface and interface energy.....	109
3.6 - DISCUSSION AND CONCLUSIONS	120
4 - EXPERIMENTAL PROCEDURES	125
4.1 - INTRODUCTION	125
4.2 - FILM DEPOSITION	126
4.3 - X-RAY TEXTURE ANALYSIS	129
4.4 - CORRECTIONS TO THE X-RAY INTENSITY.....	133
5 - EPITAXIAL GRAIN GROWTH IN AG/(001)NI	138
5.1 - INTRODUCTION	138
5.2 - PREVIOUS WORK.....	139
5.2.1 - Prediction of the interface energy.....	139
5.2.2 - Interface energy sensitive experiments	142
5.2.2.1 - Zero creep experiment	142
5.2.2.2 - Rotating Crystallite Experiments	142
5.2.3 - Epitaxial grain growth experiments in Ag/(001)Ni.....	143
5.3 - EXPERIMENTAL DETAILS.....	146
5.4 - BONDING EXPERIMENT	147
5.4.1 - Experimental procedure	147
5.4.2 - Results.....	150
5.4.3 - Discussion.....	155
5.5 - ORIENTATION EVOLUTION DURING EGG IN AG/(001)Ni/(001)MGO.....	157
5.5.1 - Introduction	157

5.5.2 - Results.....	159
5.5.3 - Discussion.....	165
5.5.3.1 - Texture evolution during grain growth	165
5.5.3.2 - In-plane orientations.....	168
5.5.3.3 - Comparison with computer simulations	173
5.6 - SUMMARY AND CONCLUSIONS.....	175
6 - GRAIN GROWTH IN FILMS ON AMORPHOUS SUBSTRATES.....	177
6.1 - INTRODUCTION.....	177
6.2 - EXPERIMENTAL DETAILS.....	178
6.2.1 - Film deposition	178
6.2.2 - Statistical analysis of films microstructure	179
6.2.3 - Grain growth temperature and thermal strain.....	181
6.3 - Ag/SiO ₂ /SUBSTRATE	182
6.3.1 - Ag/SiO ₂ /MgO	182
6.3.2 - Ag/SiO ₂ /Si	186
6.3.3 - Discussion of Ag/SiO ₂ /MgO and Ag/SiO ₂ /Si	192
6.4 - Ni/SiO ₂ /Si	197
6.4.1 - Results.....	197
6.4.2 - Discussion of Ni/SiO ₂ /Si.....	201
6.5 - Al/SiO ₂ /Si	204
6.5.1 - Results and discussion.....	204
6.6 - TEXTURE MAPS FOR FILMS ON AMORPHOUS SUBSTRATES	207
6.7 - SUMMARY	211
7 - SUMMARY AND FUTURE WORK.....	212
7.1 - SUMMARY	212

7.2 - FUTURE WORK	217
APPENDIX I GRAIN GROWTH AS A DENSIFICATION PROCESS.....	223
APPENDIX II PLANE STRESS CONDITION AND ELASTICALLY ANISOTROPY	229
II.1 - FINITE ELEMENT SIMULATION	229
<i>II.1.1 - Spring analogy</i>	<i>230</i>
<i>II.1.2 - Finite element simulation.....</i>	<i>232</i>
II.2 - ABAQUS STACK	238
APPENDIX III - EXTREMA OF THE BIAXIAL MODULUS	241
APPENDIX IV - YIELD STRESS OF A RIGHT CIRCULAR CYLINDRICAL GRAIN.....	244
APPENDIX V - PROCESSING OF RAW POLE FIGURE DATA FILES	248
APPENDIX VI KINETICS OF GRAIN GROWTH IN AG/SiO₂/SI	257
VI.1 - EXPERIMENTAL.....	257
VI.2 - RESULTS AND DISCUSSION	258
BIBLIOGRAPHY	261

List of Figures

Figure 1.1: A spherical-cap-shaped particle on a substrate which it partially wets. θ is the equilibrium contact angle determined by the values of γ_f , γ_i , γ_s , the film surface and interface free energy and the substrate surface free energy, respectively. r^* is the size of the critical nucleus. 22

Figure 1.2: Grain boundary relaxation mechanism. It is energetically favorable for the islands to have a strained lattice and eliminate some of their free surface area to extend the forming grain boundary. This process is operative when the islands coalesce and during film thickening. 27

Figure 1.3: Stress in Au (high T_{dep}) and Co (low T_{dep}) films deposited on MgF_2 on quartz at 1 Å/s, measured in-situ by Abermann et al. [13]. 28

Figure 1.4: Two dimensional grain structure undergoing grain growth. 33

Figure 1.5: Schematic view of polycrystalline films with (a) equiaxed and (b) non equiaxed columnar grains structures. 34

Figure 1.6: Differential element dA of grain boundary moving toward its center of curvature and reducing its surface area by $\delta(dA)$. One possible choice for the curvatures κ_1 and κ_2 is also indicated. 37

Figure 1.7: (a) A grain boundary groove forms at the intersection of the grain boundary and film surface. (b) The grain boundary is trapped in the groove if it intersects the film surface at an angle θ_i less than θ_0 . (c) The stable shape of a circular grain with its grain boundary pinned in grooves at the top and bottom surfaces is a catenoid for which $\kappa_m = 0$ everywhere on the surface. 39

Figure 1.8: (a) Stagnant monomodal microstructure in films after normal grain growth. (b) Secondary grains grow larger in the stagnant matrix, resulting in a bimodal grain size

distribution. (c) Film entirely constituted of secondary grains. The grain size distribution is monomodal with the average grain size shifted toward larger values compared to (a). 42

Figure 1.9: (a) Total energy of films undergoing grain growth for two initial grain sizes. (b) Stagnant grain size of films undergoing grain growth plotted versus the initial grain size, for three levels of initial intrinsic stress..... 50

Figure 1.10: Tensile stress generated in films due to grain growth induced densification, plotted as a function of the average grain size in the film, for three initial grain sizes. 51

Figure 2.1: Thin film attached to a substrate of much greater thickness. Differential thermal expansion between the film and the substrate result in a film under biaxial strain.54

Figure 2.2: Natural coordinate system S for three textures, (001), (111), and (011), and its correspondence to crystallographic directions in the lattice of a cubic material..... 59

Figure 2.3: Contour plot of the biaxial modulus of Ag on a (001) stereographic projection. The modulus is maximum for (111)-textured grains and minimum for (001)-textured grains..... 62

Figure 2.4: Biaxial moduli for (001)- and (111)-textured Ag films plotted versus temperature. The difference between the biaxial moduli is also plotted. 63

Figure 2.5: Geometry of the slip system of an idealized grain undergoing plastic deformation..... 65

Figure 2.6: Orientation dependence of the yield stress in an Al film, plotted on a (001) stereographic projection. 71

Figure 2.7: Stress plotted versus strain for a perfectly elastic-plastic bulk material under uniaxial tension. The elastic and plastic components of the strain energy density are also indicated..... 73

Figure 2.8: Strain energy density of Al grains at the onset on yielding, plotted on a (001) stereographic projection.	76
Figure 2.9: (a) The surface and interface energy of films on amorphous substrates depends solely on the texture of the grains. (b) For epitaxial systems, the interface energy also depends on the in-plane orientation of the film with respect to the substrate lattice..	78
Figure 2.10: Right circular cylindrical grain with combined surface and interface energy γ_1 embedded in a uniform matrix with surface and interface energy γ_2	78
Figure 2.11: Canonical texture map showing the texture domains defined by equations (2.31), (2.33), and (2.34). The materials parameter chosen to generate the texture map are: $M_{111} = 170$ GPa, $M_{001} = 100$ GPa, $M_{011} = 140$ GPa, $C_h(111) = 165$ GPaÅ, $C_d(111) = 150$ GPaÅ, $C_h(001) = 150$ GPaÅ, $C_d(001) = 140$ GPaÅ, $C_h(011) = 120$ GPaÅ, $C_d(011) = 110$ GPaÅ, $b = 2.9$ Å, $\Delta\gamma_1 = 0.35$ J/m ² , $\Delta\gamma_2 = 0.65$ J/m ²	84
Figure 3.1: Motion of grain boundary points during one time step in the simulation. The triple points are moved such that the force balance is satisfied.....	91
Figure 3.2: Combined surface and interface energy for (001) and (111) Ag on (001)Ni as a function of twist orientation, as adapted from refs. [94, 95].....	94
Figure 3.3: (a) Elastic and total strain energy density of Ag grains plotted versus their grain diameter for a strain of 0.7%. (b) Elastic strain energy density difference between (001) and (111) Ag grains with the same grain diameter. The surface and interface energy density is also plotted, and in both cases the film is 1000 Å thick.	98
Figure 3.4a-b: Simulation of the effect of strain energy density alone. (a) $\tau = 5$, (b) $\tau = 43$	102
Figure 3.4c-d: (c) Structure at $\tau = 200$. No (111) grains remain. (d) Surface fraction of (001)- and (111)-textured grains plotted versus τ	103

Figure 3.5: Stagnated structures for simulations including the effect of strain energy density and the stagnation condition $F_{\text{stag}} = 0.4/\sqrt{A_0}$. (a) $\varepsilon = 0.001$, (b) $\varepsilon = 0.005$, (c) $\varepsilon = 0.01$ 104

Figure 3.6: Surface fraction of (001) grains, in excess of 50%, for stagnated structures and plotted as a function of the applied strain. The stagnation condition $F_{\text{stag}} = 0.4/\sqrt{A_0}$ was enforced. 106

Figure 3.7: (a) Surface fraction of grains with (001) and (111) textures as a function of twist orientation, as initialized at $\tau = 0.1$. (b) Stagnated structure when surface and interface energy and the stagnated condition $F_{\text{stag}} = 0.4/\sqrt{A_0}$ are introduced. (c) Distribution of orientations in the stagnated structure. 108

Figure 3.8: (a) Stagnated structure when the effects of surface and interface energy and of the stagnation condition $F_{\text{stag}} = 0.2/\sqrt{A_0}$ are simulated. (b) Distribution of orientations for the stagnated structure: all grains are (111)-textured. 110

Figure 3.9: Dominant texture at stagnation plotted as a function of the structure thickness and the applied strain. This constitutes a texture map for the simulation results. The solid line represents the driving force balance in the elastic regime (eq. 3.9) and the dashed line represents the driving force balance when (001) grains are yielded (eq. 3.10). 112

Figure 3.10a-b: Combined effects of strain energy anisotropy, surface and interface energy anisotropy and of the stagnation condition $F_{\text{stag}} = 0.4/\sqrt{A_0}$. The structure and the orientation distribution are shown at $\tau = 5$ 116

Figure 3.10c-d: Simulated grain structure and orientation distribution at $\tau = 20$ 117

Figure 3.10e-g: (e) Stagnated structure, $\tau = 103$. (f) Distribution of orientation of (001) and (111) as a function of twist orientation. (g) Surface fraction of (001)- and (111)-textured grains as a function of τ 118

Figure 3.11: Evolution of the relative surface fraction of grains in the (001);26° and (111);0° twist orientations as a function of τ	119
Figure 4.1: Geometry for x-ray texture analysis. The source and detector are in the symmetric θ -2 θ geometry. Only grains with (hkl) planes parallel to the reference plane contribute to the intensity. (a) The film is parallel to the reference plane ($\alpha = 0^\circ$). (hkl)-textured grain diffract the beam. (b) The film is tilted by an amount α and rotated by an amount β , bringing the (hkl) planes of other grains in diffraction condition.....	131
Figure 4.2: Pole figure chart. α is the angular radial coordinate and β is the azimuthal coordinate.	134
Figure 5.1: Combined surface and interface energy for (001)Ag l(001)Ni and (111)Ag l(111)Ni as calculated by Gao, Dregia and Shewmon [94, 95] using an embedded atom potential and molecular static atomic relaxation. A similar plot can be found in ref. [47]......	141
Figure 5.2: Hydrogen bonding furnace.....	149
Figure 5.3: Ag/(001) Ni as bonded at 350°C for 20 min. (a) $\langle 111 \rangle$ Ag pole figure. (b) Intensity integrated with respect to β and plotted versus α . The data presented in this figure and all figures in this chapter are corrected for background scattering, finite thickness and defocussing (chapter four, section 4.3)	152
Figure 5.4a-b: Bonded sample after annealing at 600°C for 1 h. (a) $\langle 111 \rangle$ Ag pole figure. Crystallographic direction in the Ni lattice are also indicated. (b) Intensity at $\alpha = 71^\circ$, characteristic of (111)-textured Ag, plotted versus β	153
Figure 5.4c: Intensity integrated with respect to β and plotted versus α	154

Figure 5.5: $\langle 111 \rangle$ Ag β -scan at $\alpha = 55^\circ$ for a 4000 Å thick Ag film bonded at 300°C for 20 min and annealed at 550°C for 1 h. The four peak of intensity correspond to the (001);0° orientation.	154
Figure 5.6: $\langle 111 \rangle$ Ag polefigure of an as-deposited 2500 Å thick Ag films deposited at -47°C.....	160
Figure 5.7: $\langle 111 \rangle$ Ag poles figure of a 2500 Å thick film deposited at 30°C and annealed at 400°C for 3h.....	162
Figure 5.8: $\langle 111 \rangle$ Ag pole figures of films annealed at 400°C for 3h. (a) 1000 Å thick film deposited at -158°C . (b) 3400 Å thick film deposited at -148°C.....	163
Figure 5.9: Texture map for Ag/(001) Ni/(001) Ag/(001) MgO.	164
Figure 5.10: FIB image of a 3500 Å thick film deposited at -53°C at annealed at 400°C for 3 h.	165
Figure 5.11: (a) In-plane strain (ϵ_1) in the Ag film due to differential thermal expansion between Ag and MgO. (b) Yield strain of (001) and (111) Ag grains as a function of the film thickness and for two different relationship between grain diameter and film thickness.	167
Figure 5.12: Results of the computer simulation and of the EGG experiments in Ag(001)/(001)Ni(001)Ag/(001)MgO plotted on the same texture map. The lines defined by equations (2.31) and (3.10) are also plotted.	174
Figure 6.1: Thermal strain in films when heated from the deposition temperature to the grain growth temperature.	182
Figure 6.2: $\langle 222 \rangle$ Ag rocking curve for a 2500 Å thick Ag/SiO ₂ /MgO film deposited at 30°C and annealed at 400°C for 1h.....	183

Figure 6.3: Ratio of diffracted intensity for (001) and (111) textures, plotted versus film thickness for as-deposited Ag/SiO ₂ /MgO films. The x-ray data was acquired with the <222> Ag Bragg peak.	185
Figure 6.4: Texture map for Ag/SiO ₂ /MgO.....	186
Figure 6.5a-c: <111> Ag rocking curves of Ag/SiO ₂ /Si samples. (a) film deposited at 4°C, 3800 Å thick, as-deposited. (b) 600 Å thick film deposited at -80°C, and annealed at 350°C for 35 min. (c) 3800 Å thick film deposited at 5°C, and annealed at 350°C for 30 min.....	188
Figure 6.5d: 4000 Å thick film, deposited at -125°C and annealed at 350°C for 30 min.	189
Figure 6.6: TEM micrographs of Ag/SiO ₂ /Si films. (a) 600 Å thick film deposited at 5°C, as-deposited. (b) 2200 Å thick film deposited at 3°C and annealed at 350°C for 30 min.	190
Figure 6.7: Average grain size in as-deposited and annealed Ag/SiO ₂ /Si films. 90% confidence intervals are also plotted.....	191
Figure 6.8: Texture map Ag/SiO ₂ /Si.	192
Figure 6.9: Strain energy density differences and surface and interface volumetric energy differences between (001) and (111) Ag grains plotted versus film thickness. The strain energy of yielded grains is calculated assuming $d = h$	193
Figure 6.10: <111> Ni rocking curves of Ni/SiO ₂ /Si samples. (a) film deposited at 20°C, 2000 Å thick, as-deposited. (b) 2100 Å thick film deposited at 75°C, and annealed at 560°C for 45 min. (c) 3800 Å thick film deposited at -171°C, and annealed at 560°C for 45 min.....	198
Figure 6.11: TEM micrographs of Ni/SiO ₂ /Si films. (a) 600 Å thick film deposited at 20°C, as-deposited. (b) 600 Å thick film deposited at 20°C and annealed at 560°C for 45 min.....	200

Figure 6.12: Average grain size in annealed Ni/SiO ₂ /Si films. 90% confidence intervals for the average grain size are also plotted.	201
Figure 6.13: Texture map for Ni/SiO ₂ /Si.....	202
Figure 6.14: Strain energy density differences and surface and interface volumetric energy differences between (001) and (111) grains in Ni/SiO ₂ /Si film, plotted versus film thickness. The strain energy of yielded grains is calculated assuming $d = h$. ΔT is given in °C for $T_{gg} = 550^\circ\text{C}$	203
Figure 6.15: $\langle 222 \rangle$ Al rocking curves for Al/SiO ₂ /Si samples. (a) 6000 Å thick film deposited at 30°C. (b) 2000 Å thick film deposited at 0°C and annealed at 300°C for 1 h.	205
Figure 6.16: Texture map for Al/SiO ₂ /Si. The boundary corresponds to equation (2.32) and is plotted for $\Delta\gamma = 0.5 \text{ J/m}^2$. The squares correspond to pure Al films. The triangle correspond to an Al-0.3%Cr-2%Cu film and is from ref. [120].	206
Figure 6.17: Strain energy density differences and surface and interface volumetric energy differences between (011) and (111) Al grains plotted versus film thickness. The strain energy of yielded grains is calculated assuming $d = h$. ΔT is given in °C for $T_{gg} = 250^\circ\text{C}$	207
Figure 7.1: Texture map for Ag/(001)Ni/(001)Ag/(001)MgO, Ag/SiO ₂ /MgO, Ag/SiO ₂ /Si, and Ni/SiO ₂ /Si. The total strain (ϵ) is the sum of the thermal (ϵ_{th}), the intrinsic (ϵ_i), and the densification (ϵ_d) strains. The adimensional parameter g is defined as $g = (M_{111} - M_{001})h/\Delta\gamma$	218
Figure I.1: Effect of the anisotropy of surface and interface energy on the total energy of the film. (a) $d_0 = 20 \text{ \AA}$, (b) $d_0 = 50 \text{ \AA}$. The materials parameter chosen are $\gamma_{gb} = 0.2 \text{ J/m}^2$, $M = E/(1-\nu) = 137 \text{ GPa}$, $\Delta a = 1 \text{ \AA}$, $\Delta\gamma = 0.5 \text{ J/m}^2$, $h = 1000 \text{ \AA}$, $M_1 = 157 \text{ GPa}$, $M_2 = 117 \text{ GPa}$	227
Figure II.1: Spring analogy of neighboring grains with different orientations in an elastically anisotropic film.....	231

Figure II.2: The simulated grain structure consists of an infinite square array of alternating (001)- and (111)-textured grains. It is sufficient to discretize one-half of a (001) grain and one half of a (111) grain to simulate this grain structure as shown by the dashed square. .233

Figure II.3: Initial and relaxed position for a structure where the film thickness and grain diameter are equal ($2r = d = h$). The displacement are multiplied by a factor of 10..... 234

Figure II.4: Contour plot of ϵ_{11} , ϵ_{33} , σ_{11} , σ_{33} for a relaxed film with $d = 8h$. The other components of the stress and strain are also non-uniform with strong gradients near the grain boundary. 235

Figure II.5: Strain energy density of (001) and (111) grains as calculated by Abaqus, normalized by the strain energy density of grains in the same orientation and under uniform biaxial strain and plane stress, plotted versus the aspect ratio of the grain diameter to the film thickness..... 236

Figure III.1: Function $f(\theta, \varphi)$ plotted versus θ and φ for $0 \leq \varphi \leq \pi/2$ and $0 \leq \theta \leq \pi$. The maximum is found at $\theta = \varphi = \pi/4$, or equivalently at $h = k = 1 = 1/\sqrt{3}$ 243

Figure IV.1: The intersection of the glide plane with the grain is a truncated ellipse. ... 245

Figure IV.2: Yield stress for (001)-textured Al grains plotted versus film thickness and assuming $d = h/2$. (a) Analytic expression for the yield stress as given by equation (2.20), (b) Equation (IV.5). The difference between the two expressions can be substantial at small thicknesses and/or grain sizes. 246

Figure VI.1: Relative intensity of the (111) Ag Bragg peak for Ag/SiO₂/Si samples during isothermal anneals. 259

Figure VI.2: Arrhenius plot for the rate of change of the intensity of the (111) Ag Bragg peak with time. 260

List of Tables

Table 2.1: Stiffnesses and anisotropy ratio for the materials investigated in this thesis. The values are characteristic of bulk material and are from ref. [74].	63
Table 2.2: Orientation-dependent coefficients for the thickness and grain size of the yield stress of polycrystalline films used in this work. The magnitude of the Burgers vector for each material is also given.	69
Table 4.1: X-ray absorption coefficients for Cu $K_{\alpha 1}$ radiation at $\lambda = 1.5405 \text{ \AA}$	136
Table 6.1: Average grain sizes in one as-deposited and two annealed sample. 90% confidence intervals for the grain sizes are also given.	204

Acknowledgments

I am indebted to more people who have contributed to this work than I can acknowledge in a few sentences. May those I neglect or to mention here forgive me.

I am especially grateful to my thesis advisor, Carl Thompson who showed me new ways of approaching scientific problems. I would also like to thank my thesis committee members, Subra Suresh and Stuart Brown for their insights on mechanical properties, Samuel Allen for his detailed reading of this thesis, and Bernhardt Wuensch for accepting to attend my final defense. I would also like to thank Harold Frost for enlightening me on the differences between mechanical properties of thin films and of bulk materials.

Joe Adario, Peter Klouman, John Martin, Tim McLure, and Rich Perilli were all invaluable sources of information and of technical help.

Jerry Floro had infinite knowledge of vacuum systems tricks and traps, and I am very grateful to him for having provided me as much knowledge as I could absorb. He is also at the origin of many of the ideas in this thesis, and I am especially grateful to him for that.

Thanks to Brett Knowlton, Steve Seel, Young-Chang Joo, Heather Inglefield, Srikar Vengallatore, Steve Cooperman, Hal Kahn, Hai Longworth, and all of the MIT students I had a chance to interact with.

Finally, I would like to acknowledge Sheila Carel who is the primary reason for my coming to MIT and completing this Ph. D.. Her moral support and her editorial help were also invaluable for the writing of this thesis.

Chapter 1

Grain Growth and Stress Generation in Thin Films

1.1 - Introduction

Polycrystalline thin films are technologically very important for a wide range of products and applications. They are used for example as wear resistant coatings, as catalytic elements [1], as optically active coatings and optical device elements [2-3], as magnetic media for information storage [4], as electrical conductors [5], and electrically active elements of microelectronics devices [6]. For all of these applications, the properties and characteristics of the film depend strongly on its microstructure and orientation. For example, the reliability of aluminum interconnects in integrated circuits as defined by a median time to failure can vary by a factor of three or more when the average grain size varies for a given line width [7] and by a factor of more than eight for single crystal lines with different crystallographic orientations [8]. The average grain size, the distribution of grain sizes, and the distribution of grain orientations are important parameters to control to optimize the functionality, performance, and reliability of polycrystalline films.

Grain growth is known to influence and often determine the microstructure of thin films. This is due to the large driving forces available for grain growth arising from three main sources of excess energy: grain boundary energy, the energies of the film surfaces, and strain energy.

The focus of this thesis is to develop and validate a formalism describing the evolution of the microstructure and orientation in metallic thin films during grain growth for different materials systems processed under different conditions. This approach can ultimately lead to a predictive model for grain growth in thin films which could be used as a guide to optimize the properties of polycrystalline films for specific applications.

1.2 - Organization of this thesis

In this chapter, film formation and intrinsic stress generation during deposition are first reviewed. The phenomenology of grain growth is then examined as well as the effect of the film free surface and the film interface, and the effect of thermal grooves at the grain boundaries. Tensile stress generation during grain growth is also discussed. Chapter two is devoted to the development of an analytic model for texture evolution during grain growth. Chapter three presents results of computer simulations of two-dimensional grain growth, including two orientation-dependent driving forces arising from surface and interface energy anisotropy and strain energy density anisotropy. Chapter four describes experimental procedures and reviews x-ray texture analysis. Chapter five presents experimental results on orientation and microstructural evolution occurring during grain growth in Ag/(001)Ni. Chapter six is devoted to the case of grain growth in films on amorphous substrates and presents experimental results for a number of film/substrate materials systems. In chapter seven, the results of this work are summarized and conclusions are drawn. The usefulness of the model developed in this thesis and its predictive value is reviewed, and additional experiments are proposed. Finally, appendixes

develop issues related to this thesis, including a kinetic study of grain growth in Ag/SiO₂/Si.

1.3 - Film Formation and Intrinsic Stress

We review film formation focusing particularly on orientation selection and intrinsic stress generation during deposition. This discussion is restricted to physical vapor deposition (PVD) processes such as evaporated or sputtered films, even though many of the concepts presented here are valid for films deposited by chemical vapor deposition (CVD). The goal is to present an accurate description of the as-deposited structure of films in which subsequent grain growth can occur and to understand how deposition conditions affect the as-deposited microstructure and orientation of films.

We restrict our discussion to materials that partially wet the substrate on which they are deposited, as illustrated in Figure 1.1, and that grow by the Volmer-Weber growth mode where isolated islands are nucleated and grow to impingement, forming the grain boundaries of the as-deposited grain structure. This requires that the free energy of the substrate γ_s , the free surface energy of the material γ_f , and the free energy of the film-substrate interface γ_i satisfy the inequalities [9]:

$$\gamma_s + 2\gamma_f > \gamma_i + \gamma_f > \gamma_s, \quad (1.1)$$

which is satisfied for the films examined in this thesis.

In this section, we assume for simplicity that γ_i , γ_f , and γ_s are isotropic. The influence of anisotropic free surface/interface energies is treated in detail in sections 1.4.5 and 2.5.

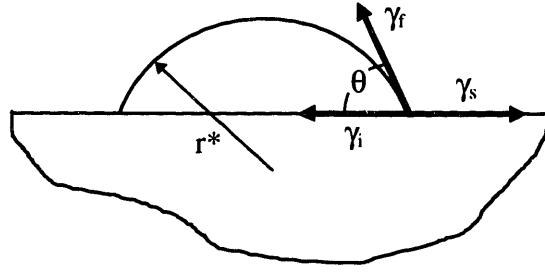


Figure 1.1: A spherical-cap-shaped particle on a substrate which it partially wets. θ is the equilibrium contact angle determined by the values of γ_f , γ_i , γ_s , the film surface and interface free energy and the substrate surface free energy, respectively. r^* is the size of the critical nucleus.

1.3.1 - Nucleation

Consider a film formed through heterogeneous nucleation (Figure 1.1). We determine an estimate for the size r^* of the critical nucleus. The classical extremum determination of the free energy change associated with the formation of the nucleus yields the size of the critical nucleus [9]

$$r^* = -\frac{2\gamma_f}{\Delta g_v} \quad , \quad (1.2)$$

where Δg_v is the free energy of condensation of the vapor phase into the solid phase and can be expressed as a function of the supersaturation of the vapor phase

$$\Delta g_v = -RT_{\text{subs}} \ln \left(\frac{p_{\text{act}}}{p_{\text{eq}}} \right) \quad , \quad (1.3)$$

where p_{act} and p_{eq} are the actual and equilibrium pressures of the nucleating species at the substrate surface, respectively, and T_{subs} is the substrate temperature. p_{eq} can be estimated from thermodynamic data [10] and is typically quite low for films deposited by a PVD process on substrates at or below room temperature. For example, for Al, Au, Cu, Ni, Ag at room temperature, the equilibrium partial pressures are 1×10^{-47} Torr, 1×10^{-54} Torr,

1×10^{-49} Torr, 1×10^{-64} Torr, 1×10^{-40} Torr, respectively. The actual pressure at the substrate surface can be estimated from kinetic gas theory [9] as

$$P_{\text{act}} \cong \sqrt{2\pi mkT_{\text{subs}}} \frac{\rho D}{m}, \quad (1.4)$$

where m is the atomic mass, k is Boltzman's constant, D is the deposition rate, and ρ is the density of the material to be deposited, and where the sticking coefficient of the impinging species is assumed to be 1. The actual pressure is therefore of order 5×10^{-16} Torr for a fcc metal film grown at a typical rate of 1 \AA/s , and equations (1.2)-(1.4) yield a critical radius r^* of about 1 \AA . It is therefore not meaningful to discuss orientation-selection or intrinsic stress generation during nucleation under these conditions.

1.3.2 - Island Formation

When the islands are large enough to be described by the continuum approach presented in section 1.3.1, they grow primarily by adatom attachment on their perimeter. Atoms in the vapor phase impinge on the substrate and migrate by surface diffusion to get incorporated in the islands. The islands have different sizes and orientations relative to the substrate and therefore different free energy density. The atoms can migrate from island to island by surface diffusion, and it is possible that some coarsening occurs at this stage of film formation, leading to the preferential growth of islands with minimum values of surface and interface energy [11]. The growth rate can be surface diffusion limited or interface limited, leading to different island size distribution. However, because there is little or no barrier to nucleation, the island spacing should be on the order of the dimer spacing which is expected to be small, of order 100 \AA or less [12]. The as-deposited grain

size of continuous metallic films is usually observed to be greater than this expected island spacing, indicating that coarsening of the microstructure occurs during or after nucleation.

At this pre-coalescence stage of the film formation, several stress generation mechanisms have been proposed [13-15]. We review one of them, of particular interest to this work. Consider an elastically isotropic particle with the equilibrium bulk lattice spacing. The particle can decrease its free surface and interface energy by decreasing its volume, i.e., its lattice spacing. Neglecting surface and interface stresses, the energetic penalty for doing so is the corresponding strain energy density of the compressively strained particle. For a hemispherical particle of radius R , the equilibrium lattice spacing d corresponding to the minimum energy state is [14]

$$d = d_0 \left(1 - \frac{2\gamma_f}{3RK} \right), \quad (1.5)$$

where d_0 is the bulk lattice spacing and K the bulk modulus of the material. The equilibrium lattice spacing increases with the size of the particle, asymptotically reaching the lattice spacing of the bulk. If the crystallite is firmly attached to the substrate in a zero stress state when its size is R_1 , the lattice of the particle is constrained to have the spacing defined by equation (1.5). If the particle grows as a single crystal, and assuming that the lattice parameter is uniform throughout the particle, an increase in size $\Delta R = R_2 - R_1$ leads to the development of a compressive stress $\Delta\sigma$ as the lattice parameter of the particle is constrained to be the same as it was at R_1 [13]:

$$\Delta\sigma \cong -2\gamma_f \left(\frac{1-2\nu}{1-\nu} \right) h \frac{\Delta R}{R_1^2} , \quad (1.6)$$

where h is the average film thickness and ν the Poisson ratio of the film¹. Compressive stresses in discontinuous films of fcc metals deposited on amorphous substrates have been observed and are attributed to this mechanism [13].

1.3.3 - Island Coalescence and Film Thickening

As islands coalesce and form grain boundaries, coarsening can occur through surface diffusion and through grain boundary motion, which is a form of grain growth. Grain growth during film coalescence has been observed experimentally [16, 17] but has not been studied or modeled in detail. In the case of Au e-beam evaporated on an oxidized Si substrate [16], the discontinuous film consists of small ($< 100 \text{ \AA}$), randomly oriented islands. As the film coalesces, a few (111)-textured grains grow in the film, much larger than the other grains. As the film is further thickened, (111)-textured grains represent an increasing volume fraction in the film.

Grain growth during film coalescence can control the microstructure and texture of the film. Grains with low free surface and interface energy density grow faster than grains in other orientations and can occupy a large volume fraction of the film. (111) grains of fcc materials deposited on amorphous substrates are expected to be in the surface and interface energy minimizing orientation since (111) crystallographic planes are close-packed and minimize the number of frustrated atomic bonds at the surface and interface of

¹ The derivation in reference [13] is incorrect and the expression for the compressive stress $\Delta\sigma$ is different from equation (1.6). Equation (1.6) is the correct expression for the compressive stress resulting from equation (1.5).

the grains. The strain energy density anisotropy can also potentially drive orientation evolution at this stage of film formation. However, for very thin films, the surface to volume ratio is large and the influence of the surface is expected to dominate volume anisotropies. The occurrence of grain growth during deposition can be the origin of the often observed as-deposited (111) texture of fcc metallic thin films.

The mechanism of intrinsic stress development of thickening films has been analyzed in refs. [15, 18-21]. Most proposed stress generation mechanisms are related to a density deficit of the film compared to the equilibrium bulk value and predict a tensile intrinsic stress. For example, Hoffman [20] and Doener and Nix [15] proposed that a tensile stress is generated through grain boundary relaxation. This mechanism, illustrated in Figure 1.2, considers the energetic penalty of straining the lattice of the two adjacent grains to extend the forming grain boundary and the energetic gain of eliminating two elements of free surface and forming one element of grain boundary. The equilibrium tensile stress generated can be as high as several GPa, as calculated by Nix [21].

Abermann has argued that isolated islands are compressively strained, as described in the previous section and that film growth post coalescence occurs by homoepitaxy on the already formed grains [13]. If the growth rate of the grains is orientation dependent, high growth rate grains can widen when the film thickens, occluding grains with smaller growth rates. Growth rate anisotropy requires that impinging atoms migrate by surface diffusion [15] (Figure 1.5b p. 34) from grain to grain and only occurs if the mobility of the atoms at the surface of the film is high. This is the case for materials deposited at high

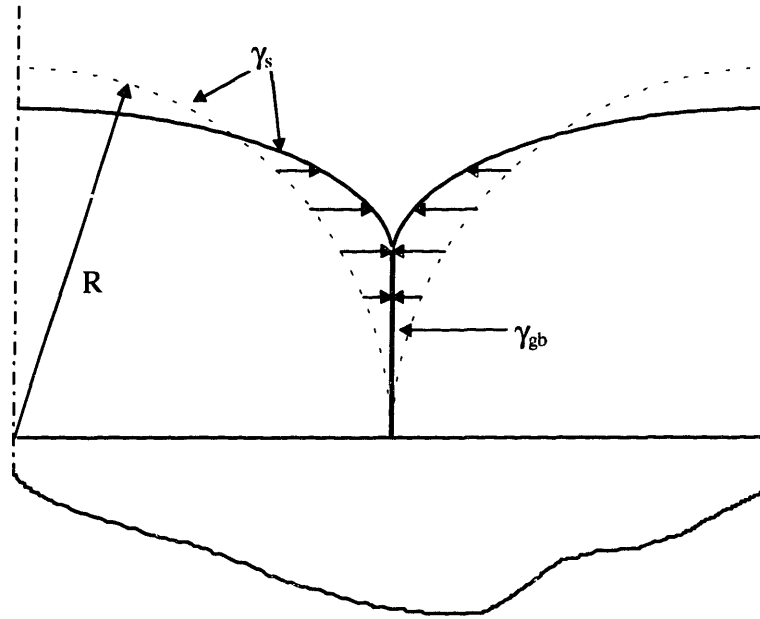


Figure 1.2: Grain boundary relaxation mechanism. It is energetically favorable for the islands to have a strained lattice and eliminate some of their free surface area to extend the forming grain boundary. This process is operative when the islands coalesce and during film thickening.

temperature relative to their melting point ($T_{\text{dep}}^r = T_{\text{dep}}(K)/T_m(K)$). This leads to a decreasing grain boundary length per unit area of the film free surface as the film thickens, and to a decreasing influence of the tensile stress generated by grain boundary relaxation. As the compressive stress due to the smaller than equilibrium lattice parameter of the grains generates a compressive stress that increases linearly with film thickness, it ultimately dominates the global state of stress of the film. Figure 1.3 illustrates the stress in films of Au and Co during deposition as measured in-situ by Abermann et al. [13]. They found that the maximum compressive stress measured was around -200 MPa for Au and less than -40 MPa for other fcc metals. Whether as-deposited films of high mobility

materials are under compressive stress or if the stress measured is an artifact of the temperature change occurring during deposition is still under debate [22]. For refractory metals such as W and Co, the predicted and measured states of stress in as-deposited films are tensile and as high as several GPa [13].

Grain growth in thickening films is more likely in high mobility materials, where T_{dep}^r is high [12]. Grain growth during deposition in high mobility materials will upset the compressive stress generation mechanism proposed by Abermann et al. if the time scale for grain boundary migration is faster than the time scale for film growth, as the microstructure of the film will be formed of columnar grains (Figure 1.5a p. 34), with uniform width through the thickness of the film, and therefore constant grain boundary

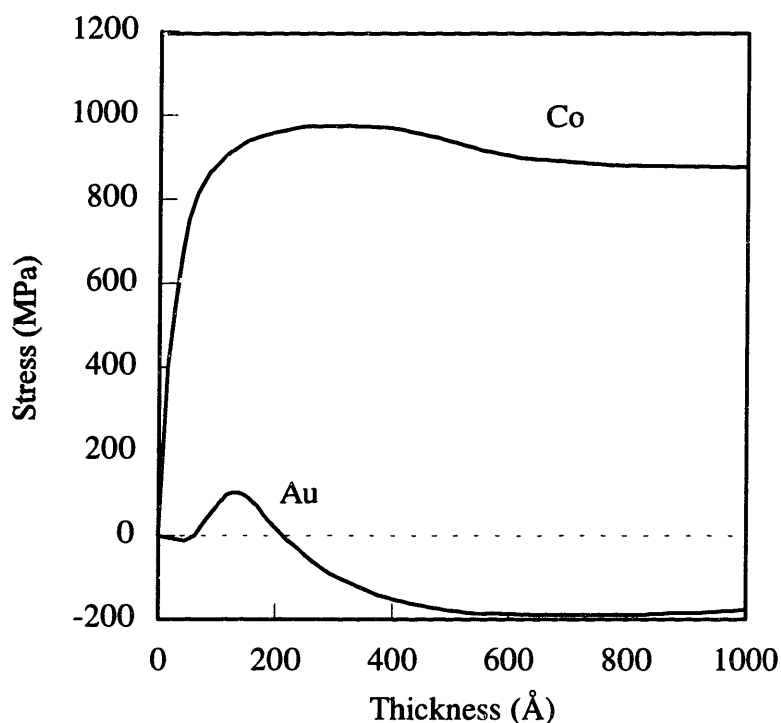


Figure 1.3: Stress in Au (high T_{dep}^r) and Co (low T_{dep}^r) films deposited on MgF_2 on quartz at 1 \AA/s , measured in-situ by Abermann et al. [13].

length per unit surface area through the thickness of the film. Grain growth occurring in thickening films or after deposition also generates a tensile stress in the film. We postpone the discussion of this mechanism until section 1.5 as part of the review of grain growth in thin films.

1.3.4 - Non-equilibrium growth

Non-equilibrium growth can occur at any stage of film formation and thickening and is likely to induce tensile stresses in the material [15, 23]. Films deposited in a metastable state in which subsequent atomic rearrangement takes place are often under tensile stress. For example, in metallic films, excess vacancy concentration can induce diffusion and annihilation of these vacancies at the grain boundaries, generating a tensile stress. If the film is not allowed to change structurally, no stress will develop. For metallic films, a “frozen-in” structure is only possible below 4 K [23] and is not of interest here. The magnitude of the tensile stress depends on the kinetic processes active during film formation. It involves the rate of atomic motion on the surface during deposition compared to the deposition rate, the kinetics of the rearrangement process, and the kinetics of stress relaxation. It is difficult to accurately quantify each of these processes and separate their relative contributions. Intrinsic stresses arising from non-equilibrium growth are most likely to occur in films of refractory metal [15] and less likely in high mobility materials such as the fcc metals.

1.3.5 - Surface and interface stresses

Surface and interface stresses arise because the nature of the chemical bonding of the atoms at the surface and interface of films is different from the bonding of atoms in the bulk. As chemical bonding determines the equilibrium position of atoms, and as the atoms at the surface and interface are constrained in their position, the interior of the film can be considered as exerting a stress on the surface and interface. While surface and interface stresses are localized at the surface and interface of films and do not lead to intrinsic stresses in the interior of the films, they contribute along with bulk intrinsic and extrinsic stresses to substrate bending [15]. This effect is significant only in very thin films or multilayers with periodicity less than 100 Å [24]. In such films or multilayers, surface and interface stresses can also lead to modulus enhancement as the displacement of atoms associated with surface and interface stresses can be large and anelastic effects have to be considered [24]. This effect is examined in more detail in chapter two. Another potentially important consequence of surface and interface stresses is that they can induce changes in the surface and interface free energy of strained films [24]. This effect is examined in the context of the epitaxial grain growth experiments in Ag/(001)Ni presented in chapter five.

1.3.6 - Epitaxial films and misfit dislocations

When a film is grown with an epitaxial relationship with the substrate, strain can develop in the film because of the lattice mismatch between the film and the substrate. The strain energy density in the film increases until it is energetically favorable for a series of misfit dislocations to form at the film/substrate interface and relieve part of the

mismatch between the film and the substrate. There is a critical thickness below which the coherently strained film is stable and above which an array of misfit dislocations forms. The critical thickness can be calculated based on a minimum energy criterion [25] or measured using a variety of experimental techniques [26, 27]. When the film thickness is greater than the critical thickness the density of the array of misfit dislocations increases with thickness until the film/substrate interface is incoherent, at which point all the epitaxial strain in the film is relieved. For most systems, the critical thickness is usually small, of order 200 Å or less [25]. When the film/substrate interface is incoherent, the intrinsic stress associated with the array of misfit dislocations is localized near the film-substrate interface [27]. Misfit dislocations offer a convenient description of film-substrate interfaces for simple epitaxial relationships between films and substrates when the misfit is sufficiently small to avoid overlap of the dislocation cores. When this is not the case, atomistic simulations are necessary to describe the interface structure, energy, and stress field.

1.3.7 - Microstructure and stress state of as-deposited films

As reviewed in the previous sections, the microstructure and stress state of as-deposited films is potentially influenced by many physical phenomena. The mechanisms dominating microstructure formation and intrinsic stress generation depend greatly on the film/substrate materials system and the processing conditions of the film, i.e., the deposition temperature, the growth rate, the thickness, and the base and deposition pressure. It is beyond the scope of this thesis to separate the respective contributions to the stress in the as-deposited film of each of the mechanisms reviewed in the previous

section. However, since the object of study of this thesis is post-deposition quasi two-dimensional grain growth, the important facts relevant here are:

1 - For all the fcc metals investigated by Abermann et al. [13], except Au, the magnitude of the as-deposited stress is less than 40 MPa. It is shown in subsequent chapters that the strains and stresses arising from differential thermal expansion between the film and the substrate are easily greater than the as-deposited stress. Intrinsic stresses will be considered when appropriate.

2 - Some grain growth can occur during deposition or after deposition, due to the large driving forces available, without the need of a significant temperature change. We will call the as-deposited microstructure, the stagnant microstructure of the film post-deposition when no evolution can be detected. Subsequent grain growth is induced in the film by raising the temperature of the film/substrate system until substantial grain boundary motion occurs. Evidence of athermal grain growth and a discussion on its consequences for texture evolution is found in chapter six.

1.4 - Review of grain growth

1.4.1 - Phenomenology

Most materials are polycrystalline. The grain boundaries have excess energy associated with them which provides a thermodynamic driving force for normal grain growth. Normal grain growth in a polycrystalline material is a coarsening mechanism driven by the reduction of the total grain boundary surface area present in the material. Unlike most other phase transformations, there is usually no chemical component of the

free energy change associated with the transformation. As grain boundary area is reduced in the material, the average grain size must increase and the total number of grains must decrease. This is illustrated in Figure 1.4 which shows a two-dimensional grain structure undergoing grain growth. We focus on the grains numbered one to three on the Figure 1.4a. After some grain growth has occurred (Figure 1.4b), grain one has increased in size and grain three has decreased in size.

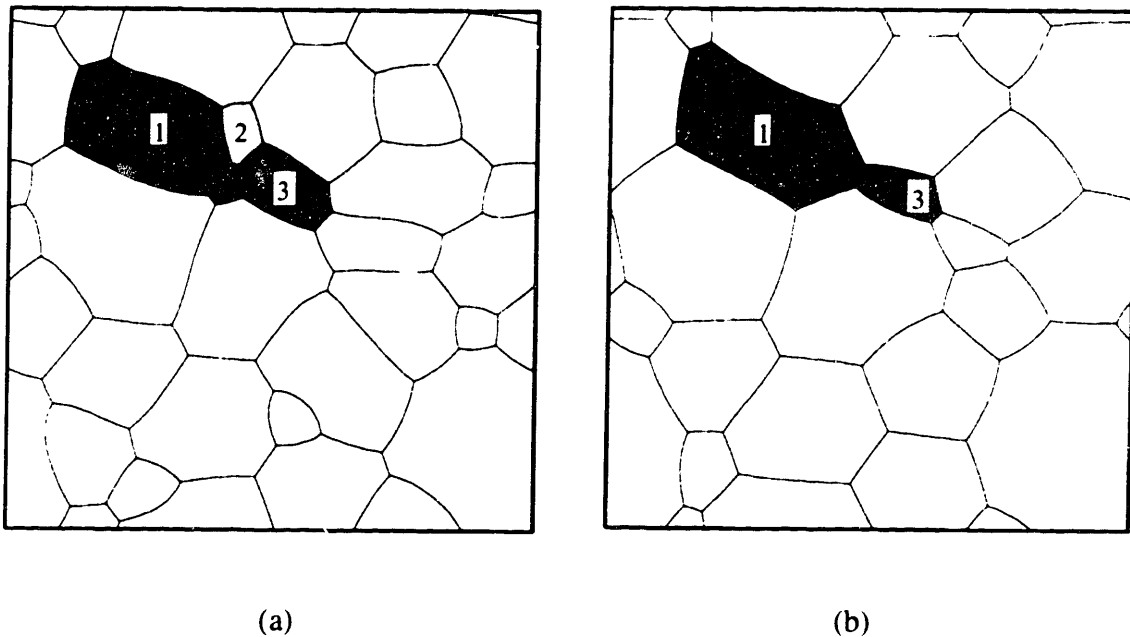


Figure 1.4: Two dimensional grain structure undergoing grain growth.

Grain two in Figure 1.4a has disappeared from Figure 1.4b and grains one and three share a common grain boundary in Figure 1.4b as they do not in Figure 1.4a. This illustrates the possible topological events occurring during grain growth: grain disappearance and neighbor switching. Contrary to recrystallization, no new grains are nucleated during grain growth. This constrains the distribution of grain sizes observed as

grain growth proceeds. Grain growth is a self-similar process which means that the grain structure seen at different times only differs by a size scale. The steady state grain size distribution function is invariant through time for a polycrystalline material undergoing normal grain growth, when the grain size is normalized by the average grain size in the film.

1.4.2 - Grain growth as a quasi two-dimensional process

Grain growth in bulk materials is usually a three dimensional process where the average grain size is much smaller than the macroscopic dimensions of the material. In thin films, the average grain size can be greater than the thickness of the film which results

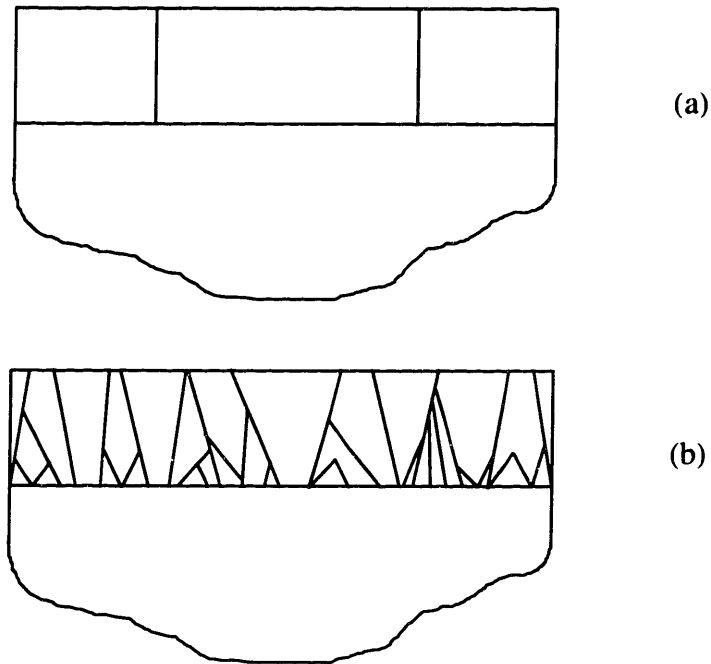


Figure 1.5: Schematic view of polycrystalline films with (a) equiaxed, and (b) non equiaxed columnar grains structures.

in a columnar grain structure such as illustrated on Figure 1.5a. Such films constitute the main object of study of this thesis. When the microstructure of films is columnar, grain boundary motion proceeds primarily parallel to the plane of the film and not perpendicular to it. It is sufficient to observe the motion of the one dimensional intersection of the grain boundaries with the surface of the film to characterize the motion of the grain boundaries. Grain growth in thin films can therefore be idealized as a quasi-two-dimensional process. Because of the presence of the film surface and the film-substrate interface, grain growth is however not a truly two dimensional process. We show in the following sections how it is possible to account for the effects of the surface and the interface while still representing grain boundary motion as a two-dimensional process.

1.4.3 - Driving force for normal grain growth

Grains meet at two dimensional grain boundaries and grain boundaries meet at one dimensional triple junctions. For a polycrystal with isotropic grain boundary energy, the equilibrium condition at triple junctions [28] requires that the dihedral angle between the grain boundaries be 120° . For grains with a given number of sides, this requires in general that the grain boundaries be curved in the plane of the film. This in-plane curvature of the grain boundaries is identified with the deterministic driving force for grain boundary motion and grain growth in the absence of other driving forces. Because each triple junction connects three grain boundaries, the motion of one grain boundary changes the position of the triple junction and therefore the curvature of the other two grain boundaries, locally with respect to the triple junction. This in turn induces the motion of the other two grain boundaries. Grain growth is a highly coupled phenomenon where the

motion of one grain boundary can influence the motion of grain boundaries not connected to that grain boundary. Studying this coupling is the object of topological models of grain growth [29-31]. While the stable equilibrium state of a polycrystalline film is the single crystal state where all grain boundaries have been eliminated, there is a metastable equilibrium state where the film consists of grains in the shape of regular hexagonal right cylinders. Since it is possible to tile a plane with regular hexagons and since the angle between sides of regular hexagons is 120° , the grain boundaries of such a structure do not have any curvature and are not prone to motion.

The quantitative expression for the thermodynamic driving force for grain boundary motion can be derived as follows. Consider a differential element of grain boundary dA as represented on Figure 1.6. The mean curvature of the element is the sum of two principal curvatures κ_1 and κ_2 , defined along two orthogonal directions on the element [32]. When the element moves a distance $d\lambda$ toward its center of curvature, the change in surface area of the element is

$$\delta(dA) = \kappa_m d\lambda dA \quad . \quad (1.7)$$

The free energy per unit area of the grain boundary being γ_{gb} , the change in free energy corresponding to the motion of the grain boundary element is $\gamma_{gb}\delta(dA)$, and the energy change per unit volume ($d\lambda dA$) defined by the initial and final position of the grain boundary is the thermodynamic driving force for grain boundary motion:

$$\Delta G = \gamma_{gb} \kappa_m \quad . \quad (1.8)$$

Equation 1.8 expresses the local driving force for grain boundary motion as κ_m is a local quantity. If κ_1 is chosen to be the curvature in the plane of the film and κ_2 the

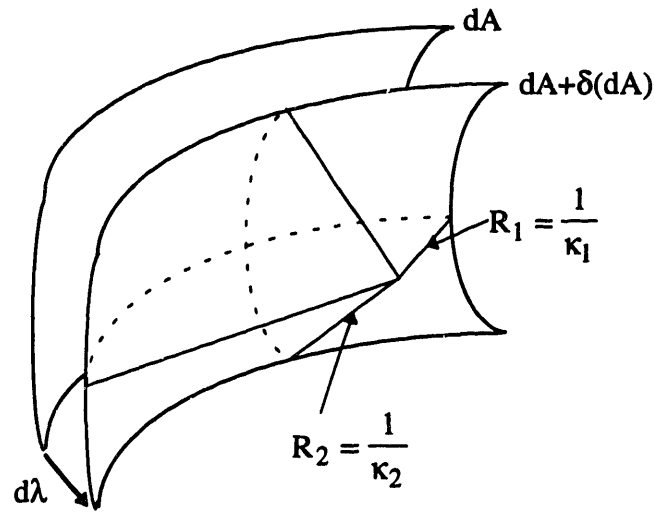


Figure 1.6: Differential element dA of grain boundary moving toward its center of curvature and reducing its surface area by $\delta(dA)$. One possible choice for the curvatures κ_1 and κ_2 is also indicated.

curvature out of plane of the film, it can be shown that in the case of normal grain growth, $\kappa_2 = 0$ [33]. The case of $\kappa_2 \neq 0$ corresponds to surface and interface energy driven grain growth [33].

1.4.4 - Grain boundary grooving

It is frequently observed in films with a columnar grain structure that have undergone normal grain growth that there exists a relationship between the film thickness h and the film average grain diameter d : $d \approx 1.5 h$. This is known as the specimen thickness effect [34]. As the driving force for normal grain growth vanishes only in single crystal films, normal grain growth can not explain this phenomenon. The specimen thickness effect arises because the grain boundaries of the columnar grain structure

become pinned and are not free to move. One important possible type of pinning site is grain boundary grooves that develop at the intersection of the grain boundary and the film free surface because of the surface tension requirement. In the case of constant grain boundary energy and constant free surface energy, the equilibrium condition at the intersection is the simple force balance requirement [28] illustrated on Figure 1.7a. Mullins has analyzed the influence of grain boundary grooves on grain growth for static and dynamic grooves [35]. In the dynamic regime, the grain boundary drags the groove with it when moving. In the static regime, the grain boundary is immobile and the groove has the same shape on each side of the grain boundary. We summarize the results of the static model, illustrated of Figure 1.7b-c, as it is simpler than the dynamic model and imposes a more stringent constraint on grain growth.

The force balance defines the grain boundary groove θ_0 :

$$\sin\theta_0 = \frac{\gamma_{gb}}{2\gamma_s} . \quad (1.9)$$

If the grain boundary intercepts the surface at an angle less than θ_0 , it is trapped in the groove as it must increase its surface area in order to migrate (Figure 1.7b). If the angle of the grain boundary with the surface is greater than θ_0 , it can escape and shrink its surface area. If the grain boundary is pinned in the groove and the in-plane radius of the grain is r , capillarity will induce grain boundary motion until the two principal curvatures κ_1 and κ_2 are of the same magnitude and opposite in sign, i.e., $\kappa_m = 0$. For a circular grain, this corresponds to a stable catenoid shape illustrated on Figure 1.7c. The contact angle of the grain boundary with the surface is θ_i defined by [35]

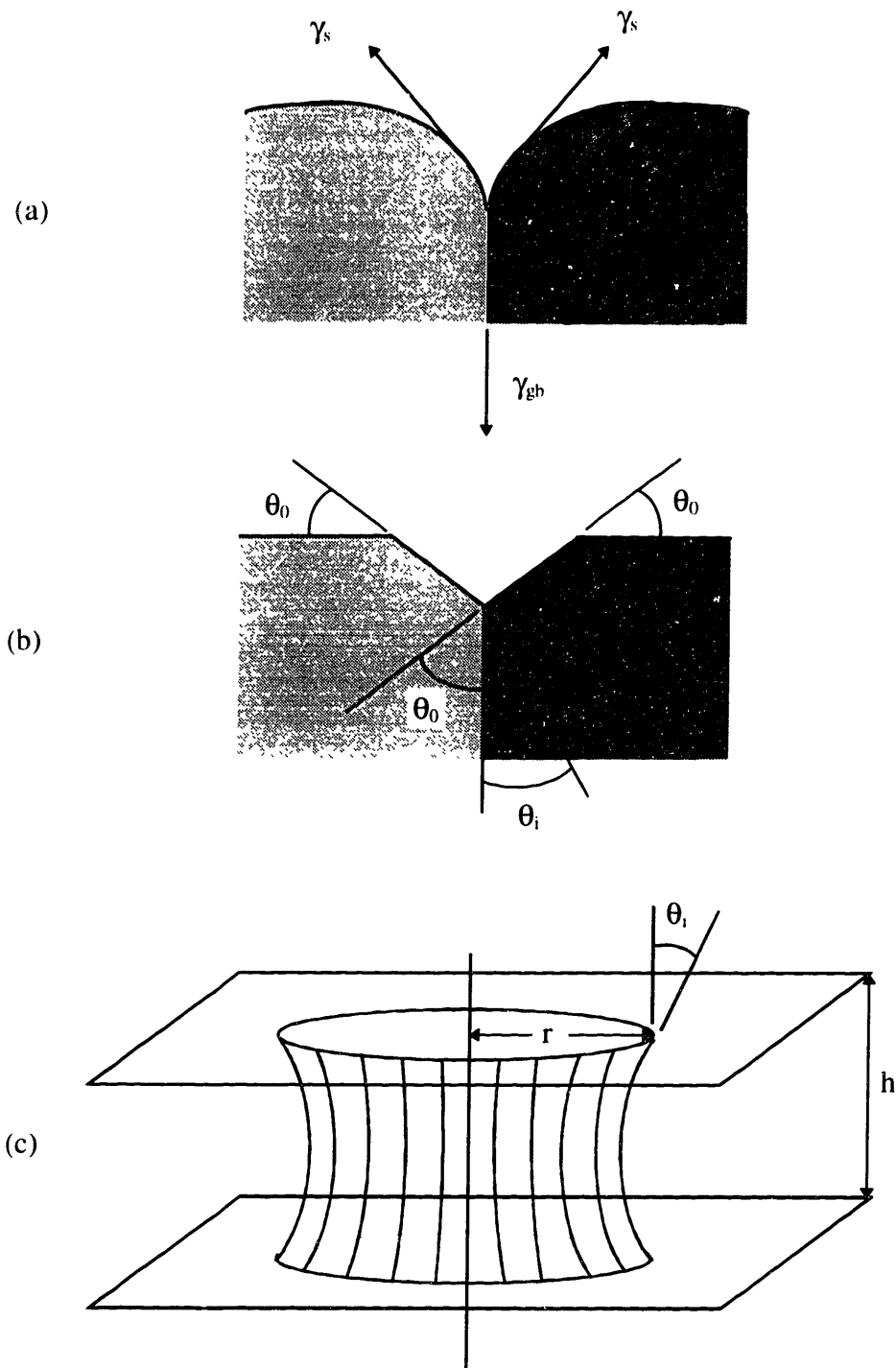


Figure 1.7: (a) A grain boundary groove forms at the intersection of the grain boundary and film surface. (b) The grain boundary is trapped in the groove if it intersects the film surface at an angle θ_i less than θ_0 . (c) The stable shape of a circular grain with its grain boundary pinned in grooves at the top and bottom surfaces is a catenoid for which $\kappa_m = 0$ everywhere on the surface.

$$\sin \theta_i = \frac{h}{2r} . \quad (1.10)$$

The grain boundary can escape the groove if $\theta_i > \theta_0$ which, assuming small θ_i and θ_0 , corresponds to

$$\kappa_l = \frac{1}{r} > \frac{\gamma_{gb}}{h\gamma_s} . \quad (1.11)$$

The grain boundary can move if its in-plane curvature is large enough. Stagnation is reached when $r = h\gamma_s/\gamma_{gb}$. As grain boundary energy and surface energy are of the same order of magnitude, grain boundary grooving induced grain growth stagnation occurs for $r \approx h$, which is consistent with the experimentally observed specimen thickness effect.

The effect of grain boundary grooving on grain growth also affects the grain size distribution function of the grain structure. Experimentally determined grain size distribution functions of stagnant grain structures in thin films are well described by lognormal probability distributions [36]. Computer simulations have shown that while the grain size distribution function of a structure undergoing normal grain growth is not lognormal, the grain size distribution of stagnant structures, when the effect of grain boundary grooving is accounted for, is [37]. Computer simulations have also shown that solute drag of the grain boundaries, which is distinct from grain boundary grooving but can contribute to grain growth stagnation, also result in a lognormal grain size distribution [38].

1.4.5 - Abnormal and secondary grain growth

While some thin film systems undergo normal grain growth, have a lognormal grain size distribution function (Figure 1.8a), and satisfy the specimen thickness effect required by grain boundary grooving, many others do not. It is often observed that the grain diameter to thickness ratio in stagnant grain structures is larger than that predicted for normal grain growth. The process leading to this characteristic is called *abnormal grain growth*. The grain size distribution function of such grain structures which have undergone abnormal grain growth is sometimes *bimodal*, with two maxima. The second maximum, shifted toward larger grain sizes compared to the first maximum, arises from a population of grains that have grown in a matrix of stagnant grains. This type of abnormal grain growth is called *secondary grain growth* and the grains are called secondary grains. Secondary grain growth can proceed until the film entirely consists of secondary grains. In that case, the grain size distribution is monomodal again (Figure 1.8c) but the average grain size is many times the film thickness, larger than the grain size that can result from normal grain growth. Secondary grain growth is also often characterized by an evolution in the grain orientation distribution function as secondary grains do not have random orientations in the film. This suggests that the global driving force for grain growth is orientation selective and depends on the anisotropy of the properties of the material. Secondary grain growth was first observed in Fe-Si alloy sheets [39-41]. Secondary grain growth has also been investigated in detail in a number of thin film systems [42-47]. For fcc metal films, the texture evolution during grain growth often favors (111)-textured

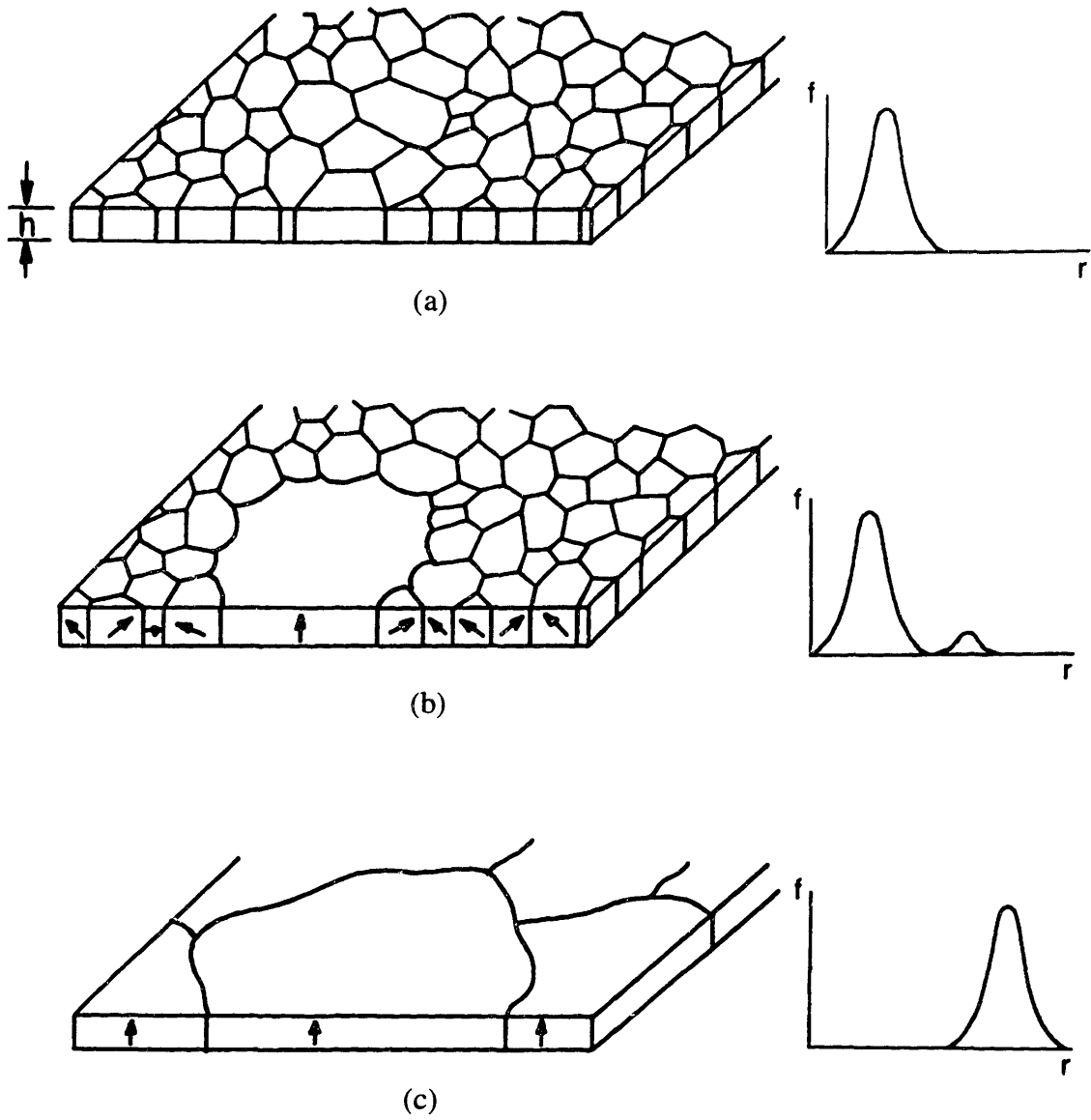


Figure 1.8: (a) Stagnant monomodal microstructure in films after normal grain growth. (b) Secondary grains grow larger in the stagnant matrix, resulting in a bimodal grain size distribution. (c) Film entirely constituted of secondary grains. The grain size distribution is monomodal with the average grain size shifted toward larger values compared to (a).

grains. (111) planes in fcc metals are closed packed and (111) surfaces have a minimum density of frustrated bonds. (111) surfaces have therefore the lowest free surface energy of all possible orientations in fcc metals. (111) grains also often have minimum interface energy as examined in chapters four and five. Surface and interface energy anisotropy driven grain growth has been studied extensively, both experimentally [42-47] and through computer simulations [48-50].

Surface energy driven grain growth occurs for films on both amorphous substrates [44, 45], leading to the preferential growth of (111)-textured grains, and on single crystal substrates [46, 47]. Thompson et al. [46] proposed that for films on single crystal substrates, the analysis of the orientations developing preferentially during grain growth can be used to probe the variation of surface and interface energy with the relative crystallographic orientations of the film and the substrate lattices. This requires that surface and interface energy anisotropy be the only orientation dependent driving force for grain growth. While this can be the case in some systems, for many others it is important to consider strain energy density anisotropy as an available driving force for grain growth.

Vook and Witt performed grain growth experiments in Au and Cu films deposited on glass at 80 K [51, 52]. They recognized that elastic strain energy density anisotropy could favor the growth of (001)-textured grains in the film. They did not systematically study the influence of the processing conditions of the film on the distribution of grain orientations after grain growth. The effect of yielding on grain growth is also absent in their analysis.

Sanchez proposed that the yield stress of grains in a thin film should depend on their orientation² [53]. He argued that in Al films, grains with low yield stresses can grow preferentially at the expense of grains with high yield stresses, and that the strain energy density anisotropy arising from the orientation dependence of the yield stress could supersede surface and interface energy anisotropy. We show in chapter six that while this can be the case for Al under special experimental conditions, this is not the common case. Floro performed grain growth experiments on Ag/(001)Ni [47]. Films deposited at 77 K developed a (001) texture when undergoing grain growth, and films deposited at room temperature developed a (111) texture. He proposed that the anisotropy of the yield stress in Ag favors the growth of (001) grains in highly strained films, such as those deposited at low temperatures. He also recognized that elastic strain energy density anisotropy could play an important role in texture selection during grain growth. Reference [54] and chapter five show that elastic strain energy density anisotropy provides the main driving force for the growth of (001) grains in Ag and that it is unlikely that the anisotropy of the yield stress alone explains the observed orientations.

1.4.6 - Macroscopic models of grain growth

Many macroscopic models of grain growth have been proposed. A comprehensive review of normal grain growth can be found in ref. [55]. In this section we focus on

² A detailed model for the yield stress of grains in a polycrystalline thin film is presented in chapter two. The interplay of the surface and interface energy driving force and the strain energy driving force for grain growth constitutes the bulk of this thesis and we only review here results obtained in earlier work by other authors.

analytic theories of grain growth. Analytic theories of grain growth are generally based on the continuity equation

$$\frac{\partial f}{\partial t} = -\frac{\partial j}{\partial r} \quad , \quad (1.12)$$

where f is the distribution function of size r at time t , and where j is the current in size space. Hillert [56] adapted the mean field analytical approach of coarsening developed by Lifshitz and Syolov [57] and by Wagner [58] to grain growth. He proposed that the current j could be expressed as

$$j_H = c \left(\frac{1}{r} - \frac{1}{r^*} \right) f \quad , \quad (1.13)$$

where r^* is a time-dependent critical radius, and where c is a constant. Hillert showed that asymptotically the distribution function becomes self-similar when expressed as a function of r/r^* , and that r^* grew as $t^{1/2}$. While growth laws of the form $r \propto t^\alpha$, with $1/3 \leq \alpha \leq 1/2$ are often observed for grain growth in thin films, the distribution function predicted by Hillert does not match the experimentally observed distribution. Louat proposed that j should be analogous to a diffusion current [59]

$$j_L = -D \frac{\partial f}{\partial t} \quad , \quad (1.14)$$

where D is the analog of a diffusivity. The predictions resulting from equation (1.14) have been shown to violate mass conservation and will not be discussed. Hunday and Ryum have suggested that grain growth contains elements of both deterministic drift and random walk [60]. They proposed that a diffusional correction could be added to Hillert's model:

$$j_{HR} = j_H + j_{\text{diffusion}} \quad . \quad (1.15)$$

Wu showed that local mass conservation constrains $j_{\text{diffusion}}$ such that the growth law resulting from equations (1.12) and (1.15) is asymptotically $r \propto t^{1/2}$ [61]. The effect of the diffusion current are asymptotically dominated by the drift current and the solution of the equations (1.12) and (1.15) is identical to Hillert's model.

Floro and Thompson have included the effect of surface and interface energy anisotropy in Hillert analysis [50]. They obtained a numerical solution for the distribution of grain sizes and of grain orientation as a function of time. They found that including surface and interface energy could result in a transient bimodal grain size distribution, consistent with experimental observations of secondary grain growth. Whether or not the distribution function takes a bimodal character was found dependent upon the detailed shape of the interface energy function [50].

1.5 - Grain growth as a densification process

To conclude this chapter, we present a quantitative analysis of the stress developing in films as a result of grain growth. This analysis is an extension of references [15, 62].

Consider a columnar microstructure with right circular cylindrical shaped grains. The grain boundaries have lower than equilibrium density and there is an excess volume associated with them. As grain growth proceeds, the total grain boundary area and the excess volume in the film decreases. If the material is constrained to maintain its macroscopic dimensions, as in the case of a film attached to a substrate, the elimination of free volume in the film is associated with the development of a tensile stress. We present the simple case of an elastically isotropic film with uniform surface and interface energy.

Elastic anisotropy and surface and interface energy anisotropy are readily incorporated in the model as presented in appendix I, and do not modify significantly the conclusions of the analysis.

The grain boundary area per unit volume associated with a grain of diameter d and thickness h is $4/d$. For a volume of film V_0 , V_0 not including the excess volume associated with the grain boundaries, the total excess volume is

$$V_{gb}^{xs} = V_0 \frac{4}{d} \Delta a \frac{1}{2}, \quad (1.16)$$

where the $1/2$ factor is introduced as each grain boundary is shared by two grains, and where Δa is the excess volume per unit area of grain boundary. The results presented in this section are sensitive to the magnitude of Δa . For fcc metals, $\Delta a \cong 1\text{\AA}$ is a reasonable value [56] and will be chosen here. The total volume of the crystal, including the excess volume is

$$V_T = V_0 + V_{gb}^{xs} = V_0 \left(1 + \frac{2\Delta a}{d} \right). \quad (1.17)$$

The transformation strain [15] necessary to accommodate this excess volume in the plane of the film is

$$e_T = 2 \Delta a \left(\frac{1}{d} - \frac{1}{d_0} \right), \quad (1.18)$$

where we have assumed that the film is isotropic. The components of the strain in the plane of the film³ are then

³ A detailed description of the natural coordinate system for describing the mechanical properties of thin films is presented in chapter two. The description of the assumptions underlying the solution of the elastic problem is also found in chapter two.

$$\epsilon_{11} = \epsilon_{22} = -\frac{e_T}{2} . \quad (1.19)$$

Assuming an as-deposited initial stress σ_0 , the total state of stress in the film is

$$\sigma_{11} = \sigma_{22} = -\frac{E}{1-\nu} \frac{e_T}{2} + \sigma_0 = \frac{E}{1-\nu} \Delta a \left(\frac{1}{d_0} - \frac{1}{d} \right) + \sigma_0 , \quad (1.20)$$

where E and ν are the Young's modulus and Poisson's ratio of the film, respectively.

The corresponding elastic strain energy density change in the film when the average grain size increases from d_0 to d is:

$$W_\epsilon = \frac{1}{2} \epsilon_{ij} \sigma_{ij} = \frac{E}{1-\nu} \left\{ \left[\Delta a \left(\frac{1}{d_0} - \frac{1}{d} \right) + \epsilon_0 \right]^2 - \epsilon_0^2 \right\} , \quad (1.21)$$

where the intrinsic strain $\epsilon_0 = \sigma_0 (1-\nu)/E$ has been substituted for the intrinsic stress.

The energy change corresponding to the reduction of grain boundary area when the grain size increases from d_0 to d is

$$W_{gb} = 4\gamma_{gb} \left(\frac{1}{d} - \frac{1}{d_0} \right) . \quad (1.22)$$

Combining equations (1.21) and (1.22), the total energy change in the film when the grain size increases from d_0 to d is

$$W_{tot} = 4\gamma_{gb} \left(\frac{1}{d} - \frac{1}{d_0} \right) + \frac{E}{1-\nu} \left[\Delta a \left(\frac{1}{d_0} - \frac{1}{d} \right) + \epsilon_0 \right]^2 - \frac{E}{1-\nu} \epsilon_0^2 . \quad (1.23)$$

The total energy change is plotted on Figure 1.9a for two values of d_0 and assuming that $\epsilon_0 = 0$. For large values of d_0 , the reduction of grain boundary energy is always greater than the increase in strain energy resulting from the tensile stress developing in the film, for any d greater than d_0 . For small values of d_0 , there is a

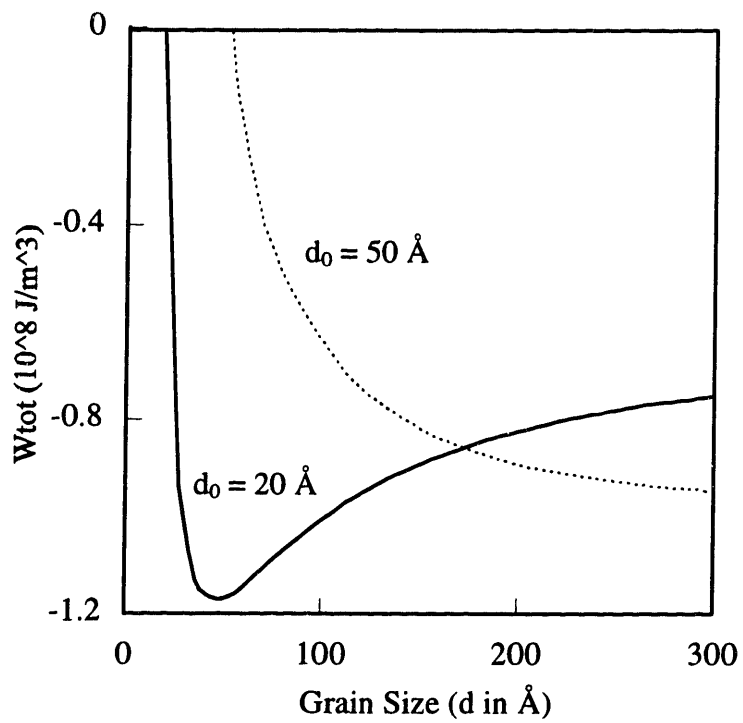
minimum in the total energy of the film and grain growth will stop for the value of d_{stag} that realizes this minimum, i.e., $\partial W_{tot}/\partial d=0$:

$$\frac{1}{d_{stag}} = \frac{1}{d_0} - \frac{2\gamma_{gb}(1-\nu)}{E(\Delta a)^2} + \frac{\epsilon_0}{\Delta a} \quad (1.24)$$

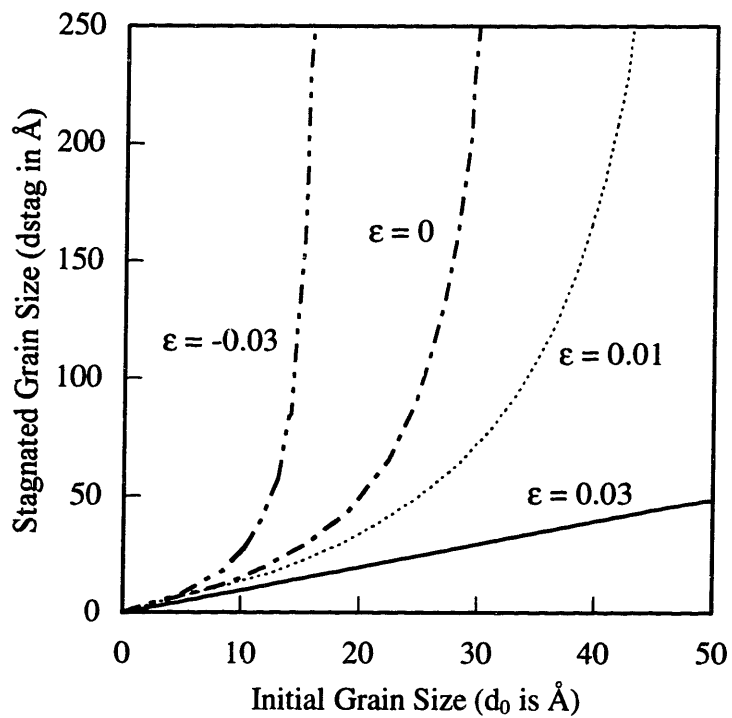
The value of d_{stag} is plotted versus d_0 on Figure 1.9b for three values of ϵ_0 . For a given intrinsic strain, there can be a critical value of d_0 above which there is no minimum in the total energy of the film and for which grain growth does proceed until grain boundary grooving induced stagnation. When the initial intrinsic stress/strain is compressive, the critical value of d_0 is low as the strain energy in the films is low as indicated by equation (1.23). When the initial intrinsic stress is tensile, the critical value of d_0 is shifted toward greater grain sizes as the strain energy in the film is increased. The critical value of d_0 can be found by setting $d_{stag} = \infty$ in equation (1.24):

$$d_0^{crit} = \frac{E(\Delta a)^2}{2\gamma_{gb}(1-\nu) - \epsilon_0 E \Delta a} \quad (1.25)$$

d_0^{crit} tends toward infinity when $\epsilon_0 \geq 2\gamma_{gb}(1-\nu)/E\Delta a$, or for a typical metal $\epsilon_0 \geq 3\%$. In a film subjected to this intrinsic strain, grain growth stagnates due to the large strain energy in the film, independently of the initial grain size d_0 . While this is a large strain, it is possible that intrinsic stress generation during film formation, for example the grain boundary relaxation mechanism presented in section 1.3.3, can generate such strains in some films. When $d_0 \leq d_0^{crit}$ grain growth stagnation is the result of the combined effects of grain boundary grooving and the strain energy density in the film, and the grain size at stagnation is less than indicated by equation (1.24).



(a)



(b)

Figure 1.9: (a) Total energy of films undergoing grain growth for two initial grain sizes. (b) Stagnant grain size of films undergoing grain growth plotted versus the initial grain size, for three levels of initial intrinsic stress.

Fcc metals are unlikely to sustain strains of the order of a few percent and stay in the elastic regime. Stress relaxation decreases the magnitude of the strain energy density in the film and in effect increases d_{stag} for a given initial grain size d_0 . If the intrinsic strain ϵ_0 is less than 1% in magnitude, the critical values of d_0 is less than 52 Å. As presented in previous sections, island spacing in a discontinuous fcc metal film is on the order of 100 Å and the grain size in as-deposited films is on the order of several hundred angstroms [47]. If the as-deposited state is taken to define the initial grain size d_0 , grain growth stagnation is not the result of increasing strain energy density in the film. This is confirmed by the experimental validity of the specimen thickness effect, indicating grain boundary grooving induced grain growth stagnation.

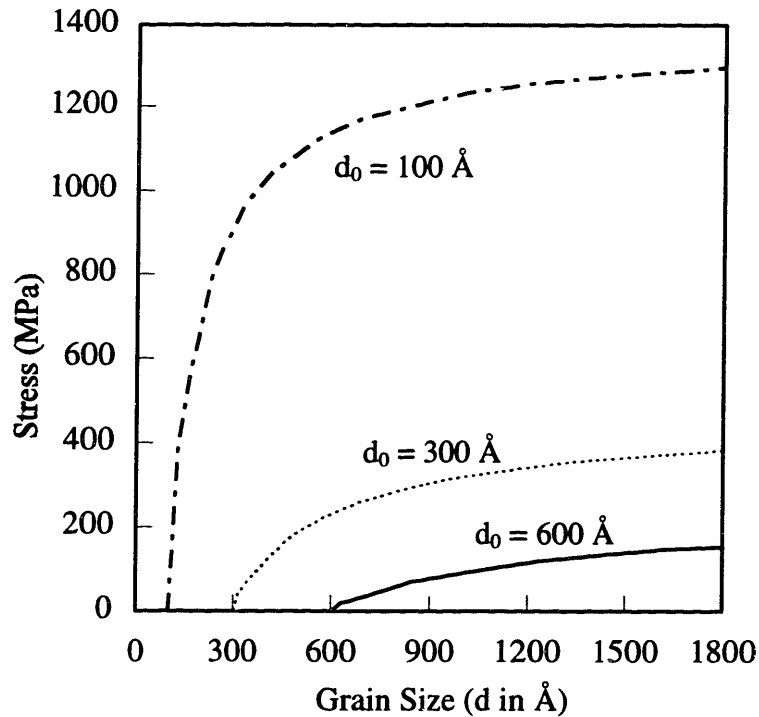


Figure 1.10: Tensile stress generated in films due to grain growth induced densification, plotted as a function of the average grain size in the film, for three initial grain sizes.

Figure 1.10 represents the stress that develops in the film versus the average grain diameter for three values of the initial grain size and no intrinsic strain. For small initial grain sizes, the stress resulting from densification increases rapidly with the average grain size, reaching values greater than 1 GPa. For larger grain sizes, the increase in stress is still significant and can have important consequences for orientation evolution during grain growth as shown in chapter two, five, and six.

1.6 - Summary

We have shown that several intrinsic stress generation mechanisms can be operative at different stages of film formation. It is likely that coarsening occurs during and after deposition even if the homologous deposition temperature $T_{dep}^r = T_{dep}(K)/T_m(K)$ is only of order 0.2. Grain growth during and after deposition is one possible explanation for the observed as-deposited average grain size in films. Subsequent temperature rises promote further grain boundary motion in the film. This type of grain growth rapidly leads to columnar, pseudo two-dimensional microstructures which are the object of study of this thesis. Normal grain growth usually stops when the grain diameter reaches one and a half times the film thickness, due to grain boundary grooves at the film surface. Additional orientation dependent driving forces can induce secondary grain growth in films, where favored grains can grow much larger than the grains in the stagnant matrix. Secondary grain growth also results in preferred orientations in the film. Grain growth in thin films leads to excess volume annihilation which creates a tensile component of the stress. This stress has to be considered when analyzing the global state of stress of films, and the coupling between mechanical properties of films and grain growth.

Chapter 2

Analytical Model for Texture Development during Grain Growth in Thin Films

2.1 - Introduction

In this chapter we present a model for texture development and microstructural evolution during grain growth in thin films. Two orientation dependent driving forces, surface and interface energy anisotropy and strain energy density anisotropy¹ compete to favor the growth of different orientations. Depending on the processing conditions for films, the relative magnitude of these driving forces is different and grain growth favors different orientations. We aim at understanding this dependence of texture development as a function of processing conditions in two ways. In this chapter, we derive an analytical model that predicts which orientation is expected to dominate by comparing the magnitude of the orientation dependent driving forces averaged over the film microstructure.

¹ Both surface energy anisotropy and interface energy anisotropy influence orientation evolution during grain growth. Grains with low surface energy do not necessarily have low interface energy and the anisotropy of surface energy and the anisotropy of interface energy can promote the growth of different orientations. However, because surface and interface are not independent, surface and interface energy anisotropy can be seen as a single driving force that favors the growth of grains with low combined surface and interface energy anisotropy. This is further detailed in section 2.5.

2.2 - State of strain and stress of a thin film on a substrate

Consider a thin film attached to a substrate of much greater thickness than the film (figure 2.1). Unless otherwise stated, all vectorial and tensorial quantities used in this chapter are written in the Cartesian natural coordinates system S of the film shown in figure 2.1 and defined by two orthogonal axis in the plane of the film and one axis normal to the plane of the film.

When the temperature of the film and substrate is changed uniformly, the substrate will expand or contract according to its thermal expansion coefficient. If the film is firmly attached to the substrate and the substrate is much thicker than the film, the in-plane

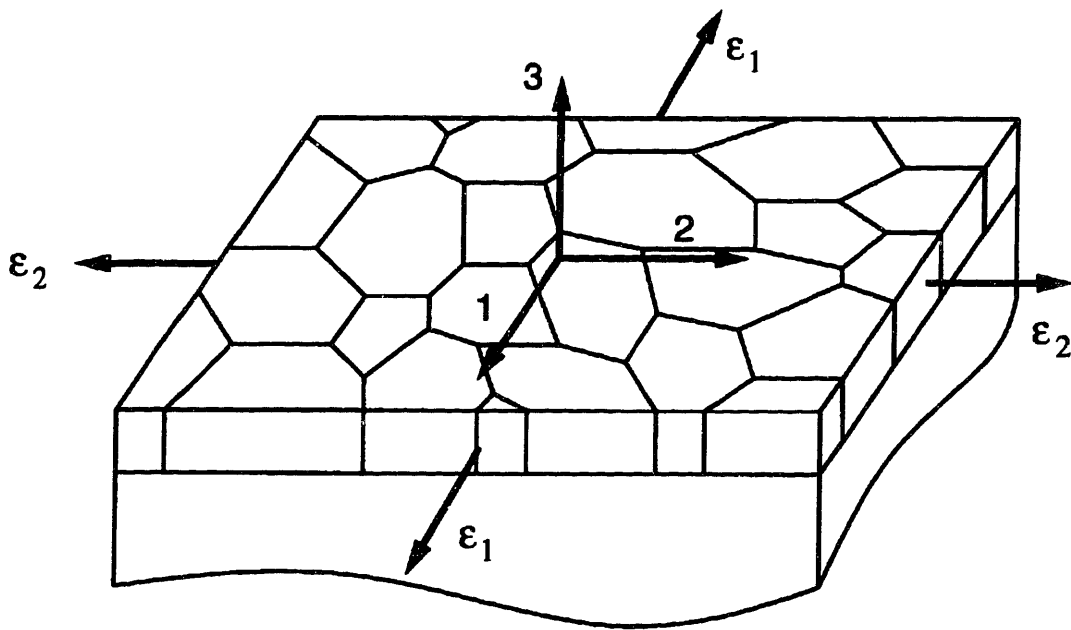


Figure 2.1: Thin film attached to a substrate of much greater thickness. Differential thermal expansion between the film and the substrate result in a film under biaxial strain.

dimensions of the film are constrained to contract or expand the same amount as the in-plane dimensions of the substrate. In general, the film and the substrate have different thermal expansion coefficients and the film, when deposited at a temperature T_{dep} and annealed to a temperature T_{gg} to induce grain growth, is subjected to a uniform thermal biaxial strain:

$$\varepsilon_{ij} = \begin{pmatrix} \varepsilon_1 & 0 & 0 \\ 0 & \varepsilon_1 & 0 \\ 0 & 0 & \varepsilon_3 \end{pmatrix}, \quad (2.1)$$

where

$$\varepsilon_1 = \int_{T_{\text{dep}}}^{T_{\text{gg}}} [\alpha_s(T) - \alpha_f(T)] dT \equiv (\alpha_s - \alpha_f)(T_{\text{gg}} - T_{\text{dep}}). \quad (2.2)$$

We have assumed in equation (2.2) that the symmetry of the film and the substrate is high enough so that the thermal expansion coefficients of the film and the substrate are isotropic² and $\varepsilon_{11} = \varepsilon_{22} = \varepsilon_1$. The latter expression in equation (2.2) is valid when the thermal expansion coefficients are only weakly temperature dependent. The most precise expression for the thermal strain is obtained by integrating the temperature dependent thermal expansion coefficients for the film and the substrate over the temperature range $[T_{\text{dep}} \text{ to } T_{\text{gg}}]$.

² Thermal expansion is a tensorial quantity of rank two and for materials with at least two distinct three fold axes of symmetry, such as the films and the substrates investigated in this thesis, thermal expansion is isotropic and reduces to a scalar quantity.

When the surface of the film is unconstrained, there is no stress applied normally to the film surface³, i.e., $\sigma_{33} = 0$ at the surface of the film. It is a reasonable approximation to extend this boundary condition through the thickness of the film [15, 64]. In this plane stress condition, the stress tensor takes the form

$$\sigma_{ij} = \begin{pmatrix} \sigma_1 & 0 & 0 \\ 0 & \sigma_2 & 0 \\ 0 & 0 & 0 \end{pmatrix}. \quad (2.3)$$

If the crystallographic plane at the surface of the film has at least three fold symmetry, $\sigma_1 = \sigma_2$. This is the case for example for (001)- and (111)-textured films but it is not the case for (011)-textured films.

Plane stress conditions are strictly valid only in the case of elastically isotropic films, far from the edges of the film. Edge effects can influence the strain and stress in the film at a distance several times the film thickness from the edges of the film [15]. For a film with macroscopic in-plane dimensions and a thickness of less than one micron, edge effects do not significantly affect the average properties of the film and will be neglected. In appendix II we examine the validity of the plane stress conditions in elastically anisotropic films. The plane stress approximation in elastically anisotropic films is strictly justified when the ratio d/h of the grain diameter to the film thickness is large such that the influence of the discontinuity of the elastic properties at the grain boundaries is small. However, even when the aspect ratio d/h is small, assuming plane stress conditions is still a good approximation, compatible with the first order model for texture evolution

³ When the film is exposed to air, atmospheric pressure imposes a stress $\sigma_{33} = 1$ bar, which is several orders of magnitude lower than the typical stresses in the plane of the film, σ_{11} and σ_{22} . Neglecting the stress arising from atmospheric pressure is a good approximation.

during grain growth developed in this chapter. The advantage of assuming plane stress conditions is that the strain/stress relationships for biaxially strained films are analytic and convenient for developing analytical models of texture development during grain growth. Unless otherwise stated, we will consider that the film is uniformly biaxially strained and under plane stress conditions.

2.3 - Elastic Anisotropy

The anisotropy of the elastic properties of fcc metals is extensively used in this thesis to explain and predict the experimentally observed behavior of metallic thin films undergoing grain growth. It is also used in the computer simulations of grain growth presented in chapter three. We now derive the state of stress in thin films under uniform biaxial strain and plane stress, following and adapting refs. [15, 65].

The elastic properties of materials are described by a fourth rank tensor. Because of this high dimensionality, even materials with high symmetry can display some degree of elastic anisotropy. In general, the constitutive relation for linear elastic materials, also known as Hooke's law, can be expressed as [66]

$$\sigma_{ij} = c_{ijkl}\epsilon_{kl} \quad , \quad (2.4)$$

where σ_{ij} is the stress tensor, ϵ_{kl} is the strain tensor and c_{ijkl} is stiffness tensor. σ_{ij} and ϵ_{kl} are two dimensional tensors and c_{ijkl} is four dimensional. Here and in the following sections we use Einstein's convention of summation on repeated indices⁴. For materials

⁴Einstein's convention expresses summation of terms in tensorial operations implicitly, by repeating indices. For example, if $u = (u_1, u_2, u_3)$ and $v = (v_1, v_2, v_3)$ are two vectors, the dot product

with cubic symmetry, c_{ijkl} is entirely specified with three values [67], c_{11} , c_{12} and c_{44} , and takes the following form when reduced to a two dimensional matrix C_{ij} [67],

$$C_{ij} = \begin{pmatrix} c_{11} & c_{12} & c_{12} & 0 & 0 & 0 \\ c_{12} & c_{11} & c_{12} & 0 & 0 & 0 \\ c_{12} & c_{12} & c_{11} & 0 & 0 & 0 \\ 0 & 0 & 0 & c_{44} & 0 & 0 \\ 0 & 0 & 0 & 0 & c_{44} & 0 \\ 0 & 0 & 0 & 0 & 0 & c_{44} \end{pmatrix}. \quad (2.5)$$

The degree of elastic anisotropy for cubic materials is expressed by the Zener anisotropy ratio $A = 2c_{44}/(c_{11}-c_{12})$. An elastically isotropic material has an anisotropy ratio of 1.0 and materials with anisotropy ratio greater or smaller than 1.0 are elastically anisotropic. When single crystals of elastically anisotropic materials are strained along different crystallographic directions, the induced stress, and the elastic strain energy density in the crystal varies with the direction of the applied strain. For an elastically isotropic material, the stress-strain relationship is independent of the direction along which the crystal is strained.

In equation (2.5), the stiffness matrix is written in the natural coordinate system S_0 for a cubic material, formed on the [001], [010], and [001] directions in the lattice. We want to solve the elastic problem, i.e., solve explicitly equation 2.4, for a thin film under biaxial strain and plane stress for grains with different orientations. The strain is known in the natural coordinate system S of the film defined in section 2.2 and in figure 2.1. In

$$\mathbf{u} \cdot \mathbf{v} = \sum_{i=1}^3 u_i v_i \text{ is written } u_i v_i. \text{ The multiplication of two } 3 \times 3 \text{ matrices } A_{ij} \text{ and } B_{kl}, \text{ which is defined as}$$

$$(AB)_{ij} = \sum_{m=1}^3 A_{im} B_{mj} \text{ is written } A_{im} B_{mj}.$$

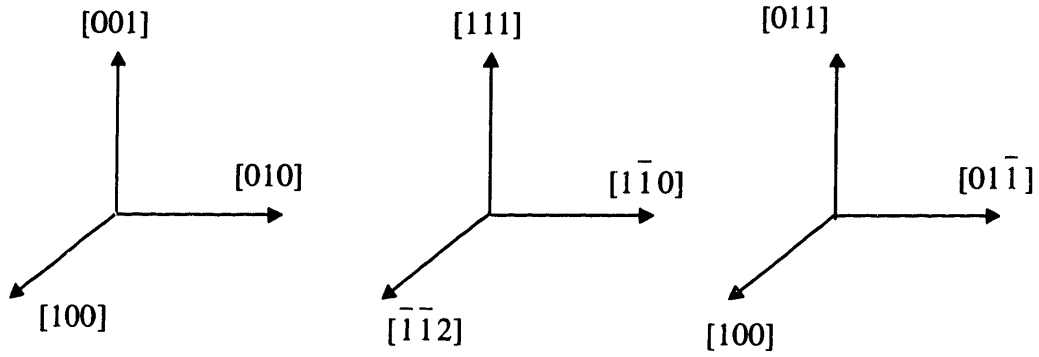


Figure 2.2: Natural coordinate system S for three textures, (001), (111), and (011), and its correspondence to crystallographic directions in the lattice of a cubic material.

order to solve the elastic problem for grains with arbitrary textures, it is necessary to express the stiffness tensor in the coordinate system S of the grain, so strain, stress, and stiffness are expressed in the same coordinate system. Possible choices for the coordinate system S are represented in figure 2.2 for several textures. The stiffness tensor in the coordinate system of the film S , c'_{ijkl} , is related to the stiffness tensor in the natural coordinate system for cubic materials S_0 , c_{ijkl} , by the relation [67]

$$c'_{ijkl} = t_{im}t_{jn}t_{kp}t_{lq}c_{mnpq} \quad , \quad (2.6)$$

where t_{ij} is the transfer matrix for transforming coordinates from S_0 to S . For orthonormal coordinate systems such as S_0 and S , t_{ij} is defined as:

$$t_{ij} = U_i u_j \quad , \quad (2.7)$$

where U_i and u_j are unit vectors along the axis i and j of S_0 and S , respectively. Figure (2.2) shows the relation between possible choices of S and crystallographic directions in

the crystal, for three different textures. The corresponding transfer matrixes for these orientations are:

$$t_{ij}(001) = \begin{pmatrix} 1 & 0 & 0 \\ 0 & 1 & 0 \\ 0 & 0 & 1 \end{pmatrix},$$

$$t_{ij}(111) = \frac{1}{\sqrt{6}} \begin{pmatrix} -1 & -1 & 2 \\ \sqrt{3} & -\sqrt{3} & 0 \\ \sqrt{2} & \sqrt{2} & \sqrt{2} \end{pmatrix}, \quad (2.8)$$

$$t_{ij}(011) = \frac{1}{\sqrt{2}} \begin{pmatrix} \sqrt{2} & 0 & 0 \\ 0 & 1 & -1 \\ 0 & 1 & 1 \end{pmatrix}.$$

For materials with cubic symmetry, equation (2.6) simplifies to [68]

$$c'_{ijkl} = c_{ijkl} - H(t_{in}t_{jn}t_{kn}t_{ln} - \delta_{ij}\delta_{kl}\delta_{jk}), \quad (2.9)$$

where $H = 2c_{44} - c_{11} + c_{12}$ [see footnote⁵], and where δ_{ij} is the usual Kronecker delta. Stiffness, strain, and stress being expressed in the same coordinate system S, equation (2.4) can be solved for the component of the strain ϵ_3 and the components of the stress σ_1 and σ_2 .

$$\epsilon_3 = -\frac{c'_{3311} + c'_{3322}}{c'_{3333}} \epsilon_1, \quad (2.10a)$$

$$\sigma_1 = \left[c'_{1111} + c'_{1122} - \frac{c'_{1133}}{c'_{3333}} (c'_{3311} + c'_{3322}) \right] \epsilon_1, \quad (2.10b)$$

⁵For elastically isotropic cubic materials, $A=1.0$, $H=0.0$ and equation (2.9) reduces to $c'_{ijkl} = c_{ijkl}$. The stiffness tensor of elastically isotropic materials is independent of the coordinate system in which it is expressed.

$$\sigma_2 = \left[c'_{2211} + c'_{2222} - \frac{c'_{2233}}{c'_{3333}} (c'_{3311} + c'_{3322}) \right] \epsilon_1 . \quad (2.10c)$$

The elastic strain energy density of a grain with strain ϵ_{ij} and stress σ_{ij} is

$$W_\epsilon = \frac{1}{2} \epsilon_{ij} \sigma_{ij} = M_{hkl} \epsilon_1^2 , \quad (2.11)$$

where M_{hkl} is an orientation dependent biaxial modulus easily calculated using equation (2.10). The biaxial modulus can be expressed as a function of c_{11} , c_{12} and c_{44} and of the normal to the grain surface $[hkl]$ as [69]

$$M_{hkl} = c_{11} + c_{12} + K - \frac{2(c_{12} - K)^2}{c_{11} + 2K}$$

$$K = H (h^2 k^2 + k^2 l^2 + h^2 l^2) \quad . \quad (2.12)$$

$$h^2 + k^2 + l^2 = 1$$

For all fcc metals, the anisotropy ratio A is greater than 1.0 [67]. It is shown in appendix III that when this is the case, the effective biaxial modulus M_{hkl} is minimum for (001)-textured grains and maximum for (111)-textured grains⁶. This implies that for all fcc metals, (001) textured grains, when subjected to a biaxial strain and under plane stress have the lowest elastic strain energy density of all orientations in the film, and that (111) textured grains have the highest elastic strain energy density of all orientations. Figure 2.3 shows a contour plot of the biaxial modulus of Ag on a (001) stereographic projection. A similar plot for Cu can be found in ref. [70]. As the magnitude of the modulus drops sharply near the (001) orientation, the elastic strain energy density of (001) grains is significantly lower than the elastic strain energy density of most orientations in the film.

⁶This is in fact true for all pure cubic metals, except Mo which has an anisotropy ratio less than 1.0 [64].

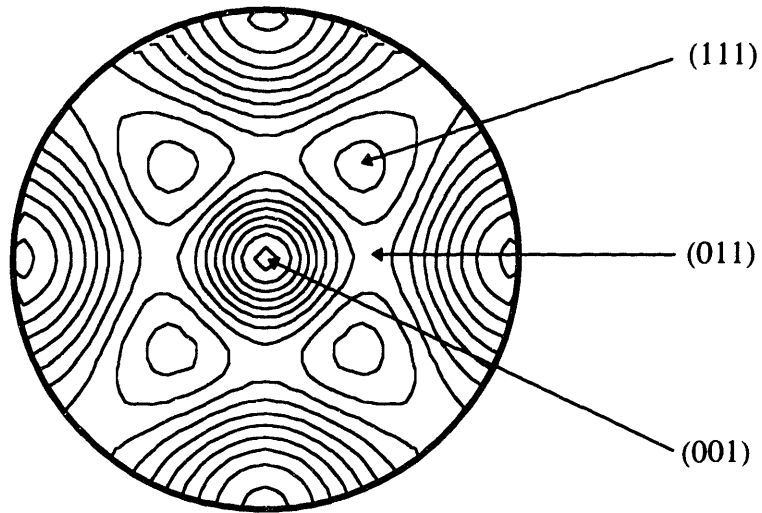


Figure 2.3: Contour plot of the biaxial modulus of Ag on a (001) stereographic projection. The modulus is maximum for (111) textured grains and minimum for (001) textured grains.

The stiffnesses chosen to generate figure 2.3 and for analyses throughout this thesis are values characteristic of bulk material. There are reports in the literature that the elastic constants of thin films are different from the elastic constants of bulk material. Biaxial moduli measured by the bulge test are sometimes found to be much larger than what is calculated from the bulk stiffnesses [71]. However, it has been shown that if the film is wrinkled, the modulus measured by the bulge test can yield values twice the real modulus [24]. This effect can account for most reports of anomalous values of the modulus in films [72]. Surface stresses can induce large displacements of atoms in the vicinity of the surface of films and induce anelastic effects. The modulus enhancement resulting from this effect is on the order of 20% for 50 Å thick Cu films [73]. For films thicker than 200 Å, the enhancement of the modulus due to surface stresses is insignificant [24]. As the minimum thickness of the films investigated in this thesis is on the order of

300 Å, we will ignore anelastic effects and use the elastic constants characteristic of bulk materials. The values of the stiffnesses used throughout this thesis are summarized in table 2.1.

Material	c_{11} (GPa)	c_{12} (GPa)	c_{44} (GPa)	$A = 2c_{44}/(c_{11}-c_{12})$
Al	106	60.5	28.2	1.21
Ag	124	94.0	46.5	3.01
Ni	251	150	124	2.45

Table 2.1: Stiffnesses and anisotropy ratio for the materials investigated in this thesis. The values are characteristic of bulk material and are from ref. [74].

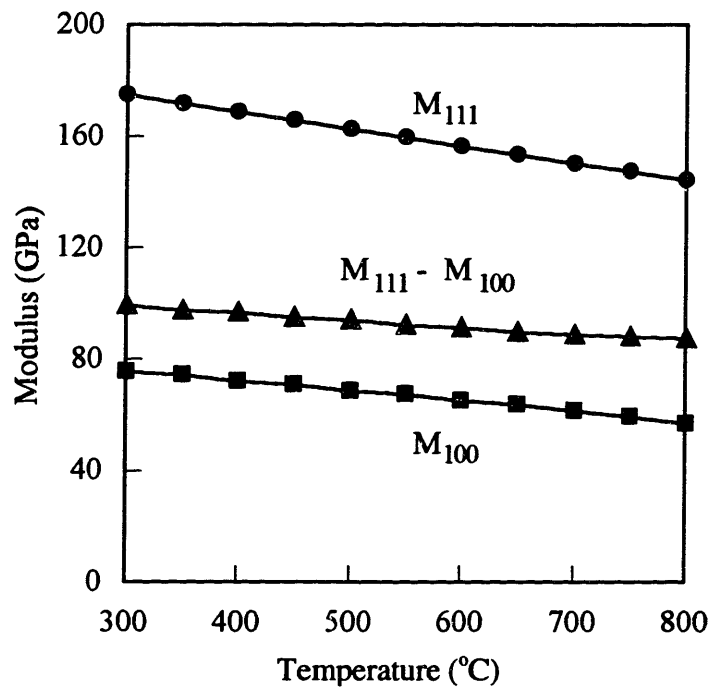


Figure 2.4: Biaxial moduli for (001)- and (111)-textured Ag films plotted versus temperature. The difference between the biaxial moduli is also plotted.

The elastic constants of materials depend in general on temperature. Figure 2.4 shows the biaxial moduli for (001)- and (111)-textured Ag and the difference between the moduli, as a function of temperature and using values for the stiffnesses from ref. [74]. The change in the difference between the moduli of (111)-and (001)-textured Ag crystals from room temperature to the grain growth temperature of Ag, about 400°C, is less than 10%. The change of elastic constants with temperature will be ignored for all thin film materials considered here.

The strain energy density difference between two neighboring grains with orientations $(h_1k_1l_1)$ and $(h_2k_2l_2)$ in an elastically deformed film is

$$\Delta W_{\epsilon} = \left(M_{h_1k_1l_1} - M_{h_2k_2l_2} \right) \epsilon^2 \quad , \quad (2.13)$$

which is an available driving force for grain growth, and depends solely on the orientations of the two grains, independent of their geometry.

2.4 - Yield stress of a polycrystalline thin film

The intrinsic and thermal strains present in films can be large and exceed the linear elastic limit. It is therefore necessary to consider plastic behavior in the film. However, it is important to recognize that the strengthening effects due to the small sizes in thin films are large enough for thin films with small grain sizes to sustain very large stresses without undergoing plastic deformation. The ability of films on substrates to remain elastically deformed prior to grain growth even when the difference between the deposition temperature and the annealing temperature is several hundred degrees Celsius underlies the interpretation of most of the experimental results presented in chapters five and six.

We first review one model of yielding in polycrystalline thin films. The coupling between yielding and grain growth is then examined.

2.4.1 - Functional form for the yield stress of polycrystalline thin films

Thompson has derived a simple model for the yield stress of grains in a polycrystalline thin film that captures the important functional dependencies on the grain orientation and geometry [75]. We briefly review the derivation.

Consider an idealized grain in the shape of a right circular cylinder as illustrated in figure 2.5. The grain is subjected to a plane state of stress as described in section 2.2, with both components of the stress equal, i.e., $\sigma_1 = \sigma_2 = \sigma$. A dislocation half-loop,

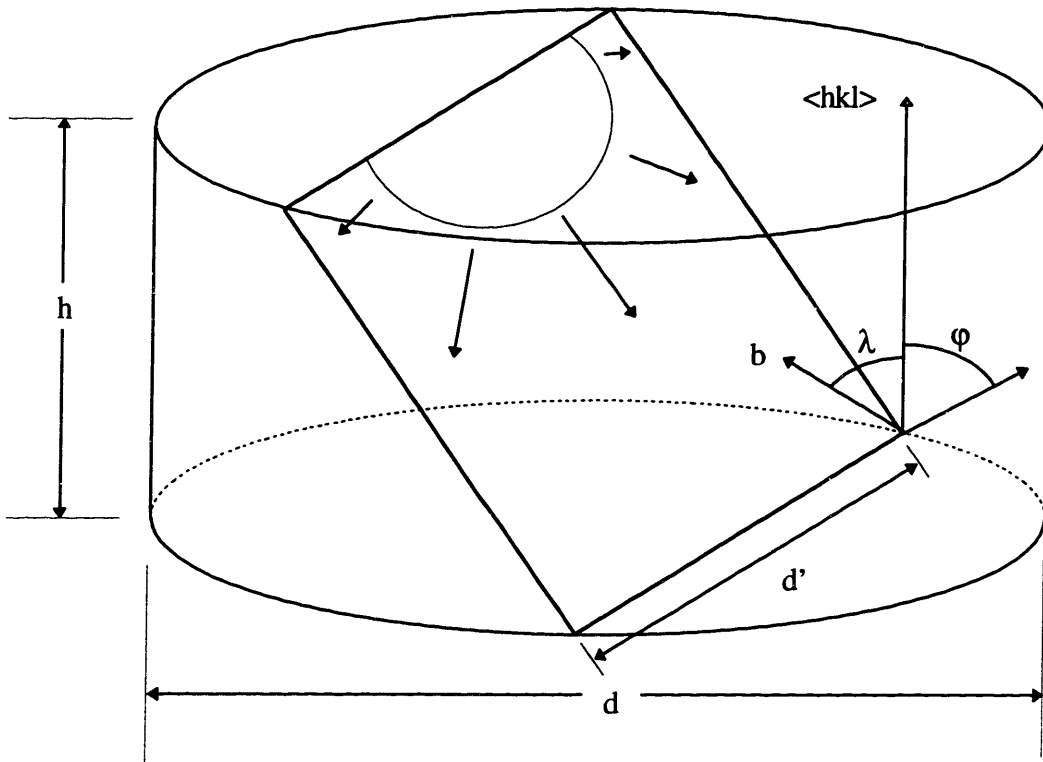


Figure 2.5: Geometry of the slip system of an idealized grain undergoing plastic deformation.

nucleated at the surface of the grain propagates down a glide plane. The length of the intersection of the glide plane with the side of the grain is approximately:

$$l \cong \frac{h}{\sin \varphi} \quad , \quad (2.14)$$

where φ is the angle between a normal to the glide plane and a normal to the grain surface and h is the film thickness.

The work done by the stress field when the dislocation has entirely swept out the glide plane is approximately given by

$$W_{\text{out}} \cong \tau b l d \quad , \quad (2.15)$$

where b is the magnitude of the Burgers vector of the dislocation, d is the grain diameter, and τ is a resolved shear stress on the glide plane:

$$\tau = \sigma \cos \varphi \cos \lambda \quad , \quad (2.16)$$

and where $\cos \varphi \cos \lambda$ is the Schmid factor for the slip system [760], and λ is the angle between the Burgers vector of the dislocation and a normal to the grain surface. Equations (2.15) and (2.16) are strictly valid only for the case of a pure edge straight dislocation that moves by translation from the top to the bottom of the grain. For convenience, we use equations (2.15) and (2.16) to treat the case of a half loop of dislocation as we are more interested in a functional form of the yield stress rather than exact numerical values.

After the dislocation has fully traversed the glide plane, segments of interfacial dislocation are left at the sides of the grain and at the film-substrate interface. The total energy of these segments of dislocation is

$$W_{in} \cong 2l W_{side} + d W_{bottom} , \quad (2.17)$$

where W_{bottom} is the energy per unit length of the dislocation at the film-substrate interface [76],

$$W_{bottom} \cong \frac{b^2}{2\pi(1-\nu)} \frac{\mu_f \mu_s}{\mu_f + \mu_s} \ln\left(\frac{h}{b}\right) , \quad (2.18)$$

and where W_{side} is the energy per unit length of the dislocations at the edges of the grain [76],

$$W_{side} \cong \frac{b^2 \mu_f}{4\pi(1-\nu)} \ln\left(\frac{d}{b}\right) . \quad (2.19)$$

Here ν is the film Poisson's ratio, μ_f and μ_s are the shear moduli of the film and the substrate respectively. It is energetically favorable to propagate the half-loop of dislocation through the grain if $W_{out} \geq W_{in}$. When those two energies are equal, the grain yields and the yield stress is given by:

$$\sigma_y = C_{hkl} \left(\frac{K_s}{d \sin \varphi} + \frac{K_b}{h} \right) , \quad (2.20)$$

where

$$C_{hkl} = \frac{\tan \varphi}{\cos \lambda} , \quad K_s = \frac{2}{b} W_{side} , \text{ and } K_b = \frac{1}{b} W_{bottom} . \quad (2.21)$$

The yield stress as given by equation (2.20) depends on the grain diameter, the film thickness and the texture of the grain. As grain growth proceeds, and the orientation and average grain diameter of the film evolve, the yield stress and the strain energy density of yielded grains changes. The coupling between yielding and grain growth is examined in section 2.4.3.

The derivation leading to equation (2.20) is based on a simplified grain geometry. A more exact treatment is given in appendix IV. The result of this more exact analysis does not differ enough from equation (2.20) to replace this conveniently simple expression for the yield stress of grains in a polycrystalline film. More importantly, the derivation leading to equation (2.21) considers a simplification of the yielding process and focuses on the glide of a straight dislocation from the top to the bottom of the grain. The nucleation of the dislocation is ignored as well as the interaction of the dislocation with the segments of interfacial dislocation deposited along the sides of the grain as the dislocation propagates toward the bottom of the grain. The critical shear stress for the nucleation of a dislocation half loop at a ledge on a free surface has been calculated to be greater than the stress given by equation (2.20) [66]. Equation (2.20) therefore provides a lower bound of the magnitude of the yield stress in real films, and more importantly, a functional dependence of the yield stress on the grain diameter, the film thickness, and the texture of the grain. In this thesis, we take the yield stress to be

$$\sigma_y = C_h \frac{\ln\left(\frac{h}{b}\right)}{h} + C_d \frac{\ln\left(\frac{d}{b}\right)}{d} , \quad (2.22)$$

where C_h and C_d are orientation dependent coefficients extrapolated for the material and orientation of interest as presented in the next section.

2.4.2 - Orientation and geometry dependent yield stress

Venkatraman and Bravman [78] have experimentally determined the yield stress of (111) textured aluminum thin films on amorphous SiO_2 as a function of the Al film thickness and of the average grain diameter in the film. We have fitted their data to

the functional form given by equation (2.22) and obtained $C_h = 116 \text{ GPa}\text{\AA}$, and $C_d = 126 \text{ GPa}\text{\AA}$.

We can infer the yield stress of (hkl)-textured grains in Al/SiO₂ by scaling the coefficients C_h and C_d by the appropriate trigonometric functions of the angles ϕ and λ for (hkl)-textured grains as described by equations (2.20) and (2.21). The yield stress of (hkl)-textured grains of a polycrystalline thin film of a metal M deposited on SiO₂ are then obtained by scaling the yield stresses obtained for Al by the ratio of the Young's moduli for M and Al. Finally, the yield stress of a film M on a substrate S for (hkl)-textured grains is obtained by scaling the thickness dependent term of the yield stress for M/SiO₂ by the ratio of geometric averages of the shear moduli for M and S, and M and SiO₂, as suggested by equation (2.18). Table 2.2 summarizes our choice of C_h and C_d for different materials and orientations.

Material	Orientation	b (Å)	C_h (GPaÅ)	C_d (GPaÅ)
Al	(111)	2.86	116	126
Al	(011)	2.86	48	84
Ag	(111)	2.88	137	149
Ag	(001)	2.88	79	99
Ni	(111)	2.49	341	371
Ni	(001)	2.49	197	214

Table 2.2: Orientation dependent coefficients for the thickness and grain size of the yield stress of polycrystalline films used in this work. The magnitude of the Burgers vector for each material is also given.

The experimental values of the yield stresses as determined in ref. [78] were obtained through multiple thermal cycling of an Al film. Multiple yielding in the film is likely to induce some hardening, and it is therefore expected that the values of the yield stress found in ref. [78] are greater than for an as-deposited film, which has not been plastically deformed.

Figure 2.6 shows a contour plot on a (001) stereographic projection of the orientation dependence of the yield stress as expressed by equation (2.22), i.e., $[h/\ln(h/b)]\sigma_y$, with $d = h$. The values shown are representative of Al but plots generated for Ag or Ni are similar. The value of C_h and C_d chosen for a given grain orientation were those obtained following the scaling procedure of the coefficients for (111)-textured Al as outlined above. To determine the appropriate values of ϕ and λ necessary for the orientation scaling, all the possible slip systems of the general form (111)<110> were examined for that particular orientation and the values ϕ and λ that minimized

$\left| \frac{\tan \phi}{\cos \lambda} \right| + \left| \frac{1}{\cos \phi \cos \lambda} \right|$ were used as suggested by equation (2.20). The derivation leading to

equation (2.20) considers only one slip system in the grain, and figure 2.6 represents the yield stress calculated for the slip system that produces the lowest possible yield stress. For materials subjected to large plastic strains, hardening and cyclic hardening can affect the yield stress and it is important to consider all the slip systems available. However, as shown in the next section and in chapter six, hardening is expected to be negligible at the onset of grain growth for the systems studied in this thesis. It is therefore appropriate to consider only the slip system for which dislocation glide is easiest.

Figure 2.6 shows that the yield stress is highest for (111)-textured grains. (011)-textured grains correspond to a local minimum for the yield stress. There are other grain orientations for which the yield stress is lower than for (011) grains but the difference in the yield stress is small. The yield stress is minimum for (210)-textured grains.

In this thesis we use the yield stress given by equation (2.22) along with the values in tables 2.1 and 2.2. to analyze the effect of plastic deformation on grain growth. There are some physical limitations to this model for the yield stress of a polycrystalline thin films. Experimentally, the yield stress of a thin film is dependent upon time and temperature. The only temperature dependencies captured by equation (2.20) are that of the shear moduli of the film and substrate and of the Poisson's ratio of the film. Diffusive stress relaxation mechanisms are not accounted for in this model. The experimental temperature dependence of the constants C_h and C_d in the scaled expression of the yield

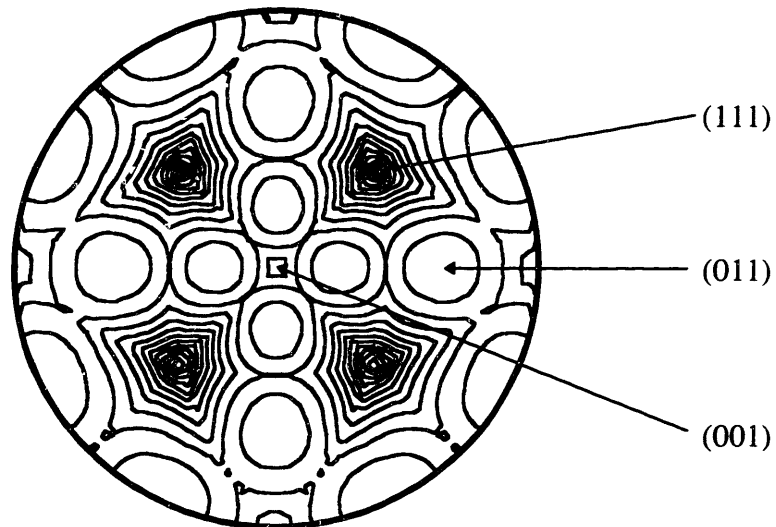


Figure 2.6: Orientation dependence of the yield stress in an Al film, plotted on a (001) stereographic projection.

stress expressed by equation (2.22) is unknown. For materials like Al, annealed at a relatively high homologous temperature to induce grain growth ($T_r = T_{gg}(K)/T_m(K) \cong 0.6$), time-temperature dependent stress relaxation mechanisms are potentially important for the grain growth process but will not be considered further.

We aim at understanding qualitatively or semi-quantitatively the influence of mechanical properties on grain growth in thin films. When plasticity is important, equation (2.22) can be used as a first order approximation to identify and explain experimental results. It represents the best experimental data available for this work as the coefficients C_h and C_d have only been measured for (111)-textured Al films.

2.4.3 - Coupling between yield stress and grain growth

The yield stress of grains in a polycrystalline thin film depends on both grain size and grain orientation. The strain energy density of plastically deformed grains therefore also depends on grain size and grain orientation. Assuming that grains yield uniformly throughout the volume of the grain, the strain energy density of a yielded grain with texture (hkl) is defined as [6]

$$W_\epsilon = \int_0^\epsilon \sigma_{ij} d\epsilon_{ij} , \quad (2.23)$$

where ϵ satisfies $\epsilon \geq \sigma_y/M_{hkl}$ for a yielded grain.

If the plastic strain in the film is large, there are interactions of the dislocations in the material and hardening has to be considered. This can be the case for example of multiply thermally cycled films where the accumulated plastic strain can be important. For the materials systems of interest in this thesis, the maximum thermal strain imposed on the

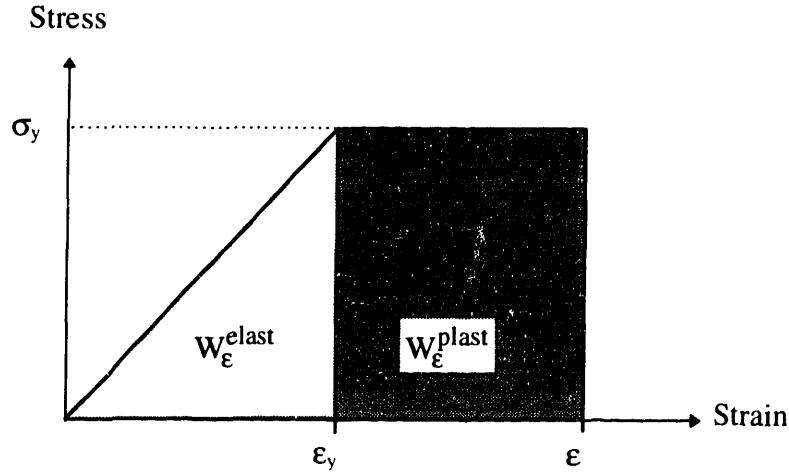


Figure 2.7: Stress plotted versus strain for a perfectly elastic-plastic bulk material under uniaxial tension. The elastic and plastic components of the strain energy density are also indicated.

film is less than 1%, some of which is accommodated elastically. In a typical grain growth experiment, the film is heated only once from the deposition temperature to the grain growth temperature. Even for materials with low stacking fault energy, for example Ag, which are particularly prone to hardening, plastic strains on the order of 1% do not induce significant hardening [79].

Figure 2.7 schematically shows the strain-stress relationship for a perfectly elastic-plastic bulk material for which there is no accumulated hardening with increasing plastic strain. For a perfectly elastic-plastic film under a uniform biaxial state of strain and plane stress, the strain energy density of a plastically deformed grain is

$$W_\epsilon = W_\epsilon^{\text{elast}} + W_\epsilon^{\text{plast}} = \frac{\sigma_y^2}{M_{\text{hkl}}} + 2\sigma_y \left(\epsilon - \frac{\sigma_y}{M_{\text{hkl}}} \right). \quad (2.24)$$

The strain energy density of a plastically deformed grain is the sum of the elastic strain energy density and the plastic strain energy density. Equation (2.24) can be simplified as

$$W_{\epsilon} = \sigma_y \left(2\epsilon - \frac{\sigma_y}{M_{hkl}} \right), \quad (2.25)$$

where σ_y is the yield stress of the grain and depends on both the texture and geometry of the grain. In equation (2.25), it is assumed that the work of the stress field and the strain energy density in the film are equal. Dislocations propagating through the thickness of a thin film can be annihilated at the film surface and create a ledge or stop at the film-substrate interface. In both cases, part of the dislocation energy is not associated with the film and should not be included in the strain energy density. Equation (2.25) represents therefore an upper bound for the strain energy density of plastically deformed grains. A lower bound for the strain energy density of plastically deformed grains is obtained by neglecting the plastic strain energy density: $W_{\epsilon} = \sigma_y^2 / M_{hkl}$. The exact expression for the strain energy density of yielded grains in thin films is not known. In this thesis, we examine the effects on texture evolution during grain growth of both the upper and lower bound for the strain energy density. We show in chapter three that taking the lower bound for the strain energy density of plastically deformed grains maximizes the effect of yielding on grain growth. When all the plastic work is included in the strain energy density, the effect of yielding on grain growth is less important. In both cases, the dependencies of strain energy density on orientation, grain size and film thickness are similar, and the effect of yielding on grain growth is predicted to favor the same populations of grains. For a given thin film materials system, the yield stress of the film is expected to be a decreasing function of both the grain size and the film thickness and for a film of given thickness, grains with large sizes are expected to have a lower yield stress than grains with small

sizes. It is therefore possible to have a film in which some of the grains are yielded and some of the grains are in the elastic regime.

When yielded, the stress state and the strain energy density of a grain depend on both the orientation and the geometry of the grain, and therefore vary from grain to grain in the film, even in elastically isotropic materials. This leads to free energy differences for grains with different orientations and/or grain diameter, which can drive abnormal grain growth. Since the grain size of individual grains changes during grain growth, the strain energy density and the driving force for grain growth of yielded grains change too. Yielded grains which are growing have a stress level decreasing with time and therefore an increasing energetic advantage. Yielded grains which are shrinking have their yield stress pinned at the value determined by the maximum size they reached while yielded and have therefore a time independent strain energy density.

Figure 2.8 shows the orientation dependence of the strain energy density of plastically deformed grains at the onset of yielding, i.e., $[(h/\ln(h/b)\sigma_y)^2/M_{hkl}]$ with $d = h$, plotted on a (001) stereographic projection. The plot was generated with the coefficients C_h and C_d characteristic of Al but plots with similar shapes can be generated for Ag and Ni. The general shape of the plot is the same as for the yield stress (figure 2.5). (111) grains have the highest strain energy density of all orientations and (011) grains are in local minimum of the strain energy density. (001) grains have an intermediate strain energy density, closer to the strain energy density of (111) grains than the strain energy density of (011) grains. (210) grains have the minimum strain energy density. Figure 2.8 suggests that when the film is plastically deformed as grain growth proceeds, low strain

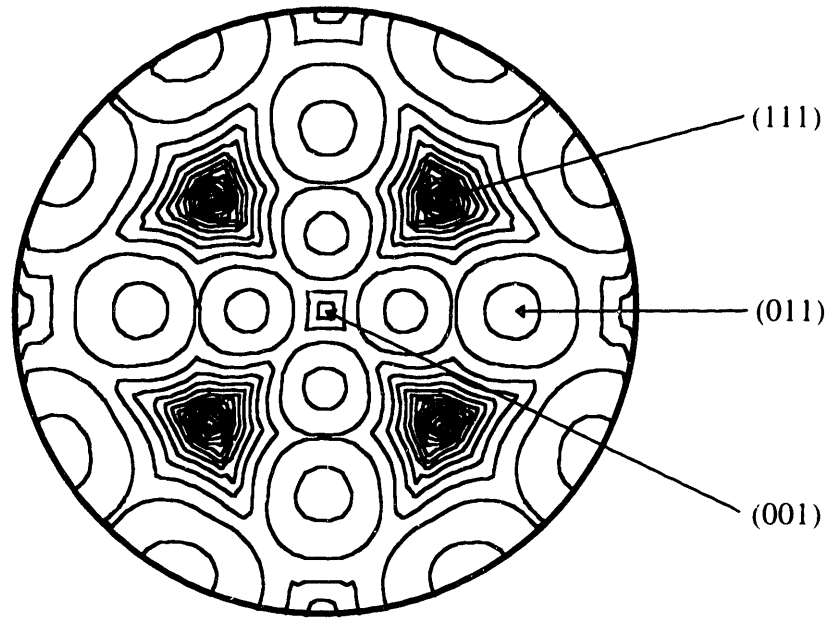


Figure 2.8: Strain energy density of Al grains at the onset on yielding, plotted on a (001) stereographic projection.

energy density grains and in particular (011)-textured grains can grow preferentially in the film. It is shown in chapter six that the growth of (210)-textured grains is usually not seen, due to the small volume fraction of (210) grains in as-deposited films. The influence of yielding on grain growth is expected to be most important for nearly elastically isotropic materials, for which elastic strain energy density anisotropy has little influence on grain growth.

2.5 - Surface and interface energy

Surface and interface energy anisotropy provides a driving force for grain growth. Grains with low combined surface and interface energy have an energetic advantage and can grow preferentially. A crystallographic orientation that minimizes the film surface

energy γ_s , need not necessarily be the orientation with lowest film/substrate interface energy γ_i . There are systems for which surface and interface energy minimization cooperate or compete during grain growth [47]. However there is always a specific crystallographic orientation which produces a global minimum in the sum of the surface and interface energies. In an as-deposited polycrystalline film with homogeneously distributed grains sizes, this orientation should have the maximum average growth rate in the absence of other orientation dependent driving forces for grain growth [47].

The variation of the interface energy with the crystallographic orientation of the grains in the film is determined in part by the structure of the substrate. If the film is free standing or if the substrate is amorphous, surface and interface energy driven grain growth results in the development of a fiber texture. This results from the fact that if the substrate were rotated relative to film about an axis perpendicular to the plane of the film, the structure of the film/substrate would be unchanged and so would be the interface energy, as illustrated in figure 2.9a. If the substrate is single crystal, the interface energy is generally anisotropic and depends not only on the texture of grains but also on the in-plane orientation of the grain lattice with respect to the substrate lattice, as illustrated in figure 2.9b. In that case, surface and interface energy driven grain growth leads not only to the development of a fiber texture, but to preferred in-plane orientations as well. The orientations growing are in this case are fully three-dimensionally constrained with respect to the substrate lattice.

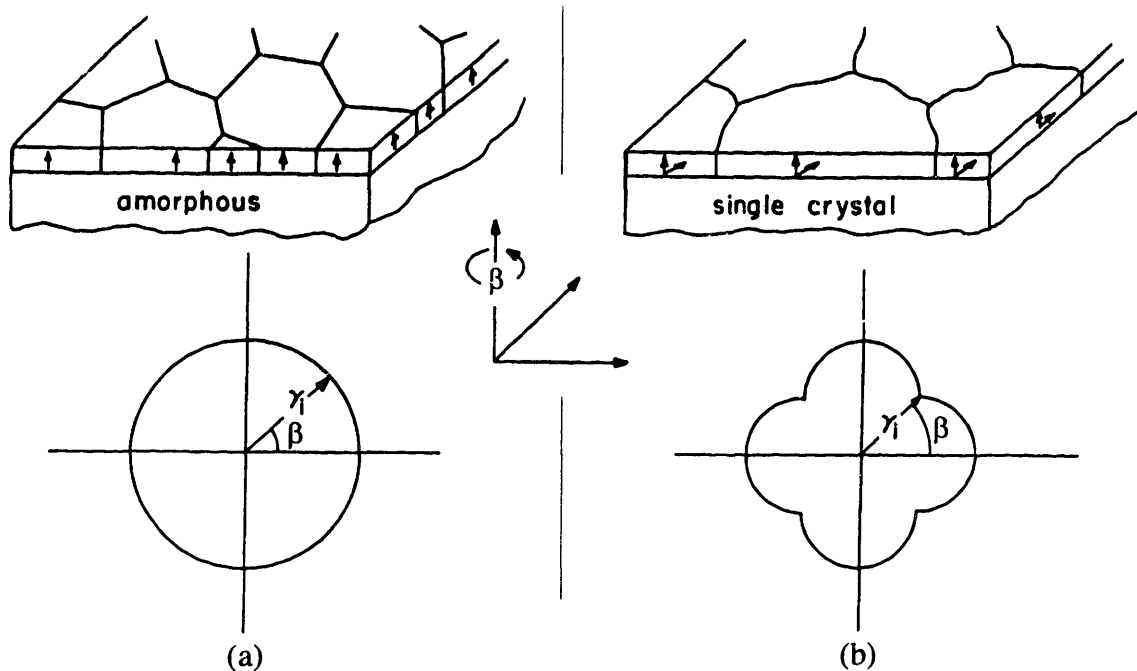


Figure 2.9: (a) The surface and interface energy of films on amorphous substrates depends solely on the texture of the grains. (b) For epitaxial systems, the interface energy also depends on the in-plane orientation of the film with respect to the substrate lattice.

2.6 - Driving forces for grain growth

It was shown in chapter one that the driving force for grain growth due to capillarity is $\Delta G = \gamma_{gb} \kappa$. Grain boundary energy and grain boundary mobility are strongly dependent on grain boundary structure. There can be some films for which the orientations of all the grains are strictly constrained (e.g., epitaxially), and where this constraint affects the orientations favored by grain growth through preferential motion of special boundaries. In most systems however, curved grain boundaries change their local curvature as they migrate, thereby changing their structure and energy. On the time scale of grain growth, this change in grain boundary energy with time averages so that grain

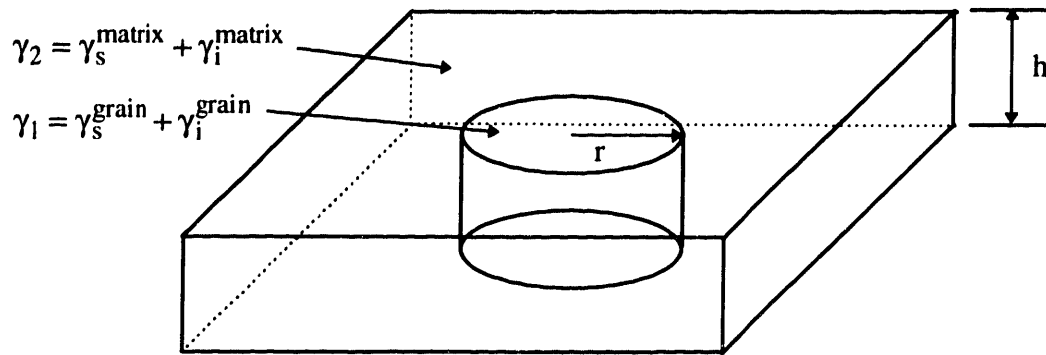


Figure 2.10: Right circular cylindrical grain with combined surface and interface energy γ_1 embedded in a uniform matrix with surface and interface energy γ_2 .

growth in the film is well described by considering that all grain boundaries have the same energy and mobility. When this is the case, the driving force for normal grain growth can be identified with local grain boundary curvature κ , and other driving forces for grain growth can be expressed as curvatures by dividing the thermodynamic driving forces by the grain boundary energy.

The driving force corresponding to surface and interface energy is easily derived for the case of a right circular cylindrical grain with radius r and thickness h , and combined surface and interface energy γ_1 , embedded in a uniform matrix with surface and interface energy γ_2 as illustrated in figure 2.10 [48]. When the grain size changes by dr , the total energy of the system changes to first order by $\Delta F = 2\pi r (\gamma_2 - \gamma_1) dr$. The volume swept by the grain boundary when the grain size changes by dr is approximately $V = 2\pi r h dr$ and the energy change per unit volume corresponding to the grain boundary motion is:

$\Delta F/V = (\gamma_2 - \gamma_1)/h$. Normalizing the energy change by the grain boundary energy yields the driving force corresponding to surface and interface energy anisotropy [48]:

$$\Gamma = \frac{\Delta\gamma}{h\gamma_{gb}} \quad (2.26)$$

Equation (2.26) is only strictly valid for the geometry illustrated in figure 2.10. We have ignored the out of plane curvature of the grain boundary and idealized the grain as a cylinder. For grains with sufficiently large diameter to thickness ratio, equation (2.26) is a good approximation and will be used throughout this thesis to express the driving force due to surface and interface energy anisotropy.

The driving force corresponding to strain energy density anisotropy and expressed as a curvature is [80]:

$$F_{\epsilon} = \frac{\Delta W_{\epsilon}}{\gamma_{gb}} \quad (2.27)$$

The driving force for grain growth locally to an element of grain boundary area is the sum of the individual driving forces arising from capillarity, surface and interface energy anisotropy and strain energy density anisotropy:

$$F = \kappa + \Gamma + F_{\epsilon} \quad (2.28)$$

Equation (2.28) can be used as a local law describing the driving force for grain growth for each element of grain boundary in the film. Results of computer simulation based on equation (2.28) are presented in chapter three. Equation (2.28) can also be used to develop an analytic model for texture development during grain growth in thin films as shown in the next section.

2.7 - Orientation selection during grain growth

Equation (2.28) represents the total driving force for grain growth on an element of grain boundary. Assuming that orientation evolution can not be induced by anisotropies in grain boundaries mobility, the orientation dependent driving force for grain growth on an element of grain boundary is then

$$F_a = \Gamma + F_\epsilon \quad (2.29)$$

F_a can be calculated for any pair of neighboring grains in the film. If only two orientations $(h_1k_1l_1)$ and $(h_2k_2l_2)$ are present in the film, the sign of the average of F_a over the volume of the film determines which orientation will grow preferentially during grain growth. In general, there are more than two orientations present in polycrystalline thin metal films. In order to predict which orientations are likely to dominate during grain growth, F_a can be calculated for the orientations that maximize its magnitude.

The average value of F_a for a pair of orientations over the film volume depends on the film thickness, the strain in the film, the film elastic properties, the anisotropy of the surface and interface energy, the distribution of grain sizes of grains in a given orientation and the anisotropy of the yield stress. For a given materials system, the film thickness and the thermal component of the strain are the variables easily controlled experimentally. There are values of the thickness and of the thermal strain for which the average of F_a is zero. These values define experimental conditions for which neither of the orientations chosen is favored compared to the other and correspond to the condition:

$$\Gamma = -F_\epsilon \quad , \quad (2.30)$$

where F_ϵ is averaged over the volume of the film. When grains are elastic, F_ϵ does not

depend on the grain size and the average of F_ϵ over the volume of the film is the same as the value of F_ϵ calculated locally between any two neighboring grains with the proper orientations. When grains are plastically deformed, equation (2.30) can be approximated by using the average grain size of the film to calculate the yield stresses and the strain energy density difference.

Equation (2.30) expresses a relationship between the film thickness and the deposition temperature of the film, or equivalently the thermal strain, and can be plotted as a line in the (h, ϵ) plane. This defines domains of thicknesses and deposition temperatures for which one orientation grows preferentially compared to the other. The plot of the lines defined by equation (2.30) in the (h, ϵ) plane constitutes a texture map for grain growth, indicating which orientation are favored by grain growth as a function of experimentally controlled variables. Grain growth experiments in films deposited at different temperatures and with different thicknesses can be compared to the predictions of equation (2.30). This is the object of chapters five and six. Alternatively, equation (2.30) can be used along with grain growth experiments to estimate the value of materials parameters of the film/substrate system, for example $\Delta\gamma$.

Surface energy for fcc metal films is minimized by (111) surfaces and interface energy for the films on substrates studied in this thesis is also minimized by (111) planes. In elastically deformed films, (111)- and (001)-textured grains, respectively, maximize and minimize strain energy density. When grain growth occurs with the film mostly in the elastic regime, (001) and (111) are therefore the relevant textures to consider. When

surface and interface energy anisotropy is of the same magnitude than elastic strain energy density anisotropy, the relationship between strain and thickness is

$$\varepsilon_{th} = \sqrt{\frac{\Delta\gamma_1}{M_{111} - M_{001}}} \frac{1}{\sqrt{h}} - \varepsilon_d - \varepsilon_i \quad , \quad (2.31)$$

where $\Delta\gamma_1$ is the difference in surface and interface energy between (001)- and (111)-textured grains and where ε_{th} , ε_i , and ε_d are the thermal, intrinsic, and densification strains in the film, respectively. The dependence of the densification strain on the as-deposited and stagnant grain diameter is explicitly given by equation (1.19).

When the strain in the film is large, or when some grains in the film have low yield stresses, plasticity has to be considered. In a film at the onset of plastic deformation, there is a grain size regime for which high yield stress grains are still elastic and low yield stress grains are plastically deformed. (111)-textured grains have the highest yield stress of all orientations and (011)-textured grains have a low yield stress. The driving force balance when the strain energy density of (111) grains is given by equation (2.11) and the strain energy density of (011) grains is given by equation (2.25) is

$$\varepsilon_{th}^2 + 2b|\varepsilon_{th}| + c = 0 \quad , \quad (2.32a)$$

$$b = \varepsilon_d + \varepsilon_i - \frac{\sigma_y(011)}{M_{111}} \quad , \quad (2.32b)$$

$$c = (\varepsilon_d + \varepsilon_i)^2 + \frac{\sigma_y^2(011)}{M_{011}M_{111}} - \frac{\Delta\gamma_2}{hM_{111}} \quad , \quad (2.32c)$$

where $\Delta\gamma_2$ is the difference in surface and interface energy between (011)- and (111)-textured grains and $\sigma_y(011)$ is the yield stress of (011)-textured grains with a diameter

equal to the average grain diameter in the film. Equation (2.32) can be explicitly solved for the thermal strain:

$$|\varepsilon_{th}| = -b + \sqrt{b^2 - c} \quad . \quad (2.33)$$

If the strain is large, all the grains in the film yield. Using the upper bound for the strain energy density of yielded grains, the driving force balance reduces to

$$\varepsilon_{th} = \frac{\frac{\Delta\gamma_i}{h} - \frac{\sigma_y(001)}{M_{001}} + \frac{\sigma_y(111)}{M_{111}}}{2(\sigma_y(001) + \sigma_y(111))} - \varepsilon_d - \varepsilon_i \quad , \quad (2.34)$$

where the driving force balance is taken between (001) and (111) grains but could be easily expressed between any two orientations. If the thermal strain in the film is less than the value defined by equation (2.34), (001) grains are energetically favored. If the thermal strain is greater than the value defined by equation (2.34), (111) grains are favored by grain growth. This occurs because the yield stress and strain energy density of plastically deformed grains is a decreasing function of the film thickness and of the grain size. As the surface and interface energy driving force for grain growth is size independent, it can overcome the strain energy density driving force for thick films and thermal strains with low magnitude. Whether or not this can occur depends on the elastic constant, the yield stresses and the difference in surface and interface energy $\Delta\gamma_i$. For some materials, equation (2.34) defines thermal strains that can be elastically accommodated by the grains. When this is the case, equation (2.34) does not define an experimentally observable boundary. This is the case for example for Ag/SiO₂/Si and Ni/SiO₂/Si as shown in chapter six.

Equations (2.31), (2.33), and (2.34) can be used to plot a texture map for grain growth such as shown in figure 2.11. Three textures, (111), (001), and (011) were considered in plotting this texture map, as they correspond to experimentally observed textures that develop during grain growth (chapters five and six). In region I, surface and interface energy anisotropy is of greater magnitude than strain energy density anisotropy

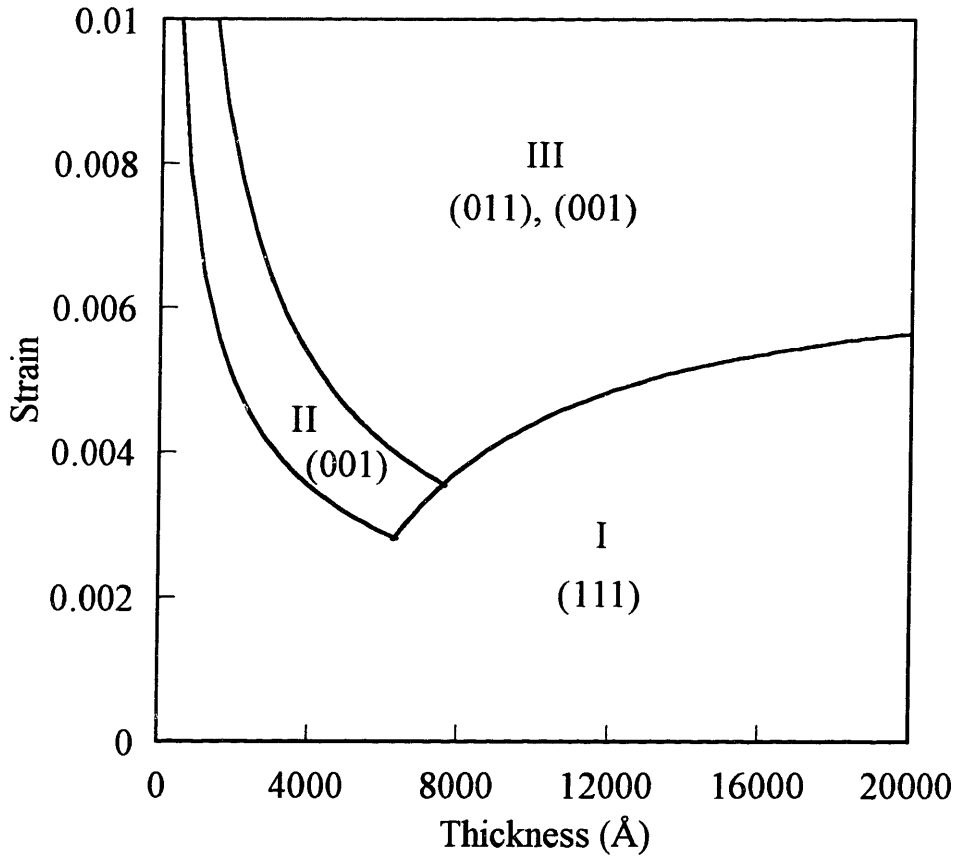


Figure 2.11: Canonical texture map showing the texture domains defined by equations (2.31), (2.33), and (2.34). The materials parameter chosen to generate the texture map are: $M_{111} = 170$ GPa, $M_{001} = 100$ GPa, $M_{011} = 140$ GPa, $C_h(111) = 165$ GPaÅ, $C_d(111) = 150$ GPaÅ, $C_h(001) = 150$ GPaÅ, $C_d(001) = 140$ GPaÅ, $C_h(011) = 120$ GPaÅ, $C_d(011) = 110$ GPaÅ, $b = 2.9$ Å, $\Delta\gamma_1 = 0.35$ J/m², $\Delta\gamma_2 = 0.65$ J/m².

and (111) grains are favored by grain growth. Region II represents the case, when elastic strain energy anisotropy is dominant and (001) grains are favored by grain growth. In region III, both (011) yielded grains and (001) elastically or plastically deformed grains have an advantage compared to (111) grains. The positions of the boundaries between texture domains depend strongly on the materials properties of the film. The position of the lines resulting from equations (2.33) and (2.34) also depend on the relationship between film thickness and grain diameter. We have assumed for simplicity that $d = h$ to generate figure 2.11. The boundary defined by equation (2.34) is relevant when the thickness exceeds 5000 \AA , for the materials parameters chosen to generate the texture map. For some other materials parameters, this line can shift toward infinite thicknesses and disappears from the texture map, as shown in chapter six.

For fcc metals with large anisotropy ratios, strain energy driven texture evolution during grain growth is expected to be mostly due to elastic strain energy density anisotropy. For these materials, the orientation dependence of the yield stress is of secondary importance and the orientations that can grow during grain growth are (001) and (111). The most important boundary in the texture map of these material is defined by equation (2.31). For materials that are nearly elastically isotropic, for example Al, the strain energy density anisotropy arising from the orientation dependence of the yield stress can drive orientation evolution during grain growth. For these materials, equations (2.33) and (2.34) define the texture domains on the texture map. Examples of these two classes of materials are examined in chapter five and six. The relative influence of elastic and

plastic strain energy anisotropy and of intrinsic and densification strains is also discussed in chapter five and six.

The analysis described above implicitly assumes that the orientations considered exist in the as-deposited films in large enough volume fractions so that they are represented by grains of various sizes and that the grain boundary energy driving force does not favor any orientation. If the as-deposited grain size of one orientation is larger than the as-deposited grain size of the other orientation, equation (2.28) should be used rather than equation (2.30) as the average curvature of the grain boundaries will favor the growth of the subpopulation of grains with the larger average grain size.

Texture maps can be plotted using the deposition temperature or the difference between the grain growth temperature and the deposition temperature rather than the strain by using equation (2.2) to relate these quantities. While equations (2.31), (2.33), and (2.34) are more compact when expressed using strain, experimental texture maps presented in chapters five and six are plotted using these alternative variables as they are directly experimentally controlled.

2.8 - Summary and conclusions

A detailed analysis of the state of strain and stress in thin films was presented and a model for the yield stress of polycrystalline thin films was reviewed. The strain energy density of thin films depends in general on the orientation of the individual grains in the film and strain energy density differences provide a driving force for the growth of low strain energy density grains. The orientation dependence of the strain energy density is different for elastically and plastically deformed films, potentially leading to the growth of

different orientations depending on the strain in the film and the magnitude of the yield stress of grains. Surface and interface energy anisotropy provides another orientation dependent driving force for grain growth that competes with the strain energy density driving force to determine orientation evolution during grain growth. The total driving force for grain growth can be expressed as the sum of the individual driving forces for grain growth on an element of grain boundary. An analytic model of orientation evolution during grain growth can be developed from the local total driving force by averaging it over the film volume. The orientations that are expected to grow preferentially as a function of the processing condition of the film can be visualized using a texture map. The orientation domains on the texture map are defined by the strains and thicknesses for which the sum of the orientation dependent driving forces for grain growth vanishes. Experimentally determined texture maps are compared to the predictions of the analytic model in chapters five and six. Computer simulations of grain growth including the two identified orientation dependent driving forces for grain growth and using the local driving force for grain growth are presented in the next chapter.

Chapter 3

Computer Simulation of Grain Growth in Thin Films

3.1 - Introduction

In this chapter, we present results of computer simulations of grain growth in thin Ag films on single crystal (001) Ni. In chapter two, a model for orientation evolution during grain growth in thin films was developed from equation (2.28). Equation (2.28) describes the local driving force for grain growth on an element of grain boundary and is now used to simulate grain growth in two dimensions.

3.2 - Simulation Techniques

The computer simulator used in this work was originally developed at Dartmouth College by Professor H. J. Frost and his students. We debugged and adapted it, and introduced modifications to simulate the effect of strain energy both in the elastic and plastic regime. Programs in C/X11 were also written to visualize and statistically analyze the results from the simulator. Listings from the simulator and these programs are not included in this thesis as they represent in excess of 15,000 lines of code. The main algorithms of the simulator, especially the treatment of strain energy density, are described briefly in the next sections.

3.2.1 - Front tracking model

The simulator treats grain growth in thin films as a two-dimensional process. The grain boundaries are discretized and represented as a list of points. The simulation is similar to molecular dynamics in that the equations of motion are solved numerically for a large number of discrete entities. Assuming proportionality between velocity and driving force [48], the equation of motion applying to one grain boundary point is

$$\vec{v} = \mu F \vec{n} \quad , \quad (3.1)$$

where \vec{v} is the velocity of the grain boundary point, F is the local driving force for grain growth, \vec{n} is the principal normal vector to the grain boundary, and μ is a mobility constant which depends on the grain boundary energy. We will assume that μ is the same for all grain boundaries. For a small enough interval of time Δt , equation (3.1) is approximated by the Euler forward numerical scheme:

$$\Delta \vec{x} \cong \mu F \Delta t \vec{n} \quad , \quad (3.2)$$

where $\Delta \vec{x}$ is the change in position of the grain boundary point in the interval of time Δt .

The factors influencing the driving force F are presented in chapter two and the expression for F is

$$F = \kappa + \Gamma + F_{\epsilon} \quad , \quad (3.3)$$

where κ is the local curvature of the grain boundary, Γ is the driving force arising from the anisotropy of surface and interface energy of grains and is given by equation (2.26) and F_{ϵ} is the strain energy density driving force given by equation (2.27).

To simulate the effect of grain boundary pinning due to formation of grain boundary grooves at the film surfaces, we have followed Mullins [35], and taken the local

velocity of a boundary segment to be zero if the magnitude of the total driving force for grain boundary motion, F , falls below a critical value F_{stag} . The boundary velocity is then given by

$$\begin{aligned} \bar{v} &= 0; & \text{if } |F| \leq F_{\text{stag}} , \\ \bar{v} &= \mu F \bar{n}; & \text{if } |F| > F_{\text{stag}} . \end{aligned} \quad (3.4)$$

For our simulations, a cellular structure is first generated through simulation of nucleation and growth [81, 82]. Grain boundary motion is then simulated by allowing, in incremented time steps, the motion of points on the grain boundaries, followed by the motion of the triple junctions which are the points where the grain boundaries meet (Figure 3.1). For each grain boundary point, the local driving force for grain growth is calculated using equation (3.3), and compared to the critical driving force (F_{stag}). If the local driving force is greater than the critical driving force, the grain boundary point is moved a distance proportional to the local driving force for grain growth in the direction

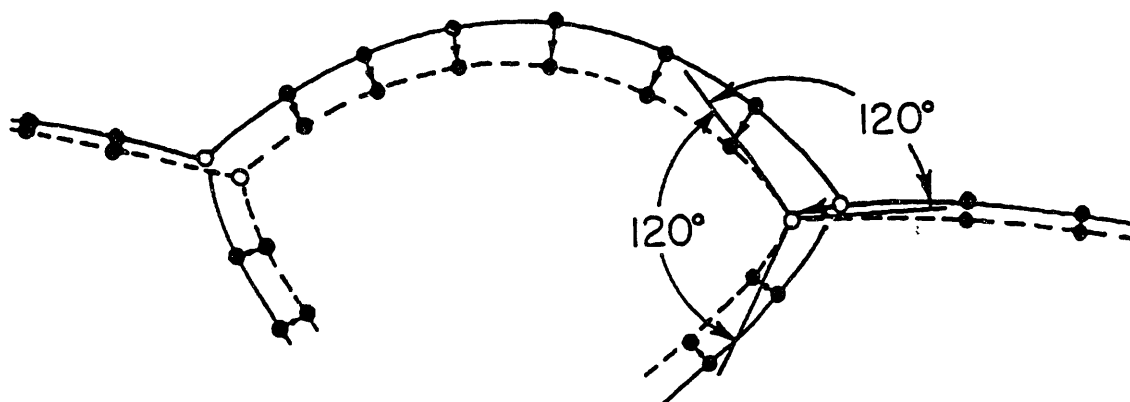


Figure 3.1: Motion of grain boundary points during one time step in the simulation. The triple points are moved such that the force balance is satisfied.

of the local grain boundary in-plane normal. If the local driving force is less or equal to the critical driving force, the grain boundary point is not moved. The triple junctions are then moved such that a force balance is satisfied. This requires that the grain boundaries meet at 120° if it is assumed that all the boundaries have the same energy, as is the case in all the simulations discussed here. Stagnation is reached when no grain boundary point is moved in one time step. For a typical simulation starting with on the order of 10,000 grains, 24 h of computation on a Digital 5000/200 workstation are required to reach stagnation.

There are several alternative simulation methods for grain growth in thin films [55, 83-91] that will not be reviewed here. One advantage of simulating grain growth using a front tracking method is that grain boundary motion laws are easily implemented and modified. The simulator has been previously used to simulate normal grain growth [37, 92], the effect of surface and interface energy [48], variable grain boundary mobility and energy [93], and the effect of solute drag [38].

3.2.2 - Implementation of the strain energy density driving force

For simplicity, we have considered that only two orientations are present in the films, (001) and (111), although extending the simulation to more than two orientations is straightforward. The densification strain due to the elimination of the free volume associated with the grain boundaries is neglected and the strain in the Ag films is constant throughout a simulation.

When strain energy density is included in the simulation, the yield stress of each grain is calculated and compared to the elastic stress for that grain. The stress and strain

energy density in the grain are initialized using the elastic or plastic values as appropriate. At each time step, the size of each grain is first calculated. As the yield stress is a decreasing function of the grain size, a yielded shrinking grain has a stress pinned at the value of the yield stress for the maximum grain size reached by that grain while yielded. A growing yielded grain can decrease its yield stress and therefore strain energy density. If the size of a grain is less than what it was at the previous time step, the strain energy density of the grain is left unchanged. If its size is larger than what it was at the previous time step, the yield stress for that size is calculated and compared to the stress of the grain at the previous time step. If the yield stress is less than the stress at the previous time step, the stress and energy density of the grain is updated. The onset of yielding is also recorded for each grain to allow tracking of yielding statistics. When the strain energy density is updated for all grains, each grain boundary point is individually considered and the driving force F is calculated and the point is moved according to equations (3.2) and (3.4).

3.3 - Ag/Ni system

3.3.1 - Surface- and interface energy of the Ag/Ni system

For the purpose of comparison with the experimental results presented in chapter five, we have used parameters characteristic of the Ag/Ni system in our simulations. The interface energy as a function of in-plane orientation has been calculated by Gao et al. using embedded atom potentials and molecular static relaxation of (001)Ag|(001)Ni and

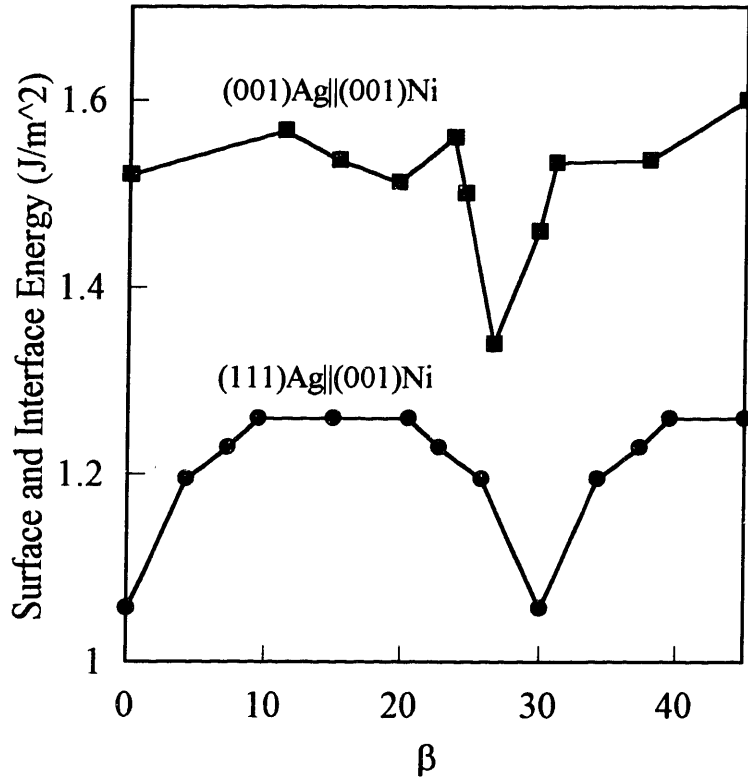


Figure 3.2: Combined surface and interface energy for (001) and (111) Ag on (001)Ni as a function of twist orientation, as adapted from refs. [94, 95].

(111)Ag||(001)Ni twist interface boundaries [94, 95]. For these boundaries, the deepest minimum for the sum of the surface energy and the interface energy corresponds to a (111)Ag||(001)Ni twist boundary with [110]Ag||[001]Ni in-plane alignment. This orientation will be referred to as (111);0°. The minimum of the sum of the surface energy and the interface energy for the (001)Ag||(001)Ni twist boundaries occurs for a 26° twist away from the cube-on-cube orientation, i.e., 26° from [001]Ag||[001]Ni, referred to here as (001);26°. In our simulations, we use a simplified version of these energy curves

(Figure 3.2) with fewer in-plane orientations than in Gao et al¹. However, the shapes of the energy curves, and notably the energy cusps for the (111);0° and (001);26° orientations, are preserved. We have initially populated each orientation with an equal, statistically significant number of grains (on the order of 4000).

3.3.2 - Mechanical properties of the Ag/Ni system

The biaxial moduli of (001) and (111) textured Ag grains are 76 GPa and 174 GPa, respectively, and the strain energy density of elastically deformed grains is given by

$$W_{\epsilon} = M_{hkl}\epsilon^2 \quad . \quad (3.5)$$

(111) grains always have a higher yield stress than (001) grains with the same diameter and thickness, but for a film under biaxial strain, they also have a higher state of stress since the biaxial modulus of (111) grains is of greater magnitude than the biaxial modulus of (001) grains. In the simulation, the strain energy density of a yielded grain is taken to be equal to the elastic strain energy density stored in the grain:

$$W_{\epsilon} = \frac{\sigma_y^2}{M_{hkl}} \quad , \quad (3.6)$$

where σ_y is given by equation (2.22). The plastic strain energy density of yielded grains is not included in the simulations. Figure 3.3a shows the elastic strain energy density and the total strain energy density, elastic and plastic, of (001)- and (111)-textured Ag grains plotted versus grain diameter for a 1000 Å thick film. When the plastic strain energy density is added to the elastic strain energy density of yielded grains, the rate of decrease

¹ More details on the work of Gao et al. are presented in chapter five, including the detailed dependence of the combined surface and interface energy on in-plane twist misorientation for (111)Ag|| (001)Ni and (001)Ag|| (001)Ni.

of the strain energy density of yielded (001) and (111) grains is not as pronounced as the rate of decrease of the elastic strain energy density. This results in a diminished influence of yielding on grain growth, as the difference in strain energy density anisotropy between elastically and plastically strained grains is decreased. Using the lower bound (eq. 3.6) for the strain energy density of yielded grains maximizes the effect of yielding on grain growth. In this chapter, we aim at identifying and separating the effects on grain growth of strain energy density anisotropy of elastically and plastically deformed grains. Using the lower bound rather than the upper bound (eq. 2.25) for the strain energy density of yielded grains is helpful in separating the influence of elastic and plastic deformation. The sensitivity of the simulation results to the choice of equation (3.6) to describe the strain energy density of yielded grains is discussed, when appropriate, in section 3.5.

For the simulations, the yield stress of grains was calculated using

$$\sigma_y^{111} = 113 \frac{\ln\left(\frac{h}{b}\right)}{h} + 99 \frac{\ln\left(\frac{d}{b}\right)}{d} , \quad (3.7a)$$

and

$$\sigma_y^{001} = 35 \frac{\ln\left(\frac{h}{b}\right)}{h} + 58 \frac{\ln\left(\frac{d}{b}\right)}{d} , \quad (3.7b)$$

where the yield stress is given in GPa when h and d are expressed in Å. The coefficients C_h and C_d in equation (3.7) have values intermediate between those found in table 2.2 and those calculated using the analytic model for the yield stress (eqs. (2.20)-(2.21)).

The elastic strain energy density of (001) grains under a given biaxial strain is the lowest of all possible orientations, and the strain energy density of (111) grains is the

highest of all orientations. The effects of the differences in elastic strain energy driving force for grain growth is therefore maximized for (001) and (111) textures. Figure 3.3b shows the strain energy density difference between (001) and (111) textured Ag grains as a function of the grain diameter for grains of equal size and using equation (3.6) for the strain energy density of yielded grains. At small grain diameters, the yield stresses of the grains are large and the grains are in the elastic regime. The strain energy density difference is therefore independent of the grain diameter. When the grain size is large, both grains are yielded and the strain energy density difference between them is a decreasing function of the grain size, as indicated by equations (2.11). For intermediate grain sizes, there is an intermediate regime for which (001) grains are yielded and (111) grains are still fully elastically strained.

For the Ag/Ni system, surface and interface energy minimization favors the growth of grains in the (111);0° orientation and strain energy favors the growth of (001) textured grains. When both driving forces are accounted for in the simulations, they compete to determine the final orientation and microstructure of the film.

3.4 - Initial Condition

The grain structure used as an initial condition for the simulation is a Johnson-Mehl structure [96], resulting from continuous crystal nucleation at a constant rate and growth at a constant rate, leading to impingement and coalescence to form a continuous film. A dimensionless measure of time is used in the simulation; $\tau = \mu t/A_0$, where t is time and A_0 is the initial mean grain area.

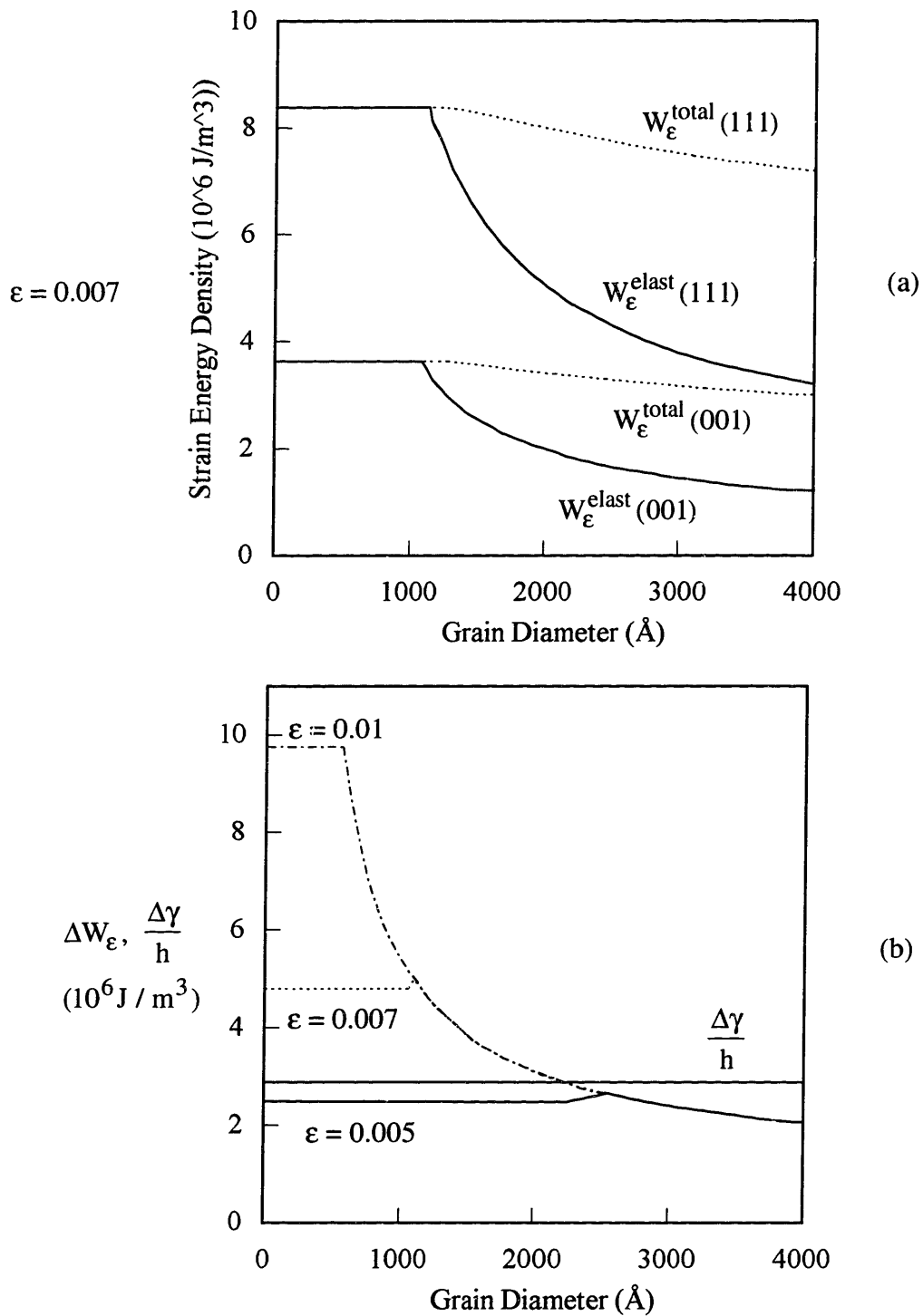


Figure 3.3: (a) Elastic and total strain energy density of Ag grains plotted versus their grain diameter for a strain of 0.7%. (b) Elastic strain energy density difference between (001) and (111) Ag grains with the same grain diameter. The surface and interface energy density is also plotted and in both cases the film is 1000 \AA thick.

We started with a Johnson-Mehl structure comprised of 9,943 grains and allowed normal grain growth, without driving forces other than κ or a stagnation condition ($F_{\text{stag}} = 0$), up to normalized time $\tau = 0.1$, at which point 7,732 grains remained. The resulting structure is characteristic of the steady-state normal grain growth regime where a parabolic growth law is obtained as well as a self similar grain structure [37]. At time $\tau = 0.1$, half of the grains are randomly chosen and assigned a (001) texture. The other grains are assigned a (111) texture. Grains with a given texture are then randomly assigned an in-plane orientation, and therefore an interface energy, thereby ensuring that all possible in-plane orientations for a given texture are equally represented in the initial grain structure. Once the thickness of the film is chosen, the average grain diameter d is chosen such that it scales with the film thickness h , typically $d/h = 1$. In some simulations, the initial grain size was chosen to be 400 \AA , as observed in grain growth experiments in Ag/Ni [47]. The texture of the structures at stagnation was not found to be strongly dependent on the choice of the initial grain size. The additional driving forces and the stagnation condition are then introduced, and the simulation is run until stagnation of the whole structure occurs.

In the work of Frost et al. on normal grain growth [37], the dependence of the grain size distribution function and the ratio of the average grain diameter to the film thickness as a function of the stagnation condition was studied. It was found that for a stagnation condition

$$F_{\text{stag}} = \frac{a}{\sqrt{A_0}} \quad , \quad (3.8)$$

with a ≤ 0.4 , the grain size distribution function is lognormal for stagnated structures, and the average grain diameter at stagnation is three times the film thickness, as observed experimentally [34, 44]. For most simulations in the current work, the stagnation condition $F_{\text{stag}} = 0.4/\sqrt{A_0}$ was chosen.

3.5 - Simulation results

For all figures in this chapter, (111) textured grains are shaded with gray and (001) textured grains are not shaded. The distribution of grain twist orientations is illustrated using the plot of GDS data in Figure 3.2, indicating the surface fraction of grains with a given twist orientation above the corresponding combined surface and interface energy. When simulated grain structures are shown in figures, only 25% of the simulated structure is represented.

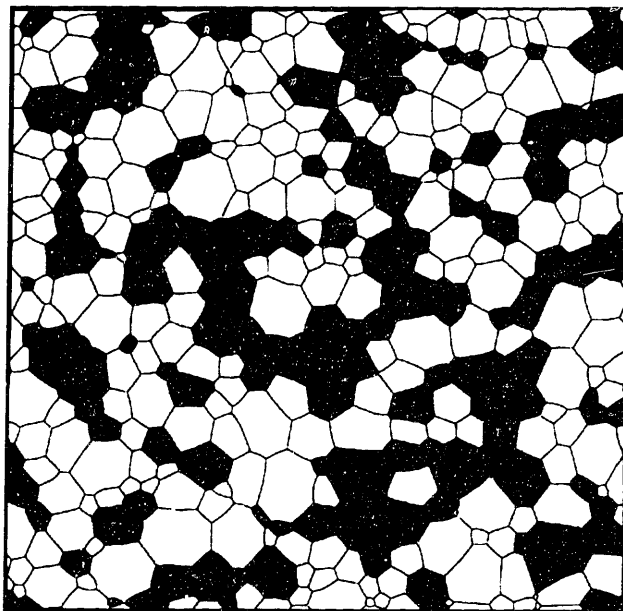
3.5.1 - Strain energy alone

Figure 3.4 shows the evolution of a grain structure subjected to a strain of 0.3%. No surface and interface energy driving force or stagnation condition are introduced. The surface fraction of (001) grains in the structure increases continuously with time until no (111) grain remains (Figure 3.4d). Because (001) grains have lower strain energy density than (111) grains in the elastic regime, they are favored by grain growth and consume the (111) grains. (001) grains also have a lower yield stress than (111) grains of the same geometry (same grain diameter and thickness), they therefore yield earlier than (111) grains in the simulation, increasing their energetic advantage. Including plastic strain

energy density in the simulation would lead to the same result, although (111) grains would not disappear as quickly.

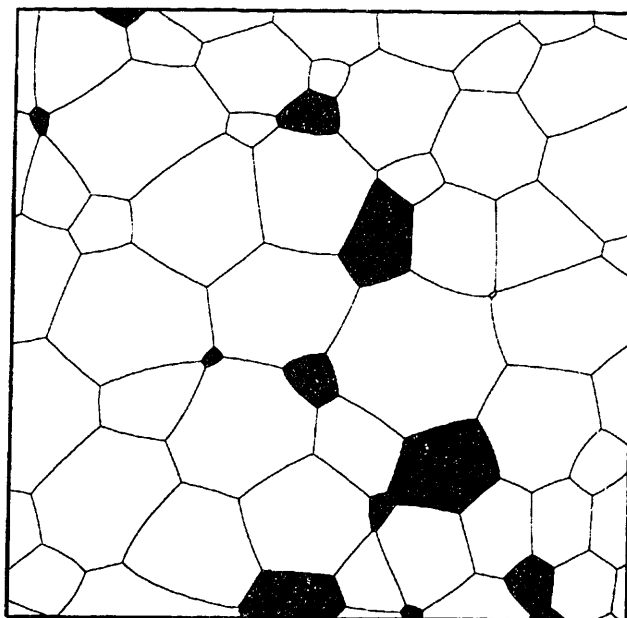
The influence of enforcing a stagnation condition is illustrated in Figure 3.5. The grain structures at stagnation, for increasing values of strain, are shown for the stagnation condition $F_{\text{stag}} = 0.4/\sqrt{A_0}$. At low values of strain, all the grains remain elastic until stagnation occurs. Because (001) grains have lower elastic strain energy densities than (111) grains, they occupy 63% of the surface of the grain structure at stagnation (Figure 3.5a). If the value of the strain is increased, yielding occurs before stagnation. (001) grains have lower yield stresses than (111) grains, and tend on average to yield earlier in the simulation. However, while (111) grains have higher yield stresses for comparable geometry, they also have a higher state of stress due to their biaxial modulus. A small number of (111) grains that were larger than average at time 0.1 therefore grew at the expense of smaller neighboring (111) grains and reached the critical grain diameter at which they yielded. Once yielded, the state of stress, and therefore strain energy density, is a decreasing function of the grain size. The yielded (111) grains were able to continue growing due to their size advantage, not only with respect to the surrounding (111) grains, but also with respect to smaller (001) grains. At stagnation, the microstructure of the film is mainly composed of (001) grains but a few large (111) grains are also present (Figure 3.5b).

$\tau = 5$



(a)

$\tau = 43$



(b)

Figure 3.4a-b: Simulation of the effect of strain energy density alone. (a) $\tau = 5$, (b) $\tau = 43$.

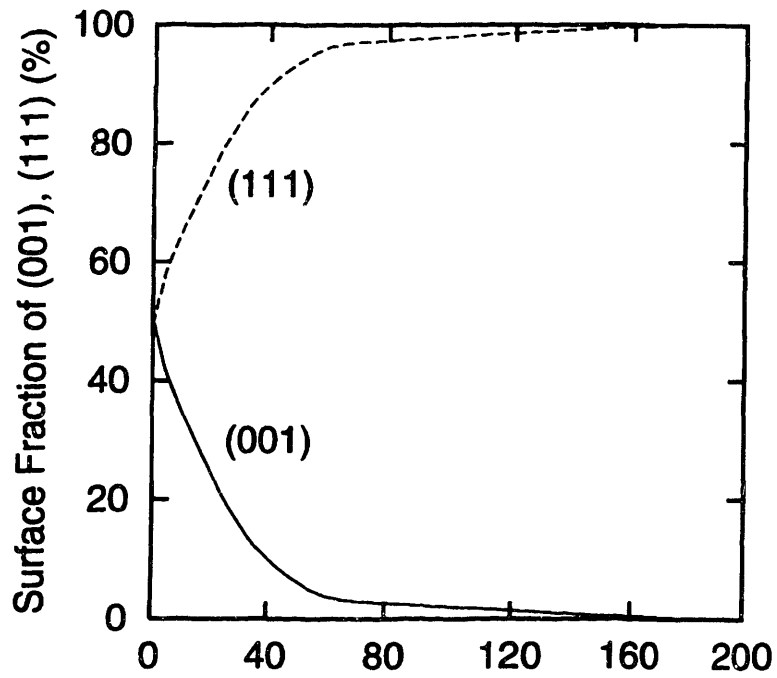
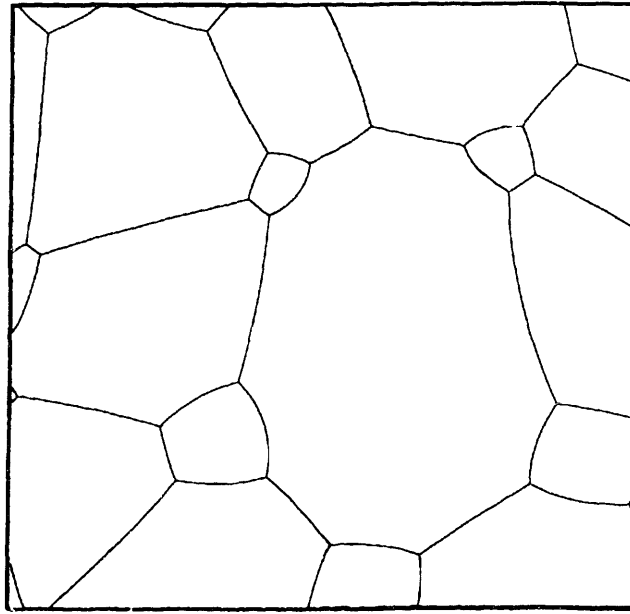
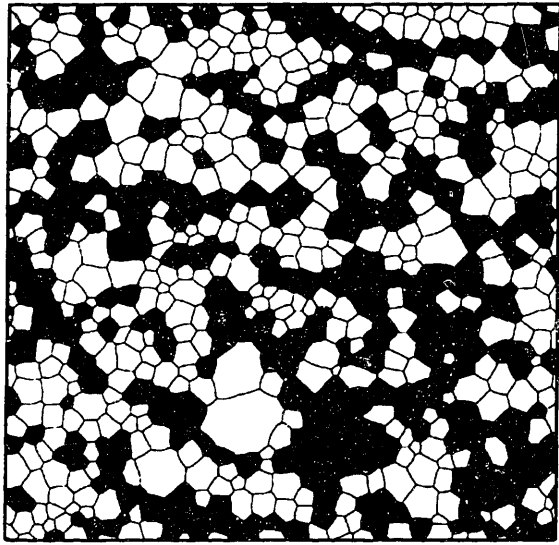
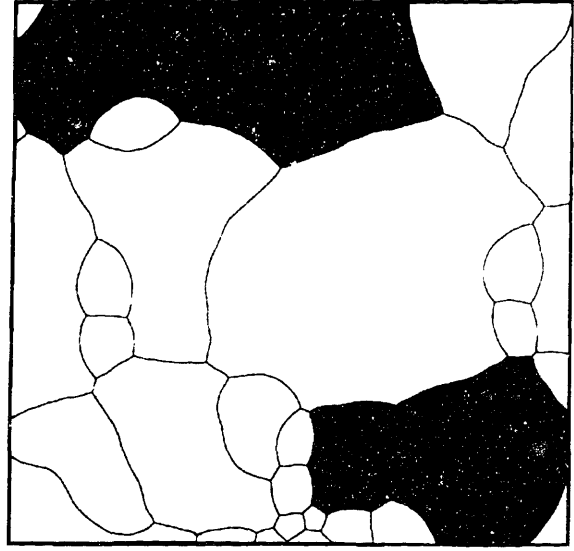


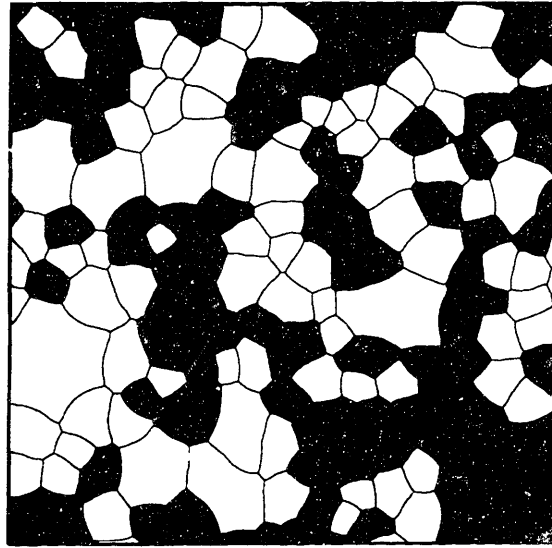
Figure 3.4c-d: (c) Structure at $\tau = 200$. No (111) grains remain. (d) Surface fraction of (001)- and (111)-textured grains plotted versus τ .



(a) $\varepsilon = 0.001$



(b) $\varepsilon = 0.005$



(c) $\varepsilon = 0.01$

Figure 3.5: Stagnated structures for simulations including the effect of strain energy density and the stagnation condition $F_{\text{stag}} = 0.4/\sqrt{A_0}$. (a) $\varepsilon = 0.001$, (b) $\varepsilon = 0.005$, (c) $\varepsilon = 0.01$.

Clusters of small grains are also present between large grains. When grains have yielded, clusters of grains with approximately the same size and the same orientation tend to be stabilized, since the driving force due to strain energy density anisotropy is minimized. Little grain boundary motion occurs for the grains at the center of the cluster and the cluster can only disappear through the shrinkage and disappearance of the grains at its border. Clusters of small grains of the same orientation tend to resist annihilation longer than isolated small grains. If the stagnation condition is stringent enough, they appear in the stagnated structure. For a weaker stagnation condition, further grain growth leads to the elimination of all small grains so that no clusters of small grains appear at stagnation.

At high values of strain (Figure 3.5c), the area fraction of the structure occupied by (001) grains at stagnation is smaller than for a medium value of the strain (Figure 3.5b). At high strains, the time during which the strain is elastically accommodated is shortened, and most of the grains yield at early times, independent of their orientation. When two grains with different orientations and similar geometry have yielded, the strain energy difference decreases as the grain size increases. The advantage of (001) grains over (111) grains therefore decreases as grain sizes increase, and the rate of grain growth in the film diminishes with time. As a result, stagnation occurs for a lesser degree of transformation of the film.

Figure 3.6 shows the increase of the surface fraction of (001) grains, over 50%, as a function of the applied strain. As the strain is increased from zero, the (001) grains occupy an increasing fraction of the structure at stagnation, due to their low strain energy

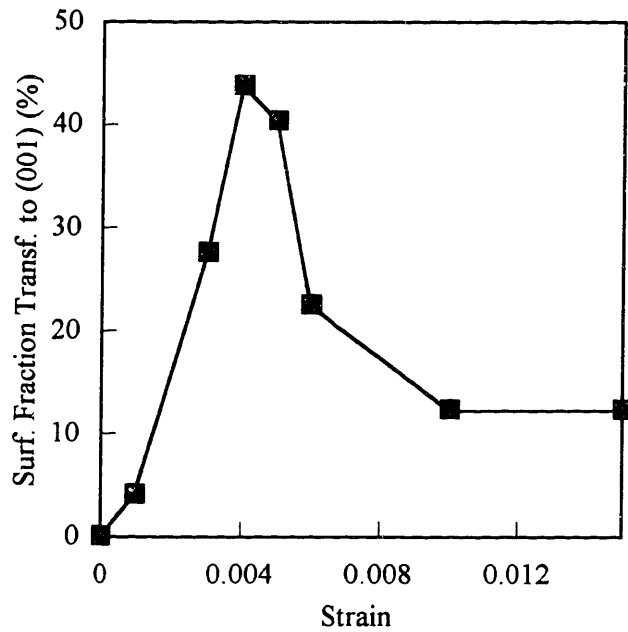


Figure 3.6: Surface fraction of (001) grains, in excess of 50%, for stagnated structures and plotted as a function of the applied strain. The stagnation condition $F_{\text{stag}} = 0.4/\sqrt{A_0}$ was enforced.

density in the elastic regime. When the strain is high enough to induce significant yielding long before stagnation, the (001) grains, although still favored by grain growth, occupy a smaller fraction of the structure at stagnation due to the small strain energy density differences between (001) and (111) textures for large grain sizes. At $\epsilon = 0.4\%$, the interplay of the onset of yielding and the effect of the geometry-dependent yielding produces the strongest (001) texture, with 94% of the surface area of the structure occupied by (001) grains.

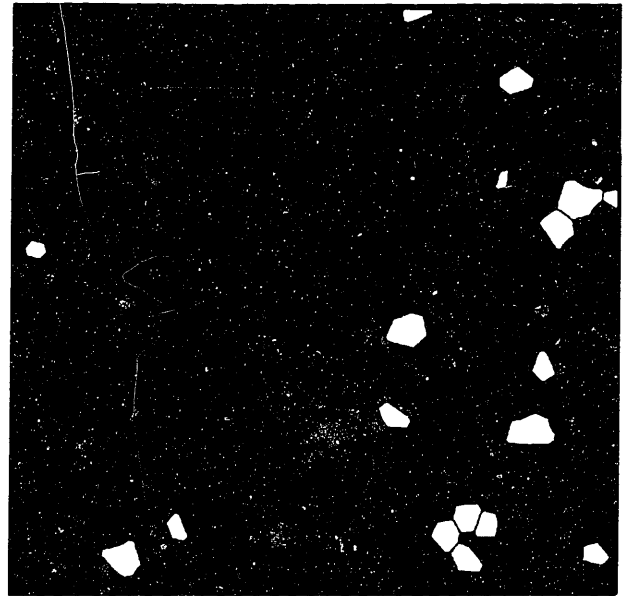
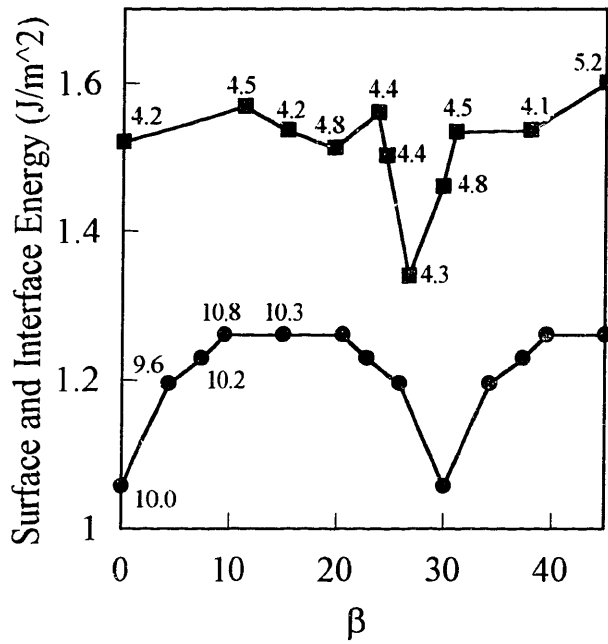
The effects described in this section remain qualitatively the same if the upper bound for the strain energy density of yielded grains is used rather than equation (3.6). The influence of large strains on the grain size and orientation distributions is similar but

the magnitudes of the effects are reduced. For large strains, the average grain size is expected to be larger than shown in figure 3.5c and the surface fraction of (001) grains is expected to be larger than shown in figure 3.6.

3.5.2 - Surface and interface energy alone

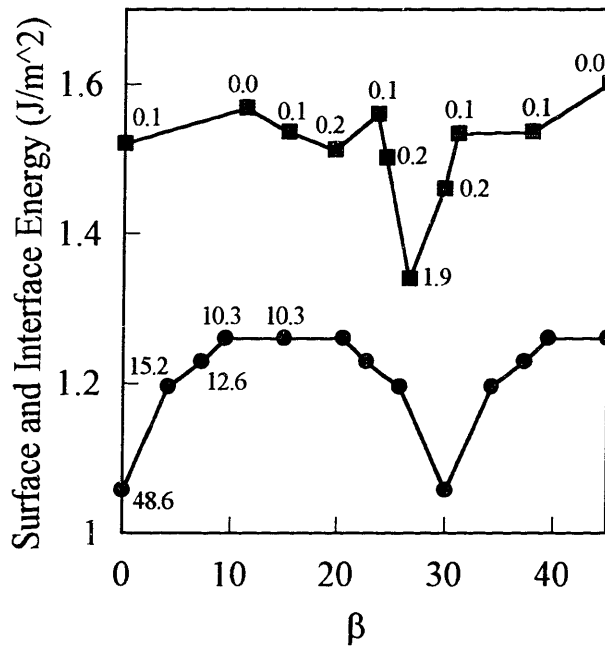
Figure 3.7 shows results from simulations in which only the surface and interface energy driving force and the stagnation condition were introduced. The surface fractions of grains with various orientations are given for the initial structure and at stagnation. Most of the grains in the stagnant structure are (111)-textured, and about half of the grains are specifically in the energy-minimizing (111);0° orientation. Only a marginal surface fraction of (001) grains remains at stagnation. The (001) grains which have not been consumed by the (111) grains are mainly in the (001);26° orientation, which corresponds to the deepest cusp of the (001)Ag||l(001)Ni energy curve.

The fraction of grains in a given orientation at stagnation is a strong function of the stagnation condition. The less stringent the stagnation condition, the more grain growth will occur. Since the grains in the (111);0° orientation have an advantage over all other orientations, they will always dominate to an extent determined by the value of F_{stag} . This is illustrated on Figure 3.8 where $F_{\text{stag}} = 0.2 / \sqrt{A_0}$, and for which the surface fraction of (111);0° grains for the stagnant structure is 95% and no (001) grains remain.



(a)

(b)



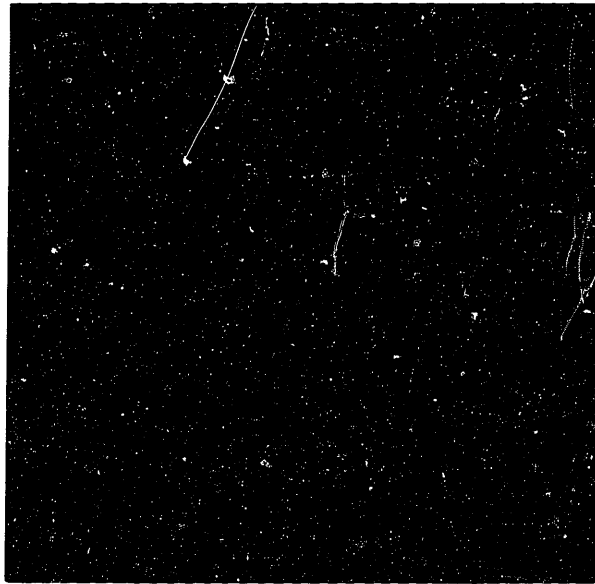
(c)

Figure 3.7: (a) Surface fraction of grains with (001) and (111) textures as a function of twist orientation, as initialized at $\tau = 0.1$. (b) Stagnated structure when surface and interface energy and the stagnated condition $F_{\text{stag}} = 0.4/\sqrt{A_0}$ are introduced. (c) Distribution of orientations in the stagnated structure.

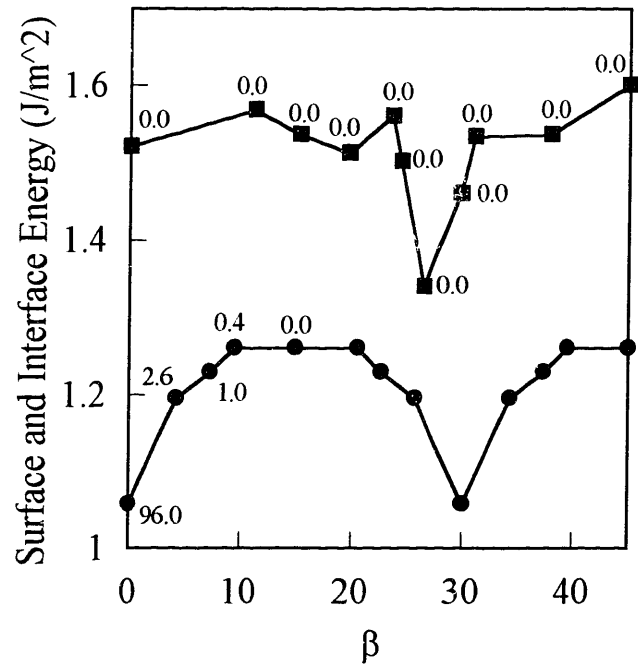
3.5.3 - Combined effects of strain energy and surface and interface energy

Surface and interface energy reduction promotes the growth of (111) grains and strain energy reduction promotes the growth of (001) grains. When both are allowed in the simulation, these two orientation-dependent driving forces compete to determine the texture of the film.

Whether or not a (001) texture can develop in the film is strongly dependent on the yielding criteria. When the yield stress is taken to be given by equation (2.20), and for the stagnation condition given by equation (3.8), the texture of the structure at stagnation is always (111) for any magnitude of the strain. This is due to the fact that (111) grains can yield at early times in the simulation, and that once they are yielded, their strain energy density is a decreasing function of the grain size. Since the (111) grains have also a grain diameter independent advantage due to surface and interface energy over the (001) grains, the (111) grains can, once yielded, overcome the energetic disadvantage, due to their high elastic strain energy density, and consume the neighboring (001) grains. This results in the development of a (111) texture in the film. For a (001) texture to develop in the film, the (111) grains must remain in the elastic regime until they reach a sufficiently large grain diameter, so that (001) grains can consume a large fraction of the (111) grains. This can occur for sufficiently large yield stresses of the (111) grains. Plastic strain energy density would also tend to diminish the advantage of (111) grains since when it is added to the elastic strain energy density of yielded grains, the rate of reduction in strain energy density with increasing grain size is decreased.



(a)



(b)

Figure 3.8: (a) Stagnated structure when the effects of surface and interface energy and of the stagnation condition $F_{\text{stag}} = 0.2/\sqrt{A_0}$ are simulated. (b) Distribution of orientations for the stagnated structure: all grains are (111)-textured.

Figure 3.9 shows the predominant texture of the film at stagnation ($F_{\text{stag}} = 0.4/\sqrt{A_0}$), as a function of film thickness and applied strain. At small thicknesses and low strains, the surface and interface energy driving force dominates due to its $1/h$ dependence, and the stagnant texture is (111). At high thicknesses and high strains, the strain energy driving force dominates, and the film is (001)-textured. The transition between these two domains can be determined by equating the two orientation dependent driving forces for grain growth as presented in section 2.7. If grains are still in the elastic regime ΔW_ϵ is given by equation (2.13), and the driving force balance (eq. 2.30) reduces to

$$\epsilon = \sqrt{\frac{\Delta\gamma}{(M_{111} - M_{001})h}} \quad , \quad (3.9)$$

which is equation (2.31), when the intrinsic and densification strains are ignored. The value of $\Delta\gamma$ chosen to generate the curve on Figure 3.9 was taken to be the calculated difference for grains with (001); 26° and (111); 0° orientations.

The texture transition is described by equation (3.9) only if grains remain elastic or yield shortly before stagnation. In that case, the driving force for grain growth arising from strain energy anisotropy is similar in nature to the surface and interface energy driving force in that it is a size independent driving force, determined solely by the texture of the grains meeting at a grain boundary. The elastic regime covers most of the time needed to reach stagnation for low values of strain, for which relatively large grain sizes must be obtained in order for the stress to reach the yield stress of the grains. This texture transition is dependent on the value of the yield stress in the sense that if the yield stress of

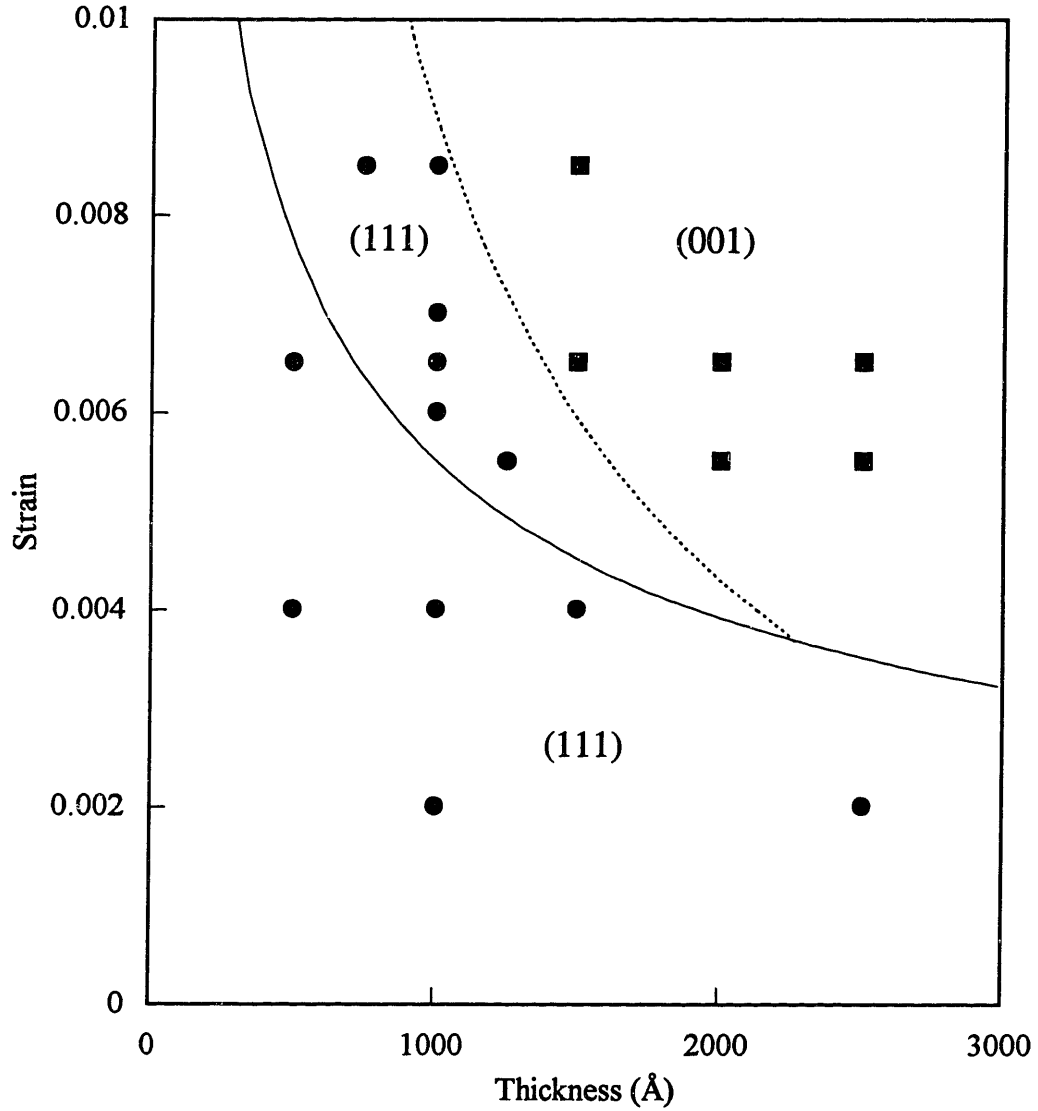


Figure 3.9: Dominant texture at stagnation plotted as a function of the film thickness and the applied strain. This constitutes a texture map for the simulation results. The solid line represents the driving force balance in the elastic regime (eq. 3.9) and the dashed line represents the driving force balance when (001) grains are yielded (eq. 3.10).

(111) grains is too low, the time domain over which (111) grains are elastically strained is short and the structure is (111)-textured at stagnation, even if the applied strain is high.

At high values of strain, yielding occurs at early times, and equation (3.9) can not be used to describe the texture transition. The few (111) grains which are significantly larger than the average grain size of the structure at time $\tau = 0.1$ yield before neighboring (001) grains can consume them. Since they have a low surface and interface energy, they are favored by the grain growth process and consume the (001) grains in the structure, even if they have yielded, and the film's texture at stagnation is (111) with most grains in the (111); 0° orientation. In the high strain regime, the dominant texture of the structure at stagnation is determined by whether or not the (111) grains can yield at early times, when (001) grains are still in the elastic regime. The transition between (001)- and (111)-textured structures at stagnation is therefore still described by the balance of the orientation dependent driving forces for grain growth in which W_ϵ for (111) grains is calculated assuming yielding and W_ϵ for (001) grains is calculated assuming an elastic response. The driving force balance (eq. 2.30) then becomes,

$$M_{111}\epsilon^2 - \frac{\sigma_y^2(001)}{M_{001}} = \frac{\Delta\gamma}{h} \quad , \quad (3.10)$$

which can be solved for ϵ as a function of d and h . The curve generated by equation (3.10) is plotted on Figure 3.9. The position of this curve depends on the actual choice of the yielding criterion and has been plotted on Figure 3.9 for the yield stress defined by equation (3.7). If plastic strain energy density is included, the domain of thicknesses and

strains defined by the curves resulting from equation (3.9) and (3.10) shrinks in size as the curve defined by equation (3.10) shifts toward smaller thicknesses and larger strains.

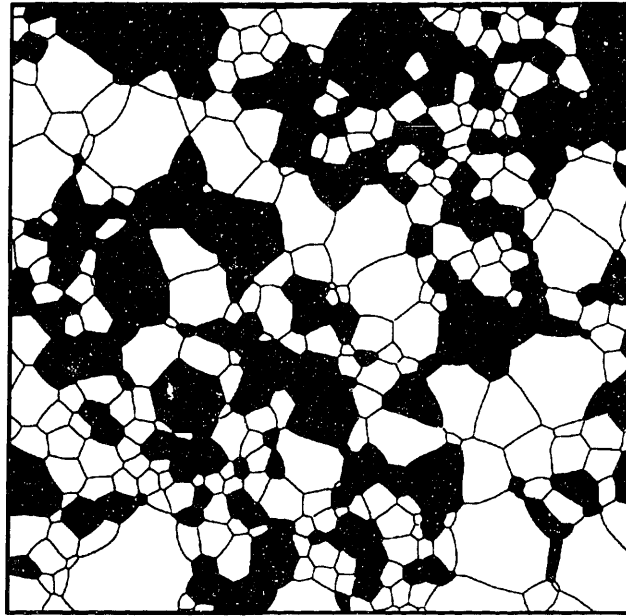
When yielding is introduced, structures with thickness and strain that would allow strain energy density differences for grains in the elastic regime to supersede differences of surface and interface energies, and therefore result in a (001)-textured structure at stagnation, are predicted to be (111)-textured at stagnation. This is due to the decrease with grain size of strain energy density in (111) grains once they are yielded. This allows surface and interface energy anisotropy to dominate in the grain growth process. The effect of accounting for yielding of the grains in the structure extends the range of thicknesses and strain for which the structure is (111)-textured at stagnation, compared with the range of strain and thicknesses for which the balance of the elastic strain energy driving force with the surface and interface energy driving force predicts a (111)-textured structure at stagnation.

Figure 3.10 shows the grain structures and the surface fraction of (001) grains and (111) grains, for a 1500 Å thick film subjected to a strain of 0.65%, as a function of time. Even when the final texture of the film is (111), the (001) orientation originally dominated in the structure. At early times, most grains are still in the elastic regime and (001) grains have an advantage due to their low strain energy density. These (001) grains consume (111) grains which are still elastically strained, and the surface fraction of (001) grains raises sharply.

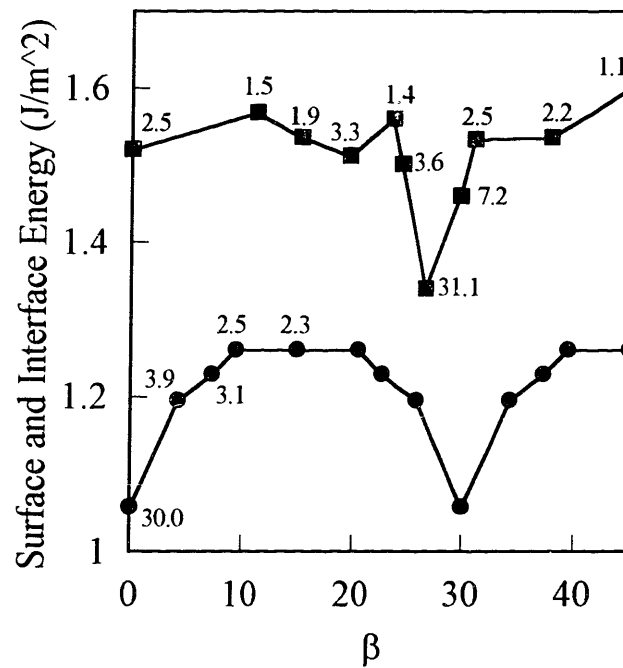
The few (111) grains larger than average at time $\tau = 0.1$ yielded at early times in the simulation due to their large stresses. Upon increasing their size, they decreased their

strain energy density. As surface and interface energy favored them, they were able to grow. Once the (001) grains yielded, the (111) grains were already large enough to continue to grow at the expense of the (001) grains. At stagnation, 65% of the structure consists of (111)-textured grains, all of which are in the (111);0° surface and interface energy minimizing orientation (Figure 3.10f). This effect is similar in nature to the case shown in Figure 3.5b, when the strain energy driving force and a stagnation condition are present, but no surface and interface energy driving force is allowed. In that case some (111) grains which yielded early in the simulation are able to grow, and a few large (111) grains are present in the stagnated structure. When surface and interface energy is allowed, the same (111) grains have an additional advantage and can reverse the initial texture evolution, and eventually consume most of the structure before stagnation occurs. This effect never appears when only the strain energy driving force is allowed because the (111) grains need the size independent advantage provided by the surface and interface energy driving force to reverse the initial advantage of the (001) grains. The texture reversal shown in Figure 3.10g does not occur for just any value of the strain or the thickness. At low values of strain and small thicknesses, the low surface and interface energy of (111) grains can overcome the strain energy advantage of (001) grains and the surface fraction of (111) grains increases from time $\tau = 0.1$. Texture reversal only occurs for conditions chosen in the domain defined on Figure 3.9 by the curves resulting from equations (3.9) and (3.10). At thicknesses and strains smaller than those defined by equation (3.9), elastic strain energy anisotropy can not overcome surface and interface

$\tau = 5$



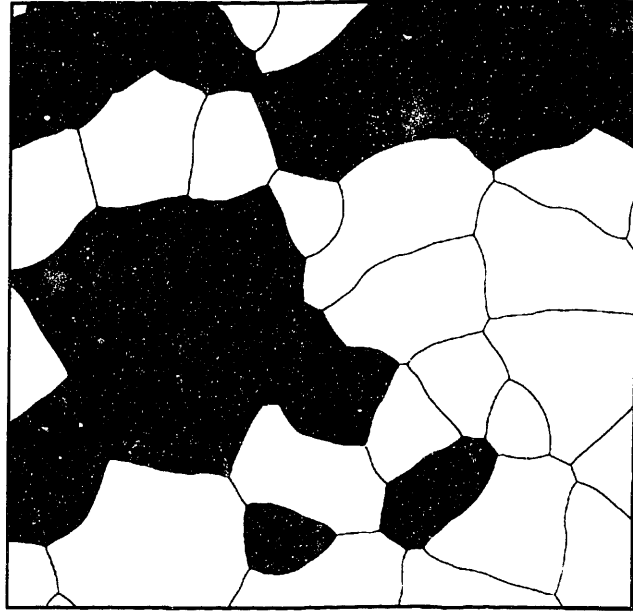
(a)



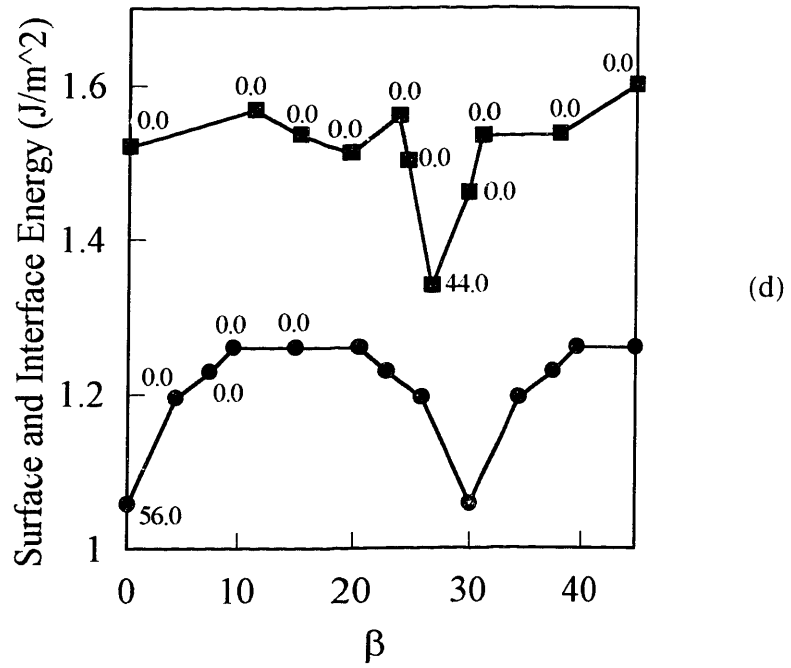
(b)

Figure 3.10a-b: Combined effects of strain energy density anisotropy, surface and interface energy anisotropy and of the stagnation condition $F_{\text{stag}} = 0.4/\sqrt{A_0}$. The structure and the orientation distribution are shown at $\tau = 5$.

$\tau = 20$

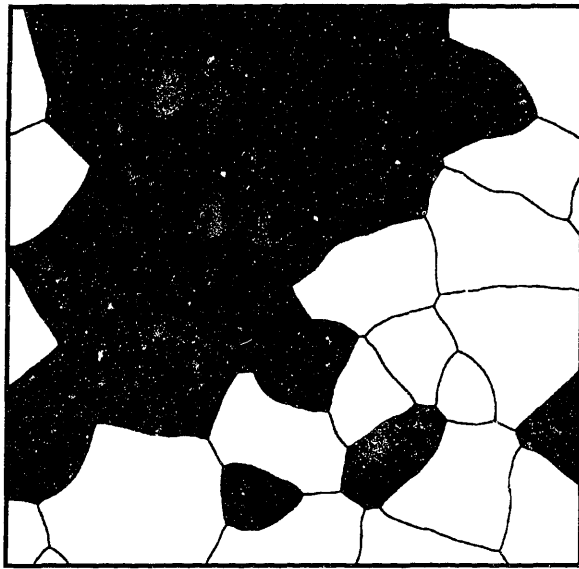


(c)

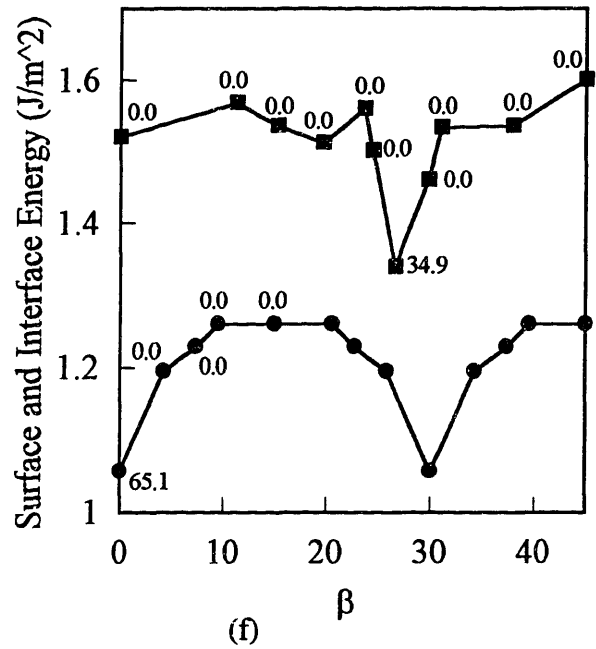


(d)

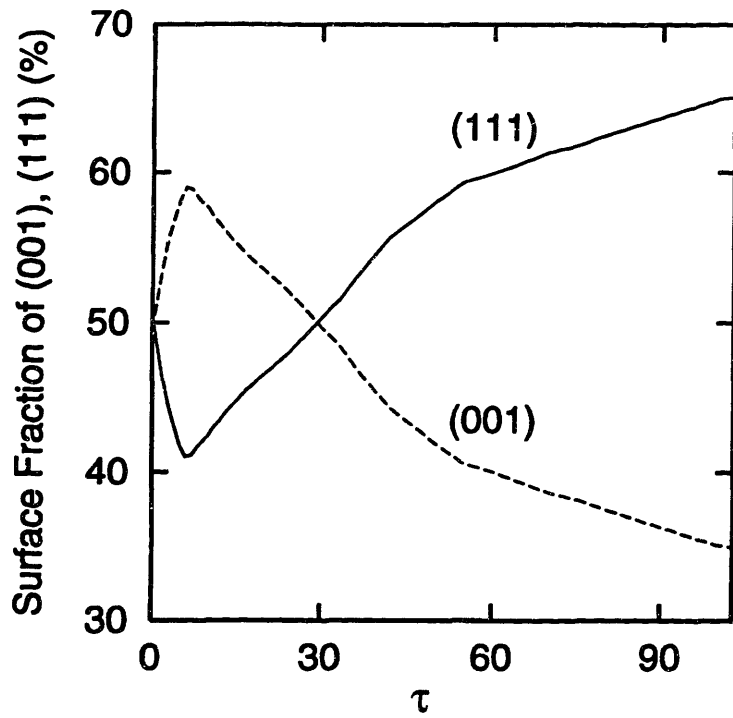
Figure 3.10c-d: Simulated grain structure and orientation distribution at $\tau = 20$.



(e)



(f)



(g)

Figure 3.10e-g: (e) Stagnated structure, $\tau = 103$. (f) Distribution of orientation of (001) and (111) as a function of twist orientation. (g) Surface fraction of (001)- and (111)-textured grains as a function of τ .

energy anisotropy and the dominant texture of the structure is (111) at any time of the simulation. At thicknesses and strains greater than those defined by equation (3.10), (001) grains are favored and the dominant texture is always (001).

Figure 3.11 shows the surface fraction of grains in the (001);26° orientation as a percentage of the surface fraction of (001)-textured grains, and the surface fraction of grains in the (111);0° orientation as a percentage of the surface fraction of (111)-textured grains, for the simulation shown on Figure 3.10. As surface and interface energy is the only in-plane orientation dependent driving force, (001);26° grains are favored over all other (001)-oriented grains and (111);0° grains are favored over all other (111)-oriented

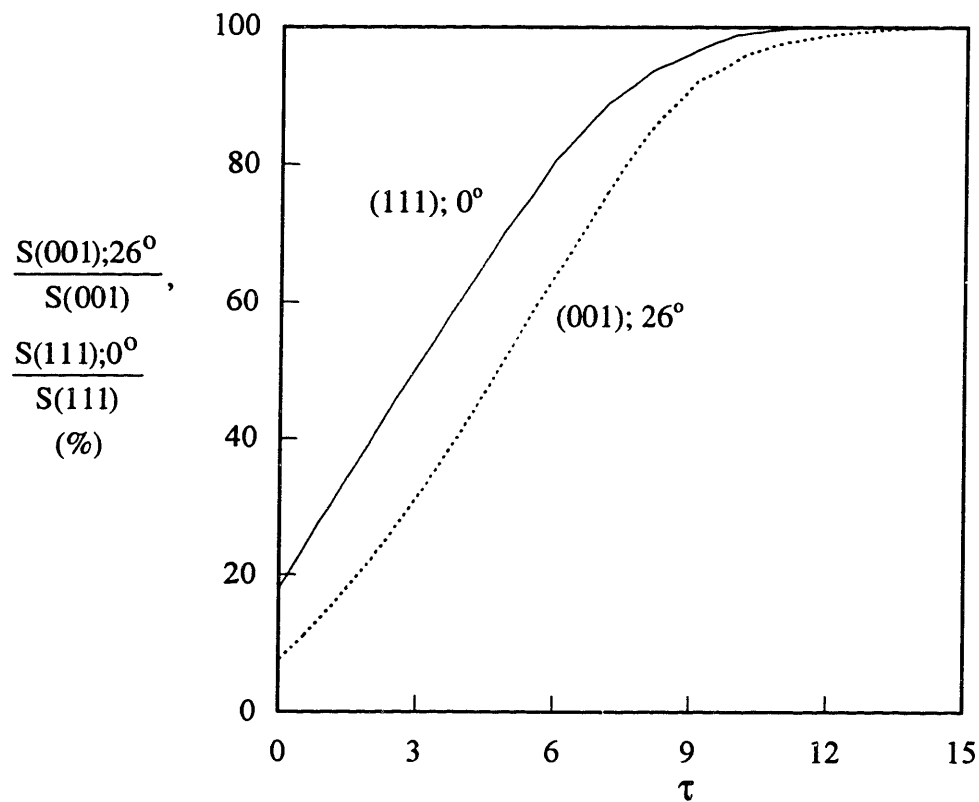


Figure 3.11: Evolution of the relative surface fraction of grains in the (001);26° and (111);0° twist orientations as a function of τ .

grains and the curves of Figure 3.11 monotonically increase with time, both in the early stages of the simulation, when the absolute surface fraction of (001) grains is increasing, and in the later stages, when the structure develops a (111) texture. At times greater than $\tau = 12$, all the grains remaining in the structure are in the (001); 26° and (111); 0° orientations. This justifies taking $\Delta\gamma$ to be the difference in surface and interface energy for grains with (001); 26° and (111); 0° orientations in equations (3.9) and (3.10), since grains with other orientations are rapidly consumed.

3.6 - Discussion and conclusions

The main result of these simulations is to show that strain energy anisotropy can drive abnormal grain growth and texture evolution in thin films. When this is the case, the texture of the film after grain growth is determined by the strain energy minimizing orientation of the material when subjected to a biaxial state of strain. For all fcc metals, (001)-textured grains are in the elastic strain energy minimizing orientation. Elastic strain energy density anisotropy and surface and interface energy anisotropy generate two orientation-dependent driving forces for grain growth which can favor different orientations. For a thin film on a substrate, surface and interface energy is always a driving force for grain growth which favors surface and interface energy minimizing orientations. Strain energy density anisotropy can overcome the effect of surface and interface energy differences if the anisotropy ratio $A = 2c_{44}/(c_{11}-c_{12})$ is sufficiently greater than 1.0 for the material considered, if the biaxial strain applied to the film is large, and if the magnitude of the yield stress of surface and interface energy minimizing grains is sufficiently large to prevent them from yielding at the early stages of grain growth. In that

case, strain energy density differences arising from elastic energy anisotropy are larger than surface and interface energy differences and strain energy anisotropy dominates in texture selection during the grain growth process. If the anisotropy ratio is close to 1.0, the main source of strain energy differences arises from the orientation-dependence of the yield stresses of grains. The yield stress is a decreasing function of the grain size, so that the strain energy density difference between two yielded grains also decreases with grain size. For Ag/(001)Ni, the yield stresses of the (001) and (111) orientations, as given by equation (3.7), are close enough that there is a critical grain radius above which the size independent energetic advantage of (111) grains has a greater magnitude than the strain energy driving force (e.g., for films thicker than 16 Å). If substantial grain growth occurs after the average grain size of the structure exceeds the critical radius, the texture at stagnation is determined by the surface and interface energy minimizing orientation. In the case of Ag, if the elastic strain energy anisotropy is artificially removed from the simulation, and strain energy density differences arise only because of the orientation and geometry dependence of the yield stress, the texture at stagnation is (001) for any thickness and strain. *The range of thicknesses and strains for which strain energy anisotropy dominates strongly depends on the elastic anisotropy of the material considered, the magnitude of the yield stresses of different orientations and on the stagnation criterion.*

The results of the simulation are sensitive to the magnitude of the yield stress. If the yield stresses are calculated using equation (2.20) instead of equation (3.7) the final texture of the structure at stagnation, when both strain energy and surface and interface

energy are accounted for, and the stagnation condition given by equation (3.8) is enforced, is always (111), independent of the thickness of the film and the applied strain. This is due to the early yielding of all grains which allow surface and interface energy to dominate and determine the texture at stagnation. For the simulations where yielding is important, the results are sensitive to the choice of the upper or lower bound for the strain energy density of yielded grains. The effect of yielding is maximized for the lower bound of the strain energy density and is minimized for the upper bound of the strain energy density. Choosing the upper bound decreases but does not eliminate the sensitivity of the strain energy density anisotropy to grain size. The domain of texture reversal defined by equations (3.9) and (3.10) is narrowed and the average grain size at stagnation as well as the width of the distribution of grain sizes is decreased.

The texture of the structure at stagnation also depends strongly on the stagnation criterion. In the case of values of h and ϵ such that a texture reversal occurs from (001) at early times to (111) at later times, a high value of F_{stag} can induce stagnation of the structure before the surface fraction of (111) grains becomes greater than the surface fraction of (001) grains, and the texture of the structure at stagnation is (001). For a less stringent stagnation criterion, the texture would be (111). The surface fraction of (001) grains at stagnation is also a function of the stagnation criterion. Because of yielding, the maximum (001) texture in thick and highly strained films occurs prior to stagnation and the surface fraction of (001) grains decreases monotonically once most grains, especially (111) grains, have yielded. The effect of the stagnation criterion is to progressively stop grain growth before the texture can revert to (111). For a less stringent

stagnation criterion, it is expected that for large thicknesses, the texture of the structure at stagnation is (111). When plastic strain energy density is added to the elastic strain energy density of yielded grains, the thicknesses for which the texture can reverse from (001) to (111) are pushed toward larger values than when only the elastic strain energy density of yielded grains is considered.

For most simulations, the texture at stagnation is determined primarily by strain energy density differences between elastically deformed grains. The influence of the yield stress on the texture of the structures at stagnation is important only when the strain is large and in a small range of thicknesses. If the upper bound for the strain energy density of yielded grain were used instead of the lower bound, the influence of the yield stress on texture selection during grain growth would be weaker. *This indicates that texture selection in this system is mostly driven by the strain energy density anisotropy of elastically deformed grains.*

The simulation results are in agreement with the analytic predictions of texture evolution during grain growth presented in chapter two. The texture domains predicted by the driving force balance approach presented in section 2.7 and the domains on the texture map generated with the simulation results coincide. *Although based on very simple premises, the semi-quantitative analytic model is validated by the simulation results.*

In our simulations, only two textures are considered, (001) and (111). It is shown in chapter five that this is representative of the case of the as-deposited orientations found for the system Ag||(001) Ni. However this is not the general case for a thin metallic film

on a substrate, where more than two orientations are usually present in the as-deposited film as shown, in chapter six. These more complex systems can be simulated, providing that data on the anisotropy of the surface and interface energy is available and that sufficient computer power is available.

In chapter five, grain growth experiments in polycrystalline Ag on single crystal (001)Ni are presented and compared with the simulation results.

Chapter 4

Experimental procedures

4.1 - Introduction

Before presenting experimental results in chapter five and six, we will review the experimental techniques used to prepare and characterize the thin film samples.

The basic technique used in this work consists of depositing a polycrystalline thin film of a fcc metal onto a substrate. Ideally, the film as-deposited would have a fine grain size, of order less than the film thickness, and would be randomly oriented. After deposition, the film can be annealed to promote grain growth or bonded to another film, and then annealed. The annealing time, the deposition and annealing temperatures, and the film thickness are the experimentally controlled variables. Among the parameters controlling the as-deposited microstructure of the film, the substrate temperature, the background gas pressure, and the growth rate can be optimized to obtain the best possible conditions prior to grain growth. All experimental procedures aimed at minimizing the exposure of the film to contaminants, which can segregate to the film surface, interface, and grain boundaries, and influence grain growth.

The primary characterization technique used was x-ray texture analysis. Bright field transmission electron microscopy (TEM) and focused ion beam microscopy (FIB) were also used to obtain images of the microstructure of the films. Bright field transmission electron microscopy is a standard techniques and is not reviewed here. All

metal/SiO₂/Si TEM samples were prepared using a standard wafer back-etching technique [47], where the back of the Si wafer is etched in a 25%HF-75%HNO₃ solution, leaving a metal/SiO₂ window, suitable for the observation of the film in the TEM. FIB images are constructed using secondary electrons resulting from the interaction of the ion beam with the sample. Ion-induced secondary electron emission depends strongly on the orientation of the crystal relative to the incident beam direction, due to ion-channeling effects [97, 98]. The microstructure of films can therefore be imaged using FIB although it is difficult to resolve grains smaller than 2000 Å in diameter and to index the orientation of the grains. X-ray texture analysis is reviewed in refs. [47, 99]. Since it is the primary technique of analysis for this work, it is briefly reviewed in section 4.3 with a focus on its applications to thin film systems.

4.2 - Film deposition

This section closely follows the film deposition procedures described in ref. [47]. Film deposition was performed by electron-beam evaporation in a Balzers UMS 500 ultra-high-vacuum (UHV) system. The system is evacuated by a turbopump backed by a mechanical pump which is also used as a roughing pump. A titanium sublimation pump surrounded by a gettering surface brings the system to UHV pressures. The base pressure prior to deposition is of order 7×10^{-10} mbar. N₂ and CO₂ constitute the primary residual gases present in the chamber prior to deposition, as monitored with a quadrupole mass spectrometer. The partial pressures of oxidizing gases, and particularly O₂ and H₂O, is typically of order 5×10^{-11} mbar. During deposition, the molten melt degas and radiative thermal energy from the electron beam promotes gas desorption from the chamber walls,

resulting in an increase in pressure of about an order of magnitude. The primary gas species during deposition are CH₄, H₂, CO, and CO₂.

The chamber is metal sealed with the exception of three Viton O-rings mounted on primary access ports. The system is vented with dry N₂ each time new substrates are loaded. The length of the exposure of the system to air is minimized as much as possible with a typical loading time of one hour. In order to obtain the minimum base pressure, the vacuum system is equipped with internal resistive bakeout coils and good thermal insulation. The optimum bakeout temperature compatible with the Viton O-rings is 170°C and should be performed for at least sixteen hours prior to deposition. In order to prevent contamination of the substrate surface with gases desorbed during the bakeout, the substrates are kept at a temperature greater than 300°C during the entire bakeout.

The films are deposited by electron-beam evaporation using a 10 kV electron beam deflected through 270° prior to impingement on the metal target. The metals used for the melts are at least 99.99% pure and are loaded directly into the water cooled Cu hearths of the e-beam assembly. Two separate e-beam assemblies are available for deposition. The deposition rate and thickness of the films are monitored using a Ag-coated quartz crystal oscillator. The oscillator is calibrated for each film material by depositing a film on a flat substrate and by comparing the change in frequency of the crystal during deposition to the thickness of the film measured ex-situ using a profilometer on a step in the film. In a typical run, the desired rate is obtained by controlling the power of the electron beams. When the desired rate is attained, the film thickness on the substrate is controlled by opening and closing a manual shutter in front of the substrates. In order to minimize the

pressure rise during deposition, the metal sources and the e-beam assemblies have to be thoroughly outgassed prior to deposition. This involves running the e-beams at low deposition rates for about 1.5 h, and at high deposition rates for short periods of time (a few minutes) every 30 min, while keeping the substrate shutter closed and the wall of the system near the bakeout temperature. This procedure limits the pressure rise during deposition within one order of magnitude of the base pressure, rather than the 2-3 orders of magnitude rise observed with no or little outgassing.

The substrates are mounted on a removable flat stainless steel plate which slides into the heating stage. The temperature of the plate is measured using a type K thermocouple that fits in a deep narrow hole in the plate that acts as a blackbody radiator. The temperature of the substrate surface is likely to be several degrees cooler than the measured temperature, but this error is assumed insignificant compared to the typical range of temperatures explored in the grain growth experiments. The substrate plate is cooled by flowing liquid nitrogen through a stainless steel tubing welded on its back side, opposite to the substrates. The minimum and maximum temperatures that can be attained using cooling and heating are -175°C and 800°C , respectively. The heater of the hot stage is feedback controlled with the thermocouple in the substrate plate and the temperature is stable within $\pm 1^{\circ}\text{C}$ for temperatures above 25°C . The flow of liquid nitrogen is manually (non-feedback) controlled and the variation of temperature during a deposition performed below room temperature is within $\pm 5^{\circ}\text{C}$.

The in-situ analysis tool available on this system is a Reflection High Energy Electron Diffraction (RHEED) gun. The gun has a maximum acceleration voltage of 30

kV, although patterns are typically obtained at 20 kV. Diffraction patterns are collected and observed on a phosphor screen mounted opposite to the gun. RHEED is an electron diffraction technique for measuring surface structure, in which the beam is incident on the substrate at grazing incidence, typically $1-2^\circ$. This small angle insures that diffraction occurs only in the first few atomic layers of the sample. It is difficult with the Balzers system to accurately control the incidence angle of the beam as the substrate plate does not allow for precise position control and rotation/tilt of the samples, which is important to collect quantitative RHEED information. The main use of RHEED for this thesis was to verify the quality of the single crystal films deposited and used as substrates for polycrystalline films (chapter five). When performing grain growth experiments in films deposited on amorphous substrates, RHEED was not used.

4.3 - X-ray texture analysis

X-ray texture analysis is well suited to the quantitative determination of preferred orientations in thin films. In the typical configuration used, the area illuminated by the x-ray beam is rectangular, 1.5 mm x 15 mm in size, and a large number of grains is sampled. The diffracted intensity, if properly corrected as described in section 4.4, provides a quantitative measurement of the orientation distribution of grains. The data are conveniently collected as a set of intensities, and are transferred and processed in electronic form. Finally, for epitaxial systems, x-ray texture analysis allows the relative film/substrate orientations to be easily measured. Because scattering of x-rays by crystals is relatively low, especially compared to the scattering of electrons, it is necessary to operate with a high intensity x-ray beam and to acquire the data for extended periods of

time to obtain good count statistics. A typical pole figure or rocking curve presented in chapters five and six is acquired in a period of time ranging from 30 min to 5 h. All measurements were performed using a Rigaku RU 200 diffractometer with a Cu rotating anode source.

X-ray texture analysis is reviewed in refs. [47, 99]. We will briefly review the basics of the technique, emphasizing the necessary corrections to the data in order to obtain quantitative information about the orientation distribution of grains in thin films. A standard x-ray diffractometer is used, with the sample mounted in an additional two-circle goniometer. The source and the detector are set at a specific (hkl) Bragg reflection in the film which is measured in advance, using a standard θ - 2θ scan. The sample is not moved between the θ - 2θ scan and the texture scan. In this geometry, only (hkl) planes parallel to the plane of the sample when the θ - 2θ scan is performed, which we call the reference plane, can produce recorded intensity. When (hkl) planes are not parallel to the reference plane, they do not contribute to the recorded diffracted intensity. In its starting position, the film is mounted parallel to the reference plane and only (hkl)-textured grains contribute to the intensity (figure 4.1a). During the texture scan, the film is moved to a new orientation in the two-circle goniometer by tilting it by an angle α and then rotating it about its normal by an angle β , as shown in figure 4.1b. In this position, grains for which this motion has brought (hkl) planes parallel to the reference plane diffract the beam and produce intensity which is proportional to the volume fraction of those grains. In the Rigaku diffractometer, the rotation angle β can be varied by a full 360° for each angle α

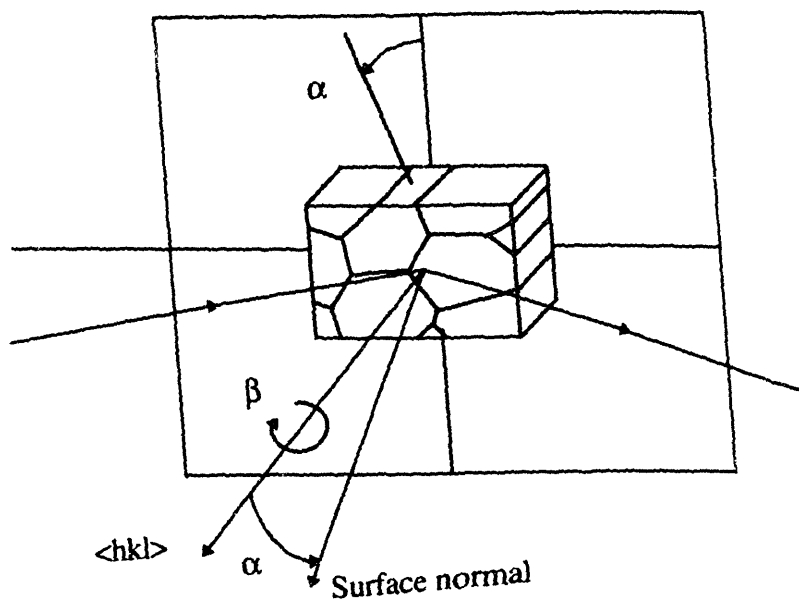
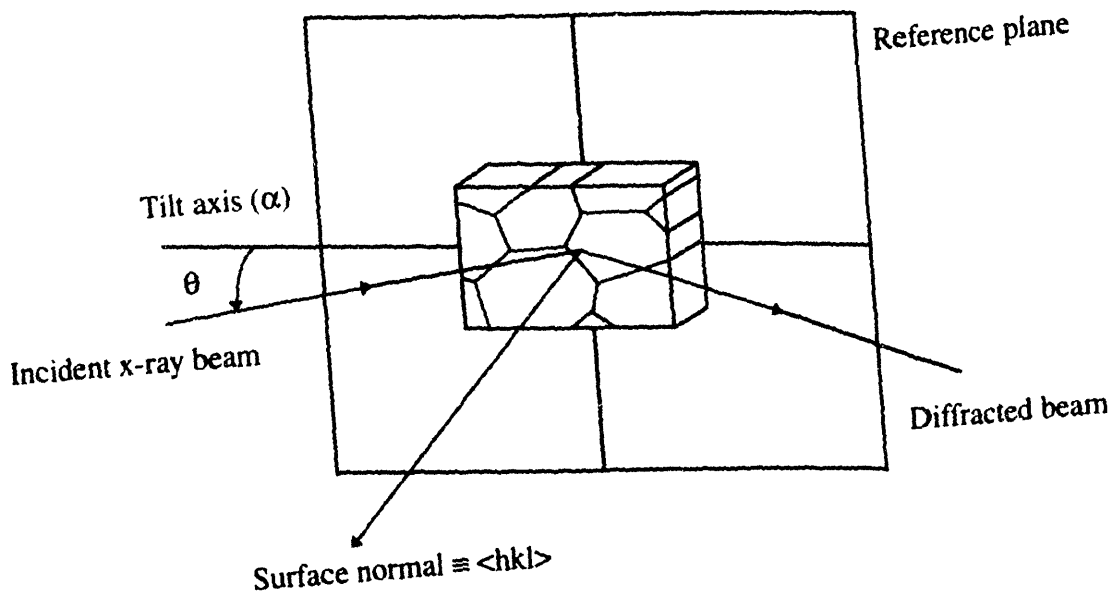


Figure 4.1: Geometry for x-ray texture analysis. The source and detector are in the symmetric θ - 2θ geometry. Only grains with (hkl) planes parallel to the reference plane contribute to the intensity. (a) The film is parallel to the reference plane ($\alpha = 0^\circ$). (hkl) -textured grains diffract the beam. (b) The film is tilted by an amount α and rotated by an amount β , bringing the (hkl) planes of other grains in diffraction condition.

and the tilt angle α can be varied in the range $[0^\circ, 75^\circ]$ with a maximum resolution of $\Delta\alpha = \Delta\beta = 1^\circ$. All data presented in this thesis is acquired in the Schultz reflection geometry [100]. The dimensions of the beam illuminating the sample are determined by the divergence slit and the Schultz slit. A 1° angular width divergence slit coupled with a 1.2° angular height slit were chosen to restrict the divergence of the beam. The Schultz is a long narrow slit that limits the illumination of the sample on the α tilt axis and minimizes the defocusing error. The angular width of the Bragg reflection chosen to diffract the x-rays increases as the tilt angle α increases, and the receiving slit should be chosen to be large enough to appropriately integrate the diffracted intensity.

A pole figure is a contour plot of the diffracted intensity as a function of α and β and is generated on a (hkl) stereographic projection. The angle α is represented as the magnitude of the stereographic radius vector and the angle β as the polar rotation angle of the radius vector (figure 4.2). Thus, if a pole of intensity appears at a radial distance α from the center of the pole figure, the texture (h'k'l') of the grains that produced that intensity satisfy

$$\cos\alpha = \frac{hh'+kk'+ll'}{\sqrt{h^2+k^2+l^2}\sqrt{h'^2+k'^2+l'^2}} \quad (4.1)$$

For example, on a $\langle 111 \rangle$ (or equivalently $\langle 222 \rangle$) pole figure, (001)-, (011)-, and (111)-textured grains produce diffracted intensity at distances $\alpha = 54.7^\circ$, $\alpha = 35.3^\circ$, $\alpha = 70.5^\circ$, respectively, from the center of the pole figure. In addition, (111)-textured grains also produce diffracted intensity at $\alpha = 0^\circ$. The angle β between poles of intensity at the same α , provides information on which variant of the {hkl} planes diffracted the x-ray beam.

The absolute value of β is not meaningful as it depends on the position of the sample in the diffractometer. However, if pole figures are separately acquired for the film and the substrate without moving the sample, the value of $\Delta\beta$, the polar angular distance between poles in the film and the substrate, indicates the in-plane orientation of grains in the film with respect to the substrate lattice. This technique is used in chapter five to identify the epitaxial orientations in Ag films deposited on single crystal (001) Ni. When the film is on an amorphous substrate, no preferred in-plane orientation in the film develops during grain growth and the pole figure is constituted of concentric rings of intensity centered on the pole figure. In that case, the intensity can be integrated with respect to β and plotted versus α , producing the equivalent of a rocking curve. The volume fraction of grains with a given texture is then proportional to the intensity at the corresponding value of α .

4.4 - Corrections to the x-ray intensity

In order to quantitatively compare the volume fraction of grains with different textures, the raw diffracted intensity must be corrected for several systematic experimental errors: background scattering, x-ray absorption and defocusing.

Background scattering arises from x-rays that are not diffracted by the chosen (hkl) planes but still reach the detector and produce recorded intensity. It can be measured by setting the geometry of scattering at 1.5° away from the θ - 2θ position used to measure the (hkl) Bragg peak and acquiring the pole figure. The background intensity $I_b(\alpha)$ is measured for this value of θ - 2θ over the entire range of α . This intensity can be

subtracted from the pole figure raw data in order to obtain the diffracted intensity from the (hkl) planes only.

The extinction depth of x-rays in metals is of order a few μm 's. This is greater than the maximum thickness (6000 \AA) of the thin films investigated in this thesis. When the sample is tilted by an amount α , the optical path of the x-rays in the film lengthens and the fraction of absorbed to diffracted x-ray photons changes with α . In order to compare intensities at different α , it is necessary to correct the data for x-ray absorption. The absorption coefficient factor $F_{\mu}(\alpha)$ is given by the equation [100]

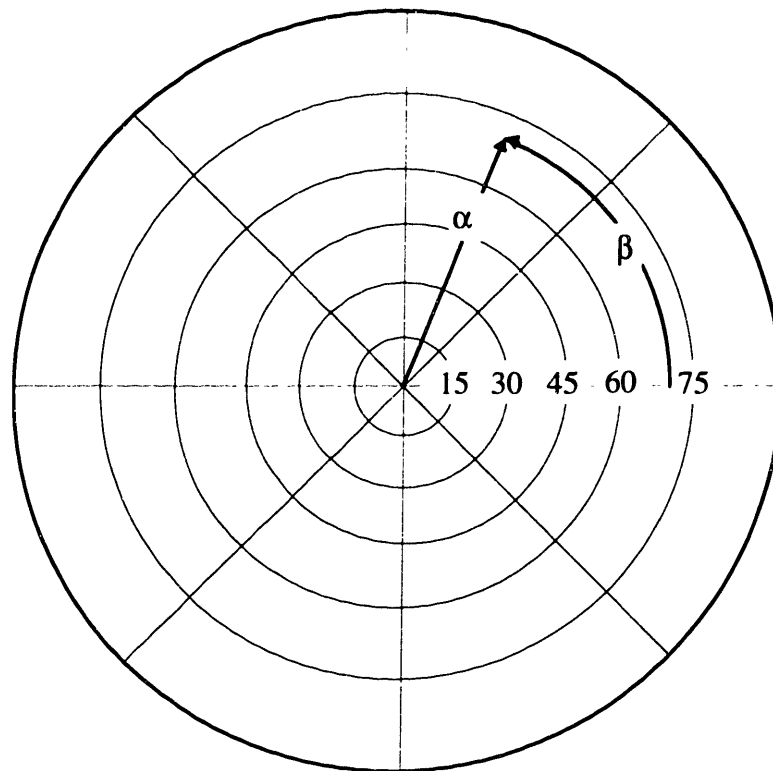


Figure 4.2: Pole figure chart. α is the angular radial coordinate and β is the azimuthal coordinate.

$$F_{\mu}(\alpha) = \frac{1 - e^{-\frac{2\mu h}{\sin\theta}}}{1 - e^{-\frac{2\mu h}{\sin\theta\cos\alpha}}}, \quad (4.2)$$

where μ is the x-ray absorption coefficient for the film at the wavelength used in the experiments (all diffraction experiments were performed using a Cu anode, producing x-rays at $\lambda = 1.5405 \text{ \AA}$). The coefficient μ was determined for Ni and Al. This was accomplished by depositing films at three thicknesses, ranging from 1000 \AA to 5000 \AA , onto a glass slide. The films were peeled from the glass slide with tape and the film and tape were then mounted on the scatter slit of the diffractometer, with the tape side first along the beam path. The intensity of the (111) peak from a Si substrate was measured with the tape and the film present on the scatter slit. The peak intensity was also measured through a piece of bare tape. The intensity attenuation $I(h)/I_0$, where $I(h)$ is the intensity through the tape and a film of thickness h , and I_0 is the intensity through the bare tape can then be fitted by linear regression to the equation

$$\ln\left(\frac{I(h)}{I_0}\right) = e^{-\mu h}, \quad (4.3)$$

which yields μ as a fitting parameter. Table 4.1 summarizes the values of the absorption coefficients for Ag, Al and Ni.

Film	Absorption coefficient (10^{-5} \AA^{-1})
Ag	1.724 (from ref. [45])
Ni	0.196
Al	0.102

Table 4.1: X-ray absorption coefficients for Cu $K_{\alpha 1}$ radiation at $\lambda = 1.5405 \text{ \AA}$.

The area of the film illuminated by the x-ray beam changes with α and produces a corresponding change in intensity. The correction factor $F_d(\alpha)$ for this defocusing error is obtained by measuring the diffracted intensity as a function of α in a random, infinitely thick polycrystalline sample. If no defocusing error existed, $I(\alpha)$ would remain constant. However, $I(\alpha)$ strongly decreases when α increases. Thick random polycrystalline samples of Ag, Al and Ni were prepared by mixing a powder of the metal ($\leq 10 \text{ \mu m}$ particle size, with purity greater than 99.9%) with a colloid and drying this solution on a glass slide. The diffracted intensity $I_{hkl}(\alpha)$ is extracted from a pole figure measured with a (hkl) Bragg reflection for the material and for $0 \leq \alpha \leq 75^\circ$. The correction factor $F_d(\alpha)$ for the material and Bragg reflection chosen is then simply given by $F_d(\alpha) = 1/I_{hkl}(\alpha)$. To facilitate further calculations $F_d(\alpha)$ is fitted to a polynomial. The degree of the polynomial is chosen such that the error between the fit and the defocusing data is comparable to the scattering present in the defocusing data. The coefficients of the polynomials chosen to fit defocusing data for Ag, Al and Ni and for several Bragg reflections are given in appendix V.

The fully corrected data are calculated from the raw data of a pole figure as

$$I_{\text{corr}}(\alpha, \beta) = F_d(\alpha) F_\mu(\alpha) (I_{\text{raw}}(\alpha, \beta) - I_b(\alpha)) . \quad (4.4)$$

A computer program was written in language C to automatically process and correct the raw data files for pole figures of Ag, Ni and Al, for several Bragg reflections. The program also integrates the data with respect to β in order to obtain a rocking curve, and calculates the ratio of the volume fractions of several low index orientations. This program would be easily extended to process pole figures of other materials, given that the appropriate absorption coefficient and defocusing data are provided. A listing of this program is given in appendix V.

Chapter 5

Epitaxial Grain Growth in Ag/(001)Ni

5.1 - Introduction

In this chapter we present experimental results on grain growth in polycrystalline Ag films on single crystal (001) Ni. As the substrate is single crystal, the interface energy γ_i depends on both the texture *and* the in-plane orientation of the Ag grains. Grain growth in such systems leads to the growth of orientations in the film with specific epitaxial relationships to the substrate lattice. This process is called epitaxial grain growth (EGG) [46, 47].

In order to understand the development of epitaxial orientations through grain growth, it is necessary to choose a materials system for which the dependence of the interface energy with orientation is known. Ag/(001)Ni corresponds to such a choice and is chosen primarily for this reason. The main advantages of Ag/(001)Ni for an experimental investigation of texture evolution during grain growth are:

1. The interface energy versus twist misorientation for two Ag/Ni twist boundaries has been calculated by Gao, Dregia and Shewmon (GDS) using an embedded atom potential [94, 95]. GDS also calculated the interface energy of several particular low index Ag/Ni interfaces.
2. The surface energy for several low index orientations of both Ag and Ni has been calculated [95].

3. Extensive EGG experiments on the Ag/(001)Ni system have already been performed [47].
4. The interface energy of (111)Ag/(111)Ni has been determined experimentally using zero creep experiments [101].
5. Rotating crystallite experiments which probe low interface energy orientations have been performed [94, 95].
6. Ag and Ni have very limited solubility at the temperatures at which grain growth in Ag occurs.

5.2 - Previous Work

5.2.1 - Prediction of the interface energy

Ag/(001)Ni is one of the few systems for which computational predictions exist for the structure of the interface and for the interface energy of several twist interface boundaries. For each material meeting at the interface, a semi-empirical potential energy function is fitted to many physical properties such as the crystal structure, the lattice constant, the reflectivity, the melting point and the mechanical constants [102, 103]. These potentials are used to determine the equilibrium structure at 0 K through *molecular static calculations*, based on a Monte Carlo algorithm, for a sandwich formed by the two materials. It is also possible to simulate the effect of temperature by using the relaxed structure obtained by the Monte Carlo simulation as the initial condition of a *molecular dynamics* calculation. The interface energy of the relaxed atomic configuration can be extracted from the simulation results. By changing the orientations of the two crystals

meeting at the interface boundary, it is in principle possible to obtain the detailed shape of the Wulff hyper-surface. In practice however, computational limitations restrict the study to cross sections of the Wulff hyper-surface. GDS considered two low index twist boundaries, (001)Ag||l(001)Ni and (111)Ag||l(001)Ni. The combined surface and interface energy calculated for these twist interfaces, as a function of the twist misorientation angle β , is shown in figure 5.1. The conventions for the definition of the angle β and the most important features of GDS results were highlighted in section 3.3.1. In the context of the grain growth experiments, it is important to observe that for all values of β , the combined surface and interface energy of (111)Ag/(001)Ni is always lower than the combined surface and interface energy of (001)Ag/(001)Ni.. Also, the “cube-on-cube” orientation, i.e., (001); 0° , is predicted to be a local energy maximum. However, it is easy to grow continuous planar epitaxial films of Ag on Ni, in the cube-on-cube orientation. Experimental results also suggest that this orientation can be favored by grain growth as shown in section 5.4. It is also of interest that the (001); 26° orientation has much lower predicted energy than all other (001); β orientations.

GDS also calculated the interface energy of several other interfaces, including two variants of (111)Ag||l(111)Ni. Averaging the energy for these two interfaces results in $\gamma_i \cong 0.88 \text{ J/m}^2$.

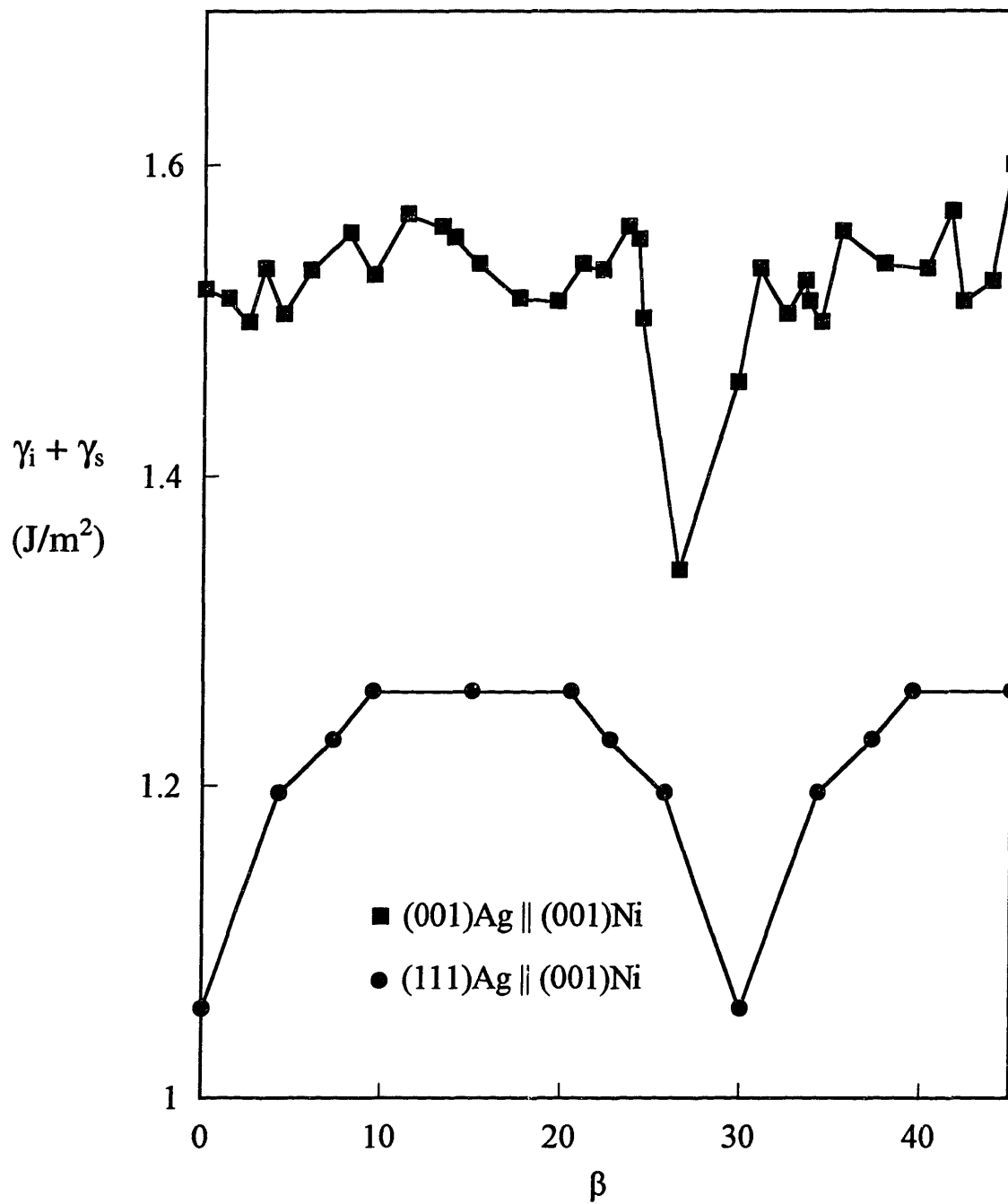


Figure 5.1: Combined surface and interface energy for (001)Ag|| (001)Ni and (111)Ag|| (001)Ni as calculated by Gao, Dregia and Shewmon [94, 95] using an embedded atom potential and molecular static atomic relaxation. A similar plot can be found in ref. [47].

5.2.2 - Interface energy sensitive experiments

5.2.2.1 - Zero creep experiment

Josell and Spaepen [101, 104] have determined the interface energy of (111)Ag/(111)Ni by performing zero creep experiments. A free standing multilayer Ag/Ni film is mechanically loaded under tension while annealed at temperatures high enough to promote creep. They found that annealing temperatures greater than 700°C were necessary to induce creep in this system¹. Creep provides a driving force for elongation, while the total surface and interface energy of the multilayer film provides a driving force for contraction. For a given annealing temperature there is a load for which the two driving forces cancel, defining the zero creep load. Using a kinetic model for Coble creep, it is possible to determine the value of the average interface energy of the multilayers. Using this technique Josell and Spaepen found $\gamma_i = 0.76 \text{ J/m}^2$ for (111)Ag||l(111)Ni, consistent with GDS results ($\gamma_i \cong 0.88 \text{ J/m}^2$). As it is difficult to control the twist orientation of the Ag||Ni interface, and as the multilayer must be polycrystalline to undergo Coble creep, the zero creep experiment does not provide information on the dependence of the interface energy with twist orientation.

5.2.2.2 - Rotating Crystallite Experiments

GDS performed rotating crystallite experiments to validate their calculations [85, 86] and identify orientations exhibiting energy minimizing interfaces. Continuous (001)

¹ The temperatures used to induced grain growth in our experiments are therefore too low to induce creep (sections 5.4 and 5.5).

epitaxial Ni film were deposited onto (001)-cleaved NaCl. Partially discontinuous Ag films were grown separately on (001) NaCl and annealed in H₂ to promote agglomeration of the film into isolated (001) epitaxial islands of approximately 1000 Å in diameter. The Ag islands were bonded in H₂ at 300°C for 10 min to the Ni films with a specific initial twist misorientation, forming (001);β Ag/(001)Ni interfaces. The NaCl substrates were dissolved and the films were mounted on TEM grids. The sample were annealed at 350°C for 3-24 h to promote crystallite rotation.

Depending on their original orientation, the crystallites rotated into either the shallow cusp at β = 4.4° or into the deep minimum at β = 26.6°. Some crystallites rotated out of the (001);β twist interface, and into the (111):0° orientation. GDS also welded epitaxial (111) crystallites onto a (001) Ni film to form (111);β twist interfaces. All the crystallites rotated into the deep minimum at β = 0°.

5.2.3 - Epitaxial grain growth experiments in Ag/(001)Ni

Floro performed epitaxial grain growth experiments in polycrystalline Ag films deposited onto single crystal (001) Ni films with the intention of obtaining information about the anisotropy of the interface energy for Ag/(001)Ni. If surface and interface energy anisotropy was the only orientation dependent driving force for grain growth, the change in orientation distribution and the preferred in-plane orientations developing during grain growth should map the shape of the combined surface and interface energy Wulff surface. We summarize his results found in refs. [45, 96].

Floro performed epitaxial grain growth in Ag/(001)Ni/(001)NaCl and Ag/(001)Ni/(001)Ag/(001)MgO. In all experiments, films were deposited and annealed

in-situ in the vacuum system. Because Ni did not grow epitaxially directly on MgO, an epitaxial Ag buffer layer was first deposited on the (001) MgO substrate, followed by the epitaxial growth of Ni on the Ag. The polycrystalline Ag overlayers were 1500 Å or 5000 Å thick.

The as-deposited Ag films were polycrystalline with a columnar grain structure as determined by TEM. Films deposited at 50°C had a grain diameter of about three times the film thickness, consistent with grain growth during and/or after deposition (section 1.3.3) and grain growth stagnation due to grain boundary grooving (section 1.4.4). Films deposited at liquid nitrogen (LN2) temperature had a much smaller grain size, of order 500 Å for a 1500 Å thick film. Texture analysis revealed that films deposited at either 50°C or LN2 temperature were mainly constituted of grains in the (001);0° and (111);0° orientations. In the films deposited at LN2 temperature, a few very large grains, with diameters more than 100 times the diameter of the surrounding grains were observed at room temperature. These grains had (001);15-20° orientations, with (001);17° being the most frequently observed orientation. In subsequent discussion, we will refer to this orientation as (001);17° with the understanding that a range of values of β about 17° are usually observed. In addition, both the (001) and (111) grains in as-deposited films were found to be tilted about 6° relative to the Ni surface. The direction of the tilt varied from sample to sample.

When annealed at 350°C for 3 h to promote grain growth, 5000 Å thick Ag films on MgO developed a strong (001) texture. The surface and interface energy minimizing (111);0° orientation was almost entirely consumed by (001)-textured grains. (001) grains

were found predominantly in the $\beta = 17^\circ$ and $\beta = 45^\circ$ in-plane orientations. A systematic uniform tilt of order 6° relative to the Ni substrate for all the (001)-textured grains was present in all samples. In addition, a square grid of dislocations associated with the Ni lattice was present at the interface of annealed films.

Floro originally interpreted the growth of (001)-textured grains at the expense of (111)-textured grains as the consequence of (001) grains having a lower yield stress and strain energy density than (111) grains when plastically deformed. Elastic anisotropy was incorrectly invoked to explain why (011)-textured grains, which have a lower strain energy density than (001) grains when plastically deformed, did not grow.

The orientation dependence of strain energy density can not explain the origin of the observed $\beta = 17^\circ$ in-plane orientation or the presence of a tilt. The thermal expansion coefficients of Ag and MgO are isotropic as both materials have cubic symmetry. The thermal strain in Ag films is therefore uniformly biaxial to a first order approximation. There is therefore no in-plane dependence of the strain or the strain energy density. Floro proposed a model of oriented recrystallization of (001) defect-free grains in a matrix of (111); 0° grains to explain the origin of the $\beta = 17^\circ$ orientation and the tilt. We will not review the details of the model which can be found in refs. [47, 54]. The sequence of events leading to (001) grains with a $\beta = 17^\circ$ orientation and to a tilt of approximately the right magnitude involves multiple twinning operations. A similar mechanism was proposed by Mader et al. [105] to explain the recrystallization of free-standing single crystal (001) Au films in polycrystalline (111) films [106]. While the transformation can generate the (001); 17° grains, it lacks a thermodynamic or kinetic criterion to explain why

the particular sequence of twinning operations that produces the observed orientations occurs preferentially to other possible twinning operations. By choosing the appropriate twinning operations, it is in fact possible to justify *any* in-plane orientation for (001)-textured grains by this mechanism. Other in-plane orientation selection mechanisms were also proposed by Floro [47]. They are reviewed in section 5.5.3.2 along with several new mechanisms.

5.3 - Experimental details

A description of the general experimental procedures for film deposition is found in chapter four. Specific details of the deposition conditions and characteristics of the films and substrates described in this chapter are presented below.

NaCl substrates: square single crystal (001) NaCl substrates, 1.5 cm x 1.5 cm in size, were cleaved in air and immediately introduced in the vacuum chamber with no further cleaning. The substrates as-cleaved are rough with macroscopic steps that can potentially affect the growth of films. The bakeout and the deposition temperatures can also induce roughening and reconstruction of the NaCl surface.

Ni films on NaCl: (001) single crystal Ni films, 1000 Å thick, are grown at 325°C on the NaCl surface at rates of about 1 Å/s. RHEED patterns, x-ray texture analysis and TEM [45] confirm that the films are (001) oriented single crystals, with dislocations and twin faults. SEM analysis of the films also reveals hillocking [47]. Polycrystalline Ag films grown on the Ni films provoke the delamination of the Ag/Ni bilayer when the thickness of the Ag films exceeds about 2000 Å, indicating poor adhesion of the Ni to the NaCl substrate.

MgO substrates: single crystal (001) MgO substrates with a 60 Å polish were used to grow films. The substrates were directly introduced into the vacuum chamber with no cleaning.

Films on MgO substrates: single crystal Ni films can not be grown directly on MgO [46]. However, it is possible to grow 1500 Å thick single crystal Ag films on MgO at 275°C. A 1000 Å thick Ni film can then be grown epitaxially on Ag at 225°C. RHEED patterns and x-ray texture analysis on the Ag and Ni films indicate good quality single crystals. Polycrystalline Ag films can be grown on the Ni at a rate of order 20 Å/s with thicknesses greater than 5000 Å without delamination, indicating good adhesion of the single crystal Ag films to the MgO substrates.

Glass substrates: microscope glass slides were cut, and cleaned successively with trichloroethane, acetone, and methanol, prior to introduction in the vacuum chamber.

Ag films on glass substrates: polycrystalline Ag films were grown at rates greater than 20 Å/s on glass substrates. No delamination was observed. Prolonged exposure of the Ag films to air results in degraded reflectivity, indicating that the surface of the film has oxidized.

5.4 - Bonding experiment

5.4.1 - Experimental procedure

In order to probe which orientations are favored by surface and interface energy anisotropy during grain growth, experiments resembling the rotating crystallites

experiments were carried out². Single crystal (001) Ni films, 1000 Å thick, were deposited on (001) single crystal NaCl substrates. In a separate deposition, polycrystalline Ag films were deposited on microscope glass slides. One Ag film/substrate and one (001) Ni film/substrate were mounted inside a vertical tube furnace shown in figure 5.2. The Ag film/substrate is mounted face down on a linear motion manipulator, far from the furnace hot zone. Several pieces of glass slides were inserted in between the substrate and the stainless steel holder to prevent fracture of the glass substrate and promote pressure uniformity across the interface during bonding. The (001) Ni film/substrate was mounted face up in a fixed position on the axis of the furnace. A piece of silver foil was inserted between the NaCl substrate and the fixed stainless steel holder to prevent the NaCl from bonding to the holder at high temperatures. The furnace was flushed with Ar and then with H₂ at a high flow rate. The H₂ flow rate was then reduced and the temperature of the hot zone was raised to about 500°C for 30 min to reduce the native oxide. The temperature was lowered to 300-350°C, the Ag film was brought in contact with the Ni film, and pressure was exerted on Ag/Ni to promote bonding. The magnitude of the pressure at the Ag/Ni interface is not known exactly and probably varies from bonding to bonding and across the interface. The bonding anneal lasted 15-20 min and the bonded samples were cooled and removed from the furnace, and the NaCl substrate was dissolved

²Dr. J. A. Floro built the hydrogen bonding furnace used for this experiment. He also carried out preliminary bonding experiments with Si/Si₃N₄/Ag and (001)Ni/(001)NaCl. All experimental results presented in this section are our own.

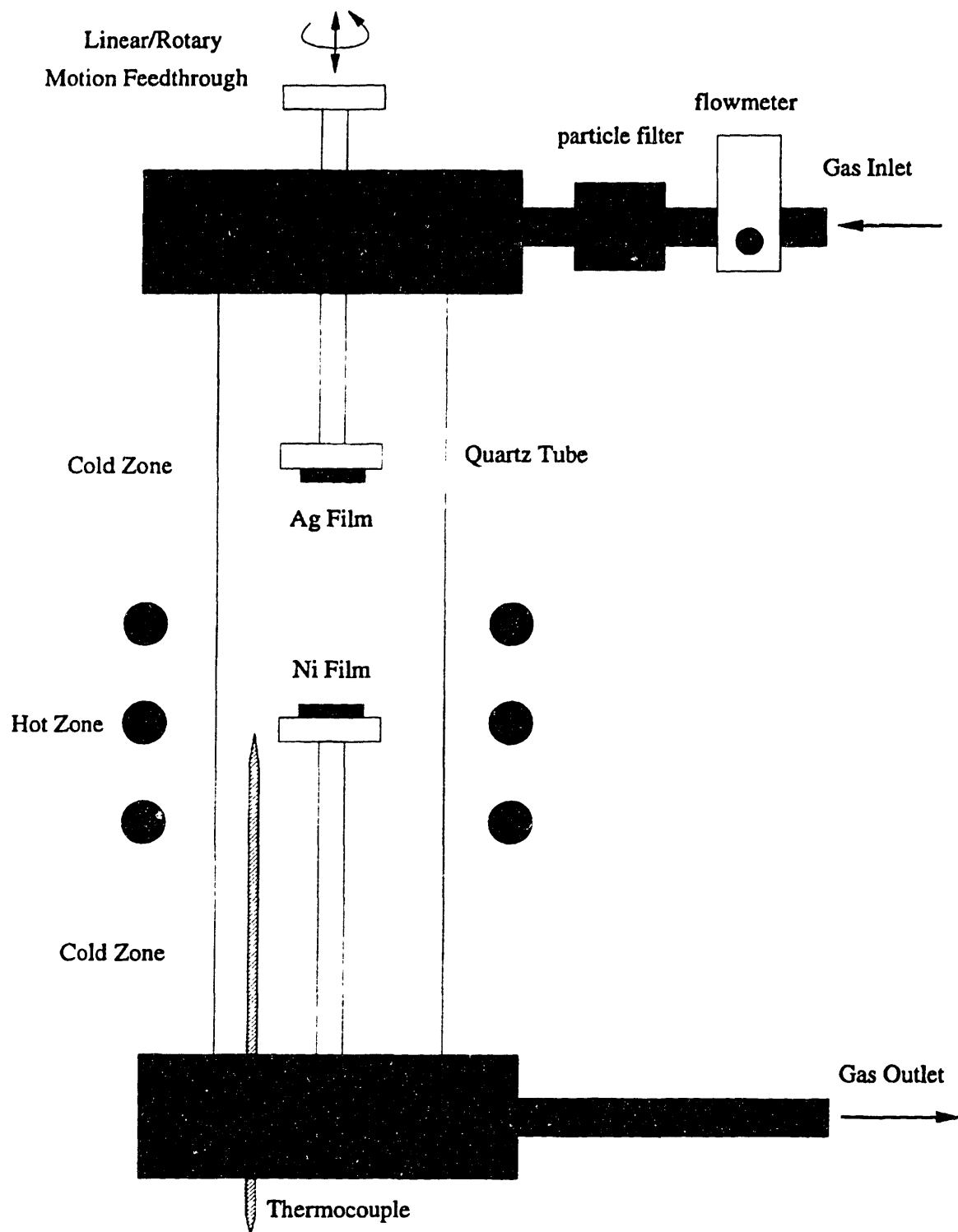


Figure 5.2: Hydrogen bonding furnace.

in water. The samples were cleaned in deionized water, and in methanol, and x-ray texture analysis was performed. The films were then reintroduced into the furnace, on the fixed holder in the hot zone, and annealed at 500-600°C for 1h in H₂ to promote grain growth. Texture analysis was performed on the annealed samples.

5.4.2 - Results

Diffraction peak intensities in standard θ - 2θ x-ray diffraction scans show that as-deposited Ag films are often (001)-textured. The relative intensities of the (002) and (111) Bragg peaks varied somewhat with thickness and deposition temperature. The orientation distribution of as-deposited films also varied from deposition to deposition, probably due to changes in cleanliness and morphology of the surface of the glass substrates.

Figure 5.3a shows an x-ray pole figure of a 6000 Å thick Ag film bonded at 350°C for 20 min. The continuous concentric rings of intensity indicate that the grains are randomly oriented in the plane on the film. The intensity of the pole figure, integrated with respect to β , is shown in figure 5.3b. The two intense peaks in figure 5.3b correspond to (001) and (111) textures. The as-bonded Ag film is (001)-textured, with a significant volume fraction of (111)-textured grains. Other bonded samples were (111)-textured with a significant volume fraction of (001)-textured grains. In all samples, other textures are also present but occupy smaller volume fractions of the films.

Figure 5.4a shows the x-ray pole figure of the same film after annealing. Twelve poles of intensity are present at $\alpha = 71^\circ$. A plot of the intensity versus β for $\alpha = 71^\circ$ is shown in figure 5.4b. The twelve peaks of intensity correspond to the (111); 0°

orientation, as determined by comparing the $\langle 111 \rangle$ Ag and $\langle 111 \rangle$ Ni pole figures of the sample. There are also twelve weak peaks in between the $(111);0^\circ$ peaks which correspond to the $(111);15^\circ$ orientation. For (001)-textured grains, no preferred $(001);\beta$ orientation can be identified for this sample. Figures 5.3b and 5.4c indicate that (111)-textured grains, and in particular grains in the $(111);0^\circ$ orientation, have grown preferentially compared to (001)-textured grains upon annealing. Note that both (001) and (111) textures are better defined in the annealed sample than they are in the as-deposited sample, with fewer grains with orientations off the true (001) and (111) textures, as indicated by the width of the peaks in figure 5.3b and 5.4c. In this experiment, grain growth has favored grains with low combined surface and interface energy, especially grains in the surface and interface energy minimizing $(111);0^\circ$ orientation, as predicted by the calculations of GDS.

Bonding anneals performed for longer times or at higher temperatures promote better adhesion of the Ag to the Ni, but also allow significant grain growth to proceed in the Ag films. X-ray texture analysis reveals that the $(111);0^\circ$ orientation is present in the as-bonded films and gets sharper upon annealing. Ag films bonded at low temperatures and for short times do not undergo significant grain growth. Under these conditions, the Ag films do not bond uniformly on the Ni, and the resulting samples consist of patches of Ag on the continuous Ni film. The x-ray intensity diffracted by these asymmetric samples depends on the angular coordinate β even if there are no preferred in-plane orientations in the Ag. This explains why the pole figure shown in figure 5.3a does not have perfect circular symmetry.

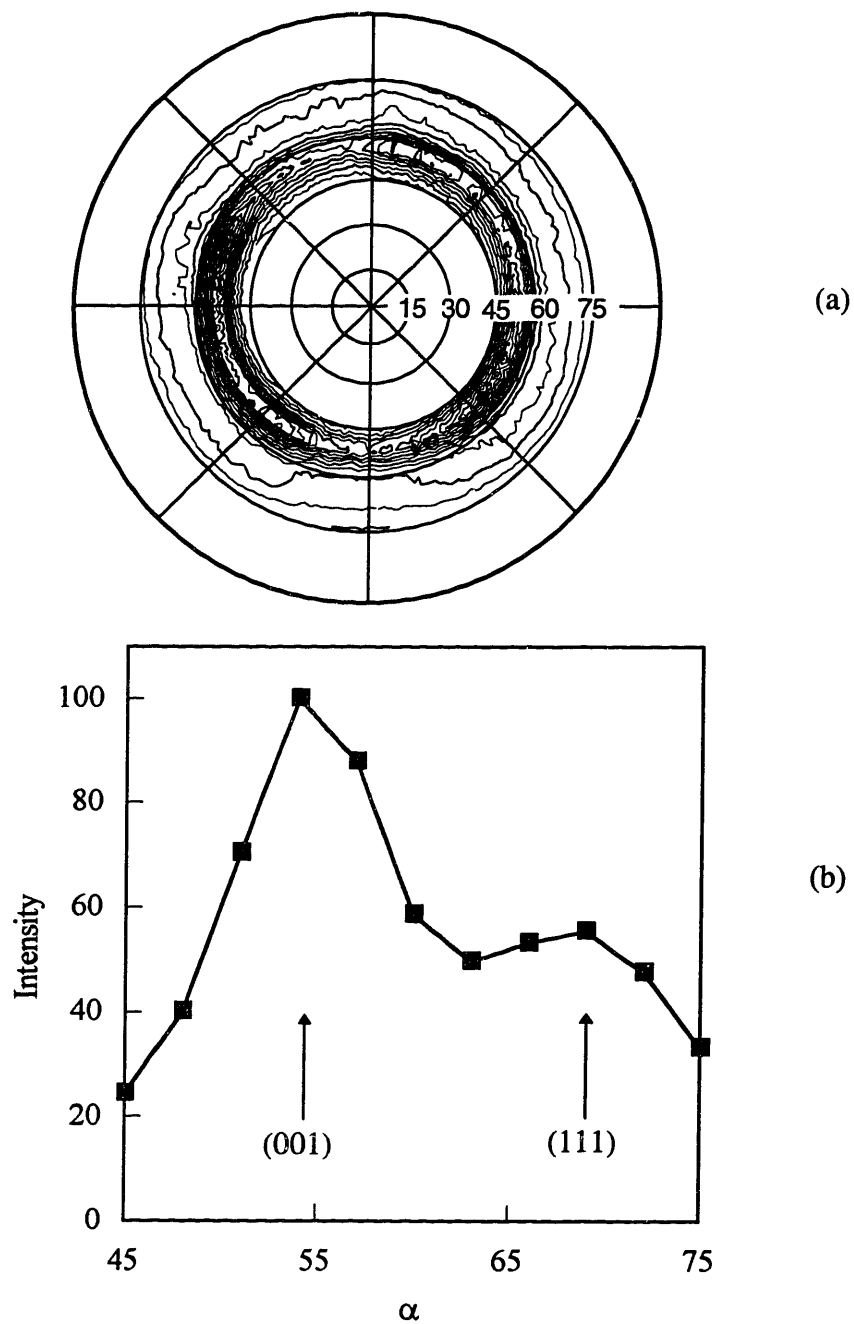


Figure 5.3: Ag/(001)Ni as bonded at 350°C for 20 min. (a) <111> Ag pole figure. (b) Intensity integrated with respect to β and plotted versus α . The data presented in this figure and all figures in this chapter are corrected for background scattering, finite thickness and defocusing (chapter four, section 4.3).

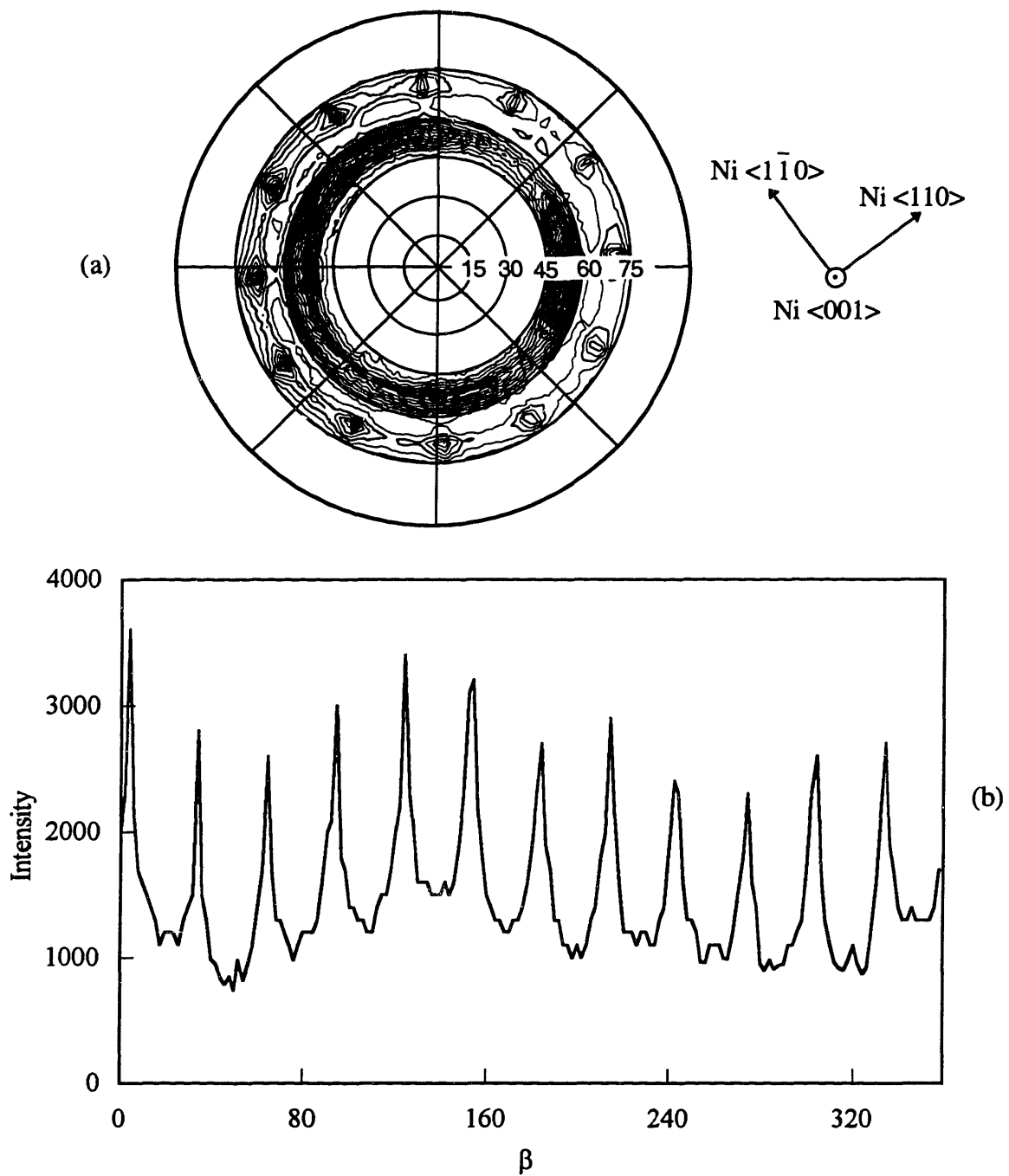


Figure 5.4a-b: Bonded sample after annealing at 600°C for 1 h. (a) $\langle 111 \rangle$ Ag pole figure. Crystallographic directions in the Ni lattice are also indicated. (b) Intensity at $\alpha = 71^\circ$, characteristic of (111)-textured Ag, plotted versus β .

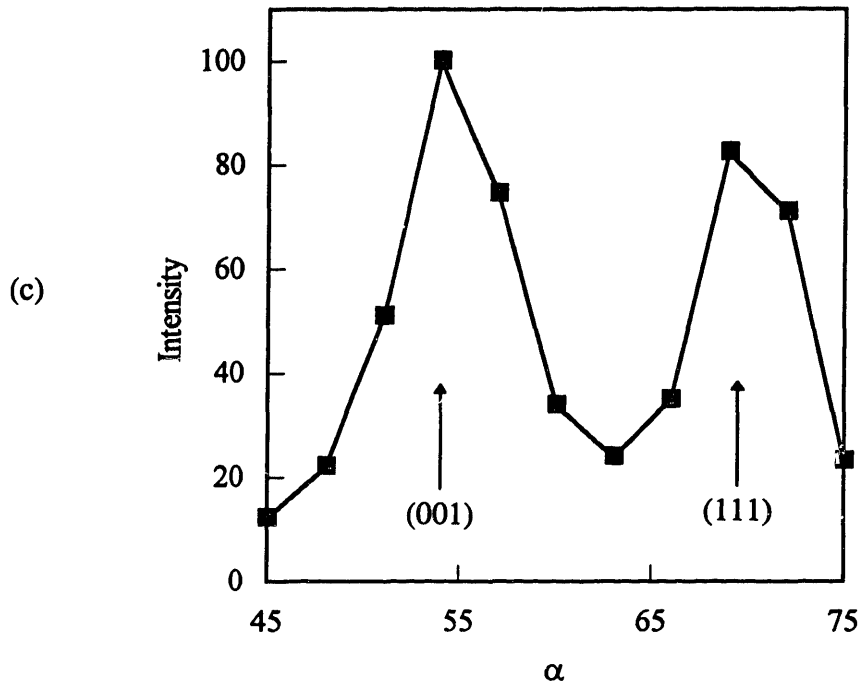


Figure 5.4c: Intensity integrated with respect to β and plotted versus α .

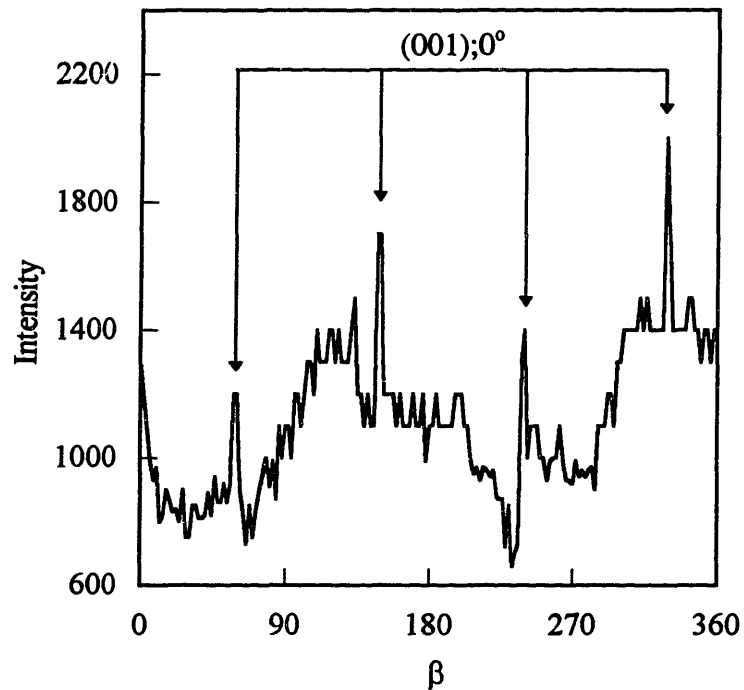


Figure 5.5: $\langle 111 \rangle$ Ag β -scan at $\alpha = 55^\circ$ for a 4000 \AA thick Ag film bonded at 300°C for 20 min and annealed at 550°C for 1 h. The four peaks of intensity correspond to the $(001); 0^\circ$ orientation.

A significant volume fraction of (001); β grains is still present in the Ag films after annealing, as shown in figure 5.4c. Figure 5.5 shows a plot of the diffracted intensity versus β at $\alpha = 54.7^\circ$, characteristic of (001) texture on a $\langle 111 \rangle$ pole figure, for a different sample than the one shown in figures 5.3 and 5.4. The four peaks of intensity in figure 5.5 are characteristic of the (001); 0° orientation. This epitaxial orientation was identified in several other samples. In most samples however, no preferred in-plane orientation for the (001)-textured grains was observed after grain growth had occurred, and in all samples, the development of the (111); 0° orientation was much stronger than the development of the (001); 0° orientation. The deep interface energy minimum at (001); 26.6° was never seen.

5.4.3 - Discussion

In this experiment, the Ag films are bonded to Ni on one side and to amorphous SiO₂ on the other side. The interface energy of Ag/a-SiO₂ is not known. Ag/a-SiO₂ is a weakly interacting system and the interface energy is independent of the in-plane orientation of Ag, as SiO₂ is amorphous. It is therefore expected that the anisotropy of interface energy in this system is similar to the anisotropy of the free surface energy. In particular, the interface energy of (111)Ag/a-SiO₂ grains should be lower than the interface energy of (001)Ag/a-SiO₂ grains, and the orientation that minimizes the sum of the two interface energies in (001)Ni/Ag/a-SiO₂ should be (111); 0° .

When heated from room temperature to 350°C, the Ag is thermally strained. Using $\alpha_{\text{glass}} \cong 4 \times 10^{-6}$ [107], and $\alpha_{\text{Ag}} \cong 19 \times 10^{-6}$ [108], the calculated thermal strain is of order 0.49% during bonding. At 600°C the microscope glass slides are above their

softening temperature and there may be some viscous flow of the glass at the Ag/glass interface, relaxing part of the thermal strain in the Ag film. While it is difficult to know exactly what the strain in the Ag is, it is likely to be small, insufficient for strain energy density anisotropy to supersede surface and interface energy anisotropy.

In this experiment, surface and interface energy is the predominant orientation dependent driving force for grain growth. The $(111);0^\circ$ orientation develops upon annealing of the film, confirming the GDS result that $(111);0^\circ$ is the interface energy minimizing orientation for Ag/(001)Ni. The possible origins of the occasional observation of weak $(001);0^\circ$ and $(111);15^\circ$ orientations are discussed in the broader context of in-plane orientation selection during grain growth in Ag/(001) Ni in section 5.5.3.2.

This experiment demonstrates that when surface and interface energy is the dominant orientation dependent driving force for grain growth, grains with the minimum calculated surface and interface energy grow preferentially. It confirms that for Ag/(001)Ni, surface and interface energy anisotropy favors (111)-textured grains, and that if a texture other than (111) develops during grain growth, there must be at least one other orientation dependent driving force for grain growth which supersedes surface and interface energy anisotropy. This experiment also suggests that the absolute minimum for the combined surface and interface energy for any orientation of Ag on (001)Ni, corresponds to the $(111);0^\circ$ orientation.

5.5 - Orientation evolution during EGG in Ag/(001)Ni/(001)MgO

5.5.1 - Introduction

In order to experimentally validate strain energy density as a driving force for grain growth, the relative magnitude of the strain energy density driving force and the surface and interface energy driving force can be systematically varied by changing the processing conditions of the film, as demonstrated in chapter two (section 2.7). Epitaxial grain growth experiments in Ag/(001)Ni/(001)Ag/(001)MgO were performed, and both the thickness and the deposition temperature (i.e., strain) of the polycrystalline Ag films were systematically varied.

The procedures followed for this experiment are detailed in chapter four and section 5.4. Single crystal Ag films were deposited onto polished MgO substrates followed by deposition of single crystal films of Ni. The temperature of the substrate was controlled by a combination of heating and cooling of the substrate plate and was stable within $\pm 5^\circ\text{C}$. Polycrystalline films of Ag were evaporated onto the Ni/Ag/MgO substrate at rates greater than 20 \AA/s . The films were heated to 400°C after deposition in-situ in the vacuum system to promote grain growth in the polycrystalline Ag films.

All $\langle 111 \rangle$ Ag pole figures for Ag/(001)Ni/(001)Ag/(001)MgO films have four very intense poles located at $\alpha = 55^\circ$, the angle between (111) and (001) planes in a cubic lattice, corresponding to the intensity diffracted by the single crystal Ag underlayer. The single crystal MgO substrate also contributes to the intensity of these epitaxial poles due to the overlap of the (111) Ag and the (222) MgO Bragg peaks. They are indicative of the (001); 0° orientation and are used as an internal reference to identify preferred in-plane

orientations in the polycrystalline Ag layer³. Arising from single crystals, these epitaxial poles have very narrow azimuthal angular widths ($\Delta\beta$), of order a few degrees. The presence of these epitaxial poles masks the intensity diffracted by the (001);0° grains in the polycrystalline Ag films as it is not possible to separate the contribution to the total signal of the epi-Ag layers and the MgO substrates from the contribution of the (001);0° oriented grains.

In order to quantitatively compare the volume fractions of (001)- and (111)-textured grains in the polycrystalline Ag films, the intensity diffracted at $\alpha = 55^\circ$ and at $\alpha = 71^\circ$ was integrated with respect to β . To avoid counting the intensity from the epitaxial (001) Ag poles and the MgO substrate, the integration at $\alpha = 55^\circ$ omitted the intensity within $\pm 4^\circ$ from the center of the epitaxial poles. The ratio of the integrated intensities $I(\alpha = 55^\circ)/I(\alpha = 71^\circ)$ was calculated and used as a measure of the relative strengths of the (001) and (111) textures in the film. Removing the epitaxial poles from the data also removes the intensities diffracted by the (001);0° grains in the poly-Ag film and the ratio of integrated intensities is not strictly equal to the ratio of the volume fractions of (001)- and (111)-textured grains. Grain growth experiments in Ag/(001)Ni/(001)NaCl have shown that the volume fraction of (001);0° Ag grains after grain growth is small compared to the total volume fraction of (001)-textured Ag grains [47]. The ratio of intensities defined

³ Alternatively, a $\langle 111 \rangle$ Ni pole figure can be acquired to identify the in-plane orientations present in the polycrystalline Ag film. The Ni underlayer is grown epitaxially on the Ag and the epitaxial poles on the $\langle 111 \rangle$ Ag pole figure, arising from the epi-Ag film and the MgO substrate, and the epitaxial Ni poles on the $\langle 111 \rangle$ Ni pole figure, arising from the epi-Ni film, overlap exactly. It is therefore not necessary to perform x-ray texture analysis using the $\langle 111 \rangle$ Ni Bragg reflection to identify the epitaxial orientations present in the poly-Ag films.

above can therefore be used to measure the change with processing conditions of the respective volume fraction of (001)- and (111)-textured grains after grain growth.

5.5.2 - Results⁴

Figure 5.6 shows the room temperature $\langle 111 \rangle$ Ag pole figure for a 2500 Å thick Ag film deposited at -47°C . The dominant orientations in the as-deposited film are (111); 0° and (001); 0° . The presence of (001); 0° grains is inferred from the width of the four poles at $\alpha = 55^\circ$ that far exceeds the width of the poles arising from the epitaxial Ag underlayer. Floro performed epitaxial grain growth experiments in Ag/(001)Ni/(001)NaCl [47]. His results and our own show that in this system, as-deposited films consist of grains in the (111); 0° and (001); 0° orientations. We were able to reproduce these results confirming the probable presence of (001); 0° grains in as-deposited poly-Ag films on (001)Ni/(001)Ag/(001)MgO. Grains in the (001); 45° orientation are also present in the as-deposited Ag films, as shown by the four weak poles 45° away from the epitaxial poles. Floro also deposited Ag films on MgO at and above room temperature. The main orientations present in the film as-deposited were found to be (111); 0° and (001); 0° [47], consistent with our results. The comparison of Floro's experiments and our own shows that when the deposition temperature is decreased, the as-deposited films tend to have more random orientations, although the main orientations as-deposited are consistently (111); 0° and (001); 0° . Varying the thickness of the films at constant deposition temperature resulted in little variation of the as-deposited orientation distribution.

⁴The experimental results shown in this section are our own. Comparisons with the epitaxial grain growth experiments carried out by Dr. J. A. Floro [47] are made when appropriate.

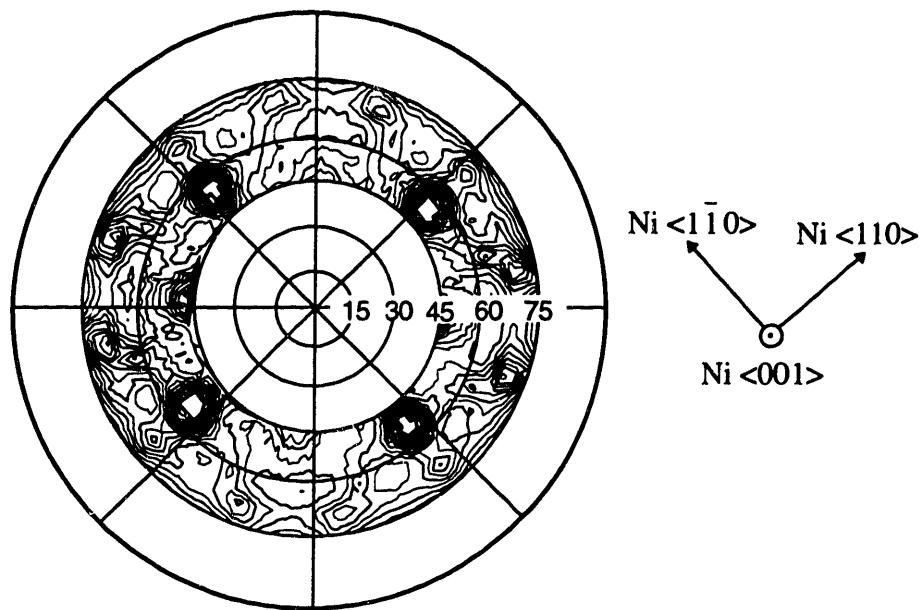


Figure 5.6: $\langle 111 \rangle$ Ag pole figure of an as-deposited 2500 Å thick Ag film deposited at -47°C .

Figure 5.7 shows a $\langle 111 \rangle$ Ag pole figure for a 2500 Å thick film deposited at 30°C and annealed at 400°C for 3 h to promote grain growth. The pole figure shows strong $(111);0^\circ$ poles. Grains in the $(001);0^\circ$ orientation are also likely present in the film as the width of the four epitaxial poles at $\alpha = 55^\circ$ is large. The shoulders of intensity on each side of the four epitaxial poles reveal the presence of grains in the $(001);17^\circ$ orientation. Very weak $(001);45^\circ$ poles are also present in the pole figure.

Figure 5.8a shows a $\langle 111 \rangle$ Ag pole figure for a 1500 Å thick film deposited at -157°C and annealed at 400°C for 3 h. As in the previous film, the film is predominantly in the $(111);0^\circ$ and $(001);0^\circ$ orientations. In figure 5.8a however, the (111) texture is not as pronounced as in figure 5.7 and weak $(001);45^\circ$ and $(001);17^\circ$ poles are present. Figure 5.8b shows the pole figure for a 3400 Å thick Ag film deposited at -148°C and annealed at

400°C for 3 h. The film is mainly in the (001);17° orientation. The (111);0° orientation is not present in the film. Increasing the thickness of the films for low deposition temperatures has a strong effect on the orientations that develop during grain growth and strongly promotes the growth of grains in the (001);17° orientation.

Figure 5.9 shows the texture map for annealed Ag/(001)Ni/(001)Ag/(001)MgO films. The number above each data point corresponds to the ratio of diffracted x-ray intensities for (001)- and (111)-textured grains (section 5.5.1). The y axis of the texture map is defined as the opposite of the deposition temperature. With this definition of the y axis, the thermal strain in the film increases with increasing values of $-T_{dep}$, providing that the grain growth temperature is constant. Because the ratio of intensities as defined in section 5.5.1 is always lower than the ratio of the volume fraction of (001)- and (111)-textured, samples were considered (001)-textured when the ratio of intensities was greater than 0.90 and were considered (111)-textured otherwise. Equation (2.31) is also plotted in figure 5.9, taking the grain growth temperature of Ag to be 350°C and neglecting the intrinsic and densification strains. The line defined by equation (2.31) represents the thicknesses and deposition temperatures of films in which the surface and interface energy driving force for grain growth has the same magnitude as the elastic strain energy density driving force for grain growth. The value of $\Delta\gamma$ chosen to plot equation (2.31) was taken to be the difference between the surface and interface energy of the (111);0° and (001);17° orientations, as these are the experimentally observed orientations that develop during grain growth:

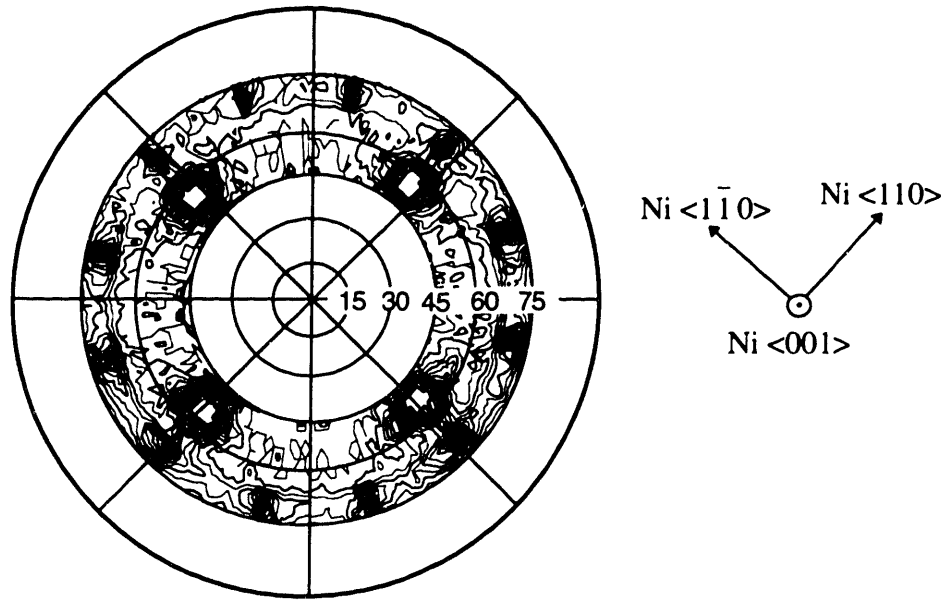


Figure 5.7: $\langle 111 \rangle$ Ag pole figures for a 2500 Å thick film deposited at 30°C and annealed at 400°C for 3h.

$$\Delta\gamma = [\gamma_s(001) + \gamma_i(001); 17^\circ] - [\gamma_s(111) + \gamma_i(111); 0^\circ] \cong 0.43 \text{ J/m}^2 \quad (5.1)$$

For large thicknesses and low deposition temperatures, i.e., large thermal strains, the (001) texture in the film is pronounced. At small thicknesses and high deposition temperatures, i.e., low thermal strains, the films is more (111)-textured.

Because single crystals of MgO are brittle and because the ion-milling rate of both Ag and Ni are much greater than the ion-milling rate of MgO, it was not found possible to prepare TEM samples of the Ag films on the MgO substrates. However, images formed with secondary electrons in a FIB microscope provided information about the microstructure of the Ag films. Figure 5.10 shows the grain structure of a 3500 Å thick

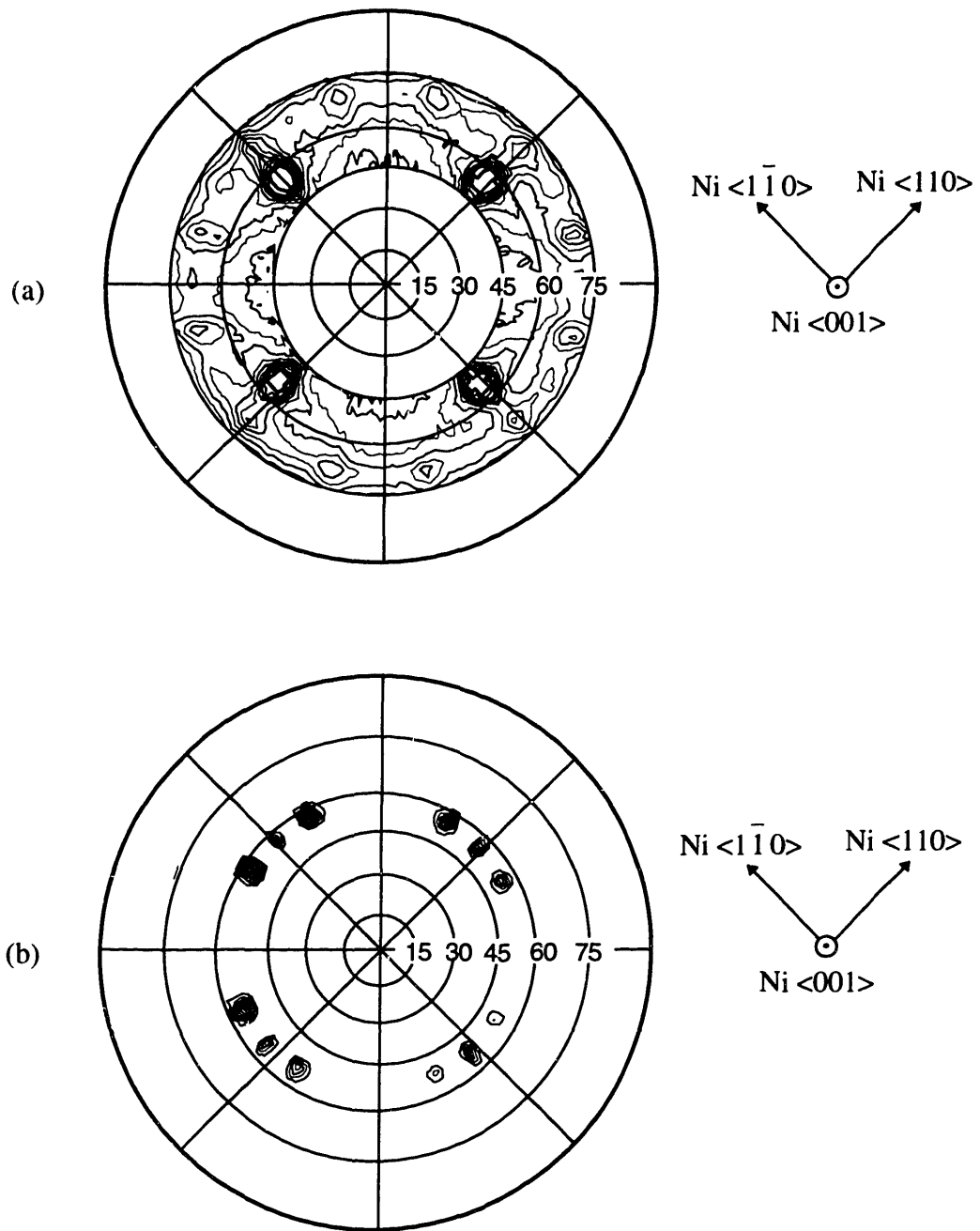


Figure 5.8: $\langle 111 \rangle$ Ag pole figures for films annealed at 400°C for 3h. (a) 1000 \AA thick film deposited at -158°C . (b) 3400 \AA thick film deposited at -148°C .

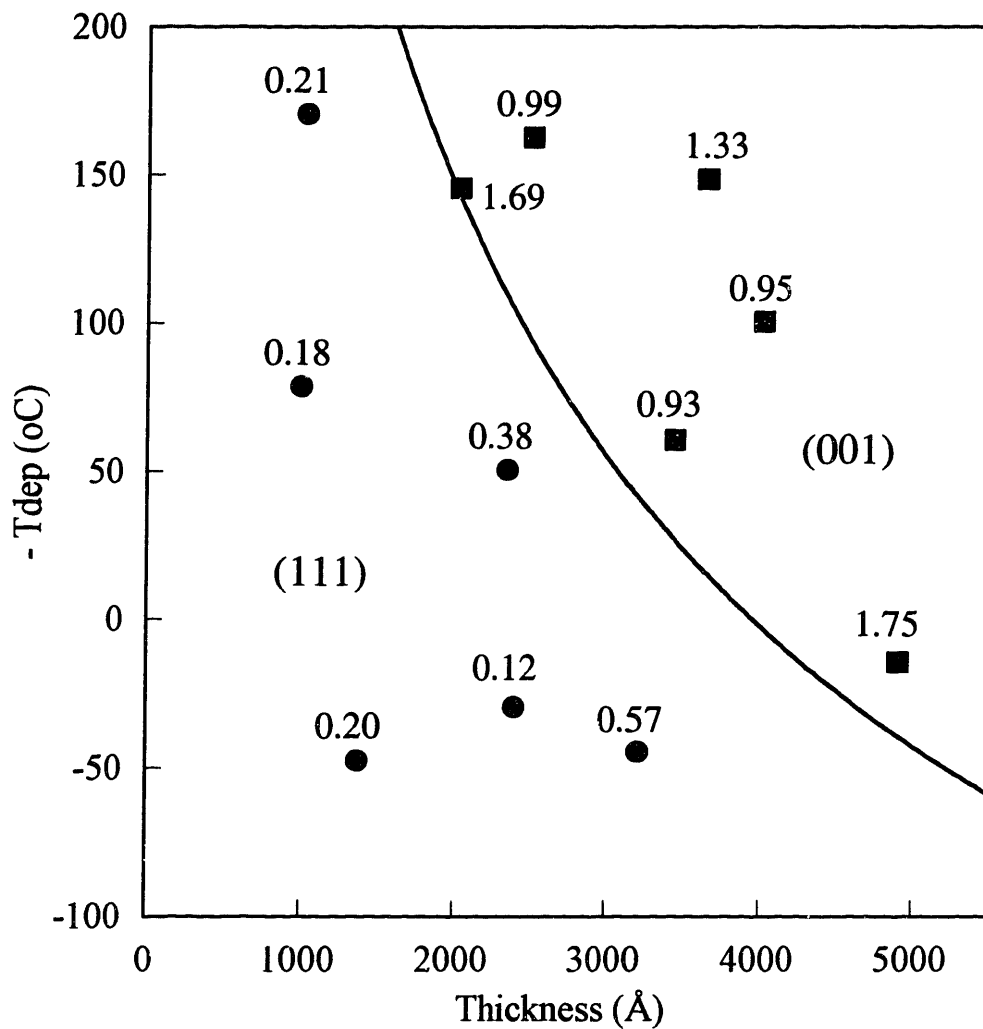


Figure 5.9: Texture map for Ag/(001)Ni/(001)Ag/(001)MgO. The line is the locus of points for which the surface and interface energy driving force for grain growth and the elastic strain energy density driving force for grain growth have the same magnitude.

sample deposited at -54°C and annealed at 400°C for three hours. The grain size can be estimated to be of order $3\ \mu\text{m}$, or about 10 times the film thickness, indicative of copious grain growth. The grain structure also appears to be bimodal as some grains are very large and some grains are small, at the limit of the resolution power of the FIB.

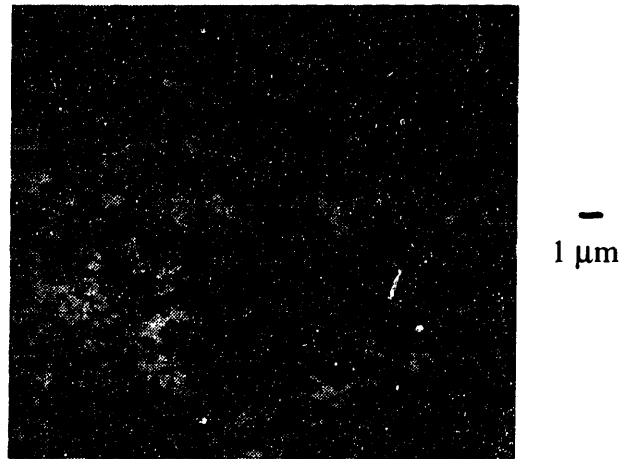


Figure 5.10: FIB image of a $3500\ \text{\AA}$ thick film deposited at -53°C and annealed at 400°C for 3 h.

5.5.3 - Discussion

5.5.3.1 - *Texture evolution during grain growth*

The texture map for $\text{Ag}/(001)\text{Ni}/(001)\text{Ag}/(001)\text{MgO}$ is consistent with the existence of two orientation dependent driving forces for grain growth: surface and interface energy anisotropy and strain energy density anisotropy. Grains in the $(111);0^{\circ}$ orientation minimize the combined surface and interface energy of $\text{Ag}/(001)\text{Ni}$ and grow preferentially when the thickness of films is small or when the deposition temperature is

high. Under these conditions, the surface and interface energy driving force for grain growth is greater in magnitude than the strain energy density driving force for grain growth in the film. Conversely, (001)-textured grains grow preferentially at large thicknesses and low deposition temperatures, when the strain energy driving force has a greater magnitude than the surface and interface energy driving force. Figure 5.11a shows the thermal strain in Ag films on MgO substrates as a function of the deposition temperature of the Ag film, and for a grain growth temperature of 350°C. The strain in the Ag is compressive since MgO has a smaller thermal expansion coefficient than Ag, and of magnitude less than 0.5%. Figure 5.11b shows the yield strain, $\epsilon_y = \sigma_y/M_{hkl}$, of (111) Ag grains as a function of the film thickness for an initial grain size of 400 Å, representative of the as-deposited grain in Ag/(001)Ni [47], and for a grain size to thickness ratio equal to 2.0, representative of a film for which substantial grain growth has occurred.

Figure 5.11 shows that the thermal strain in the (111) Ag grains is always elastically accommodated in the as-deposited structure and that yielding does not occur before the substantial grain growth has occurred. A similar conclusion can be drawn for (001) Ag grains.

In as-deposited films, (001) and (111) textures respectively minimize and maximize strain energy density. (111) texture also minimizes surface and interface energy. As-deposited films consist mainly of (111) and (001) grains, and the textures that are expected to grow upon annealing are therefore (001) or (111), consistent with the

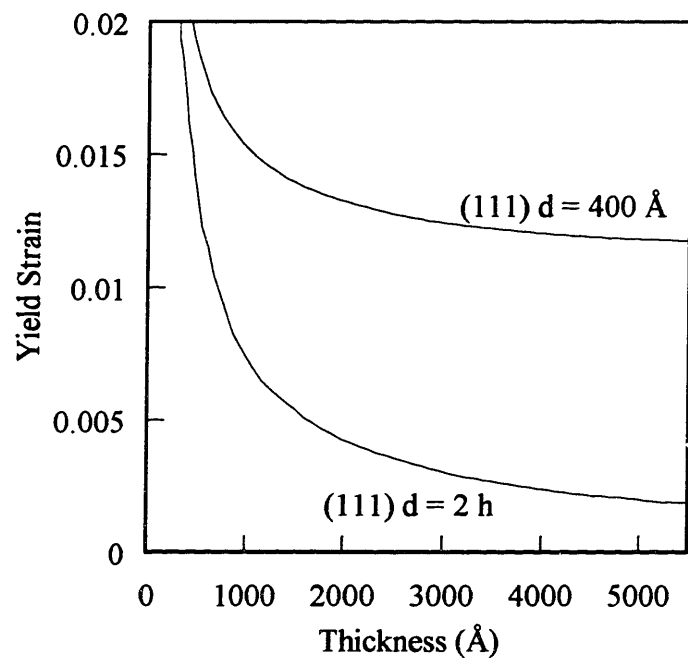
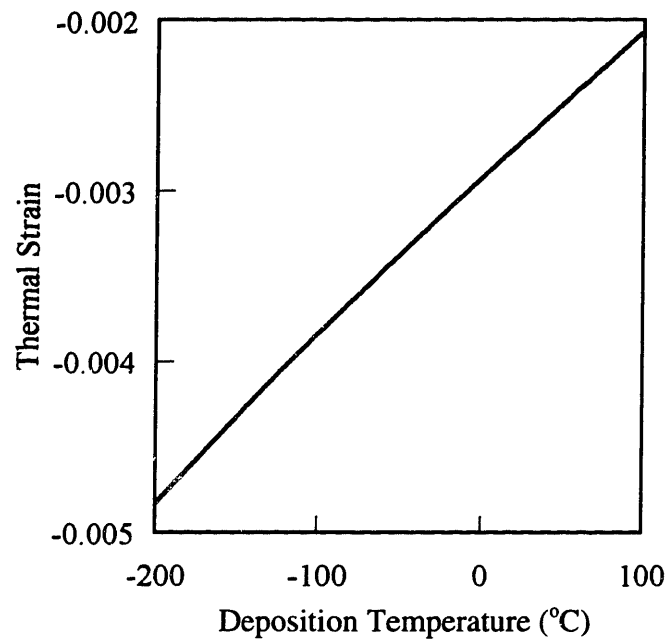


Figure 5.11: (a) In-plane strain (ϵ_1) in the Ag film due to differential thermal expansion between Ag and MgO. (b) Yield strain of (111) Ag grains plotted as a function of film thickness and for two different relationships between grain diameter and film thickness, and using the coefficients C_h and C_d found in table 2.2.

experiments. As grains grow, the yield stress decreases (equation 2.22) and part of the strain is plastically accommodated. The experimental texture map suggests that orientation evolution during grain growth in Ag/(001)Ni is accurately described by considering the strain energy density driving force for films which have undergone only elastic deformation, as shown by the calculated transition in the texture map (figure 5.9). The relative influences on grain growth of elastic strain energy density anisotropy and plastic strain energy density anisotropy are considered more quantitatively in chapter six.

5.5.3.2 - In-plane orientations

In the Ag/(001)Ni/(001)Ag/(001)MgO system, the surface and interface energy depends not only on the texture of the Ag but also on the in-plane orientation of the Ag lattice with respect to the Ni lattice. Strain energy density depends solely on the texture of grains and not on their in-plane orientation relative to the Ni. It was therefore expected that the global minimization of the energy of the film would lead to in-plane orientations that minimize the surface and interface energy for the textures that grow preferentially. When surface and interface energy is the dominant driving force for grain growth, (111);0° grains grow preferentially. This is consistent with a global energy minimization as these grains have the lowest combined surface and interface energy of all (001);β and (111);β grains. However, when strain energy density anisotropy is dominant and promotes (001) texture, the growth of grains with the GDS predicted local surface and interface energy minimum (001);26.6° is never observed. Instead, the orientations favored by grain growth are (001);17°, (001);45°, and (001);0° in some of the bonding experiments. The preferred orientations after grain growth are also tilted relative to the Ni lattice. This can be seen in

figure 5.8b where the centers of the (001);17° poles do not lie on a circle centered on the origin of the pole figure, in contrast with the centered epitaxial poles. While the magnitude and direction of the tilt varies from sample to sample, all (001);β orientations for a given sample are tilted identically. Several mechanisms which can possibly account for these discrepancies are detailed in ref. [47]. We briefly review them and propose two additional possible causes for the growth of the observed (001);β orientations.

Validity of the embedded atom calculations

It is possible to question the validity of the interface energy calculated using an embedded atom potential and molecular static calculations. An in-depth discussion of the assumptions underlying this computational technique is beyond the scope of this thesis. This method has proven to correctly reproduce experimental results in many instances [102, 103]. For example the furnace bonding experiment and the rotating crystallite experiment confirm that (111);0° is the surface and interface energy minimizing orientation, in agreement with GDS calculations. Several of GDS calculations, including the structure and energy of the (001);26.6° interface have been successfully reproduced¹. It is however interesting to note that unlike other (001);β Ag/(001)Ni interfaces, the energy of the (001);26.6° interface is very sensitive to the detailed procedure by which it is extracted from the positions of the relaxed atoms in the computational cell [109]. The embedded atom method has also proven to yield predictions for the interface stress for (111)Ag/(111)Ni interfaces ($\gamma = 1.32 \text{ J/m}^2$) in disagreement with experimental measurements ($\gamma = -2.27 \text{ J/m}^2$) [24]. It is possible the embedded atom method does not

¹This work was accomplished by Prof. P. Bristowe.

yield the correct value of the interface energy for some of the orientations considered by GDS, in particular the (001);26.6° orientation.

Orientation-dependent grain boundary mobility

As presented in section 2.5, grain boundary energy and grain boundary mobility are both a strong functions of grain boundary structure. As grain boundaries migrate, they change their local curvature and therefore their structure, energy, and mobility. It is unlikely from that perspective that mobility anisotropy can explain the development of the observed in-plane orientations. However, since the as-deposited films consist mostly of (111);0° and (001);0° grains, the occurrence of orientation selection through mobility anisotropy in an orientation-constrained matrix can not be ruled out completely.

Modification of the interface energy by defects

The interface energy of Ag/(001)Ni as presented in section 5.2.1 results from atomic computer simulations using the embedded atom method. All simulations assume that the interface between the Ag and the Ni is atomically flat and defect free. In real films, the interface is not defect free and contains defects such as ledges, vacancies, and dislocations which can significantly affect the magnitude of the interface energy and the magnitude of the anisotropy of the interface energy [110].

As the Ag plastically deforms, dislocations slip through the grain and stop at the Ag/Ni interface. Floro analyzed this effect and calculated an order of magnitude for the induced change in interface energy of $\Delta\gamma_i \approx 52 \text{ mJ/m}^2$ [47]. He also considered the tilt that can result from slip. For a tilt of 5°, the change in interface energy is approximately $\Delta\gamma_i \approx 33 \text{ mJ/m}^2$ [47]. In both cases, the effect on the interface energy is not large to

explain the observed in-plane orientation selection. In addition, the number of dislocations necessary to generate a 5° tilt of the Ag exceeds by several orders of magnitude what is expected to result from the maximum plastic strain in the Ag films.

Another type of defect present at the Ag/Ni interface result from the yielding of the single crystal Ni film. The Ni is deposited at 275°C and cooled prior to deposition of the Ag film. The thermal strain induced by this temperature change is sufficient to cause yielding in the Ni, resulting in a grid of ledges at the Ni surface which can affect the interface energy of Ag/(001)Ni. For a film subjected to a total strain ϵ , the plastic strain in the Ni is $\epsilon^{pl} = \epsilon - \sigma_y/M_{001}$. The dislocation spacing necessary to accommodate ϵ^{pl} is shown to be [47]:

$$D = \frac{a}{2\sqrt{2}\epsilon^{pl}} \quad , \quad (5.2)$$

where a is the lattice constant of the Ni, and D is given along a [110] direction of the Ni lattice. Using equation (2.22) with $d = \infty$ and $h = 1000 \text{ \AA}$ for the yield stress of the single crystal Ni film, and equation (2.18) for the energy of the ledge at the Ag/Ni interface, the maximum modification of the Ag/Ni interface energy occurs for a Ni film deposited at 225°C and cooled at -175°C, and is of order $\Delta\gamma_i \approx 30 \text{ mJ/m}^2$. This effect is insufficient to explain the growth of the observed (001); β orientation. However, when all types of defects at the interface are considered, and assuming that the effects add up, the change in interface energy can be significant, large enough to significantly perturb the combined surface and interface energy of Ag/Ni. Detailed atomistic simulations are required to obtain more precise values for the influence of defects on the interface energy anisotropy.

Oriented recrystallization

This mechanism is discussed in section 5.2.3 and is not further detailed.

Interface stress

A general solid-solid interface has associated with it two interface stresses that correspond to the two solid phases that meet at the interface [24, 111]. The interface stress h_{ij} is associated with the reversible work per unit area needed to strain equally both solids and is the relevant interface stress to consider in this work. To first order the interface energy γ_L , expressed in the Lagrangian coordinate system of the interface [112], depends on the interface stress h_{ij} as [24]:

$$\gamma_i^L(\epsilon_{ij}) \cong \gamma_i^L(0) + h_{ij}\epsilon_{ij} \quad , \quad (5.3)$$

where $\gamma_i^L(0)$ is the interface energy of the unstrained interface. Identifying the Lagrangian and the ordinary coordinate system associated with films, and reducing h_{ij} and ϵ_{ij} to scalar quantities for an order of magnitude calculation, the change in interface energy due to the strain is $\Delta\gamma_i = \gamma_i(\epsilon) - \gamma_i(0) = 2 h \epsilon$. Using $h = 1 \text{ J/m}^2$ [24] and $\epsilon = 0.01$ yields $\Delta\gamma_i = 20 \text{ mJ/m}^2$, of the same order of magnitude as the change in interface energy induced by defects at the interface.

Conclusions

Several mechanisms for in-plane orientation selection during grain growth in Ag/(001)Ni/(001)Ag/(001)MgO were reviewed. The anisotropy of the surface energy and of the interface energy can be modified by defects and by surface and interface stresses. While the order of magnitude calculations of these effects seem to indicate that there is not a single origin to the observed in-plane orientation selection, two or more mechanisms can

cooperate to induced a significant change in surface and/or interface energy. Alternatively, the in-plane orientation selection during grain growth can be explained by variable grain boundary mobility or oriented recrystallization.

5.5.3.3 - Comparison with computer simulations

Figure 5.12 shows both the results of the computer simulations of grain growth Ag/(001)Ni (chapter three) and the results of the grain growth experiments in Ag/(001)Ni presented in this chapter, plotted versus the thermal strain in the film. Converting the deposition temperature to strain for the grain growth experiments assumes that the grain growth temperature for Ag is 350°C, and that the intrinsic and densification strains are negligible. There is good agreement between the two sets of results. In the simulation and in the EGG experiments only two main textures, (001) and (111), are present in as-deposited films in this experimental system. This minimizes the occurrence of neighboring grains with other textures, and therefore different strain energy density and surface and interface energy differences. In both cases, the texture transition is well described by taking into account elastic strain energy anisotropy alone. This is due in part to the limited range of strains which can be obtained from differential thermal expansion between MgO and Ag for a deposition temperature varying from 77 K to 325 K. This is also due to the high yield stress of the as-deposited Ag films which prevents plastic deformation in the Ag before substantial grain growth has occurred. Even when films are plastically deformed, the strain energy density difference between (001) and (111) textures is still similar to the

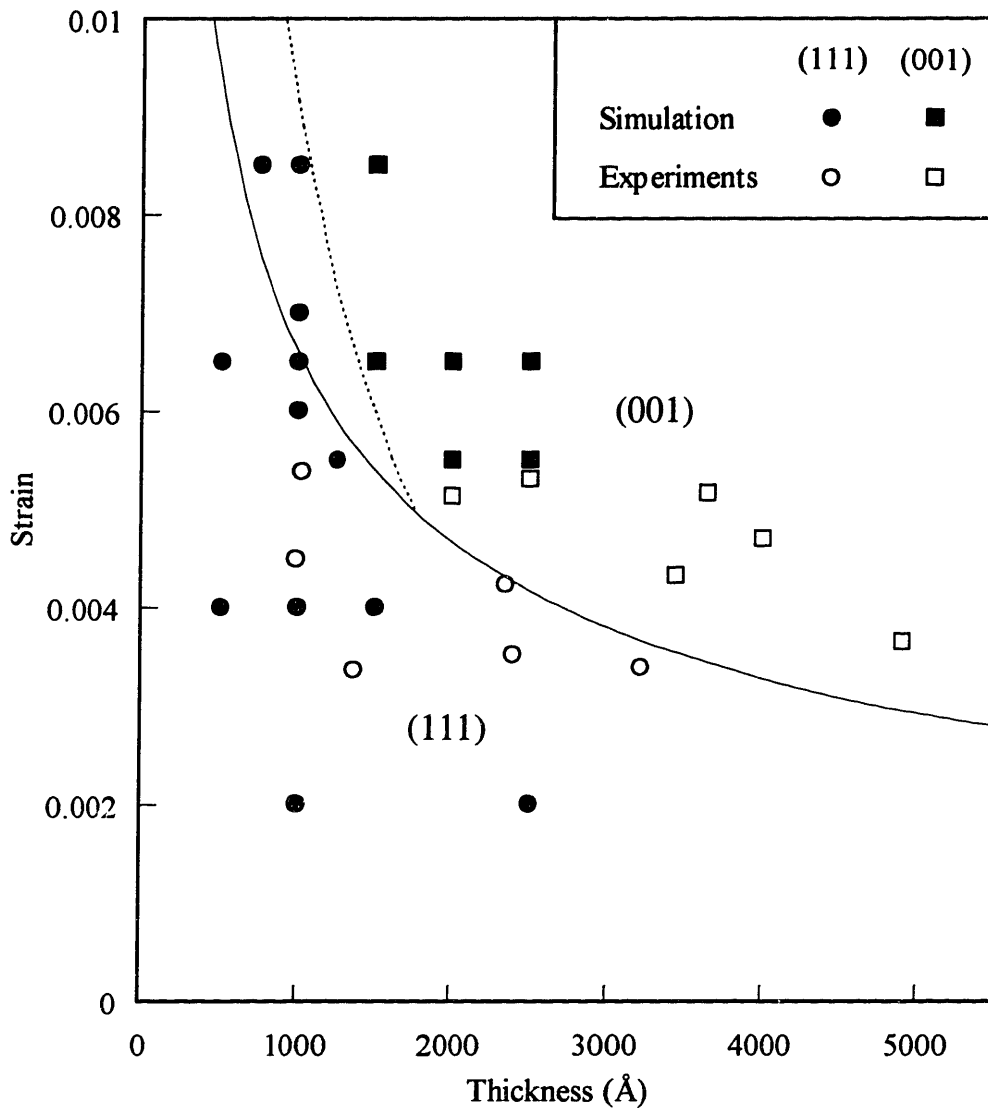


Figure 5.12: Results of the computer simulation and of the EGG experiments in Ag/(001)Ni/(001)Ag/(001)MgO plotted on the same texture map. The lines defined by equation (2.31) and (3.10) are also plotted.

strain energy density anisotropy between (001) and (111) textures in elastically deformed films. Both the simulations and the experiments confirm that yielding is not expected to play a determinant role in texture evolution during grain growth in this system.

Embedded atom calculations predict that the surface and interface energy minimizing interface for (001)Ag|| (001)Ni twist interfaces occurs for a twist of 26.6° away from the Ag/Ni cube-on-cube orientation. In the simulations, this orientation is strongly preferred among (001)-textured grains as shown in figure 3.10. In the experiments (001); 17° grains grow preferentially. The value of $\Delta\gamma$ used to plot equation (2.31) in figure 5.12 was taken between the (111); 0° and (001); 17° orientations, as observed experimentally.

5.6 - Summary and conclusions

Bonding experiments confirm that the surface and interface energy minimizing orientation in Ag/(001)Ni is (111); 0° , in agreement with GDS calculations. Direct deposition of Ag on (001) Ni results in as-deposited films mostly in the (111); 0° and (001); 0° orientations. In-situ annealing of these films to temperatures sufficient to induce grain growth results in a change in the distribution of orientations. When the thickness of the films is small and the deposition temperature is high, grains in the (111); 0° orientation grow preferentially. When the thickness of the films is large and the deposition temperature is low, (001); 17° grains are favored by grain growth. This behavior can be understood by considering two orientation-dependent driving forces for grain growth which compete to determine the texture of the film: surface and interface energy anisotropy and elastic strain energy density anisotropy. Surface energy density anisotropy favors the growth of (111); 0° grains and elastic strain energy density anisotropy favors the growth of (001)-textured grains. The analytic prediction of the orientations that grow preferentially as a function of the processing conditions of the film and the experimental

results in Ag/(001)Ni are in good agreement. There is also good agreement between the experimental results and the computer simulations of grain growth in Ag/(001)Ni presented in chapter three, indicating that yielding does not have a pronounced effect on grain growth in this system. In-plane orientation selectivity during grain growth is not completely understood. While the growth of (111);0° grains is consistent with GDS calculations, the growth of (001);17° grains, (001);0° grains, and (001);45° grains is not. Several mechanisms can account for the growth of these orientations. Additional interface energy modeling and additional experiments are required to fully understand in-plane selectivity for (001)-textured grains.

In chapter six, grain growth in films deposited on amorphous substrates is examined and the model for texture evolution presented in chapter two is further tested.

Chapter 6

Grain Growth in Films on Amorphous Substrates

6.1 - Introduction

In chapter two, a model for texture development during grain growth was proposed. In chapter five, it was shown that grain growth in Ag/(001)Ni could be driven by either surface and interface energy anisotropy or elastic strain energy density anisotropy. The orientations dominating during grain growth were found in good agreement with the analytic model developed in chapter two. While Ag/(001)Ni constitutes a useful model system where the interface energy is known in detail for two interface twist boundaries, it does not have as much practical interest as films on amorphous substrates which are used in many applications. Studying orientation during grain growth in films on amorphous substrates also allows us to further test the model developed in chapter two. In this chapter, we investigate texture evolution during grain growth in fcc films deposited on amorphous SiO₂.

In films on amorphous substrates, surface and interface energy anisotropy and strain energy density anisotropy provide orientation-dependent driving forces for grain growth as was the case in Ag/(001)Ni. However, in contrast with epitaxial systems, in-plane rotation of the film lattice with respect to the substrate for films on amorphous substrates leaves the structure and energy of the film-substrate interface unchanged. Grain

growth in these systems is therefore not expected to lead to three dimensionally constrained orientations, but only to preferred textures.

6.2 - Experimental details

6.2.1 - Film deposition

Continuous polycrystalline films were electron beam evaporated onto substrates in an ultra high vacuum environment. The deposition rates were 15 Å/s for Al, 20-25 Å/s for Ag, and 15-20 Å/s for Ni. The temperature of the substrate was monitored during deposition and did not vary by more than $\pm 5^\circ\text{C}$. The films were annealed in-situ to promote grain growth at 250°C for Al, 400°C for Ag, and 560°C for Ni. The Si/SiO₂ substrates were 500 μm thick (001) Si wafers with 1000 Å of thermally grown oxide. The MgO/SiO₂ substrates were produced by depositing 1000 Å of SiO₂ onto polished (001) MgO substrates using plasma-enhanced chemical vapor decomposition (PECVD) of SiH₄ in NO_x at 350°C. SiO₂ showed good adhesion to MgO. SEM pictures revealed that the SiO₂ films were continuous and smooth. Ag, Al, and Ni films were deposited in a temperature range of -170°C to 70°C. As in the epitaxial grain growth experiments, the thickness of the films was also varied.

X-ray texture analysis was performed using $\langle 111 \rangle$, $\langle 222 \rangle$, $\langle 220 \rangle$, and $\langle 311 \rangle$ Bragg reflections. The textures maps were constructed from either $\langle 111 \rangle$ or $\langle 222 \rangle$ pole figures. The diffracted intensity from the $\langle 111 \rangle$ Bragg reflection is greater than from the $\langle 222 \rangle$ Bragg reflection and provides good count statistics in short counting times. However, the defocusing of the x-ray beam with increasing α and the associated necessary

correction to the raw data is more severe for $\langle 111 \rangle$ pole figures than for $\langle 222 \rangle$ pole figures. Ag/SiO₂/Si, and Ni/SiO₂/Si were primarily characterized using $\langle 111 \rangle$ pole figures and Ag/SiO₂/MgO, and Al/SiO₂/Si were primarily characterized using $\langle 222 \rangle$ pole figures. It was verified in all cases that both types of pole figures produced consistent results. As the substrates are amorphous, there are no preferred in-plane orientations in the as-deposited films or after grain growth has occurred. The intensity from the pole figure can therefore be integrated with respect to β . The distribution of intensity as a function of α is then proportional to the volume fraction of grains with texture (hkl) such that the angle between (111) and (hkl) planes is α . All x-ray diffraction data presented in this chapter is integrated with respect to β , with corrections for background scattering, absorption and defocusing (chapter four).

6.2.2 - Statistical analysis of films microstructure

The microstructure of thin films can be described statistically by the grain size distribution function $f(r)$ which is such that $f(r)dr$ is the number of grains with grain radius between r and $r+dr$. While $f(r)$ completely describes the distribution of grain sizes in films, it is difficult to measure experimentally. This is due to the larger number of grain sizes that need to be collected for a single film, usually in excess of 1000 [113], to obtain an accurate estimation of the grain size distribution function. It is however possible to obtain an accurate estimate of the average grain size in films by sampling a much smaller population of grains, usually of order 100. This is done by assuming that the measured

grain sizes are related to a normally distributed random variable $N(\mu, \sigma^2)^1$, where μ is the population average grain size and σ^2 is the variance of the grain size population. When the sizes $(d_i)_{1 \leq i \leq n}$ in a random sample of n grains are measured², the sample average of these grain sizes:

$$\bar{d} = \frac{1}{n} \sum_{i=1}^n d_i \quad (6.1)$$

is then a normally distributed random variable $N(\mu, \frac{\sigma^2}{n})$. The grain size population variance σ^2 is not known but can be estimated by the grain size sample variance s^2 :

$$s^2 = \frac{1}{n-1} \sum_{i=1}^n (d_i - \bar{d})^2. \quad (6.2)$$

The random variable T ,

$$T = \frac{\bar{d} - \mu}{s / \sqrt{n}}, \quad (6.3)$$

has then a t distribution with $(n-1)$ degrees of freedom. A confidence interval can therefore be constructed for the estimator \bar{d} of the population average grain size in the film μ [106]:

¹ The grain sizes in films that have undergone grain growth are usually not normally distributed but can be represented by a lognormal or bimodal distribution. Even when the grain size is not normally distributed, it is an excellent approximation to consider that the realization of the random variable formed as the average of n grain sizes is normally distributed, providing that n is sufficiently large. In our grain size measurements, n was always greater than 80 and the sample average grain size can be considered normally distributed.

² To determine the size of a grain, the longest segment contained within the grain was measured. The longest segment perpendicular to the first segment was also measured and the grain size was taken to be the average of the lengths of the two segments.

$$\bar{d} \pm t_{n-1}^{\omega/2} \frac{s}{\sqrt{n}} \quad , \quad (6.3)$$

where $t_{n-1}^{\omega/2}$ is such that $P(-t_{n-1}^{\omega/2} \leq T \leq t_{n-1}^{\omega/2}) = 1-\omega$, and can be found in tabulated form [114]. Equation (6.3) was used with $\omega = 0.1$ to construct 90% confidence intervals for the measured average grain size in films.

6.2.3 - Grain growth temperature and thermal strain

The grain growth temperature of films was determined by preparing TEM samples from 2500 Å thick films on oxidized Si wafers (section 4.1) and by annealing the samples in-situ in the TEM. The grain growth temperature was taken to be the temperature at which significant grain boundary motion occurred in the film. The grain growth temperature for Ag, Ni, and Al was found to be of order 350°C, 550°C, and 250°C, respectively. It is assumed that the nature of the substrate does not affect the grain growth temperature of films and that all grain boundary motion in films occurred at the grain growth temperature. This last assumption is relaxed in appendix VI where the kinetics of grain growth in Ag/SiO₂/Si is examined. The thermal strain in the films was calculated using temperature dependent thermal expansion coefficients for the film and the substrate. Figure 6.1 shows the thermal strain in the combination of films and substrates examined in this chapter, when heated from the deposition temperature of the film to the grain growth temperature. In all cases, the thermal strain is compressive.

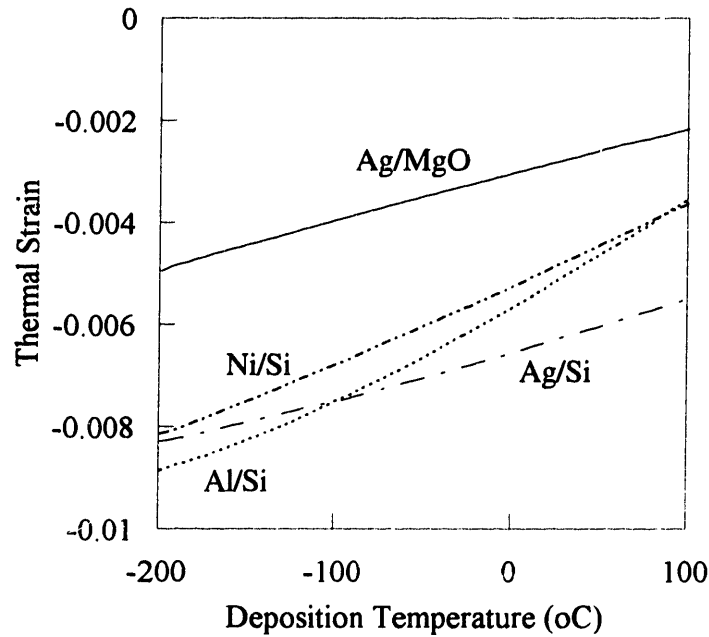


Figure 6.1: Calculated thermal strain in films when heated from the deposition temperature to the grain growth temperature.

6.3 - Ag/SiO₂/Substrate

6.3.1 - Ag/SiO₂/MgO

To cut down x-ray data acquisition time, pole figures were not measured for all the samples. Instead, β -scans at $\alpha = 71^\circ$ and at $\alpha = 55^\circ$ were acquired with the $\langle 222 \rangle$ Bragg reflection of Ag, characteristic of (111)- and (001)-textured grains, respectively. β -scans were also measured with the angle 2θ off by 1.5° from the Bragg peak to correct the data for background scattering. The intensity arising from the (444) Bragg peak of the MgO single crystal substrate was removed from the data and the intensity was integrated with respect to β . The two integrated intensities were corrected for defocusing and absorption.

The ratio $I(\alpha = 55^\circ)/I(\alpha = 71^\circ)$ was used to generate the texture map for this system. It was verified that the ratios obtained from β -scan data were identical to the ratios calculated from full pole figures.

Figure 6.2 shows the intensity from a full pole figure, integrated with respect to β , for a 2500 Å thick film deposited at 30°C and annealed at 400°C for 1 h. The peaks of intensity are characteristic of (111) and (001) textures. Other textures are only present in small volume fractions. Pole figures acquired on several other samples confirmed that (001) and (111) are the two main textures that can develop during grain growth. It is therefore sufficient to measure β -scans for (001) and (111) textures to characterize the preferred orientations in the films.

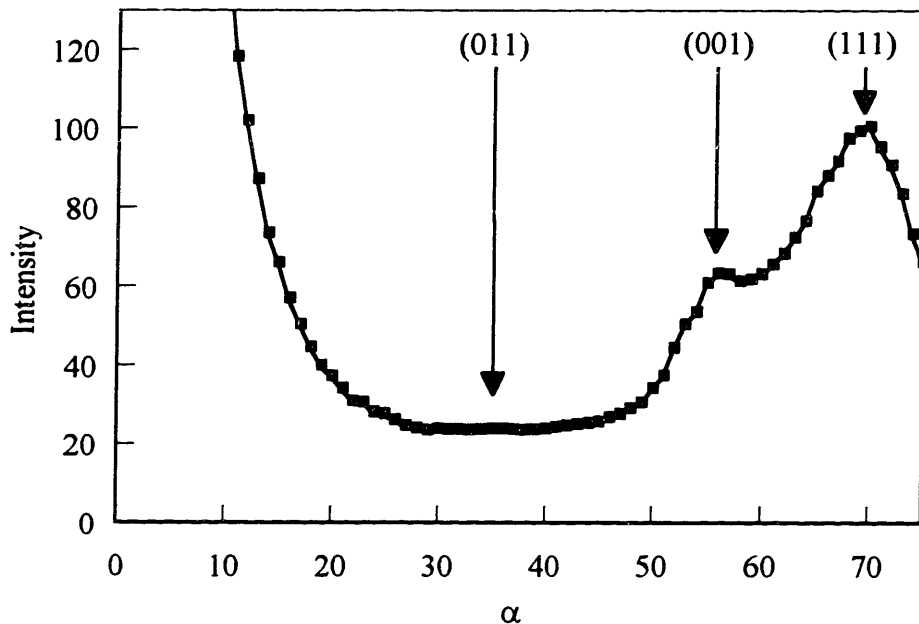


Figure 6.2: $\langle 222 \rangle$ Ag rocking curve for a 2500 Å thick Ag/SiO₂/MgO film deposited at 30°C and annealed at 400°C for 1h.

As-deposited films are not randomly oriented, and the volume fraction of (001)- and (111)-textured grains varies with the thickness of films. Figure 6.3 shows the ratio of intensities for as-deposited films, plotted as a function of film thickness. For thicker films, the texture as-deposited is more strongly (111) than for thinner films. A discussion of the possible cause of this effect is found in section 6.6. Quantitative orientation evolution during grain growth can not therefore be described merely by the ratio of intensities $I(\alpha = 55^\circ)/I(\alpha = 71^\circ)$ in annealed films. In order to measure texture evolution during grain growth, the ratio of intensities obtained from annealed films was divided by the ratio of intensities in as-deposited films with the same thickness. Ideally, the as-deposited orientation distribution would also be characterized as a function of deposition temperature. However, without in-situ texture analysis capabilities, films have to be brought to room temperature and exposed to air in order to perform x-ray diffraction texture analysis. Both temperature change and exposure to air can induce some grain growth in fcc metal thin films [47, 115-117]. The data from all annealed samples were therefore normalized with the data from films deposited at room temperature. The thickness dependence of the normalization factor was taken to be the best fitting line to the data shown in figure 6.3.

Figure 6.4 shows the texture map for Ag/SiO₂/MgO, where the number above each data point is the normalized ratio of intensities, and where the temperature change $T_{gg}-T_{dep}$ is used rather than the strain. Equivalent texture maps could be plotted using the strain or the opposite of the deposition temperature ($-T_{dep}$) as y axis variables. The only

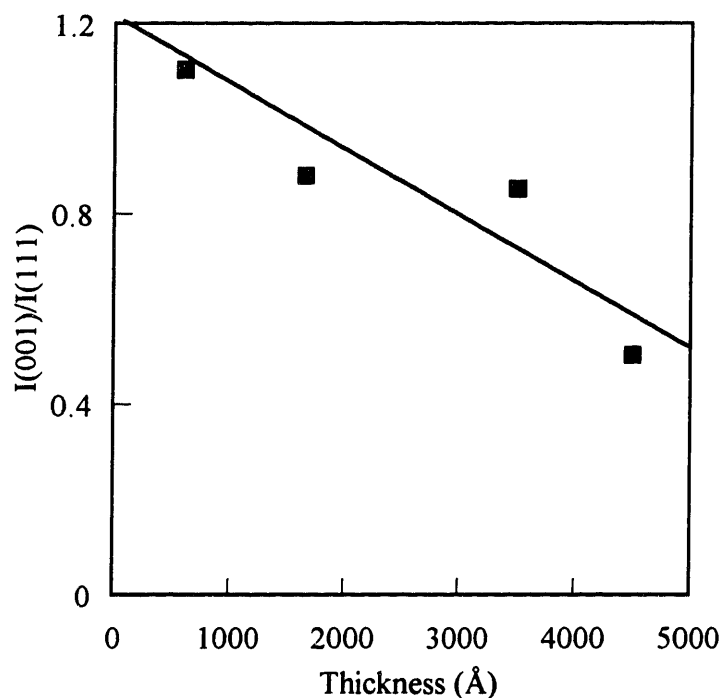


Figure 6.3: Ratio of diffracted intensity for (001) and (111) textures, plotted versus film thickness for as-deposited Ag/SiO₂/MgO films. The x-ray data was acquired with the <222> Ag Bragg peak.

difference between these equivalent texture maps is the scale of the y axis. When the normalized ratio of intensity is greater than 1.0, (001)-textured grains have grown preferentially to (111)-textured grains. When the normalized ratio is lower than 1.0, (111)-textured grains were favored by grain growth compared to (001)-textured grains. The texture map shows that (001) texture is favored by grain growth, compared to (111) texture, for thick films or for large thermal strains. Conversely, (111) texture is favored by grain growth, compared to (001) texture, for films with small thicknesses and for small thermal strains. The line defined by the equivalent of equation (2.31), where the strain is substituted with the difference between the grain growth temperature and the deposition

temperature ($T_{gg}-T_{dep}$), is also plotted in figure 6.4. This line corresponds to the experimental conditions for which the surface and interface energy driving force and the elastic strain energy density driving force for grain growth have the same magnitude. It is plotted for $\Delta\gamma = 0.3 \text{ J/m}^2$, and assuming that both the intrinsic and densification strains are negligible in the film, i.e., $\epsilon_i = \epsilon_d = 0$.

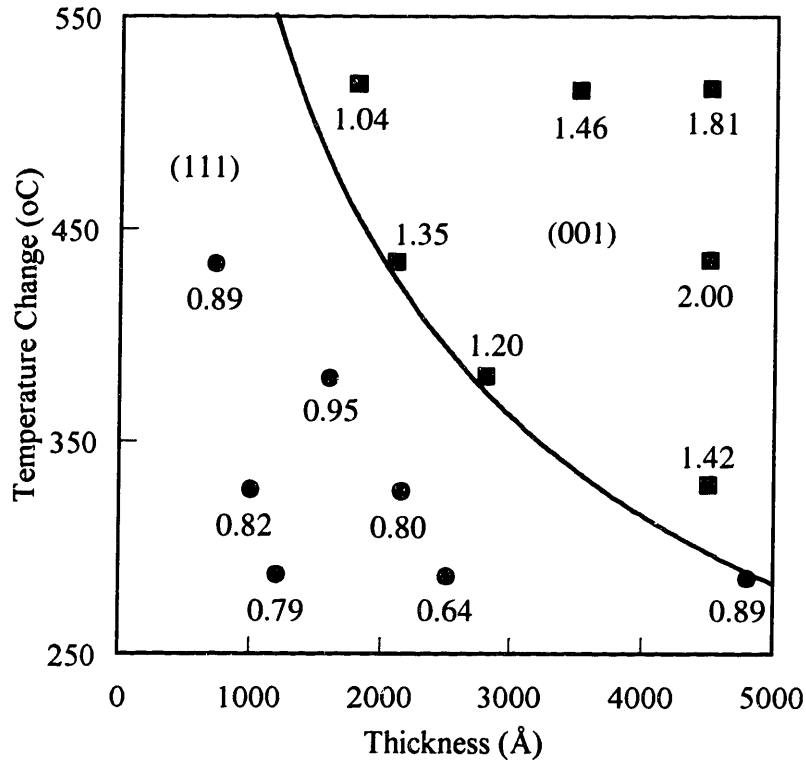


Figure 6.4: Texture map for Ag/SiO₂/MgO.

6.3.2 - Ag/SiO₂/Si

X-ray data acquired with the $\langle 111 \rangle$ Bragg reflection of Ag for Ag/SiO₂/Si films is presented in figure 6.5 for one as-deposited and three annealed films. As-deposited films are (111)-textured. The strength of the (111) texture, as measured by the ratio of

intensities for (001)- and (111)-textured grains, was found to be independent of the thickness of films. As in the case of Ag/SiO₂/MgO, only (111) and (001) textures develop in films during grain growth, as verified by performing <220> and <311> pole figures. At small thicknesses and high deposition temperatures (figure 6.5b), (111) grains are favored due to the high relative magnitude of surface and interface energy anisotropy. Figure 6.5d shows schematically that for thick films deposited at low temperatures and annealed at 350°C, the intensity maximum at that $\alpha = 60^\circ$ can be deconvoluted as the sum of two peaks two peaks characteristic of (001) and (111) textures. At low deposition temperatures and large thicknesses (figure 6.5d), (001) texture is favored due to the large relative contribution of strain energy density anisotropy. Comparison of figures 6.5a and 6.5c shows that in the 3800 Å thick film deposited at 5°C and annealed at 350°C, (111)-textured grains have grown preferentially compared to (001)-textured grains. The (001) peak at $\alpha = 55^\circ$ appears better defined in figure 6.5c than in figure 6.5a because both (001) and (111) textures have sharpened during grain growth.

TEM micrographs for one as-deposited and one annealed film are shown in figure 6.6. The very large grains in annealed films are evidence of abnormal grain growth. These large grains are never seen in as-deposited films. Selected area electron diffraction patterns confirmed the x-ray diffraction results that all orientations are represented in as-deposited and annealed films and that no in-plane orientation is preferred. Grain sizes for as-deposited and annealed films were measured from TEM micrographs and the results are plotted on figure 6.7. The average grain size and thickness of as-deposited films were

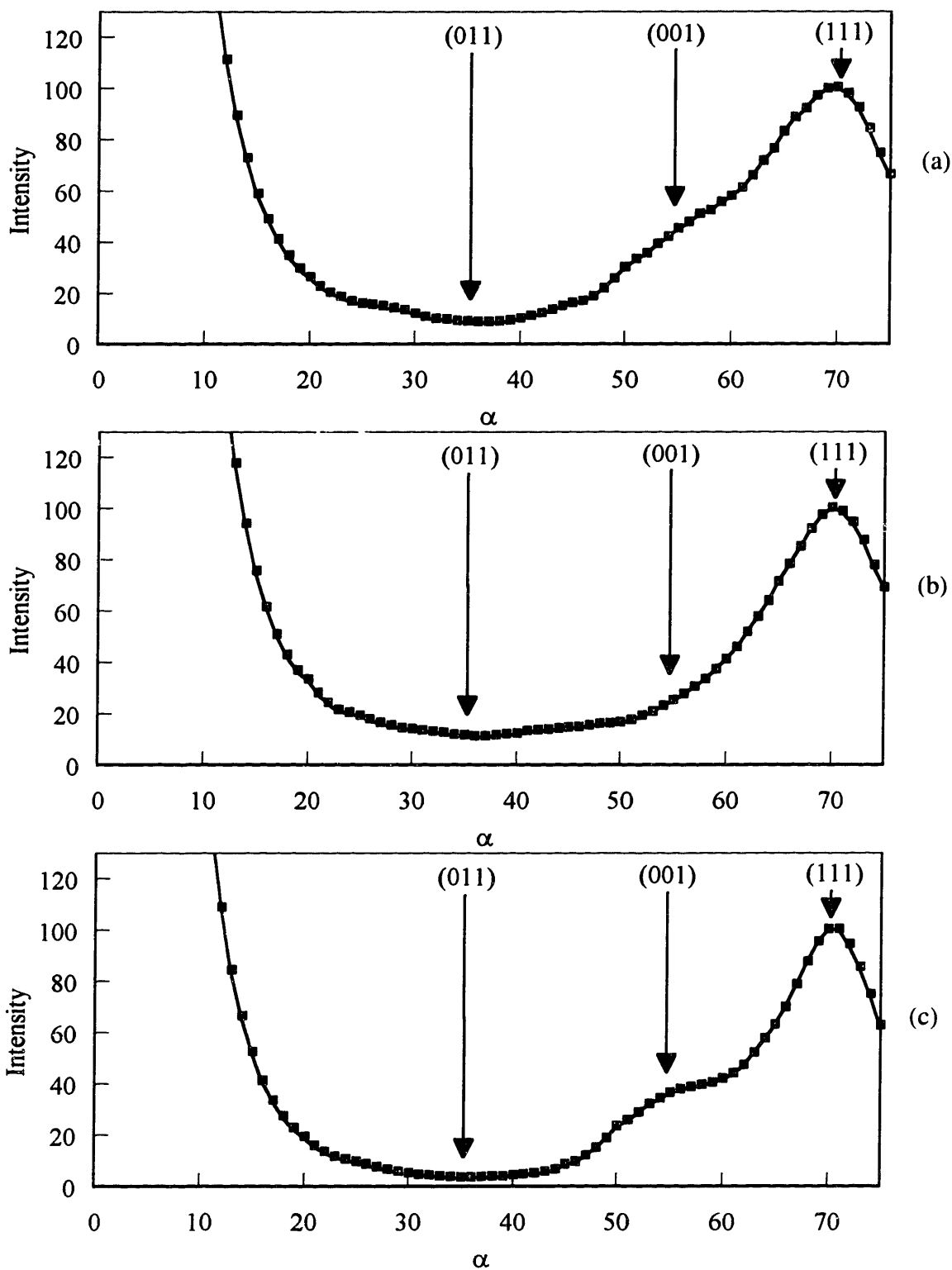
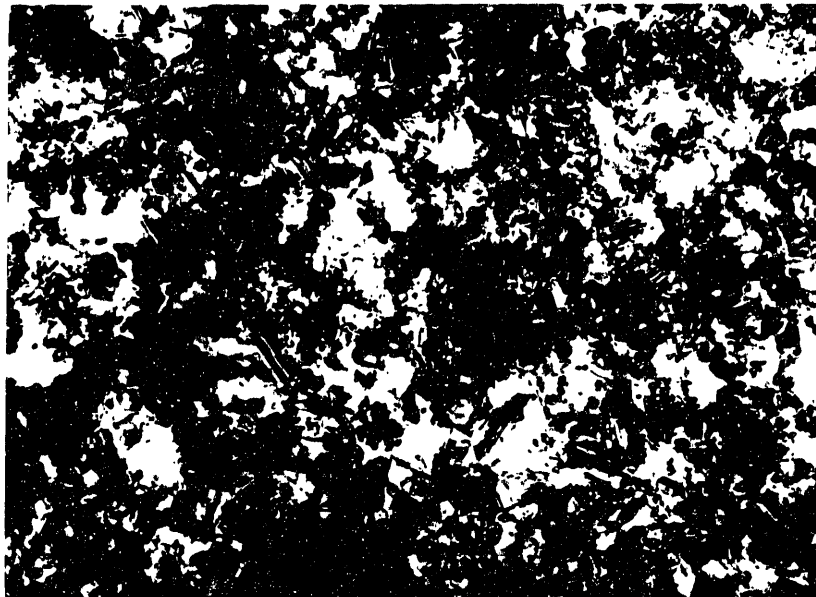
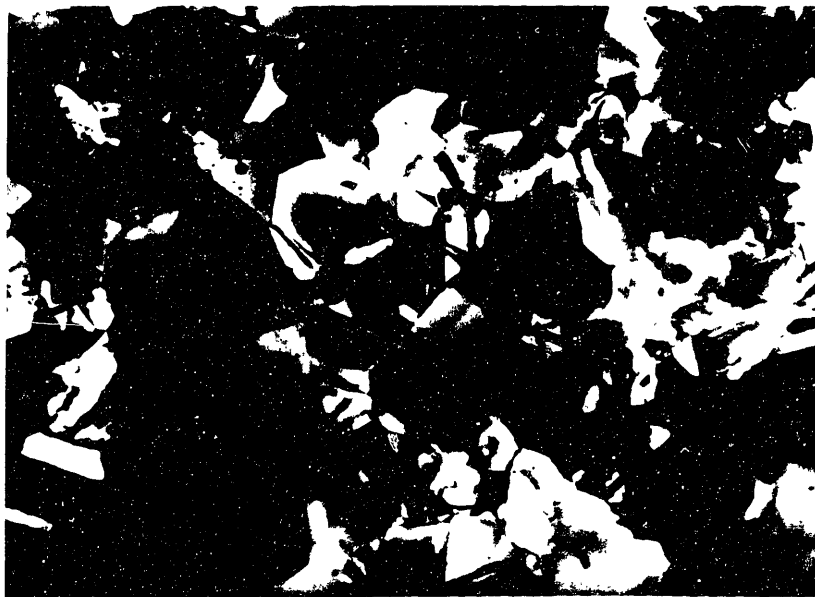


Figure 6.5a-c: $\langle 111 \rangle$ Ag rocking curves of Ag/SiO₂/Si samples. (a) film deposited at 4°C, 3800 Å thick, as-deposited. (b) 600 Å thick film deposited at -80°C, and annealed at 350°C for 35 min. (c) 3800 Å thick film deposited at 5°C, and annealed at 350°C for 30 min.



(a) ——— 1 μm



(b) ——— 1 μm

Figure 6.6: TEM micrographs of Ag/SiO₂/Si films. (a) 600 Å thick film deposited at 5°C, as-deposited. (b) 2200 Å thick film deposited at 3°C and annealed at 350°C for 30 min.

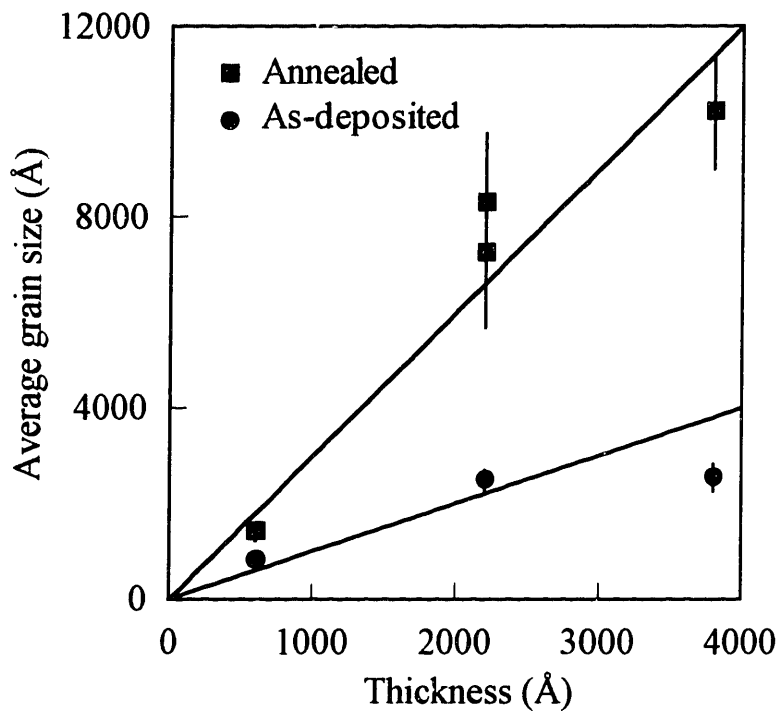


Figure 6.7: Average grain size in as-deposited and annealed Ag/SiO₂/Si films. 90% confidence intervals are also plotted.

defined by equation (2.31) is also plotted for the parameters that fit well the Ag/SiO₂/MgO data, $\Delta\gamma = 0.3 \text{ J/m}^2$, and $\epsilon_d = \epsilon_i = 0$, and also for $\Delta\gamma = 0.3 \text{ J/m}^2$, $d_0 = 400 \text{ Å}$, $k = 3$, and $\epsilon_i = 0$. For this system, it was found necessary to include the densification strain to obtain a good match between the experimental data and the model developed in chapter two. The value of $\Delta\gamma$ used here is also different from the values used for Ag/SiO₂/MgO. The reasons for these discrepancies and the differences between the two systems are discussed in the next section. A tensile intrinsic strain/stress could be used instead of the densification strain to obtain the same fit to the data of equation (2.31). As the thermal strain in Ag is compressive when the film is heated from the deposition temperature to the

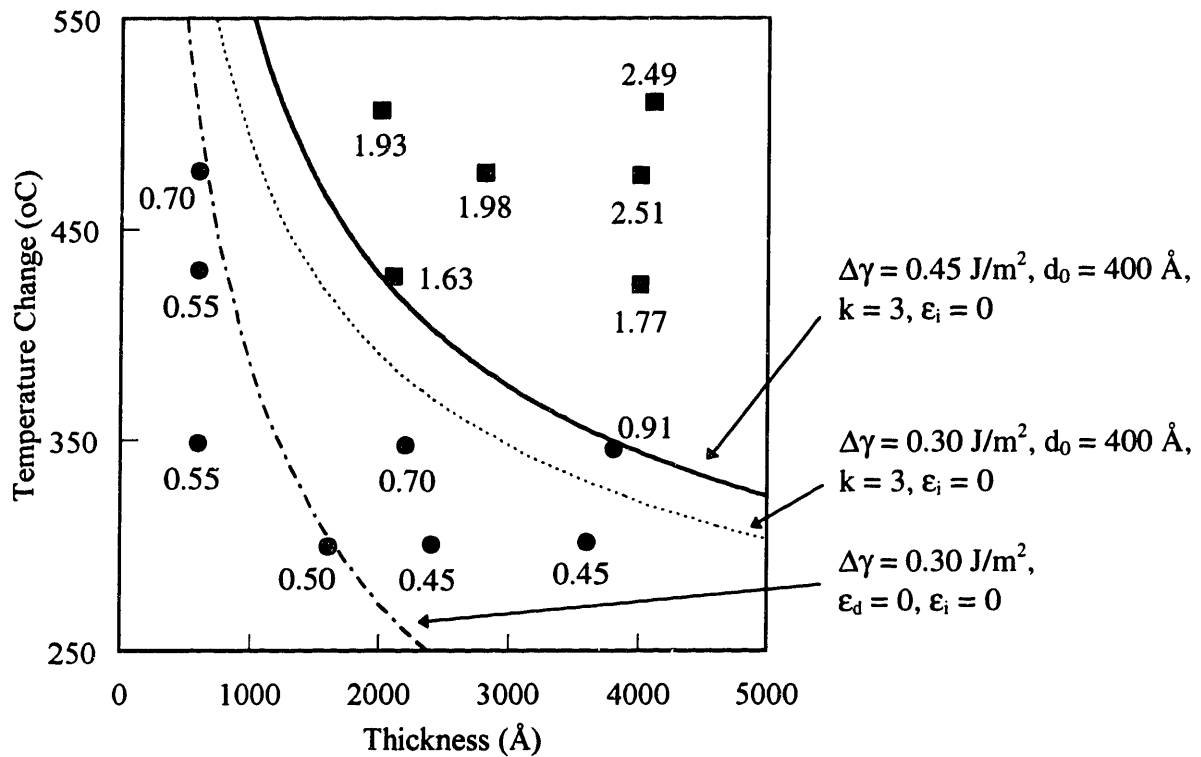


Figure 6.8: Texture map Ag/SiO₂/Si. The boundary defined by equation (2.31) is also plotted for three sets of parameters.

grain growth temperature, the effect of the tensile densification strain or of an intrinsic tensile strain/stress is to extend the domain in which surface and interface energy supersedes elastic strain energy density toward greater thicknesses.

6.3.3 - Discussion of Ag/SiO₂/MgO and Ag/SiO₂/Si

The orientation-dependent driving forces for grain growth are plotted on figure 6.9 versus film thickness and for (001) and (111) grains with the same sizes. The strain energy differences shown in figure 6.9 were calculated using the upper bound for the strain energy density of yielded grains (eq. (2.25)), where all the plastic work is included in

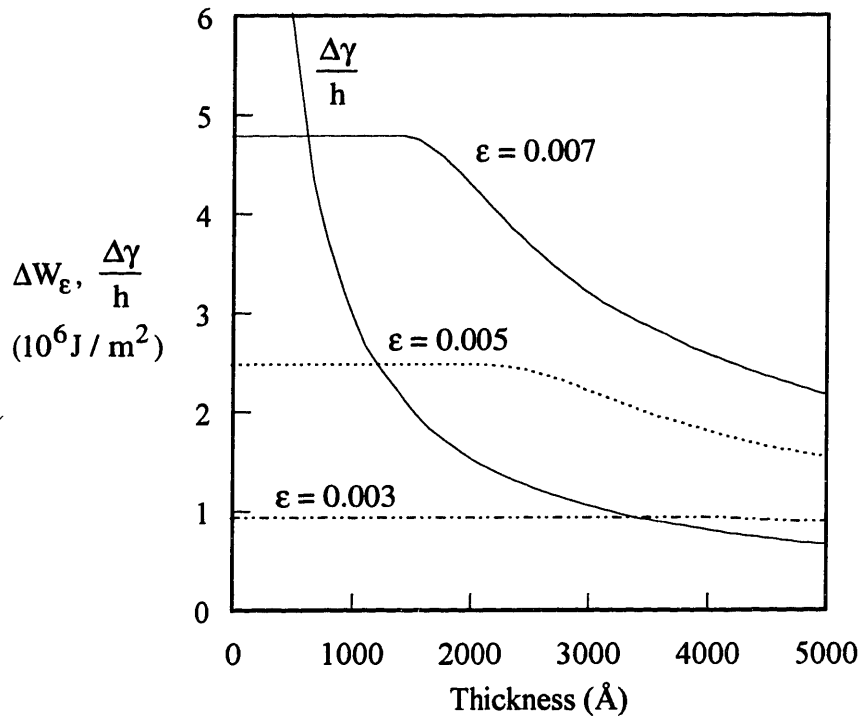


Figure 6.9: Strain energy density differences and surface and interface volumetric energy differences between (001) and (111) Ag grains plotted versus film thickness. The strain energy of yielded grains is calculated assuming $d = h$.

the plastic strain energy density (chapter two, section 2.4.3). Ag has an anisotropy ratio $A = 3.01$ and exhibits anisotropic elastic properties. Because of this strong elastic anisotropy, the equality of the magnitude of the orientation-dependent driving forces for grain growth expressed by equation (2.30) is satisfied to a good approximation when the strain energy difference is taken in the elastic regime only, and yielding is neglected (eq. (2.31)). In figure 6.9, this corresponds to the intersection of the $\Delta\gamma/h$ curve with the flat plateaus of the strain energy difference curves. For a given strain, the intersection defines

a critical thickness above which the elastic strain energy density difference is of greater magnitude than the surface and interface energy density difference and (001) grains have an energetic advantage. Conversely, when the thickness of the film is lower than the critical thickness, (111) grains have an energetic advantage. Equivalently, for a given thickness, a critical strain can be defined above which (001) grains are favored by grain growth and below which (111) grains are favored. The relationship between critical strains and thicknesses is described by equation (2.31), expressing analytically the condition of equality for the magnitude of the orientation-dependent driving forces for grain growth when the film is elastically deformed.

When the thermal strain in the film is low, yielding can occur for film thicknesses lower than the critical thickness. However, even if this is the case, figure 6.9 shows that the strain energy density difference between yielded grains for low strains is nearly identical to the strain energy density difference between elastically deformed grains subjected to the same strain. Even when yielding occurs in this system, equation (2.31) accurately describes the condition of equality of the orientation-dependent driving force for grain growth. It was shown in chapter two that in some systems, the condition of equality of the orientation-dependent driving forces for grain growth could yield two critical values of the thickness for a given strain (figure 2.11). The first critical thickness corresponds to elastically accommodated strains and the second critical thickness corresponds to plastically accommodated strains. The second critical thickness arises due to the decrease of strain energy density anisotropy with increasing thickness for yielded grains. The thicker the film, the smaller the difference between the strain energy densities

of yielded (111) and (001) grains (figure 6.9). For Ag films, only the first critical thickness has to be considered and the second critical thickness is not defined. In figure 6.9 the strain energy difference curves intersect the $\Delta\gamma/h$ curve only once and not twice. The relation between strain and the second critical thickness is described analytically by equation (2.34). For Ag, the strains defined by equation (2.34) can be elastically accommodated and the second critical thickness does not exist.

The values of $\Delta\gamma$ that fit the experimental data best for Ag/SiO₂/Si and Ag/SiO₂/MgO are not identical for both systems, with $\Delta\gamma(\text{Ag/SiO}_2/\text{Si}) - \Delta\gamma(\text{Ag/SiO}_2/\text{MgO}) = 0.15 \text{ J/m}^2$. For Si substrates, the SiO₂ was thermally grown on the Si, and for MgO substrates, the SiO₂ was deposited by PECVD. The interface energy of the Ag depends on the atomic arrangement of the interface, and it is possible that interface energy anisotropy is not identical for both systems. It is however unlikely that the difference in interface energy anisotropy is of magnitude 0.15 J/m^2 . It was also found that including the densification strain was necessary to obtain a good fit to the Ag/SiO₂/Si data, but not to the Ag/SiO₂/MgO data. The parameters yielding a good fit to the Ag/SiO₂/MgO data, $\Delta\gamma = 0.3 \text{ J/m}^2$, and $\epsilon_d = \epsilon_i = 0$, fit the Ag/SiO₂/Si data well for films with small thicknesses deposited at low temperatures but not for films with large thicknesses and deposited at high temperatures. For the parameters $\Delta\gamma = 0.45 \text{ J/m}^2$ and $d_0 = 400 \text{ \AA}$, $k = 3$, and $\epsilon_i = 0$, equation (2.31) fits all but one sample. No common value for the parameter $\Delta\gamma$ and the densification strain was found to accurately fit both sets of data. Two possible origins of these discrepancies are now discussed.

Characterization of the as-deposited orientation distribution

Since no quantitative in-situ characterization technique of texture was available, all samples were characterized at room temperature in air. It was not found possible to determine the orientation distribution of as-deposited samples as a function of deposition temperature. The metrics used to characterize texture evolution and to construct the texture maps are therefore not fully quantitative. While they capture the general trends of texture evolution with deposition temperature and film thickness, the transition between (111) and (001) textures is not perfectly defined. Figure 6.8 shows that the boundaries separating the (001) and (111) texture domains on the Ag/SiO₂/MgO and Ag/SiO₂/Si texture maps could be merged if they were moved in opposite directions. If the size of the (111) texture domain on the Ag/SiO₂/MgO texture map was increased and the size of the (111) texture domain on the Ag/SiO₂/Si texture map was reduced, both texture maps could be fit by equation (2.31) with the same parameters. It is therefore possible that the imprecision on the size of the texture domains due to the characterization of the as-deposited orientation distribution is responsible for the discrepancies of the fitting parameters for Ag/SiO₂/MgO and Ag/SiO₂/Si.

Effect of impurities

Experimental procedures for film deposition aimed to minimize the impurity content of films. Due to a change in experimental setup, the pressure during deposition of the Ag/SiO₂/MgO films was greater than the pressure during deposition of the Ag/SiO₂/Si films. The difference was about 5×10^{-9} mbar. While this is a small difference, grain

growth is very sensitive to impurity segregation at the grain boundary. Gas absorption and oxidation can also influence groove formation and affect grain boundary motion. This is supported by the experimental observation that while the strength of the (111) texture in as-deposited Ag/SiO₂/MgO films was found to decrease with increasing film thickness, the strength of the (111) texture in as-deposited Ag/SiO₂/Si film was found to be independent of film thickness. Impurities can affect both the as-deposited orientation distribution and subsequent grain growth at elevated temperature, and influence the size of the texture domains on the texture maps.

Additional experiments are proposed in chapter seven that could identify the reason of the discrepancies between the fitting parameters for Ag/SiO₂/MgO and the fitting parameters for Ag/SiO₂/Si.

6.4 - Ni/SiO₂/Si

6.4.1 - Results

X-ray data acquired with the <111> Bragg reflection of Ni for Ni/SiO₂/Si films is presented on figure 6.10 for one as-deposited and two annealed films. For the Ni <111> Bragg reflection, the SiO₂/Si substrates generate a strong and wide peak centered around $\alpha = 35^\circ$. This is the reason why the x-ray data are only shown in the interval [40°-75°]. As in the case of Ag, as-deposited films are (111)-textured (figure 6.10a). Figure 6.10b shows x-ray data for a 2100 Å thick film deposited at 77°C. The film is very strongly (111)-textured. Figure 6.10c shows the x-ray data for a 3800 Å thick film deposited at

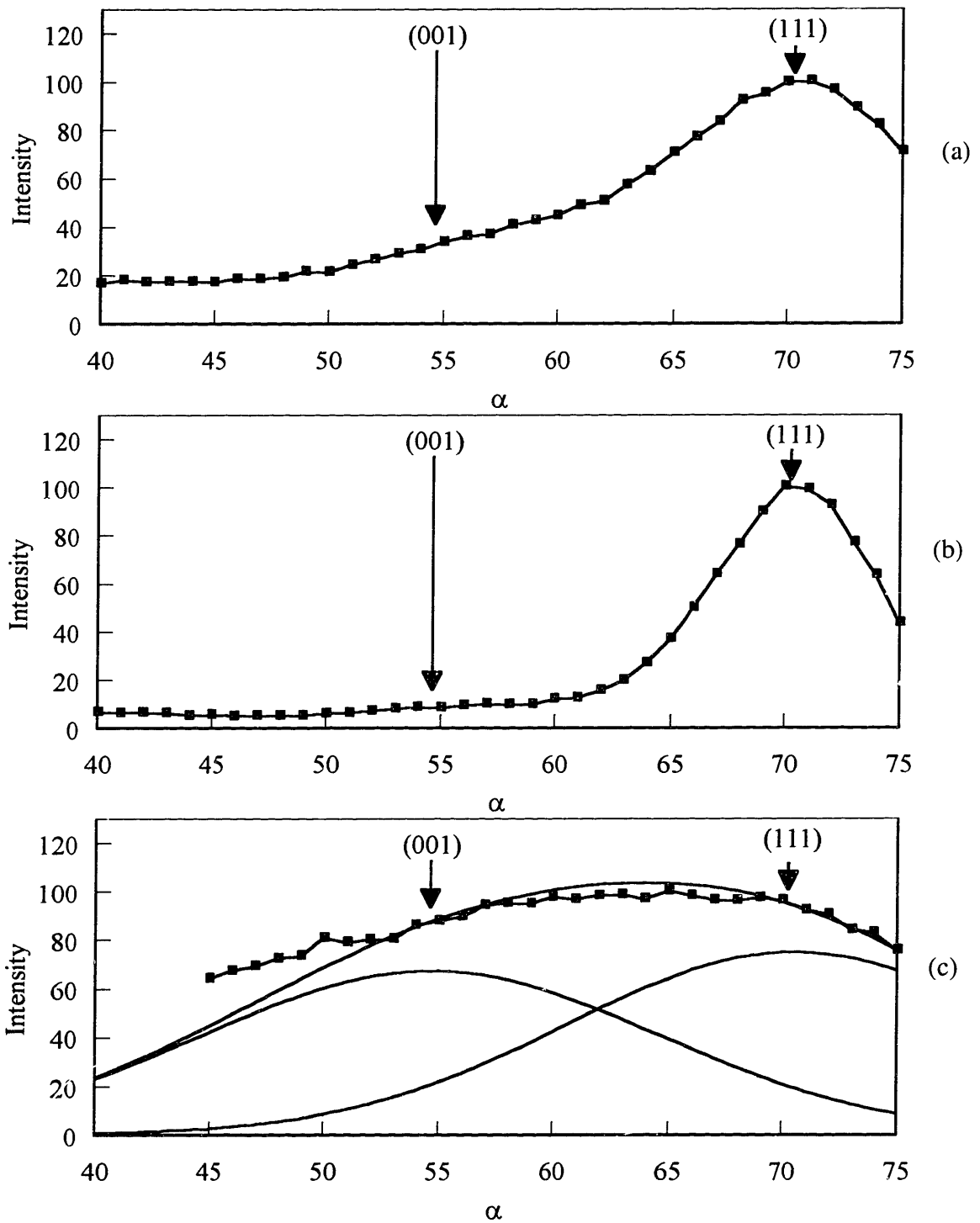


Figure 6.10: $\langle 111 \rangle$ Ni rocking curves of Ni/SiO₂/Si samples. (a) film deposited at 20°C, 2000 Å thick, as-deposited. (b) 2100 Å thick film deposited at 75°C, and annealed at 560°C for 45 min. (c) 3800 Å thick film deposited at -171°C, and annealed at 560°C for 45 min.

-171°C. As shown schematically in figure 6.10c the intensity maximum around $\alpha = 63^\circ$ can be deconvoluted as the sum of two peaks centered at $\alpha = 55^\circ$ and at $\alpha = 71^\circ$. For samples deposited at higher deposition temperatures, (001) texture appears as a shoulder of intensity at $\alpha = 55^\circ$ of the (111) peak at $\alpha = 71^\circ$. As in the case of Ag, the volume fraction of grains with (001) texture is greater at low deposition temperatures and large thicknesses than at high deposition temperatures and small thicknesses. However, for similar thicknesses and processing conditions, the volume fraction of (001)-textured grains in Ag films is generally larger than the volume fraction of (001)-textured grain in Ni films, relative to the volume fraction of (111)-textured grains.

Figure 6.11 shows TEM micrographs for one as-deposited and one annealed film. The grain size distribution in as-deposited films is clearly bimodal with large grains in a matrix of very small grains ($\approx 200 \text{ \AA}$). This constitutes evidence of grain growth or possibly recrystallization in films during and/or after deposition, and is discussed in the general context of texture maps in section 6.6. In both cases, grain boundary motion is required to generate large grains even if the deposition temperature is only 15% of the melting temperature of Ni. This is consistent with the models of microstructure formation reviewed in chapter one. In annealed films, all the small grains have disappeared, indicating coarsening of the microstructure. Figure 6.12 shows that film thickness and the average grain size in annealed films approximately verify $d = 2 h$.

Figure 6.13 shows the texture map for Ni/SiO₂/Si constructed with the ratio of intensities $I(\alpha = 55^\circ)/I(\alpha = 71^\circ)$. As for Ag/SiO₂/Si and Ag/SiO₂/MgO, the ratio was normalized with the data from as-deposited films. The texture is qualitatively similar in



(a) ——— 5000 Å



(b) ——— 5000 Å

Figure 6.11: TEM micrographs of Ni/SiO₂/Si films. (a) 600 Å thick film deposited at 20°C, as-deposited. (b) 600 Å thick film deposited at 20°C and annealed at 560°C for 45 min.

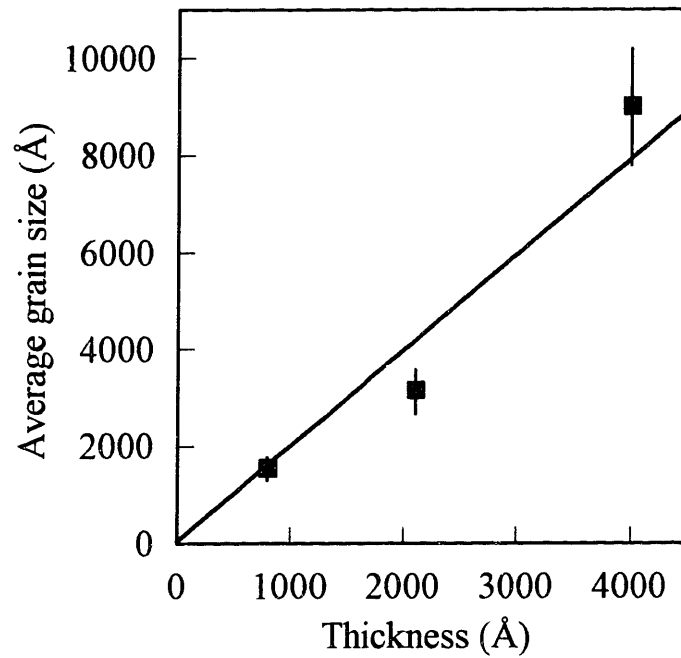


Figure 6.12: Average grain size in annealed Ni/SiO₂/Si films. 90% confidence intervals for the average grain size are also plotted.

shape to the texture maps for Ag/SiO₂/Si and Ag/SiO₂/MgO. (001) texture is favored for thick films and low deposition temperatures, and (111) texture is favored for thin films and high deposition temperatures. Equation (2.31) is also plotted in figure 6.13 for $\Delta\gamma = 0.5$ J/m², $d_0 = 250$ Å, and $k = 2$.

6.4.2 - Discussion of Ni/SiO₂/Si

Figure 6.14 shows the strain energy difference between (001) and (111) grains of Ni with the same size plotted versus the film thickness. As for Ag, the upper bound for the strain energy density of yielded grains (eq. (2.250)) was used to generate figure 6.14.

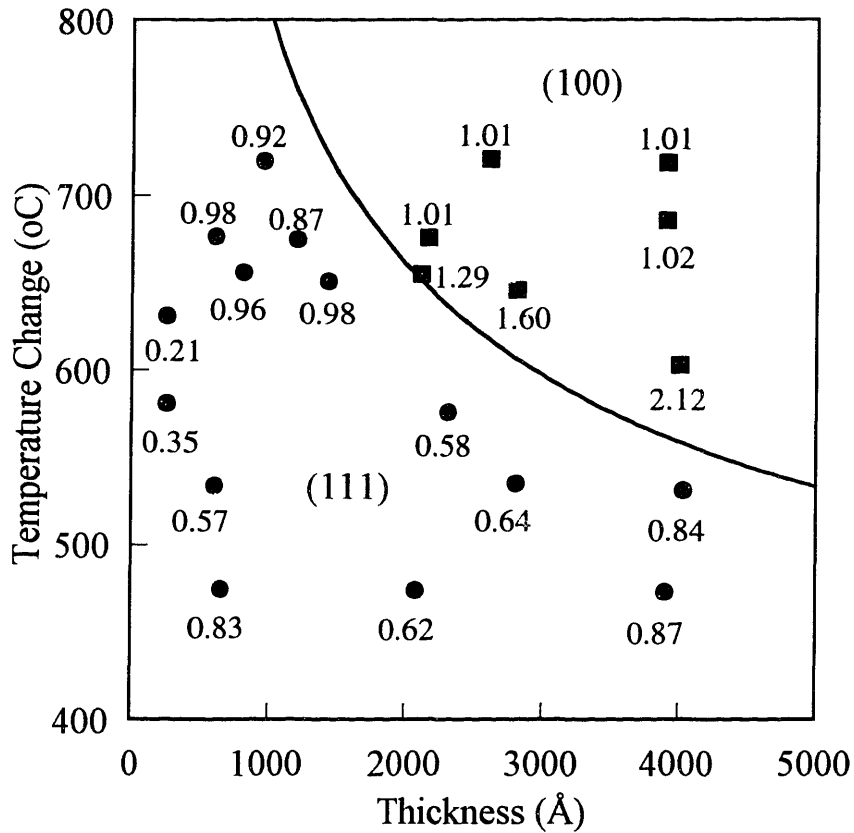


Figure 6.13: Texture map for Ni/SiO₂/Si.

In figure 6.14 it is assumed that grain size and film thickness are equal. As in the case of Ag/SiO₂/Si and Ag/SiO₂/MgO, the intersection of the two orientation-dependent driving forces for grain growth occurs for elastically deformed films, justifying plotting equation (2.31) on the texture map. The boundary defining the equality of the orientation-dependent driving forces for grain growth when all grains are yielded (eq. (2.34)) is not relevant for Ni/SiO₂/Si. In this system, the strains defined by equation (2.34) can be elastically accommodated and the boundary does not appear on the texture map. There are therefore only two texture domains on the texture map, separated by the line defined by equation (2.31).

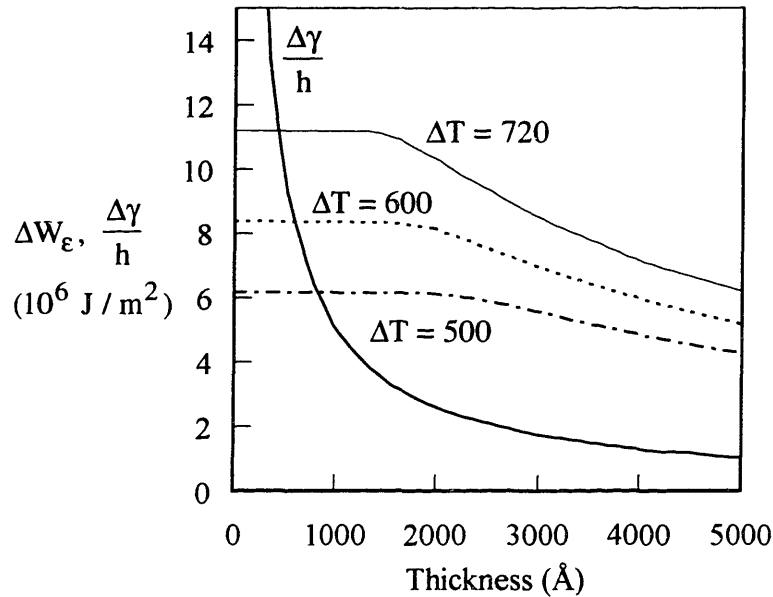


Figure 6.14: Strain energy density differences and surface and interface volumetric energy differences between (001) and (111) grains in Ni/SiO₂/Si film, plotted versus film thickness. The strain energy of yielded grains is calculated assuming $d = h$. ΔT is given in °C for $T_{gg} = 550^\circ\text{C}$.

Several of the samples shown on the texture map have normalized ratios of intensity very close to 1.0. Because of the error associated with the x-ray measurement, it is difficult to be certain whether (001) or (111) was favored during grain growth. The position of these samples on the texture map is consistent with the prediction of equation (2.31).

It was found necessary to include a densification strain to the thermal strain in order to obtain a good fit of the experimental data to equation (2.31). Alternatively, a tensile intrinsic stress could be substituted for the densification strain. Large intrinsic stresses have been measured in Ni films, as high as 3 GPa [118, 119] and make it plausible that they can have an effect on texture evolution during grain growth.

6.5 - Al/SiO₂/Si

6.5.1 - Results and discussion

Figure 6.15 shows the x-ray data acquired with the <222> Al Bragg reflection for an as-deposited and an annealed *pure* Al film. Films as-deposited are (111)-textured as shown by the intensity peak centered around $\alpha = 71^\circ$. In annealed films this peak is more intense and of decreased width than in as-deposited films, indicating that the (111) texture sharpens in the film as result of grain growth. The grain size of one as-deposited and two annealed films was measured, and the results are summarized in table 6.1, showing that substantial grain growth occurs in the films upon annealing.

Deposition Temperature (°C)	Thickness (Å)	annealed/as-deposited	# grains sampled	average grain size (Å)	90% confidence interval (Å)
25	1300	as-deposited	99	1970	1820-2130
20	2800	300°C	102	5550	4830-6270
-83	2950	300°C	100	6690	5770-7620

Table 6.1: Average grain sizes in one as-deposited and two annealed sample. 90% confidence intervals for the grain sizes are also given.

The texture map formed with the (111)/(022) intensity ratio of annealed films is plotted on figure 6.16 for $\Delta\gamma = 0.5 \text{ J/m}^2$. For any thickness and deposition temperature explored, grain growth in pure Al films favored the growth of (111)-textured grains. Figure 6.17 shows the strain energy density difference and the surface and interface energy density difference between (111)- and (011)-textured grains with the same grain diameter,

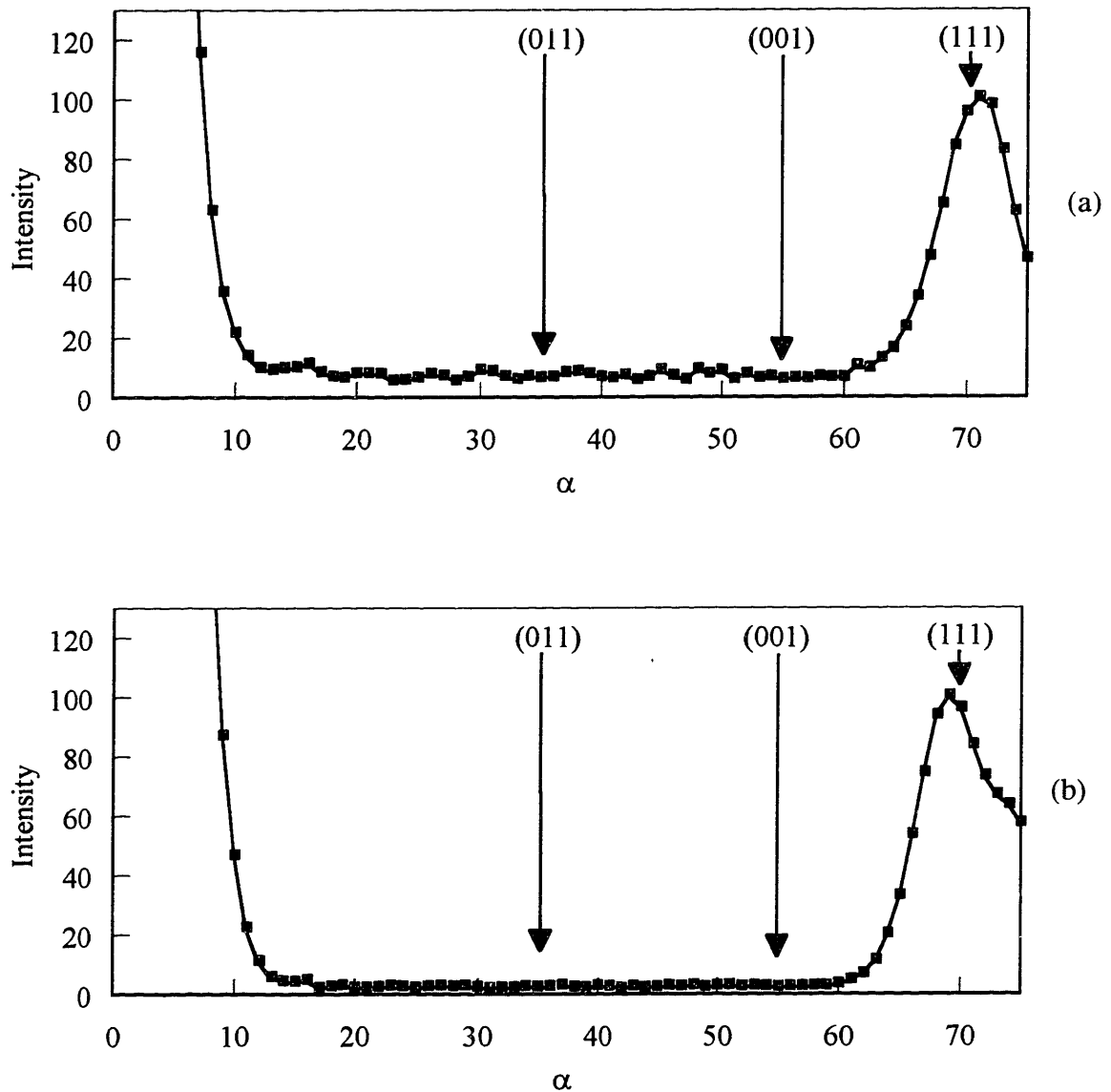


Figure 6.15: $\langle 222 \rangle$ Al rocking curves for Al/SiO₂/Si samples. (a) 6000 Å thick film deposited at 30°C. (b) 2000 Å thick film deposited at 0°C and annealed at 300°C for 1 h.

plotted versus the film thickness. The flat plateau of the strain energy density difference at low thicknesses corresponds to the elastic regime. Because Al is a nearly elastically isotropic material with an anisotropy ratio $A = 2c_{44}/(c_{11}-c_{12}) = 1.21$, strain energy density differences in the elastic regime are low. The increase and then decrease of strain energy density at greater thicknesses is the result of the anisotropy of the yield stress, as grains of

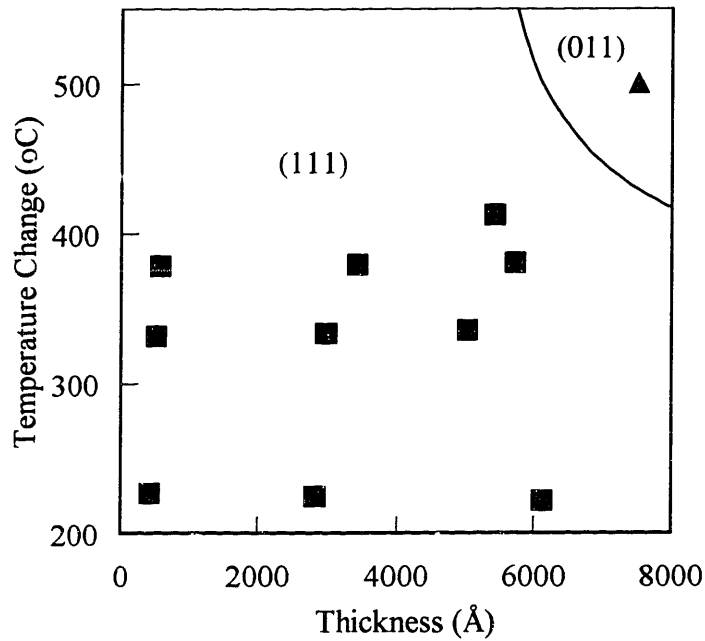


Figure 6.16: Texture map for Al/SiO₂/Si. The boundary corresponds to equation (2.32) and is plotted for $\Delta\gamma = 0.5 \text{ J/m}^2$. The squares correspond to pure Al films. The triangle corresponds to an Al-0.3%Cr-2%Cu film and is from ref. [120].

one orientation, and then both, enter the plastic regime. For the materials parameters of Al/SiO₂, surface and interface energy anisotropy is greater than strain energy density anisotropy for all thicknesses and deposition temperatures, and (111) grains are always favored by grain growth in pure Al films.

Longworth and Thompson performed grain growth experiments in Al-0.3%Cr-2%Cu films with θ phase Al₂Cu precipitates, and observed the growth of (011)-textured grains [120]. At the grain growth temperature of pure Al, around 250°C, the precipitates effectively pin the grain boundaries and little grain growth occurs in the films [121]. If the temperature is raised to 500°C, the precipitates dissolve and substantial grain growth can occur. The presence of the precipitates effectively raises the grain growth temperature in the film and increases the thermal strain at the onset of grain growth. Figure 6.17 shows that when the temperature change $T_{\text{gg}} - T_{\text{dep}}$ is 500°C, the strain energy density difference

between (011) and (111) grains is greater in magnitude than the surface and interface energy volumetric density difference, for large thicknesses. When this is the case, (011) grains are expected to grow preferentially compared to (111) grains. The textures growing preferentially in this experiment are consistent with the global minimization of the sum of surface and interface energy and strain energy density.

6.6 - Texture maps for films on amorphous substrates

Texture maps for Ag/SiO₂/MgO, Ag/SiO₂/Si, Ni/SiO₂/Si, and Al/SiO₂/Si were presented. In all cases, the films as-deposited were (111)-textured. During film formation, the surface to volume ratio is large. As (111) texture minimizes the surface and interface energy of the systems studied, the observed texture is consistent with anisotropic coarsening of the microstructure during and/or after deposition (chapter one). Evidences

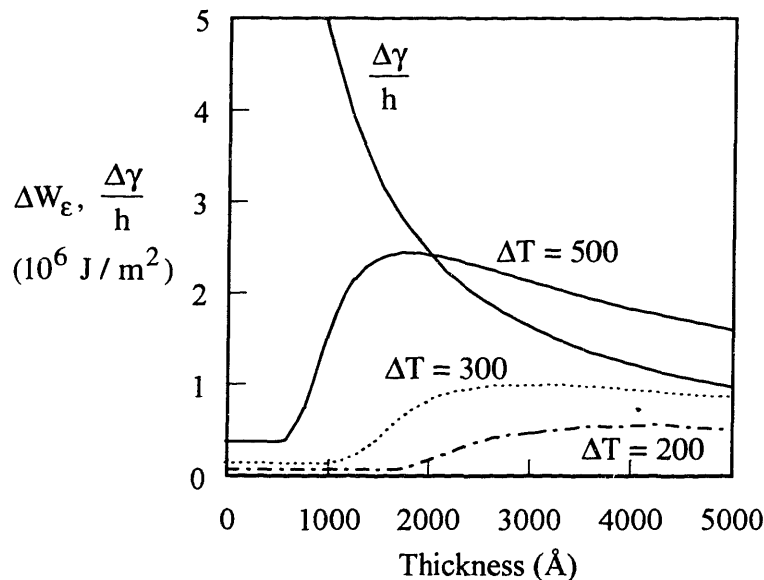


Figure 6.17: Strain energy density differences and surface and interface volumetric energy differences between (011) and (111) Al grains plotted versus film thickness. The strain energy of yielded grains is calculated assuming $d = h$. ΔT is given in °C for $T_{gg} = 250^\circ\text{C}$.

of grain boundary motion with significant temperature change were obtained for Ag/SiO₂/Si and Ni/SiO₂/Si. As presented in chapter one, there are driving forces for grain boundary motion during film deposition. It is proposed that grain boundary motion occurs during and after deposition until grooves can form at the grain boundaries and act as pinning sites. The main dominant orientation-dependent driving force during deposition is surface and interface energy anisotropy, as there is no thermal strain in the films. The (111) texture of as-deposited fcc metal film on amorphous substrates can therefore be the result of surface and interface energy driven abnormal grain growth during and/or after film formation. Subsequent anneals at elevated temperatures can induce more grain growth by increasing the mobility of the grain boundaries and increasing the strain energy density driving force for grain growth. Grain growth stagnation at elevated temperature occurs when the total driving force for grain boundary motion is too low for the grain boundaries to escape the grain boundary grooves. We have characterized orientation evolution only during the elevated temperature grain growth regime as not in-situ texture characterization tool was available. In chapter seven, we propose experiments to characterize orientation evolution during film formation and during grain growth at elevated temperature.

For elastically anisotropic materials investigated in this thesis, Ag and Ni, the orientations that grow preferentially during grain growth are (001) and (111). Because the films are (111)-textured as-deposited, the main texture after grain growth is in most cases still (111), even when (001)-textured grains have grown preferentially. In Ni/SiO₂/Si, the development of (001) texture is not as sharp as it is in Ag films. The

calculated differences in surface energy between (001) and (111) textures in Ag and Ni are $\Delta\gamma_{\text{Ag}}(111-001) = 0.09 \text{ J/m}^2$, and $\Delta\gamma_{\text{Ni}}(111-001) = 0.13 \text{ J/m}^2$ [95]. Assuming that the interface energy anisotropy scales with surface energy anisotropy, the surface and interface energy driving force for grain growth is of greater magnitude in Ni films than in Ag films, for the same processing conditions and for the same stress state. This is consistent with a more pronounced (001) texture development in Ag films than in Ni films.

For the nearly elastically isotropic material investigated in this thesis, Al, grain growth favors (111) texture in pure films, independent of the processing conditions. However, if the grain growth temperature is increased by the presence of precipitates, (011) texture can develop in the film. (011) grains have low yield stress and low strain energy density when plastically deformed. There are other orientations which have still lower yield stress and lower strain energy density than (011) (section 2.4.3). These orientations are not low index and likely have higher surface and interface energy density than (011). They also occupy a very small volume fraction in as-deposited films. Even if they grow preferentially during grain growth, they are expected to occupy a still very minor volume fraction in the film after grain growth. This can be the reason why they are never observed experimentally.

Grain growth in other fcc metal films on amorphous substrates has been studied by other authors. Vook and Witt deposited Au and Cu films on glass slides at 70 K and at room temperature [51, 52]. They characterized the orientation of as-deposited and annealed films using x-ray diffraction in the standard θ - 2θ geometry. They found that (001) texture could grow preferentially when the strain in the film was high and that (111)

texture was favored when the strain was low. They proposed that elastic strain energy density anisotropy was the reason for the growth of (001) texture but did not systematically investigate the dependence of texture evolution during grain growth upon the processing conditions of the films. Vinci et al. have investigated grain growth in Cu/Ta/Si and Cu/W/Si [70]. They also found that the (001) and (111) could grow preferentially. They also measured the strain in (001) and (111) grains in films during grain growth using x-ray diffraction and found that the when (001) grains were favored by grain growth, the elastic strain energy driving force was quantitatively consistent with equation (2.11) [121] which underlies all the analytic predictions plotted on the texture maps in this thesis, except for Al/SiO₂/Si.

When constructing the texture maps, the driving force for normal grain growth and grain growth stagnation were ignored. To a first order approximation, grain growth stagnation is independent of orientation [35], and does not promote the growth of any particular texture. However, grain growth stagnation influences the extent of the transformation. If grain growth stagnates rapidly, measuring the change in orientation distribution between the as-deposited and the stagnant microstructures is expected to be difficult. Detailed analysis of grain boundary grooving shows that stress and stress anisotropy has an effect on the shape of the groove and the kinetics of groove formation [122]. Computer simulations accounting for this effect are required to identify possible consequences on texture evolution during grain growth.

We have assumed that the reduction of grain boundary energy density does not lead to texture evolution in the film. This might not be true in all films, even if the

energies and mobilities of the grain boundaries are isotropic. If the grains with a given orientation have an average size larger than grains with other orientations in as-deposited films, these grains would grow preferentially, even in the absence of other orientation-dependent driving forces. When there are orientation-dependent driving forces for grain growth, a sub-population of grain grows preferentially, and its average grain size increases more rapidly than the average grain size of other grains. Normal grain growth can therefore provide an orientation-dependent driving force for grain growth which increases the advantage of grains already favored by the films materials properties anisotropy.

6.7 - Summary

Microstructural and texture evolution during grain growth was studied in Ag/SiO₂/Si, Ag/SiO₂/MgO, Ni/SiO₂/Si, and Al/SiO₂/Si. It was found that the model for orientation evolution during grain growth presented in chapter two could semi-quantitatively explain the observed experimental behavior. In addition, our results are consistent with those obtained by others. Grain growth in fcc metals on amorphous substrates favors either low surface and interface energy orientations or low strain energy density orientations. At low deposition temperatures and for large thicknesses, the strain energy density minimizing orientations grow preferentially and at high deposition temperatures and for small thicknesses, the surface and interface energy minimizing orientation is favored. The orientation distribution and the microstructure of as-deposited Ag/SiO₂/Si and Ni/SiO₂/Si films also indicate that grain growth can occur during and/or after deposition. Further grain growth occurs when the films are annealed at elevated temperatures.

Chapter 7

Summary and Future Work

7.1 - Summary

Model for texture development during grain growth in thin films:

A detailed analysis of the state of strain and stress in films on substrates was presented. The strain present in thin films arises from differential thermal expansion between films and substrates, from the elimination of the free volume stored in the grain boundaries during grain growth, and from intrinsic mechanisms operative during film formation. Strain energy density anisotropy in strained films arises from the anisotropy of the elastic properties of materials and from the orientation dependence of the yield stress of grains in polycrystalline films. The orientation that minimize strain energy density in elastically deformed and plastically deformed films are in general not the same. For fcc metal films subjected to a uniform and biaxial state of strain and under plane stress, (111)-textured grains maximize elastic strain energy density and (001)-textured grains minimize elastic strain energy density. The strain energy density of yielded grains, calculated from the best available experimental data for Al, and extrapolated for other materials, is maximum for (111) orientation. The strain energy density of yielded (011) grains is a local energy density minimum, close to the absolute energy density minimum. Strain energy density anisotropy provides an orientation-dependent driving force for grain growth, which favors grains with low strain energy density.

Surface and interface energy anisotropy is also an orientation dependent driving force for grain growth that favors grains with low combined surface and interface energy. For fcc metals, (111)-textured grains are in the surface energy minimizing orientation. For the materials system investigated in this thesis, (111)-textured grains are also in the interface energy minimizing orientation and surface and interface energy favors the growth of (111) texture. Grain growth minimizes the total energy of films and the orientations that grow preferentially minimize the sum of surface and interface energy and of strain energy density. When grains are yielded, strain energy density is a function of grain size and grain growth and the yield stress of grains are coupled.

Analytic predictions of texture evolution during grain growth can be made based on the equality of the orientation-dependent driving forces for grain growth. The orientation-dependent driving forces for grain growth for a pair orientations can be expressed as a function of film thickness and the strain state of the film. The condition of equality of the magnitude of these driving forces defines conditions for which neither orientation has an energetic advantage compared to the other. The strain, depending on its magnitude and on the orientation and the geometry of the grains, can be elastically or plastically accommodated in either grain. This results in general in three distinct sets of thicknesses and strains for which the orientation-dependent driving forces for grain growth are of equal magnitude. These predictions can be plotted in the thickness-strain plane. Such a plot which constitute a texture map for grain growth.

Computer simulations of strain and surface and interface energy on grain growth:

Front tracking computer simulations of grain growth in Ag/(001)Ni were presented. The computer simulations account for surface and interface energy anisotropy, strain energy density anisotropy, both in the elastic and plastic regime, and grain growth stagnation. The main result of the simulations is to validate the analytic approach of texture evolution during grain growth. The texture map constructed with the simulation results is consistent with the predictions of the analytic model. The computer simulations also show that both the detail of the microstructure and the extent of the transformation strongly depend on the magnitude of the individual driving forces for grain boundary motion and on grain growth stagnation. In particular, the interplay of plastic deformation and of the stagnation condition is complex, and can only be studied through computer simulations.

Epitaxial grain growth in Ag/(001)Ni/(001)Ag/(001)MgO:

Epitaxial grain growth experiments were carried out in polycrystalline Ag films deposited on Ni (001) single crystal films. Calculations of surface energies and of interface energies indicate that Ag grains in the (111);0° orientation have low combined surface and interface energy. Furnace bonding experiments confirm that surface and interface energy driven grain growth favors this orientation. In direct deposition experiments, the textures that develop depend on the thickness and the deposition temperature of the Ag films. At low deposition temperatures and large thicknesses, (001)-textured grains are favored. At high deposition temperatures and small thicknesses, (111)-textured grains grow preferentially. This is quantitatively consistent with both the analytic

and the computer simulations of grain growth. While the model can explain why (001) or (111) textures are favored, it does not account for the observed in-plane orientation selectivity. In-plane orientation selectivity can result from the modification of the surface and/or interface energy anisotropy of Ag/(001)Ni by defects and/or by surface and interface stresses.

Texture evolution during grain growth in films on amorphous substrates:

Texture maps for grain growth in Ag/SiO₂/MgO, Ag/SiO₂/Si, Ni/SiO₂/Si, and Al/SiO₂/Si were constructed. For elastically anisotropic materials, i.e., Ag and Ni, (001) and (111) textures can develop during grain growth. As in the case of Ag/(001)Ni, (111) texture is favored at small thicknesses and high deposition temperatures and (001) texture is favored at low deposition temperatures and large thicknesses, consistent with the analytic model. It was not found possible to fit both the Ag/SiO₂/MgO data and the Ag/SiO₂/Si data to the analytic model with a common set of fitting parameters. This discrepancy can be due to differences in the Ag/SiO₂ interface energy between these two systems. It can also result from imprecisions of the metrics used to characterize texture evolution during grain growth, or from the influence of impurities on grain growth. In addition to grain growth at elevated temperature, evidences of athermal grain growth during or after deposition were identified in Ag/SiO₂/Si and Ni/SiO₂/Si. Grain growth at low temperatures can occur before thermal grooves pin the grain boundaries. Subsequent grain growth requires enough thermal energy for the grain boundary to escape the grain boundary grooves.

For pure Al/SiO₂/Si films the texture that develops during grain growth is (111), independent of the processing conditions of the films. This is due to the near elastic isotropy of Al which induces only small differences in strain energy density between elastically deformed (001) and (111) grains. In Al films with precipitates, the grain growth temperature is raised and the thermal strain in the film at the onset of grain growth is sufficient to induce plastic deformation of the grains. Under these conditions, (011) grains can grow at the expense of (111) grains, due to the anisotropy of the yield stress. This system demonstrates the possibility of texture control through changes in the grain growth temperature as well as in the deposition temperature.

Texture maps for elastically anisotropic films

For all the film/substrate combinations investigated in this thesis, except Al/SiO₂/Si, orientation evolution during grain growth is accurately described by considering elastic strain energy density anisotropy and surface and interface energy anisotropy. For these systems, yielding does not significantly modify the texture map although it does likely affect the extent of the transformation. The equality of the orientation-dependent driving forces for grain growth when the strain is elastically accommodated (eq. (2.31)) can be written using adimensional parameters:

$$\varepsilon_{\text{tot}} = \frac{1}{\sqrt{g}} \quad (7.1)$$

where ε_{tot} is the sum of the thermal, intrinsic and densification strains, and where g is defined as

$$g = \frac{M_{111} - M_{001}}{\Delta\gamma} h \quad (7.2)$$

Using the experimental data, and the fit of equation (2.31) to each of the individual texture maps, equations (2.2) and (7.2) can be used to generate an universal texture map. The (001) and (111) domain on the universal texture map are separated by the line defined by equation (7.1). The universal texture map, generate with the data on Ag/(001)Ni/(001)Ag/(001)MgO, Ag/SiO₂/MgO, Ag/SiO₂/Si, and Ni/SiO₂/Si is shown in figure 7.1. Figure 7.1 qualitatively illustrates the dependence of orientation evolution during grain growth upon the processing conditions of films.

7.2 - Future work

Both the epitaxial grain growth experiments and the grain growth experiments in films on amorphous substrates leave unanswered questions, and thus many additional experiments can be undertaken.

Additional work on Ag/(001)Ni

High resolution transmission electron microscopy should be performed on both plane view and cross-sectional samples. High resolution microscopy would provide information on the structure of the Ag/Ni interface. The density of dislocations and of ledges at the Ag/Ni interface could be measured and compared to the model of the yield stress. It would also reveal if the Ag/Ni interface is faceted, which could have consequences on in-plane orientation selection and on tilt. In addition to microscopy, the Ag/Ni interface needs to be studied computationally. Computer modeling of the influence of defects on surface and interface energy anisotropy is needed. Computer modeling can also be used to study the influence of surface and interfaces stresses on surface and interface energy anisotropy. Both microscopy and computer modeling should provide

information on the mechanisms for in-plane orientation selectivity and tilt of the (001)-textured Ag.

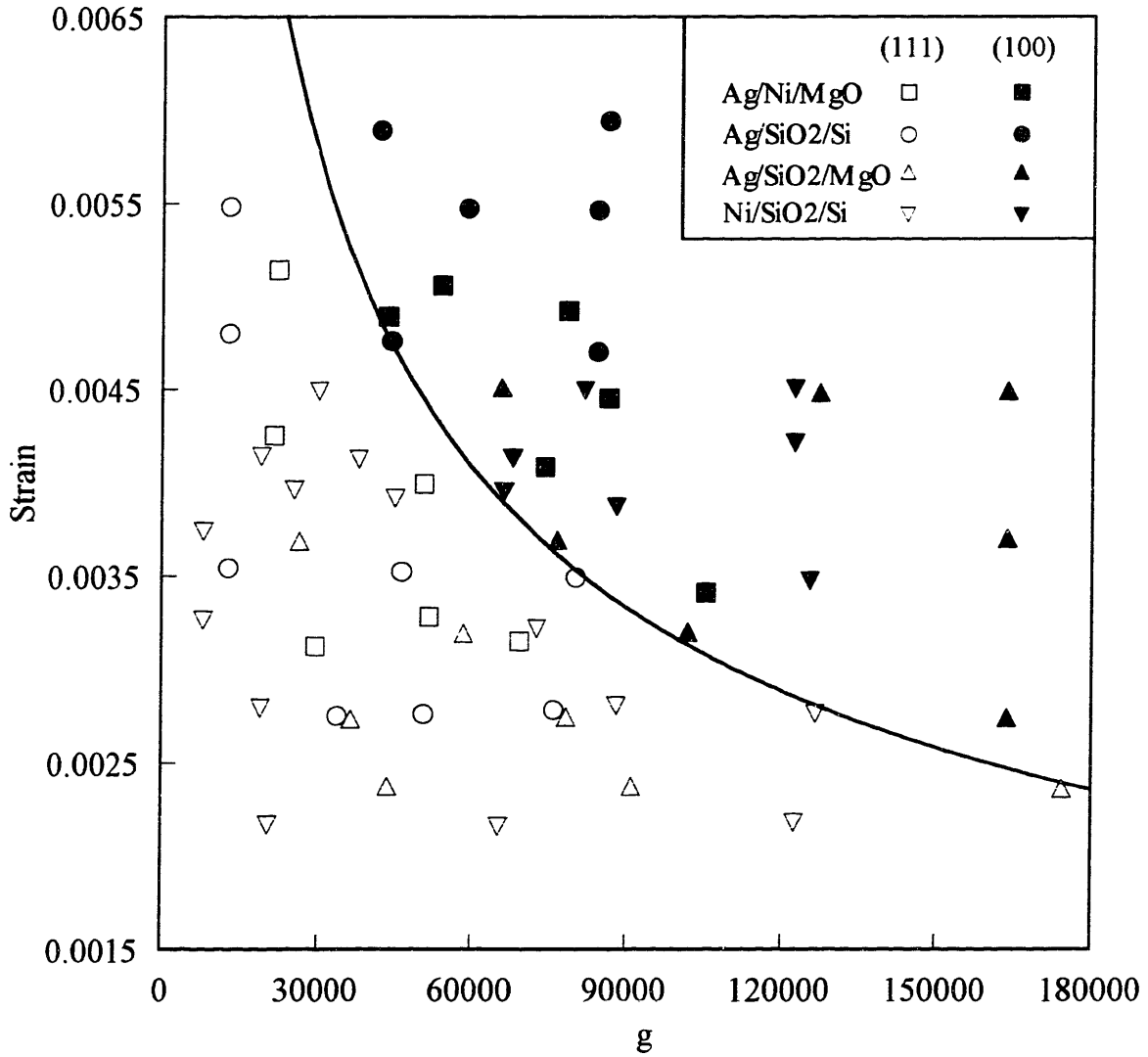


Figure 7.1: Texture map for Ag/(001)Ni/(001)Ag/(001)MgO, Ag/SiO₂/MgO, Ag/SiO₂/Si, and Ni/SiO₂/Si. The total strain (ϵ) is the sum of the thermal (ϵ_{th}), the intrinsic (ϵ_i), and the densification (ϵ_d) strains. The adimensional parameter g is defined as $g = \Delta\gamma h / (M_{111} - M_{001})$.

Other epitaxial systems can be investigated. The interface energy of (001)Ag|(001)Cu has been calculated as a function of twist misorientation and exhibits a minimum at $\beta = 26.6^\circ$. It would be interesting to perform direct deposition and bonding grain growth experiments on this system to look for this orientation. However, the miscibility of Ag and Cu would require to adequately control the thermal history of the film to avoid interdiffusion.

Additional work on films on amorphous substrates

Repeating Longworth and Thompson [120] experiments in Al-0.3%Cr-2%Cu and varying thickness and deposition temperature would allow to test the analytic model when yielding is important (equation 2.33). It would also be interesting to characterize texture evolution during grain growth in very thick films ($> 1 \mu\text{m}$) deposited at low temperatures to determine if strain energy density anisotropy or surface energy anisotropy dominates under these conditions. If surface and interface energy anisotropy dominates, there is a window of thicknesses for which strain energy density anisotropy determines which orientation grows preferentially. Outside that window, surface and interface energy anisotropy drives the growth of (111) grains (figure 2.11). This could be tested for Al-0.3%Cr-2%Cu films.

Thermally oxidized Si wafers could be coated with PECVD SiO_2 and used to generate a texture map for Ag. This would indicate whether the differences between Ag/ SiO_2 /Si and Ag/ SiO_2 /MgO described in chapter six are due to differences in the Ag/ SiO_2 interface energy. PECVD SiO_2 can be deposited on any substrate. Providing that the adhesion of the SiO_2 to the substrate is good and that the SiO_2 is smooth, texture

map of Ag/SiO₂/substrate can be generated for many substrates. Substrates for which the maximum thermal strain is large (e.g., NaCl) and for which the maximum thermal strain is small (e.g., Ni foil) could be used to further investigate the orientation evolution during grain growth in Ag/SiO₂.

Strain can be applied ex-situ the deposition system in a bending jig. Four point and three point bending jigs can be used to apply either tensile or compressive uniaxial strains of the same order of magnitude than thermal strains in Ag/SiO₂/Si films. The strained samples can then be annealed in a reducing ambient to induce grain growth. This would allow to partially control the strain and stress in the films during grain growth and would provide another test of the analytic model. As the applied strain is uniaxial, microscopy could show preferential grain elongation along the direction of the applied strain which would provide additional information on the influence of strain and stress on grain growth.

The yield stress of thin films needs to be better characterized. Of particular interest are the grain size, the film thickness, and the orientation dependence of the yield stress. Time-temperature dependent relaxation also needs to be considered. Venkatraman and Bravman experiment [78] could be repeated for other systems than Al, for example Ag. The orientation-dependence of the yield stress can be measured using hot stage x-ray diffraction on grains with a specific orientation [121]. The same technique can be used to monitor strain and stress in grains with different orientations during grain growth [121].

The substrate curvature and therefore the stress in films undergoing grain growth could be monitored in-situ or ex-situ the deposition system by measuring the deflection of

a laser by the surface of the film. This would provide information on stress relaxation during grain growth and on the yield stress of thin films.

In-situ characterization of stress, microstructure, and of orientation evolution

The ideal characterization of grain growth in thin films would allow for separate measurement of stress, strain and orientation distribution as grain growth proceeds. Strain and orientation distribution can be measured with x-ray diffraction and stress can be obtained by measuring substrates curvature. There are UHV deposition systems with a x-ray source and a curvature measurement setup. A fully in-situ study of grain growth would allow for a precise characterization of the as-deposited orientation distribution in films and of the intrinsic stress. Both the athermal and the high temperature grain growth regimes could be studied. There also are transmission electron microscopes with UHV deposition capabilities. Film formation and microstructural evolution, both at low and high temperature could be characterized. These two experiments would provide all the information needed to further test the influence of the surface and interface energy driving force and of the strain energy density driving force on grain growth and could result in a fully quantitative model of grain growth in high mobility metal films. The model, along with grain growth experiments could then be used to measure materials property of thin films, for example $\Delta\gamma$.

-

Appendix I

Grain growth as a densification process: influence of surface and interface energy anisotropy and strain energy density anisotropy

In this appendix, we show how surface and interface energy anisotropy and strain energy density anisotropy can be included in the analysis of grain growth as a densification process. For simplicity, we consider that the film is entirely constituted of grains with only two orientations. Grains with orientation 1 have combined surface and interface energy γ_1 , and biaxial modulus M_1 . Grains with orientation 2 have combined surface and interface energy γ_2 , and biaxial modulus M_2 . At time $t = 0$, the as-deposited structure consists of n_0 grains with average radius r_0 , $n_{1,0}$ of which have orientation 1 and average grain radius $r_{1,0}$, and $n_{2,0}$ of which have the orientation 2 and average grain radius $r_{2,0}$. These quantities are related by:

$$n_0 = n_{0,1} + n_{0,2} \quad , \quad (I.1)$$

$$n_0 r_0^2 = n_{1,0} r_{1,0}^2 + n_{2,0} r_{2,0}^2 \quad , \quad (I.2)$$

which express the fact that there are only two orientations present in the film. We assume for simplicity that the two subpopulations of grains are equally populated and that all grains have the same size at time $t = 0$, i.e., $n_{0,1} = n_{0,2}$ and $r_{0,1} = r_{0,2}$. At time t , the total number of grains, the average grain size in the film, the number of grains with orientation

1 and their average grain size, and the number of grains with orientation 2 and their average grain size are respectively: n_t , r_t , $n_{1,t}$, $r_{1,t}$, $n_{2,t}$, $r_{2,t}$, and the relations between these quantities are

$$n_t = n_{t,1} + n_{t,2} \quad , \quad (I.3)$$

$$n_t r_t^2 = n_{1,t} r_{1,t}^2 + n_{2,t} r_{2,t}^2 \quad . \quad (I.4)$$

The change in area fraction of grains with orientations 1 and 2 induces a change in the surface and interface energy density per unit volume of the film:

$$W_s = \frac{1}{h} \left[\gamma_1 \frac{n_{1,t} r_{1,t}^2}{n_t r_t^2} + \gamma_2 \frac{n_{2,t} r_{2,t}^2}{n_t r_t^2} - \left(\gamma_1 \frac{n_{1,0} r_{1,0}^2}{n_0 r_0^2} + \gamma_2 \frac{n_{2,0} r_{2,0}^2}{n_0 r_0^2} \right) \right] \quad . \quad (I.5)$$

If the number of grains with orientations 1 and 2 is the same at time $t = 0$, the change in surface and interface energy density per unit volume is

$$W_s = \frac{\Delta\gamma}{h} \left[\frac{1}{2} - \frac{n_{2,t}}{n_{1,t} + n_{2,t}} \frac{r_{2,t}^2}{r_t^2} \right] \quad , \quad (I.6)$$

where $\Delta\gamma = \gamma_1 - \gamma_2$ is the difference in combined surface and interface energy between the two types of grains. If we assume that the grains with orientation 1 are growing at the expense of grains with orientation 2, i.e., $\gamma_1 < \gamma_2$, it is a good approximation at early times, when the orientation distribution and the average grain size have not radically changed, to assume that $r_{2,t} \cong r_0$ and that $n_{1,t} \cong n_0$. Equation (I.6) then becomes

$$W_s = \frac{\Delta\gamma}{h} \left(1 - \frac{r_0^2}{r_t^2} \right) \quad . \quad (I.7)$$

Equation (I.7) represents the change in free surface and interface energy in the film resulting from grains with surface and interface energy γ_1 growing at the expense of grains

with surface and interface energy γ_2 , and is strictly valid only when little grain growth has occurred in the film. From time $t = 0$ to time t , the average grain size in the film increases from r_0 to r_t , and the total strain in the film is the sum of the densification strain resulting from the elimination of free volume and of the intrinsic as-deposited strain:

$$\varepsilon_t = \frac{\Delta a}{2} \left(\frac{1}{r_0} - \frac{1}{r_t} \right) + \varepsilon_0 \quad , \quad (\text{I.8})$$

where ε_0 is the intrinsic as-deposited strain. We assume that the strain is uniformly distributed over the film and that the film is elastically deformed. Under these assumptions, the change in strain energy density from time $t = 0$ to time t due to the increase in strain and to the anisotropy of the biaxial modulus is

$$W_\varepsilon = \varepsilon_t^2 \left(M_1 \frac{n_{1,t} r_{1,t}^2}{n_t r_t^2} + M_2 \frac{n_{2,t} r_{2,t}^2}{n_t r_t^2} \right) - \varepsilon_0^2 \frac{M_1 + M_2}{2} \quad . \quad (\text{I.9})$$

At early times, when the orientation distribution and the average grain size in the film have not changed too much, i.e., when $r_{2,t} \cong r_0$ and $n_{1,t} \cong n_0$, the strain energy density change from time $t = 0$ to time t is

$$W_\varepsilon = \varepsilon_t^2 \left[M_1 + (M_2 - M_1) \left(\frac{r_0^2}{r_t^2} - \frac{1}{2} \right) \right] - \varepsilon_0^2 \frac{M_1 + M_2}{2} \quad . \quad (\text{I.10})$$

The total energy change in the film is the sum of the change in grain boundary energy, surface and interface energy and strain energy density energy:

$$W_{\text{tot}} = W_{\text{gb}} + W_s + W_\varepsilon \quad , \quad (\text{I.11})$$

where W_{gb} is given by equation (1.18).

Figure I.1 compares the total energy change in the film as a function of grain size for both the isotropic case (equation (1.23)) and the simplified anisotropic case considered here (equation I.11). The materials properties chosen to generate Figure I.1 are typical of a FCC metal film. The difference in total energy between the isotropic and anisotropic case is significant. The values of d_{stag} and d_0^{crit} derived from W_{tot} also deviate significantly from the values given by equations (1.24) and (1.25) when anisotropy is taken into account. The equivalent of equations (1.24) and (1.25) can be derived from equation (I.11), but can not in general be put in closed form and have to be solved numerically. While this can readily be done, it is important to note that the general trends described in chapter one for the isotropic case are still valid and that the same general conclusions apply. The same factors that promote or impede grain growth in the isotropic case still do so when anisotropy is considered. For anisotropic films, two additional variables, $\Delta\gamma$ and M_1-M_2 , and their effect on d_{stag} and d_0^{crit} can be considered. This would be achieved by expressing d_{stag} and d_0^{crit} as a function of $\Delta\gamma$ and of M_2-M_1 but will not be pursued further here.

Equations (I.7) and (I.10) are only strictly valid at early times, in the particular case when the two populations of grains are equally populated and statistically identical in the as-deposited structure. In most real films, there are more than two orientations present as-deposited and there often are preferred orientations that develop during deposition as presented in chapter one. In that case, assuming that the two subpopulations of grains are identical at time $t = 0$ is not realistic. This limits the applicability of the

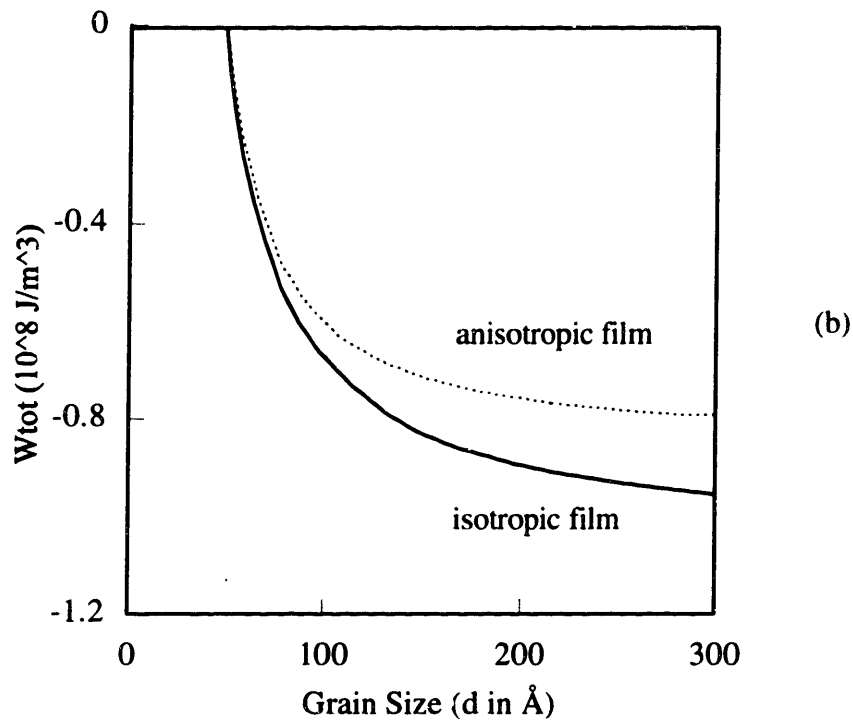
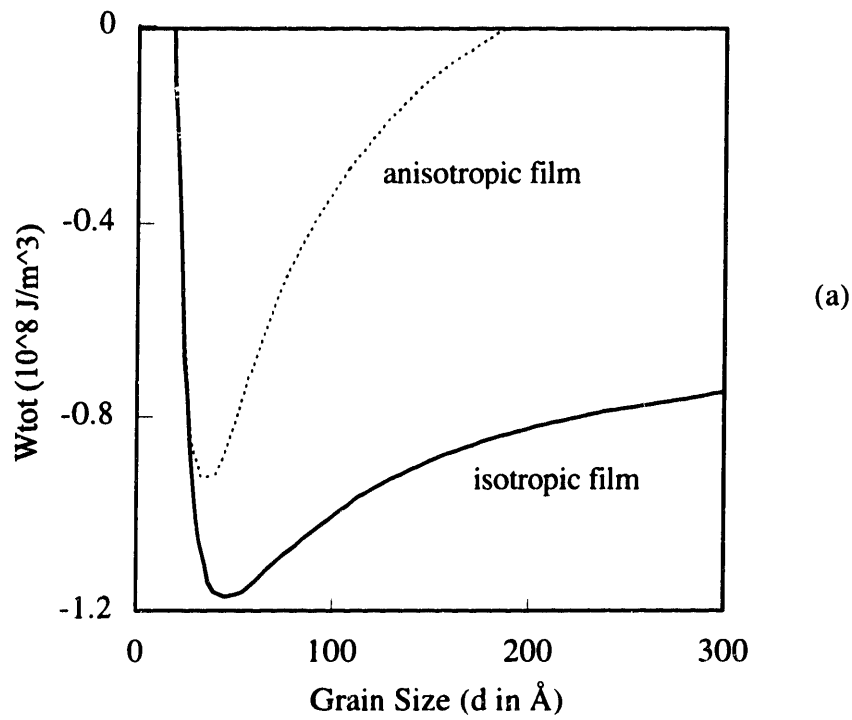


Figure I.1: Effect of the anisotropy of surface and interface energy on the total energy of the film. (a) $d_0 = 20 \text{ \AA}$, (b) $d_0 = 50 \text{ \AA}$. The materials parameter chosen are $\gamma_{gb} = 0.2 \text{ J/m}^2$, $M = E/(1-\nu) = 137 \text{ GPa}$, $\Delta a = 1 \text{ \AA}$, $\Delta\gamma = 0.5 \text{ J/m}^2$, $h = 1000 \text{ \AA}$, $M_1 = 157 \text{ GPa}$, $M_2 = 117 \text{ GPa}$.

approach presented in this appendix to incorporate in full generality the effect of surface and interface energy anisotropy and strain energy density anisotropy in the analysis of grain growth as a densification process. There is no analytic model describing the kinetics of grain growth in anisotropic systems and it is necessary to make the assumptions that $r_{2,t} \cong r_0$ and that $n_{1,t} \cong n_0$ in order to obtain explicitly the total energy of the film as a function of time. This limits the applicability of equations (I.7) and (I.10) to the early times of the transformation, when little grain growth has occurred. A more detailed and rigorous approach with wider applicability would be to use computer simulations of grain growth and to take into account the effect of the anisotropies for each grain and each grain boundary. Alternatively a kinetic model for grain growth in anisotropic systems would allow to obtain equivalents of equations (I.7) and (I.10) to calculate the total energy of the film as a function of time.

Appendix II

Plane stress condition in elastically anisotropic films

II.1 - Finite element simulation

We concentrate on polycrystalline thin films subjected to a uniform biaxial strain, imposed by differential thermal expansion between the film and the substrate. We neglect intrinsic stresses, epitaxial stresses, and densification stresses. In an ideally elastically isotropic thin film on a substrate, the stress resulting from a uniform biaxial strain verifies plane stress conditions, i.e., $\sigma_{12} = \sigma_{13} = \sigma_{23} = \sigma_{33} = 0$, where the underlying coordinate system is detailed in section 2.2. This is the case everywhere in the film, except close to the edges of the film where both the state of strain and the state of stress are triaxial [64]. We will ignore edge effects as they decay rapidly with increasing distance from the edges of the film, and as they have negligible effects on the overall strain energy density in the film [15]. If the film is elastically anisotropic and polycrystalline, assuming that the film is under plane stress is an approximation. The object of this appendix is to analyze the state of strain and stress of elastically anisotropic polycrystalline thin films and to get an estimate of the elastic strain energy density of grains subjected to these state of strain and stress.

II.1.1 - Spring analogy

In an elastically anisotropy thin film, neighboring grains with different textures do not have the same elastic properties and there is a discontinuity of the biaxial modulus at the grain boundary. If a uniform biaxial strain is externally imposed on the two grains, the equilibrium strain in the film is no longer uniform biaxial but rather triaxial and position-dependent. The equilibrium state of stress in the film does not verify plane stress conditions, and is also position-dependent. Before presenting a finite element analysis of this problem, we make a simple analogy with springs of different strengths. Figure II.1a shows two connected springs with the same length but different spring constants $k_1 > k_2$. Initially, no force is applied on the springs and the system is in equilibrium. In Figure II.1b, the two springs are both stretch by the same amount Δx while the middle point M is maintained in the same position than in Figure II.1a. This situation is the analog of a uniform biaxial strain for a thin film. Since the two springs have different strengths, there is a net force applied at point M, $F_M = (k_2 - k_1) \Delta x$. If the point M is freed, the system reaches an equilibrium position where M has moved toward the side of the spring with the lowest spring constant as illustrated in Figure II.1c. In the configuration II.b each spring has a potential energy $W_i = k_i (\Delta x)^2 / 2$ and the total energy of the system is $W = (k_1 + k_2) (\Delta x)^2 / 2$. In configuration II.1c, the total energy of the system is $W = 2 (\Delta x)^2 k_1 k_2 / (k_1 + k_2)^2$ which lower than the energy of the system in configuration Ii.1.b by $\Delta W = (k_1 - k_2)^2 / 2(k_1 + k_2)$. Note that in configuration II.1.c the energy of each spring can not be expressed only as a function of Δx and k_i but also depends on the spring constant of the other spring k_j .

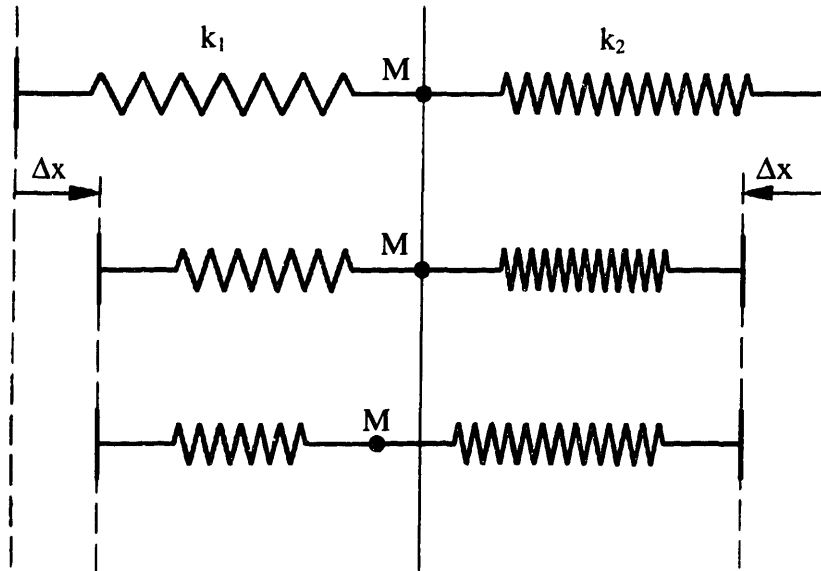


Figure II.1: Spring analogy of neighboring grains with different orientations in an elastically anisotropic film.

For a film under uniform biaxial strain and plane stress conditions, the energy density of a grain is $W = M\epsilon^2$ which depends on the biaxial modulus of the grain and on the strain but does not depend on the orientation and moduli of the neighboring grains. The strain energy density of each grain is decoupled from the strain energy density of the other grains in the film. Because of elastic anisotropy however, the real strain, stress and strain energy density in each grain depend on the other grains in the film and the elastic problem for one grain can not be decoupled from the elastic problem for all the other grains in the film. In an elastically anisotropic film subjected to a biaxial thermal strain, grains with high modulus tend to compress grains with lower modulus and the strain is not uniformly biaxial. In fact, both the strain and the stress are triaxial and non-uniform as shown by the finite element simulation.

II.1.2 - Finite element simulation

In order to estimate the change in strain energy density of elastically deformed grains in an elastically anisotropic film, a simple finite element simulation was performed using Abaqus 5.2. Figure II.2 shows the geometry of the grains in the simulation. The film consists of an infinite array of alternating (001)- and (111)-textured grains in the shape of right square cylinders with thickness h . Because of the symmetry of this grain structure, it is sufficient to simulate only one-half of a (001) grain and one-half of a (111) grain as shown in Figure II.2. The grains are discretized using parallelepiped elements with eight integration points, one at each corner of the parallelepiped, corresponding to Abaqus element type C3D8. The total number of elements used in one simulation was 1000 and the aspect ratio of the width to the thickness of the elements was kept below 2.0 to avoid integration errors. The number of elements across the surface of the grains and through the thickness of the grains was therefore varied as the grain diameter to film thickness ratio was varied. Periodic boundary conditions were imposed on the sides of the half grains and the nodes at bottom of the film were pinned to simulate the effect of a substrate. The thermal expansion of the elements was set to be $\alpha = 9 \times 10^{-6} \text{ K}^{-1}$ to simulate differential thermal expansion between the film and the substrate. The elastic properties of the elements were those of (001)- and (111)-textured Ag. The loading condition was to set a temperature change of 100°C in the structure, holding the bottom nodes in place. A typical Abaqus input stack is shown at the end of this Appendix. Abaqus calculated the energy minimizing positions of the nodes of the structure in one static step.

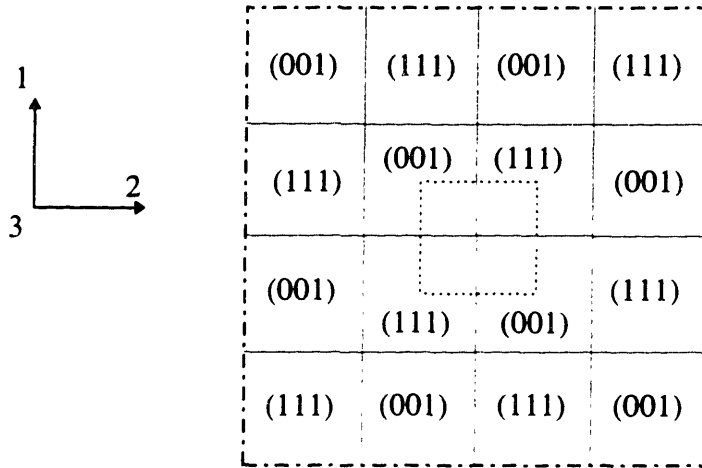


Figure II.2: The simulated grain structure consists of an infinite square array of alternating (001)- and (111)-textured grains. It is sufficient to discretize one-half of a (001) grain and one half of a (111) grain to simulate this grain structure as shown by the dashed square.

Figure II.3 shows the displacements of the nodes at a cross-section through the middle of each grain, along one side of the element structure. Because it has a higher modulus, the (111) grain has expanded along the x (and equivalently y) direction, compressing the (001) grain. For the same reason, the initially flat surface of the two grains is not flat at equilibrium as the surface of the (111) grain is below the surface of the (001) grain. Figure II.4 shows contour plots of the 11 and 33 components of the strain and the stress. Contour plots for the 12, 13, 22, and 23 components of the strain and stress are similar. Because of the discontinuity of the elastic properties at the grain boundary, high strains and stresses develop locally to the grain boundary. The state of strain and stress are both triaxial and vary across each grain. The strain energy density of each element was extracted from the Abaqus output and the strain energy density of each grain was calculated. Simulations with different aspect ratio of the grain diameter d to the

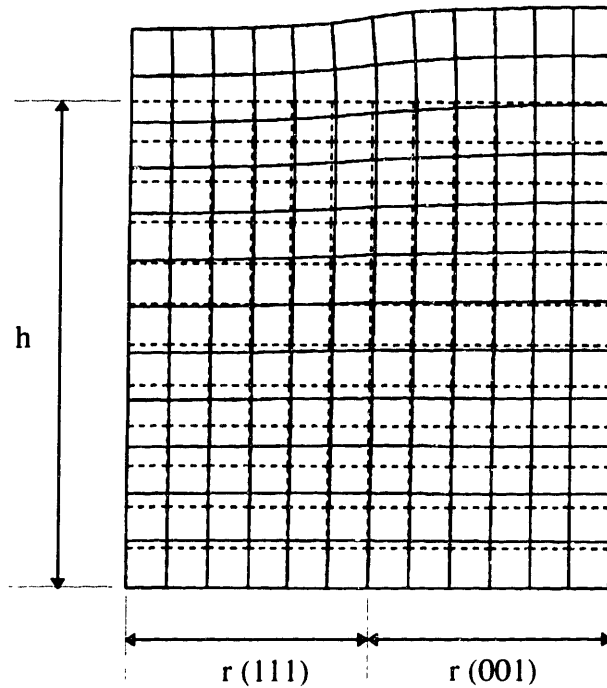


Figure II.3: Initial and relaxed position for a structure where the film thickness and grain diameter are equal ($2r = d = h$). The displacement are multiplied by a factor of 10.

grain thickness h were performed and the strain energy density of the (001)- and the (111)-textured grains are plotted in Figure II.5 as a function of the aspect ratio d/h . The strain energy densities for both (001) and (111) grains have been normalized by the strain energy density of grains with the same orientation under uniform biaxial strain and plane stress conditions. The normalized energy $W = 1.00$ represents the idealized case when $W = M_{hkl}\epsilon^2$. The strain energy density of (001) grains is higher than in the ideal case as the soft (001) grains are squeezed by the harder (111) grains and have an increased strain energy density. Conversely, the harder (111) grains decrease their strain energy density by expanding and have a lower strain energy density than in the ideal case. This situation is

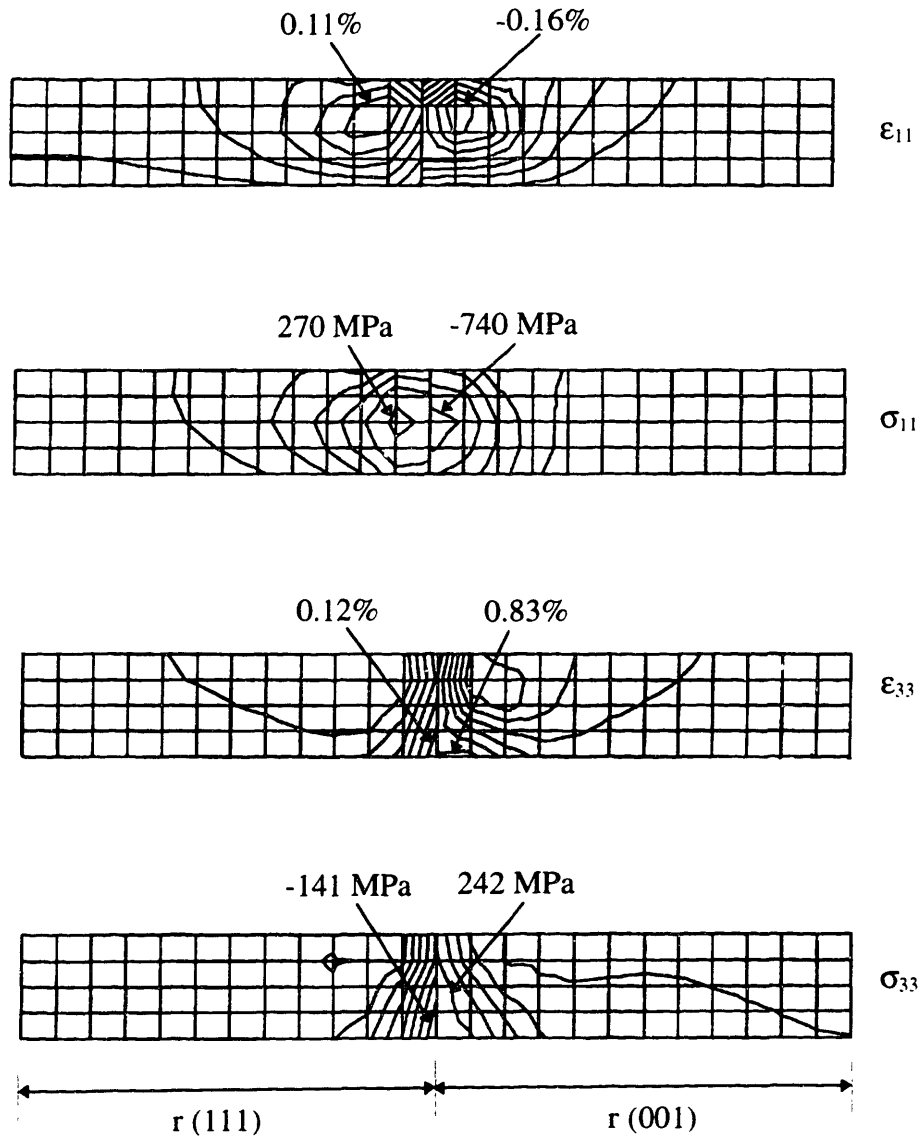


Figure II.4: Contour plot of ϵ_{11} , ϵ_{33} , σ_{11} , σ_{33} for a relaxed film with $d = 8 h$. The other components of the stress and strain are also non-uniform with strong gradients near the grain boundary.

analogous to the case of the two springs where the spring with the larger constant compresses the softer spring. It is expected that for very large aspect ratio d/h , the strain energy densities of (001) and (111) grains converge toward the ideal case as the influence of the grain boundary decays with increasing distance. However, the finite element simulation suggests that this convergence is slow, and for aspect ratio d/h of 10 the difference between the ideal case and the simulation is still substantial.

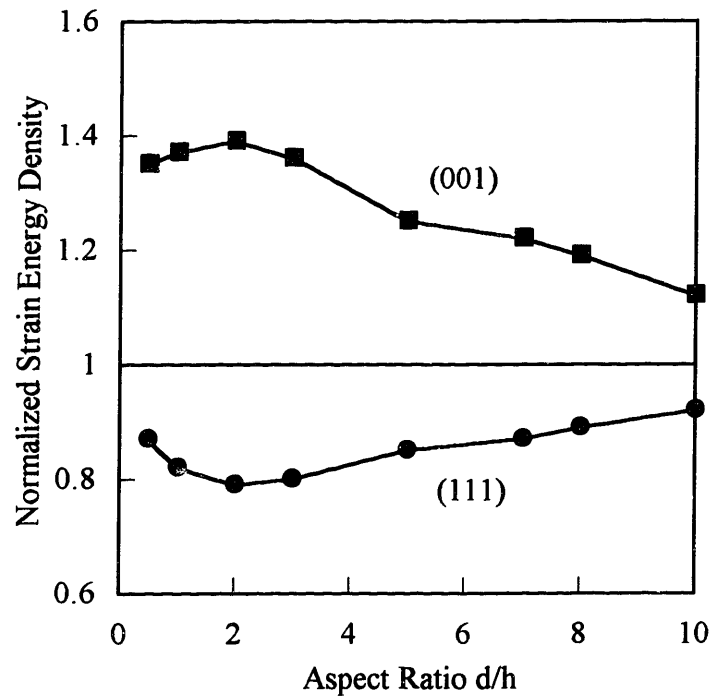


Figure II.4: Strain energy density of (001) and (111) grains as calculated by Abaqus, normalized by the strain energy density of grains in the same orientation and under uniform biaxial strain and plane stress, plotted versus the aspect ratio of the grain diameter to the film thickness.

The finite element simulation probably overestimates the effect of elastic anisotropy on the strain energy density of grains in the films. Grains in real films do not have square shapes and only three and not four grains meet at triple junctions. The strain energy density perturbation due to the triple/quadruple junctions in our simulations is probably higher than produced by real triple junctions. Considering only the orientations that minimize and maximize the biaxial modulus, i.e., (001) and (111), also enhances the effect. In real films, more than two orientations are present and not all (001) grains are neighboring (111) grains, and vice versa. Finally, it is likely that some relaxation of the large stresses and strains calculated by Abaqus would occur locally to the grain boundary in real films, diminishing the excursion of the strain energy density away from the ideal biaxial and plane stress case.

In order to keep the models of texture development during grain growth presented in chapter two simple, the influence of the anisotropy of the elastic properties of films on the strain energy density of grains is not taken into account. If it were taken into account it would result in a decrease in the strain energy density difference between (001) and (111) grains, compared with the uniformly biaxial and plane stress case. The driving force for grain growth arising from elastic strain energy anisotropy would therefore be diminished. Other simplifications used for developing grain growth models in chapter two, such as those underlying the derivation of the magnitude of the yield stress of polycrystalline films, are probably more stringent than the effect treated in this appendix and justify ignoring it.

II.2 - Abaqus stack

The following listing shows a typical Abaqus stack used to simulate the effect of elastic anisotropy on the strain energy density of (001) and (111) grains. As Abaqus requires lengthy element sets and element nodes definitions, the listing of elements and nodes in the *ELSET and *NSET command in the stack have been shortened. Only the three first lines and the two last lines of the sets are presented in this Appendix.

```
*HEADING
ANISOTROPIC THIN FILM
*RESTART, WRITE, FREQUENCY=1
PREPRINT, MODEL=NO, HISTORY=NO
**
** CREATE NODE STRUCTURE
**
** CORNERS OF THE PARALLELEPIPED
*NODE
1, 3.0E-07, 0.0, 1.5E-07
17, 0.0, 0.0, 1.5E-07
8001, 3.0E-07, 0.0, 0.0
8017, 0.0, 0.0, 0.0
1600001, 3.0E-07, 3.0E-07, 1.5E-07
1600017, 0.0, 3.0E-07, 1.5E-07
1608001, 3.0E-07, 3.0E-07, 0.0
1608017, 0.0, 3.0E-07, 0.0
** BACK UPPER EDGE
*NGEN, NSET=BUEDGE
1, 17
** BACK BOTTOM EDGE
*NGEN, NSET=BBEDGE
8001, 8017
** FRONT UPPER EDGE
*NGEN, NSET=FUEDGE
1600001, 1600017
** FRONT BOTTOM EDGE
*NGEN, NSET=FBEDGE
1608001, 1608017
** BACK FACE
*NFill, NSET=BACKFACE
BUEDGE, BBEDGE, 8, 1000
** FRONT FACE
*NFill, NSET=FRTFACE
FUEDGE, FBEDGE, 8, 1000
** WHOLE NODE STRUCTURE
*NFill, NSET=ALLNODE
BACKFACE, FRTFACE, 16, 100000
**
** DEFINE NODE SETS
**
** LEFT FACE
*NSET, NSET=LFTFACE, GENERATE
1, 1600001, 100000
1001, 1601001, 100000
2001, 1602001, 100000
...
7001, 1607001, 100000
8001, 1608001, 100000
**RIGHT FACE
*NSET, NSET=RHTFACE, GENERATE
17, 1600017, 100000
1017, 1601017, 100000
2017, 1602017, 100000
...
7017, 1607017, 100000
8017, 1608017, 100000
**BOTTOM FACE
*NSET, NSET=BTMFACE, GENERATE
8001, 8017, 1
108001, 108017, 1
208001, 208017, 1
...
1508001, 1508017, 1
1608001, 1608017, 1
**
** DEFINE ELEMENT STRUCTURE
**
*ELEMENT, TYPE=C3D8
1, 1001, 101001, 101002, 1002, 1, 100001,
100002, 2
*ELGEN, ELSET=ALLEL
```

```

1, 16, 1, 1, 8, 1000, 1000, 16, 100000, 100000
**
** DEFINE ELEMENT SETS
**
** BACK LEFT GRAIN
*ELSET, ELSET=BLG, GENERATE
1, 8, 1
1001, 1008, 1
2001, 2008, 1
...
706001, 706008, 1
707001, 707008, 1
** BACK RIGHT GRAIN
*ELSET, ELSET=BRG, GENERATE
9, 16, 1
1009, 1016, 1
2009, 2016, 1
...
706009, 706016, 1
707009, 707016, 1
** FRONT LEFT GRAIN
*ELSET, ELSET=FLG, GENERATE
800001, 800008, 1
801001, 801008, 1
802001, 802008, 1
1506001, 1506008, 1
1507001, 1507008, 1
** FRONT RIGHT GRAIN
*ELSET, ELSET=FRG, GENERATE
800009, 800016, 1
801009, 801016, 1
802009, 802016, 1
...
1506009, 1506016, 1
1507009, 1507016, 1
** MIDDLE SECTION
*ELSET, ELSET=MSECT, GENERATE
1, 16, 1
1001, 1016, 1
2001, 2016, 1
...
6001, 6016, 1
7001, 7016, 1
** CENTER ROW
*ELSET, ELSET=CROW, GENERATE
1, 7001, 1000
**
** DEFINE MATERIALS CONSTANTS
**
*MATERIAL, NAME=SILVISO
*ELASTIC, TYPE=ISO
50E9, 0.3
*EXPANSION
9E-6

```

```

*MATERIAL, NAME=SILV100
*ELASTIC, TYPE=ORTHO
124E9, 93.4E9, 124E9, 93.4E9, 93.4E9, 124E9,
46.1E9, 46.1E9,
46.1E9
*EXPANSION, TYPE=ISO
9E-6
*MATERIAL, NAME=SILV111
*ELASTIC, TYPE=ANISO
154.8E9, 83.1E9, 154.8E9, 72.9E9, 72.9E9,
165.1E9, 0.0, 0.0
0.0, 25.6E9, -14.52E9, 14.52E9, 0.0, 0.0,
25.6E9, 0.0
0.0, 0.0, 14.52E9, 0.0, 35.8E9
*EXPANSION, TYPE=ISO
9E-6
**
** DEFINE LOCAL COORDINATE SYSTEM
LOCAL TO (111)
**
*ORIENTATION,
SYSTEM=RECTANGULAR, NAME=ONE
-0.5, -0.5, 1.0, 1.0, -1.0, 0.0
*ORIENTATION,
SYSTEM=RECTANGULAR, NAME=GLOB
1.0, 0.0, 0.0, 0.0, 1.0, 0.0
**
** ASSIGN ELEMENTS TO MATERIAL
**
*SOLID SECTION, ELSET=BLG,
MATERIAL=SILV111
*SOLID SECTION, ELSET=BRG,
MATERIAL=SILV100
*SOLID SECTION, ELSET=FLG,
MATERIAL=SILV100
*SOLID SECTION, ELSET=FRG,
MATERIAL=SILV111
**
**SET BOUNDARY CONDITIONS
**
*BOUNDARY
BACKFACE, YSYMM
FRTFACE, YSYMM
RHTFACE, XSYMM
LFTFACE, XSYMM
BTMFACE, PINNED
**
** SET INITIAL CONDITION
**
*INITIAL CONDITIONS,
TYPE=TEMPERATURE
ALLNODE, -100
**
** SIMULATION CONDITIONS

```

```
**  
*STEP  
*STATIC  
** LOADING CONDITIONS  
*TEMPERATURE  
ALLNODE, 0  
*EL PRINT, ELSET=BLG  
S11, S22, S33, E11, E22, E33, ELSE  
*EL PRINT, ELSET=BRG  
S11, S22, S33, E11, E22, E33, ELSE  
*EL PRINT, ELSET=FLG  
S11, S22, S33, E11, E22, E33, ELSE  
*EL PRINT, ELSET=FRG  
S11, S22, S33, E11, E22, E33, ELSE  
*NODE PRINT, FREQ=0  
*END STEP
```

Appendix III

Minimization and maximization of the biaxial modulus

We show in chapter two that when a thin film is under uniform biaxial strain and plane stress conditions, the elastic strain energy density stored in grains is

$$W = M_{hkl}\epsilon^2, \quad (\text{III.1})$$

where ϵ is the magnitude of the biaxial strain, and where M_{hkl} is an orientation dependent effective biaxial modulus given by

$$M_{hkl} = \left[c_{11} + c_{12} + K - \frac{2(c_{12} - K)^2}{c_{11} + 2K} \right] \quad (\text{III.2})$$

$$K = H(h^2k^2 + k^2l^2 + h^2l^2), \quad (\text{III.3})$$

$$h^2 + k^2 + l^2 = 1 \quad (\text{III.4})$$

where $H = c_{12} + 2c_{44} - c_{11}$ and $[hkl]$ is the unit normal to the surface of the grain.

To find the orientations that minimize and maximize M_{hkl} , we calculate $\partial M_{hkl}/\partial K$:

$$\frac{\partial M_{hkl}}{\partial K} = \left(\frac{c_{11} + 2c_{12}}{c_{11} + 2K} \right)^2. \quad (\text{III.5})$$

$\partial M_{hkl}/\partial K$ can be written as a square and is always greater than or equal to 0. For all cubic materials, thermodynamic constraints on the c_{ij} 's require that $c_{11} + 2c_{12} > 0$ [67] and $\partial M_{hkl}/\partial K$ is therefore strictly greater than 0¹. M_{hkl} increases with K and is minimum for

¹ It is easily shown that thermodynamical constraints on the c_{ij} , i.e., $c_{44} > 0$; $c_{11} > |c_{12}|$; $c_{11} + 2c_{12} > 0$, also impose $\forall(h,k,l) c_{11} + 2K \neq 0$, and equation (III.5) is always defined.

the values of $[hkl]$ that minimize K and maximum for the values of $[hkl]$ that maximize K . For all cubic materials, except Molybdenum, H is positive [67]. In particular, H is positive for all fcc metals. Defining $f(h,k)$ as

$$f(h,k) = h^2k^2 + h^2(1-h^2-k^2) + k^2(1-h^2-k^2) , \quad (\text{III.6})$$

equations (III.3) and (III.4) can be rewritten simply as:

$$K = f(h,k) H . \quad (\text{III.7})$$

When H is positive, K is minimized, respectively maximized, when $f(h,k)$ is minimized, respectively maximized. Noting that $f(h,k)$ is always positive, and that $f(h,k) = 0$ for $[hkl] = [001]$, implies that *(001)-textured grains minimize the biaxial modulus M_{hkl}* . To find the orientation that maximizes $f(h,k)$, we rewrite $f(h,k)$ in spherical coordinates (r, θ, φ):

$$h = \sin \varphi \sin \theta, \quad k = \sin \varphi \cos \theta, \quad \text{and } l = \cos \varphi , \quad (\text{III.8})$$

$$f(\theta, \varphi) = \sin^2 \varphi (\sin^2 \varphi \sin^2 \theta \cos^2 \theta + \cos^2 \varphi) . \quad (\text{III.9})$$

$f(\theta, \varphi)$ is maximized for $\partial f / \partial \theta = \partial f / \partial \varphi = 0$, $\partial^2 f / \partial \theta^2 < 0$, and $\partial^2 f / \partial \theta^2 \times \partial^2 f / \partial \varphi^2 - \partial^2 f / \partial \theta \partial \varphi > 0$ [126], which is easily shown to yield $\theta = \varphi = \pi/4$, or equivalently $h = k = l = 1/\sqrt{3}$ (see also Figure III.1 for a graphical representation of $f(\theta, \varphi)$). *(111)-textured grain maximize the biaxial modulus M_{hkl} for all cubic materials except Mo^2 , and in particular for all fcc metals.*

² Since the stiffness coefficients c_{ij} 's of Mo are such that $H < 0$, grains in Mo thin films, biaxially strained and under plane stress conditions, minimize elastic strain energy density if they are (111)-textured and minimize elastic strain energy density if they are (001)-textured.

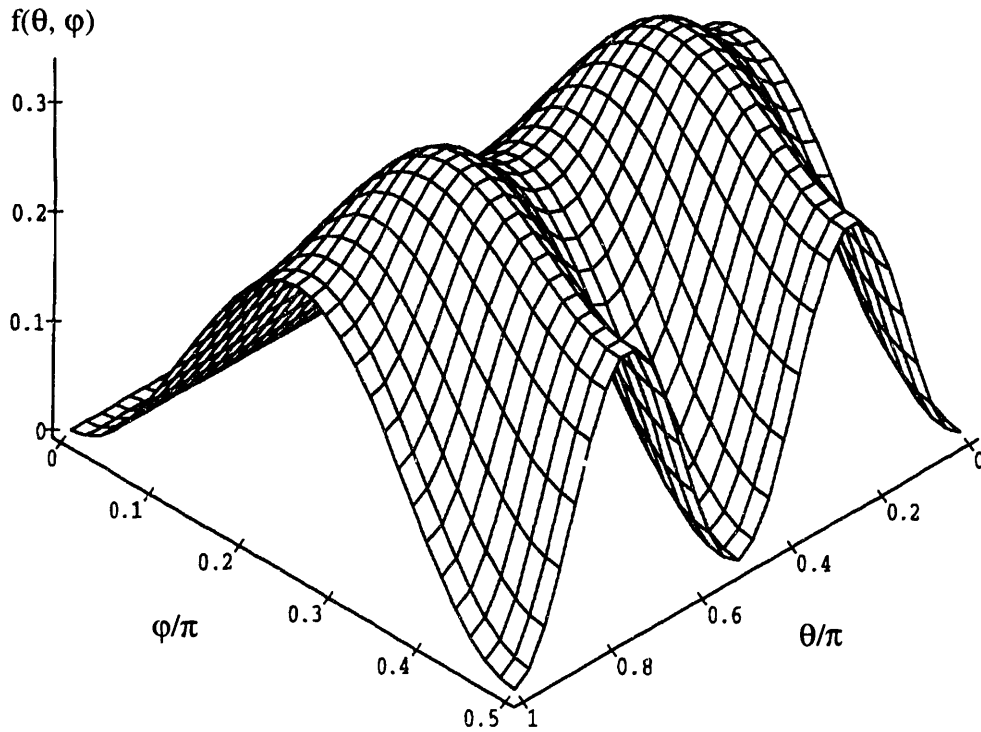


Figure III.1: Function $f(\theta, \varphi)$ plotted versus θ and φ for $0 \leq \varphi \leq \pi/2$ and $0 \leq \theta \leq \pi$. The maximum is found at $\theta = \varphi = \pi/4$, or equivalently at $h = k = l = 1/\sqrt{3}$.

Appendix IV

Yield stress of a right circular cylindrical grain

In chapter two, we present the derivation for the yield stress of a right circular cylindrical grain. In this appendix, we show how some of the approximations leading to equation (2.20) can be relaxed.

The derivation presented in chapter two assumes that the intersection of the glide plane with the grain sides and top and bottom surfaces is a rectangle. While this is a good approximation when the aspect ratio of grains d/h is large and when the angle φ of the glide plane with the surface of the grain is close to 90° , it is inaccurate when $d/h \leq 1$ or $\varphi \ll 90^\circ$.

The general non-degenerate intersection of a plane with a cylinder is an ellipse and the intersection of the glide plane with the grain, is a truncated ellipse (figure IV.1). The length of the intercept d' of the glide plane with the bottom surface of the grain is then

$$d' = \sqrt{d^2 - \frac{h^2}{\tan^2 \varphi}} . \quad (\text{IV.1})$$

The length of the intercept of the glide plane with the side of the grain is

$$L = 4 \int_0^{\theta_0} \sqrt{a^2 \cos^2 \theta + b^2 \sin^2 \theta} d\theta , \quad (\text{IV.2})$$

where a and b are the semi-axis of the ellipse, and $a = \frac{d}{2 \cos \varphi}$ and $b = \frac{d}{2}$, and where θ_0 is

defined by

$$\theta_0 = \cos^{-1} \left(\frac{d'}{\sqrt{d^2 + h^2}} \right) . \quad (\text{IV.3})$$

The surface of the glide plane in the grain is the surface of the truncated ellipse:

$$S = ab[2\theta_0 + \sin(2\theta_0)] . \quad (\text{IV.4})$$

Equations (2.14) and (2.15) can be rewritten using L and S and the yield stress is then expressed as

$$\sigma_y = \frac{1}{S \cos \lambda \cos \phi} (LK_s + d' K_b) . \quad (\text{IV.5})$$

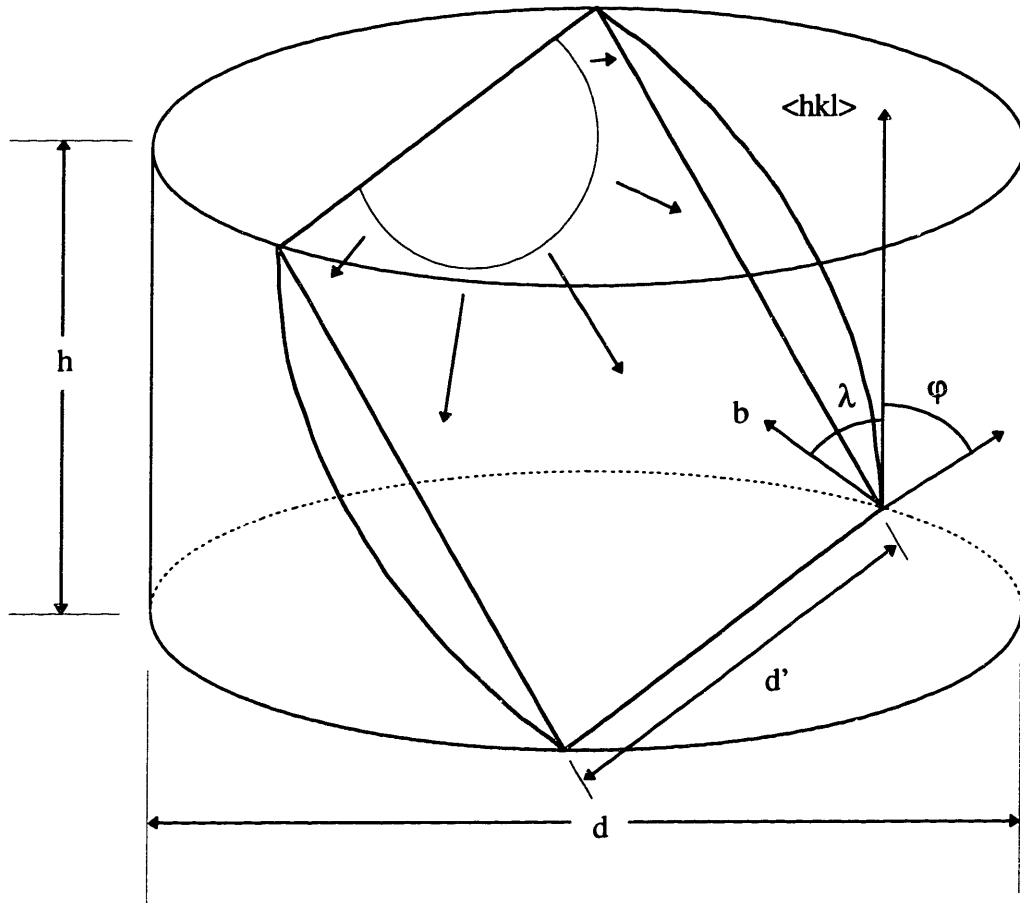


Figure IV.1: The intersection of the glide plane with the grain is a truncated ellipse

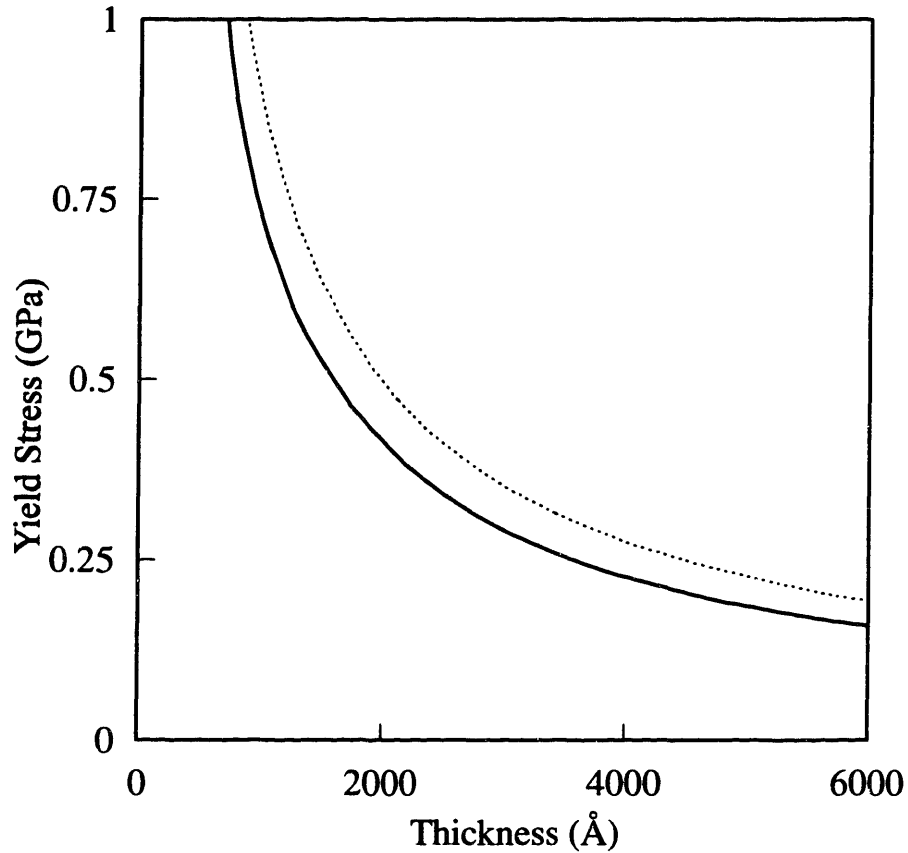


Figure IV.2: Yield stress for (001)-textured Al grains plotted versus film thickness and assuming $d = h/2$. (a) Analytic expression for the yield stress as given by equation (2.20), (b) Equation (IV.5). The difference between the two expressions can be substantial at small thicknesses and/or grain sizes.

It is not possible to put the integral of equation (IV.2) in closed form and the yield stress has to be evaluated numerically¹. Figure IV.2 shows the yield stress for a (001)-textured Al grain using the analytic expression (2.20) and equation (IV.5). While the numerical calculation of the yield stress is readily achieved, it prevents further analytic

¹ The integral in equation (IV.2) was evaluated using a Simpson discretization scheme:
$$I = \frac{2\Delta\theta}{3} \left[\frac{y_1 + y_n}{2} + 2y_{n-1} + \sum_{i=1}^{(n-3)/2} (2y_{2i} + y_{2i+1}) \right]$$
, where $\Delta\theta = \theta_0/(n-1)$ and where n is odd and is the number of intervals taken in the range $[0, \theta_0]$, and where $y_k = 4\sqrt{a^2 \cos^2(k-1)\Delta\theta + b^2 \sin^2(k-1)\Delta\theta}$. For each values of film thickness and grain diameter, n was chosen to be 400.

derivation of analytic models for texture development during grain growth that include the effect of plastic deformation (chapter two).

This appendix relaxed geometrical approximations in the derivation of an analytic expression for the yield stress of a polycrystalline thin film. There are other important approximations underlying the derivation such as the expressions for W_{side} and W_{bottom} (eqs. (2.18)-(2.19)). These are likely to influence the magnitude of the yield to a greater extent than the geometrical approximations, and the improvement of the yield stress calculation presented here is therefore not used in place of equations (2.20) and (2.22).

Appendix V

Processing and correction of raw pole figure data files

The pole figure raw data files need to be corrected for background, absorption and defocusing in order to obtain quantitative information about the volume fraction of grains with different textures, as presented in chapter four. The Rigaku software automatically corrects the data for background scattering and generates formatted ASCII files. The program listed here processes these files and extracts the diffracted intensity from the file as a function of α and β . It can correct the intensity for defocusing and absorption and integrates the data with respect to β to generate a rocking curve. The ratio of the volume fraction of grains with texture (111), (001) and (011) is also calculated. The defocusing correction factor is calculated using a polynomial fit and a Horner factorization algorithm is used to avoid numerical errors. The program is written in standard ANSI C [127].

```
/*
** integ.c
** extract intensities integrated over beta for each alpha
** from a pole figure file.
*/

/* Standard libraries */
#include <stdio.h>
#include <math.h>

/* Constant definition */
#define MAXCHAR          80
#define MEASURED         "MEASURED"
#define ANGLE            "ANGLE"
#define TOTAL            "TOTAL"
#define CORRECTED       "CORRECTED"
#define RATIO            "RATIO"
#define BETA             "BETA"
#define EQUAL            "="
#define SKIP1            5
```

```

#define SKIP2                2
#define MAXCORR              100
#define ENDCOMMENT          "*****\n"
#define PREFIX_READ          "/usr/users/rol/pf/ptx/c"
#define PREFIX_WRITE_AG      "/usr/users/rol/egg_curr/Ag/SiO2/c"
#define PREFIX_WRITE_AL      "/usr/users/rol/egg_curr/Al/c"
#define PREFIX_WRITE_NI      "/usr/users/rol/egg_curr/Ni/c"
#define SUFFIX_READ          ".ptx"
#define SUFFIX_WRITE         ".s.dat"
#define NAME_LENGTH          5
#define VOID_NAME            "00000"
#define PI                   3.141592653589793
#define MAXCOEFF             10
#define MAXOBETA             50

/* angles (alpha'=90-alpha) for the (111) and (001) orientations */
#define AN100                 35.26
#define AN111                 19.47
#define AN220                 54.74

/* defines the absorption coeff. for Ag, Ni, Al*/
#define E_AG                  0.00001724
#define E_NI                  0.00000196
#define E_NI2                 0.0000100
#define E_AL                  0.00000102

/* Functions declaration */
float correct (float i, float h, float th, float al, char sch, int pf, float e, char corr);
float absorp (float h, float th, float al, float e);
float defoc_no_Schultz_111 (float al);
float defoc_with_Schultz_111 (float al, char corr);
float defoc_with_Schultz_222 (float al, char corr);
float defoc_with_Schultz_220 (float al);
float defoc_with_Schultz_311 (float al);
float rad (float x);
float deg (float x);
float interpolate (float x0, float x1, float y0, float y1, float x);
int SkipComment (FILE *f);
int present (float beta, float *obeta, int nobeta);

main (argc, argv)
    int argc;
    char *argv[];
{
/* main () variables declaration */
char name_file[MAXCHAR], input_file[MAXCHAR], word[MAXCHAR];
char c, corr, tcorr, sch, ombeta;
int index, pftype;
float inten, alpha, total1, total2, total_prec, alpha_prec;
float inten100, inten111, inten220;
float theta, h, e;
float beta, obeta[MAXOBETA], betast;
int nobeta;

```



```

int i;
FILE *f, *fo;

/* Checks command line arguments */
switch (argc) {
case 1: /* default */
    /* get the data file name */
    printf ("\nEnter the name of the data file (%s#####%s): ",
            PREFIX_READ,SUFFIX_READ);
    scanf ("%s",name_file);
    break;

case 2:
    /* get the name from the command line argument */
    sprintf (name_file,"%s",argv[1]);
    break;

default:
    /* more than one argument */
    printf ("integ: Error. Too many arguments. Syntax integ [#####].\n");
    printf ("integ: Assuming syntax: integ %s\n",argv[1]);
    sprintf (name_file,"%s",argv[1]);
    break;
} /* end of switch */

/* Opens the data files */
printf ("Reading data.\n");
strcpy (input_file, PREFIX_READ);
strncat (input_file, VOID_NAME, NAME_LENGTH-strlen(name_file));
strcat (input_file, name_file);
strcat (input_file, SUFFIX_READ);
if ((f=fopen (input_file, "r"))==NULL) {
    printf ("integ: Can not open the file %s. Stop.\n", input_file);
    exit (-1);
}

/* Prompts the user for the type of correction to perform to the data */
printf ("Correct data for absorption, defocusing and wafer scattering? (y/n): ");
scanf ("%s", &corr);
corr = (corr=='y' || corr=='Y');

if (corr) {
    do {
        printf ("Enter the type of PF: (1) Ag, (2) Ni, (3) Al: ");
        scanf ("%s", &tcorr);
    } while (tcorr!='1' && tcorr!='2' && tcorr!='3');
    if (tcorr=='1') e = E_AG; else if (tcorr=='2') e = E_NI; else e = E_AL;
    printf ("Enter h (in angstroms): ");
    scanf ("%f", &h);
    printf ("Schultz slit used? (y/n): ");
    scanf ("%s", &sch);
    sch = (sch=='y' || sch=='Y');
    printf ("Skip some values of beta ? (y/n): ");
    scanf ("%s", &ombeta);
}

```

```

ombeta = (ombeta=='y' || ombeta=='Y');
if (ombeta) {
    nobeta = 0;
    printf ("Enter Beta values to be avoided. Type -1 to stop\n");
    do {
        printf ("beta = ");
        scanf ("%f",&(obeta[nobeta]));
        if (obeta[nobeta]==-1) break; else nobeta++;
    } while (1);
}
else
do {
    printf ("Enter the type of PF: (1) Ag, (2) Ni, (3) Al: ");
    scanf ("%s", &tcorr);
    } while (tcorr!='1' && tcorr!='2' && tcorr!='3');
/* open the output file */
if (tcorr=='1') strcpy (input_file, PREFIX_WRITE_AG);
else if (tcorr=='2') strcpy (input_file, PREFIX_WRITE_NI);
else if (tcorr=='3') strcpy (input_file, PREFIX_WRITE_AL);
else {
    printf ("Unknown material.\n");
    exit (-1);
}
strcat (input_file, name_file);
strcat (input_file, SUFFIX_WRITE);
printf ("Creating file: %s\n", input_file);
if ((fo=fopen (input_file, "w"))==NULL) {
    printf ("Could not open the result file %s.\n Stop.\n", input_file);
    exit (-1);
}

/* get PF type */
pftype = 0;
while (c = fscanf (f, "%s", word), strcmp (word, MEASURED));
fscanf (f, "%s", word);
fscanf (f, "%d", &index);
pftype = 100*index;
fscanf (f, "%d", &index);
pftype += 10*index;
fscanf (f, "%d", &index);
pftype += index;
printf ("%d Pole Figure\n", pftype);

/* get theta */
while (c = fscanf (f, "%s", word), strcmp (word, ANGLE));
fscanf (f, "%s", word);
fscanf (f, "%f", &theta);
theta = rad (theta/2);
inten100 = inten111 = total_prec = alpha_prec = 0.0;

/* get beta step */
while (c = fscanf (f, "%s", word), strcmp (word, BETA));
fscanf (f, "%s", word); fscanf (f, "%s", word);

```

```

fscanf (f, "%f", &betast);
printf ("Beta step = %.2f\n", betast);

/* get to the right line in the file*/
do {
  while (c = fscanf (f, "%s", word), c!=EOF && strcmp (word, TOTAL));
  for (i=0 ; i<SKIP1 ; i++) fscanf (f, "%s", word);
  fscanf (f, "%s", word);
  if (!strcmp(word, EQUAL)) break; /* end of file reached */
  alpha = (float) atof (word);
  for (i=0 ; i<SKIP2 ; i++) fscanf (f, "%s", word);
  fscanf (f, "%f", &total1);
  while (c = fscanf (f, "%s", word), strcmp (word, CORRECTED));
  for (i=0 ; i<SKIP2 ; i++) fscanf (f, "%s", word);
  total2 = beta = 0.0;
  while (c = fscanf (f, "%s", word), strcmp (word, RATIO)) {
    if (!present (beta, obeta, nobeta)) total2 += (float) atof (word);
    beta += betast;
  }
  if (!ombeta) total1 = (total1+total2)/2; else total1 = total2;
  if (corr)
    total1 = correct (total1, h, theta, rad(90-alpha), sch,
                    pftype, e, tcorr);

/* pass alpha */
fprintf (fo, "%.1f %.1f\n", alpha, total1); /* file written using alpha prime */

/* check if (002), (022), or (222) can be interpolated from the current reading */
if (pftype==111) {
  if (alpha>=AN111 && alpha_prec<=AN111) {
    inten111 = interpolate (alpha, alpha_prec, total1, total_prec, AN111);
    printf ("Intensity for (111): %.0f\n", inten111);
  }
  else if (alpha>=AN100 && alpha_prec<=AN100) {
    inten100 = interpolate (alpha, alpha_prec, total1, total_prec, AN100);
    printf ("Intensity for (200): %.0f\n", inten100);
  }
  else if (alpha>=AN220 && alpha_prec<=AN220) {
    inten220 = interpolate (alpha, alpha_prec, total1, total_prec, AN220);
    printf ("Intensity for (220): %.0f\n", inten220);
  }
}
alpha_prec = alpha;
total_prec = total1;
} while (1); /* loop exited by break statement */

if (pftype==111) {
  printf ("ratio (200)/(111) = %.2f\n", inten100/inten111);
  printf ("ratio (220)/(111) = %.2f\n", inten220/inten111);
}

printf ("integ completed sucessfully.\n");
fclose (f);
fclose (fo);

```

```

} /* main */

/***** Functions Implementation *****/

/* Performs data correction: absorption and defocussing */
float correct (i, h, th, al, sch, pf, e, corr)
    float i, h, th, al, e;
    char sch, corr;
    int pf;
{
    /* defocusing and absorption correction */
    if (sch) {
        switch (pf) {
            case 111:
                return (i*absorp(h, th, al, e)*defoc_with_Schultz_111(90-deg(al), corr));
                break;
            case 222:
                return (i*absorp(h, th, al, e)*defoc_with_Schultz_222(90-deg(al),corr));
                break;
            case 220:
                return (i*absorp(h, th, al, e)*defoc_with_Schultz_220(90-deg(al)));
                break;
            case 311:
                return (i*absorp(h, th, al, e)*defoc_with_Schultz_311(90-deg(al)));
                break;
            default:
                printf ("Unknown pf type: %d\n", pf);
                break;
        }
    }
    else {
        printf ("Schultz slit not used.");
        if (wcorr) {
            printf ("Can not correct for wafer scattering if");
            printf ("the Schultz slit is not used. Ignoring...\n");
        }
        switch (pf) {
            case 111:
                return (i*absorp(h, th, al, e)*defoc_no_Schultz_111(90-deg(al)));
                break;
            default:
                printf ("Unknown pf type: %d\n", pf);
                break;
        }
    }
} /* correct() */

/* Corrects intensity for absorption */
float absorp (h, th, al, e)
    float h, th, al, e;
{
    return ((1-exp(-2*e*h/sin(th)))/(1-exp(-2*e*h/(sin(th)*cos(al)))));
}

```

```

/*
** The defocussing data is fitted to a polynomial function.
** The coeffs of the polynomial fit were determined with deltagraph
** and the coeffs have been calculated for alpha prime in degrees.
** The coefficients are listed in order of decreasing power of the temperature.
*/
float defoc_no_Schultz_111 (al)
    float al;
{
    /* defocusing error - Ag (111) PF's */
    static float cof[MAXCOEFF] = {96.63387, -6.402074, 0.2029938, -3.408012e-3,
    2.875801e-5, -9.602656e-8};

    static deg = 5;
    int i;
    float fd=cof[deg];
    for (i=deg-1 ; i>=0 ; i--) {
        fd = fd*al + cof[i];
    }
    return (fd);
} /* absorp() */

float defoc_with_Schultz_111 (al, corr)
    float al;
    char corr;
{
    /* defocusing error - Ag (111) PF's */
    static float cof_Ag[MAXCOEFF] = {30.44636, -1.863237, 5.461935e-2, -8.517878e-4,
    6.655136e-6, -2.030179e-8};

    static deg_Ag = 5;
    /* defocusing error - Ni (111) PF's */
    static float cof_Ni[MAXCOEFF] = {51.31643, -4.642101, 2.050531e-1, -5.019462e-3,
    6.891464e-5, -4.968057e-7, 1.464520e-9};

    static deg_Ni = 6;
    /* defocusing error - Al (111) PF's */
    static float cof_Al[MAXCOEFF] = {67.10335, -6.377614, 2.945437e-1, -7.482422e-3,
    1.057050e-4, -7.779035e-7, 2.324864e-9};

    static deg_Al = 6;
    int i;
    float fd;
    if (corr=='1') {
        fd = cof_Ag[deg_Ag];
        for (i=deg_Ag-1 ; i>=0 ; i--) {
            fd = fd*al + cof_Ag[i];
        }
    }
    else if (corr=='2') {
        fd = cof_Ni[deg_Ni];
        for (i=deg_Ni-1 ; i>=0 ; i--) {
            fd = fd*al + cof_Ni[i];
        }
    }
    else if (corr=='3') {
        fd = cof_Al[deg_Al];
    }
}

```

```

    for (i=deg_A1-1 ; i>=0 ; i--) {
        fd = fd*al + cof_A1[i];
    }
}
else {
    printf ("Unknown materials in defoc_with_schultz_111().\n");
    exit (-1);
}
return (fd);
} /* defoc_with_Schultz_111() */

float defoc_with_Schultz_222 (al, corr)
    float al;
    char corr;
{
    /* defocusing error - Ag (222) PF's */
    static float cof_Ag[MAXCOEFF] = {8.394953, -4.282320e-1, 1.113678e-2, -1.453203e-4,
    8.754351e-7, -1.780259e-9};

    static deg_Ag = 5;
    /* defocusing error - Ni (222) PF's */
    static float cof_Ni[MAXCOEFF] = {7.107086, -4.638565e-1, 1.734127e-2, -3.385612e-4,
    3.235897e-6, -1.194205e-8};

    static deg_Ni = 5;
    int i;
    float fd;
    if (corr=='1') {
        fd = cof_Ag[deg_Ag];
        for (i=deg_Ag-1 ; i>=0 ; i--) {
            fd = fd*al + cof_Ag[i];
        }
    }
    else {
        fd = cof_Ni[deg_Ni];
        for (i=deg_Ni-1 ; i>=0 ; i--) {
            fd = fd*al + cof_Ni[i];
        }
    }
    return (fd);
} /* defoc_with_Schultz_222() */

float defoc_with_Schultz_311 (al)
    float al;
{
    /* defocusing error - Ag (311) PF's */
    static float cof[MAXCOEFF] = {13.57415, -1.002057, 3.621412e-2, -6.929774e-4,
    6.689279e-6, -2.543825e-8};

    static deg = 5;
    int i;
    float fd=cof[deg];
    for (i=deg-1 ; i>=0 ; i--) {
        fd = fd*al + cof[i];
    }
    return (fd);
} /* defoc_with_Schultz_311() */

```

```

float defoc_with_Schultz_220 (al)
    float al;
{
    /* defocusing error - Ag (220) PF's */
    static float cof[MAXCOEFF] = {16.40475, -1.242832, 4.364811e-2, -7.936329e-4,
    7.253308e-6, -2.6298291e-8};

    static deg = 5;
    int i;
    float fd=cof[deg];
    for (i=deg-1 ; i>=0 ; i--) {
        fd = fd*al + cof[i];
    }
    return (fd);
} /* defoc_with_Schultz_220() */

/* Transforms degrees in radians */
float rad (x)
    float x;
{ return (PI*x/180);}

/* Transform radians in degrees */
float deg (x)
    float x;
{ return (180*x/PI);}

/* Linear interpolation y = ax+b */
float interpolate (x0, x1, y0, y1, x)
    float x0, x1, y0, y1, x;
{return(y1*(x-x0)/(x1-x0)+y0*(x-x1)/(x0-x1));}

/* Skip comments in data files */
int SkipComment (f)
    FILE *f;
{
    char line [MAXCHAR], *c;
    while (c = fgets (line, MAXCHAR, f), (c!=NULL) && strcmp (line, ENDCOMMENT));
    if (c==NULL) return (-1); else return (1);
}

/* Debugging function */
int present (beta, obeta, nobeta)
    float beta, *obeta;
    int nobeta;
{
    int i;
    for (i=0 ; i<nobeta ; i++) if (beta==obeta[i]) return (1);
    return (0);
} /* present() */

```

Appendix VI

Kinetics of Grain Growth in Ag/SiO₂/Si

VI.1 - Experimental

Oxidized Si wafers were cut in strips, 2 cm x 5 cm in size. Ag films, 3000 Å thick, were deposited on the SiO₂/Si substrate at room temperature. The films were (111)-textured as-deposited, as shown in section 6.3.2. The Ag/SiO₂/Si samples were introduced in a hot-stage x-ray goniometer attached to a Rigaku RU 200 generator. The position of the samples was optimized to maximize the intensity of the Ag (111) Bragg peak. The (111) Bragg peak was chosen since it is the most intense diffraction peak in (111)-textured Ag films and provides a good signal to noise ratio. The hot-stage was flushed with N₂, and the N₂ flow was reduced to 30 sccm/h. The samples were heated to 280-320°C and the intensity of the (111) Bragg peak was measured as a function of time during isothermal anneals. This temperature range is lower than the grain growth temperature of 350°C determined by hot-stage TEM for Ag/SiO₂/Si. The hot stage TEM and hot stage x-ray diffraction results indicate that grain growth in Ag thin films occurs at a lower temperature when the film are in a N₂ ambient than when they are annealed under vacuum. This can be due to the TEM sample preparation process during which the grain boundaries can be contaminated, effectively raising the grain growth temperature

At the time scale of grain growth in the temperature range studied, it was not found possible to adjust the position of the sample and to compensate for thermal drift and

the associated loss of focus before significant grain growth had occurred in the films. In order to eliminate the effect of the loss of focus and compare samples annealed at different temperature, the first measure was taken a few minutes after the temperature had stabilized to allow the samples to reach an equilibrium position in the goniometer.

VI.2 - Results and discussion

Figure VI.1 shows the normalized intensity of the (111) Bragg peak for Ag versus for five isothermal anneals. The normalization is performed by dividing the intensities of each data set by the first intensity measured. The intensity of the (111) Bragg peak is proportional to the volume of (111)-textured grains in the films: $I \propto V_{111}$. The increase in volume of a right circular cylindrical grain growing uniformly at the rate $v = dr/dt$, in the interval of time dt , is $dV_{111} = 2\pi r h v dt$. The grain boundary velocity v can be expressed as [11]

$$v = m \left[\left(\frac{1}{r} - \frac{1}{\bar{r}} \right) + \frac{\Delta\gamma}{h\gamma_{gb}} + \frac{\Delta W_{\epsilon}}{\gamma_{gb}} \right], \quad (\text{VI.1})$$

where \bar{r} is the average grain size in the film, and m is a thermally activated mobility constant:

$$m = m_0 e^{-Q_{gg}/kT}, \quad (\text{VI.2})$$

where Q_{gg} is the activation energy for grain growth. Equation (VI.1) does not take into account grain growth stagnation which is responsible for the asymptotic values reached at longer times by the intensity of the (111) peak. Grain boundary grooving induced grain growth stagnation involves surface and grain boundary diffusion and is a thermally

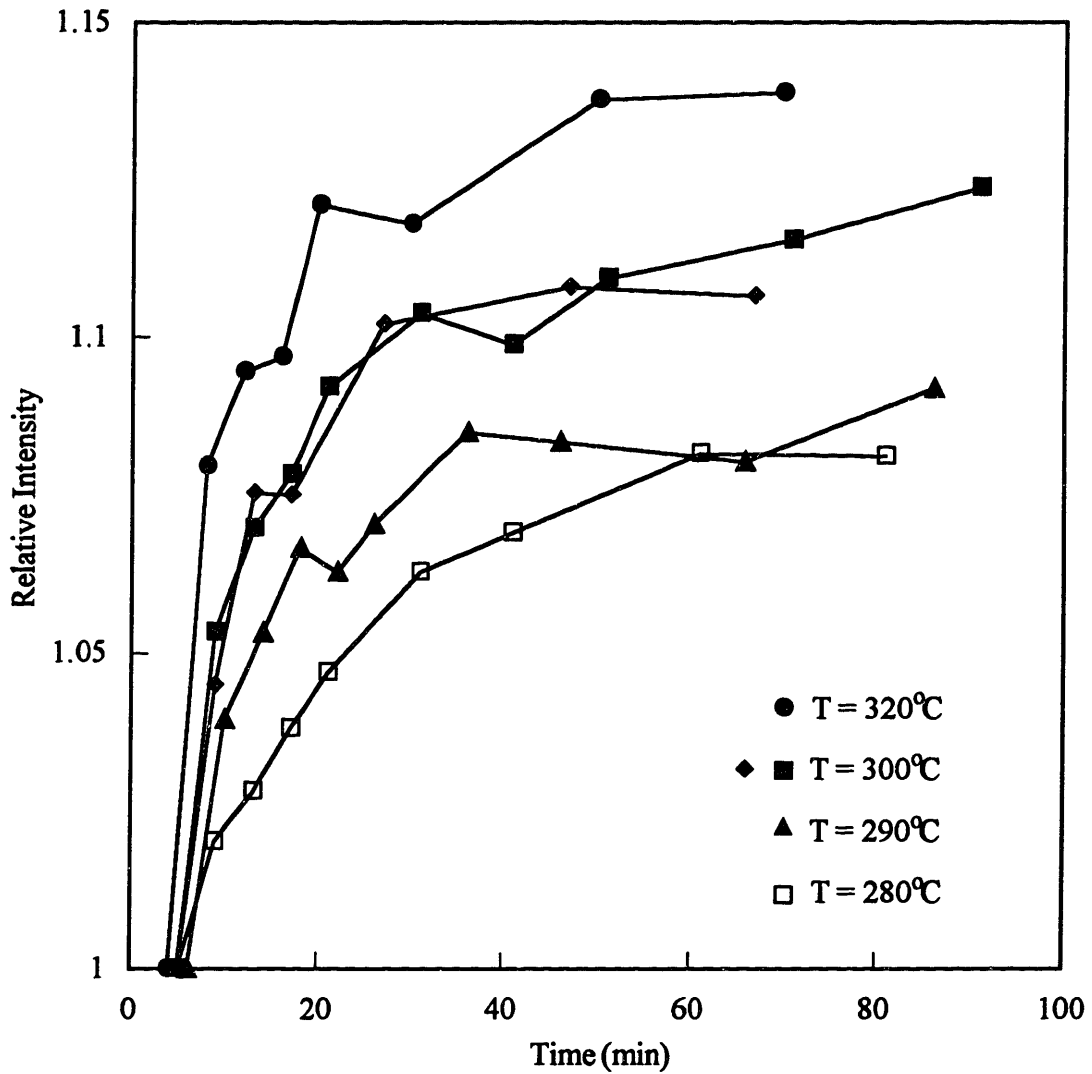


Figure VI.1: Relative intensity of the (111) Ag Bragg peak for Ag/SiO₂/Si samples during isothermal anneals.

activated process [35, 122]. To determine the activation energy for grain growth, it is preferable to use data at the early stage of grain growth, when the driving forces for grain boundary motion are large and when grain boundary grooving has only a minor effect on grain growth kinetics.

The rate of change of the intensity of the (111) Bragg peak is proportional to:
 $\partial I/\partial t \propto \partial V_{111}/\partial t \propto v \propto m \propto \exp(-Q_{gg}/kT)$. The rate of change of the normalized intensity is

$$\frac{dI_n}{dt} = \frac{1}{I(t=0)} \frac{dI}{dt} = \psi e^{-Q_{gg}/kT}, \quad (\text{VI.3})$$

where ψ is a proportionality constant. The activation energy for grain growth can be determined by fitting $\ln(dI_n/dt)$ versus $1/T$, as shown in figure VI.2. In figure VI.2, the rate of change of the intensity of the normalized (111) peak was taken as early as the thermal equilibrium of the hot stage would allow. The activation energy was found to be $Q_{gg} = 0.87$ eV. The activation energy for grain boundary self-diffusion in Ag is $Q_{gb} = 0.75$ eV [123]. As expected, Q_{gg} and Q_{gb} are similar [124].

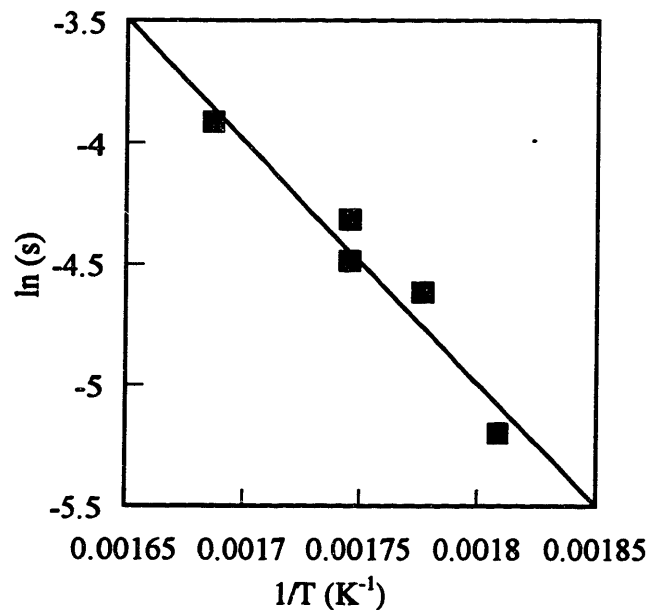


Figure VI.2: Arrhenius plot for the rate of change of the intensity of the (111) Ag Bragg peak with time.

Bibliography

1. *Microstructure and Properties of Catalysts*, ed. by M. M. J. Treacy, J. M. Thomas and J. M. White, Materials Research Society Symposium Proceedings **111** (1988)
2. *Materials for Optical Information Processing*, ed. by C. Warde, J. Stamatoff, and W. I. Wang, Materials Research Society Symposium Proceedings **228** (1991)
3. *Optical Materials: Processing Science*, ed. by D. B. Poker and C. Ortiz, Materials Research Society Symposium Proceedings **152** (1990)
4. *Magnetic Surfaces, Thin Films, and Multilayers*, ed. by S. S. P. Parkin, H. Hopster, J.-P. Renard, T. Shinjo, and W. Zinn, Materials Research Society Symposium Proceedings **231** (1991)
5. *Materials Reliability in Microelectronics II*, ed. by C. V. Thompson and J. R. Lloyd, Materials Research Society Symposium Proceedings **265** (1992)
6. *Polysilicon Films and Interfaces*, ed. by C. Y. Wong, C. V. Thompson, and K.-N. Tu, Materials Research Society Symposium Proceedings **106** (1988)
7. J. Cho, and C. V. Thompson, Appl. Phys. Lett. **54**, 2577 (1989)
8. Y.-C. Joo, Ph.D. thesis, MIT Dept. Mat. Sci. and Eng. (1995)
9. S. K. Ghandi, VLSI Fabrication Principles, (John Wiley, New York 199), p. 22
10. *CRC Handbook of Chemistry and Physics*, ed. by D. R. Lide **72** (1992)
11. C. V. Thompson, Acta Metall. **36**, 2929 (1988)
12. C. V. Thompson, and R. Carel, to appear in Mat. Sci. and Eng. B
13. R. Abermann, R. Kramer, and J. Mäser, Thin Solid Films **52**, 215 (1978)
14. C. W. Mays, J. S. Vermaak, and D. Kulhmann-Wilsdorf, Surf. Sci. **12**, 134 (1968)
15. M. F. Doerner, and W. D. Nix, CRC Crit. Rev. Sol. St. Mat. Sci. **14**, 225 (1988)
16. D. W. Pashley, M. J. Stowell, M. H. Jacobs, and T. J. Law, Philosophical Mag. **10**, 127 (1964)
17. C. C. Wong, H. I. Smith, and C. V. Thompson, Appl. Phys. Lett. **48**, 335 (1986)
18. K. Kinoshita, Thin Solid Films **12**, 17 (1972)
19. D. W. Hoffman, Phys. Thin Films **3**, 211 (1966)

20. J. A. Thornton, and D. W. Hoffman, *Thin Solid Films* **171**, 5 (1989)
21. W. D. Nix, unpublished research
22. A. Shull, private communication
23. E. Klokholm, and B. S. Berry, *J. Electrochem. Soc.* **115**, 823 (1968)
24. R. C. Cammarata, *Progress in Surface Science* **46**, 1 (1994)
25. J. W. Matthews, and A. E. Blakeslee, *J. Cryst. Growth* **27**, 118 (1974)
26. H. Inglefield, Ph. D. Thesis, MIT Dept. Mat. Sci. and Eng., 1995
27. G. Bochi, Ph. D. Thesis, MIT Dept. Mat. Sci. and Eng., 1995
28. C. Herring, *The Physics of Powder Metallurgy*, ed. by W. E. Kingston (McGraw-Hill, New York 1951), p. 157
29. F. N. Rhines, and K. R. Craig, *Metall. Trans.* **5A**, 413 (1974)
30. R. D. Doherty, *Metall. Trans.* **6A**, 588 (1975)
31. S. M. Kurtz, and F. M. A. Carpay, *J. Appl. Phys.* **51**, 5725 (1980)
32. F. B. Hildebrand, *Advanced Calculus for Applications* (Prentice Hall, New Jersey 1976), p. 281
33. C. V. Thompson, *MRS Symp. Proc.* **280**, 307 (1993)
34. P. A. Beck, M. L. Holtzworth, and P. R. Sperry, *Trans. Am. Inst. Metall. Engrs* **180**, 163 (1949)
35. W. W. Mullins, *Acta Metall.* **6**, 414 (1958)
36. M. Evans, N. Hastings, and B. Peacock, *Statistical Distributions* (John Wiley, New York 1993), pp. 102-105
37. H. J. Frost, C. V. Thompson, and D. Walton, *Acta Metall. Mater.* **38**, 1455 (1990)
38. H. J. Frost, Y. Hayashi, C. V. Thompson, and D. T. Walton, *MRS Symp. Proc.* **317**, 431 (1994)
39. J. L. Walter, and C. G. Dunn, *Trans. AIME* **215**, 465 (1959)
40. K. Foster, J. J. Kramer, and C. W. Weiner, *Trans. AIME* **227**, 185 (1963)
41. C. G. Dunn, and J. L. Walter, *Recrystallization, Grain Growth and Textures*, edited by H. Hargolin (ASM, Metals Park, Ohio, 1966), p. 461
42. C. V. Thompson, and H. I. Smith, *Appl. Phys. Lett.* **44**, 603 (1984)

43. C. C. Wong, H. I. Smith, and C. V. Thompson, *J. Appl. Phys.* **48**, 335 (1986)
44. J. E. Palmer, C. V. Thompson, and H. I. Smith, *J. Appl. Phys.* **62**, 2492 (1987)
45. H. J. Kim, and C. V. Thompson, *J. Appl. Phys.* **67**, 757 (1990)
46. C. V. Thompson, J. A. Floro, and H. I. Smith, *J. Appl. Phys.* **67**, 4099 (1990)
47. J. A. Floro, Ph. D. thesis, MIT Dept. Mat. Sci. and Eng (1992)
48. H. J. Frost, C. V. Thompson, and D. T. Walton, *Acta Metall. Mater.* **40**, 779 (1990)
49. D. J. Srolovitz, G. S. Grest, and M. P. Anderson, *Acta Metall.* **33**, 2233 (1986)
50. J. A. Floro, and C. V. Thompson, *Acta Metall.* **41**, 1137 (1993)
51. R. W. Vook, and F. Witt, *J. Vac. Sci. Technol.* **2**, 49 (1965)
52. R. W. Vook, and F. Witt, *J. Vac. Sci. Technol.* **2**, 243 (1965)
53. J. E. Sanchez, Jr. and E. Arzt, *Scripta Metall. Mater.* **27**, 285 (1992)
54. J. A. Floro, C. V. Thompson, R. Carel, and P. D. Bristowe, *J. Mat. Res.* **9**, 2411 (1994)
55. H. V. Atkinson, *Acta Metall.* **36**, 469 (1988)
56. M. Hillert, *Acta Metall.* **13**, 227 (1965)
57. I. M. Lifshitz, and V. V. Slyozov, *J. Phys. Chem. Solids* **19**, 35 (1961)
58. C. Wagner, *Z. Elektrochem.* **65**, 581 (1961)
59. N. P. Louat, *Acta Metall.* **22**, 721 (1974)
60. O. Hunderi, and N. Ryum, *J. Mater. Sci.* **15**, 1104 (1980)
61. D. T. Wu, *MRS Symp. Proc.* **343**, 55 (1994)
62. P. Chaudhari, *J. Vac. Sci. Technol.* **9**, 520 (1971)
63. H. J. Frost, F. Spaepen, and M. F. Ashby, *Scripta Metall.* **16**, 1165 (1982)
64. K. Röhl, *J. Appl. Phys.* **47**, 3223 (1976)
65. W. D. Nix, *Met. Trans.* **20A**, 2217 (1989)
66. F. A. McClintock, and A. S. Argon, Mechanical Behavior of Materials (TechBooks, Williamsburg 1965), pp. 153-214
67. J. F. Nye, Physical Properties of Crystals, (Oxford University Press, New York 1985), pp. 142-155

68. J. P. Hirth, and J. Lothe, The Theory of Dislocations (John Wiley, New York 1982), p. 435
69. M. Murikami, and P. Chaudhari, *Thin Sol. Films* **46**, 109 (1977)
70. E. M. Zielinski, R. P. Vinci, and J. C. Bravman, *J. Appl. Phys.* **76**, 4516 (1994)
71. A. Catlin, and W. P. Walker, *J. Appl. Phys.* **31**, 2135 (1960)
72. S. P. Baker, M. K. Small, J. J. Vlassak, B. J. Daniels, and W. D. Nix, Mechanical Properties and Deformation of Materials with Ultrafine Microstructures, ed. by M. Nastasi, D. M. Parkin, and H. Gleiter (Kleiver Academic, Dordrecht, 1993), p.165
73. R. C. Cammarata, Mechanical Properties and Deformation of Materials with Ultrafine Microstructures, ed. by M. Nastasi, D. M. Parkin, and H. Gleiter (Kleiver Academic, Dordrecht, 1993), p. 193
74. G. Simmon, and H. Wang, Single Crystal Elastic Constants and Calculated Aggregate Properties, (MIT Press, Cambridge, 1971), p. 86
75. C. V. Thompson, *Scripta Met. et Mat.* **28**, 167 (1993)
76. L. B. Freund, *J. Appl. Mech.* **54**, 553 (1987)
77. J. P. Hirth, The Relation Between the Structure and Mechanical Properties of Metals (National Physical Laboratory Proceedings, Symposium 15, Her Majesty's Stationary Office, London 1963), pp. 218-228
78. R. Venkatraman, and J. C. Bravman, *J. Mat. Res.* **7**, 2040 (1992)
79. E. Schmid, and W. Boas, Plasticity of Materials (Chapman & Hill, London 1969), p. 125
80. C. V. Thompson, *J. Mat. Res.* **8**, 237 (1993)
81. H. J. Frost, C. V. Thompson, *Acta Metall.* **35**, 529 (1987)
82. H. J. Frost, C. V. Thompson, *J. Electron. Mater.* **17**, 447 (1988)
83. D. Weaire, and J. P. Kermode, *Phil. Mag.* **48**, 245 (1983)
84. E. A. Ceppi, and O. B. Nasello, *Scripta Metall.* **18**, 221 (1984)
85. S. Yabushita, N. Hatta, S. Kikuchi, and J. Kokado, *Scripta Metall.* **19**, 853 (1985)
86. V. E. Fradkov, L. S. Shvindlerman, and D. G. Udler, *Scripta Metall.* **19**, 1285 (1985)
87. A. Soares, A. C. Ferro, and M. A. Fortes, *Scripta Metall.* **19**, 1491 (1985)
88. K. Kawasaki, T. Nagai, and K. Nakashima, *Phil. Mag.* **60**, 339 (1985)

89. M. P. Anderson, D. J. Srolovitz, G. S. Grest, and P. S. Sahni, *Acta Metall.* **32**, 783 (1984)
90. D. J. Srolovitz, M. P. Anderson, P. S. Sahni, and G. S. Grest, *Acta Metall.* **32**, 793 (1984)
91. D. J. Srolovitz, *J. Vac. Technol.* **A4**, 2925 (1986)
92. H. J. Frost, C. V. Thompson, C. L. Howe, and J. Whang, *Scripta Metall.* **22**, 65 (1988)
93. H. J. Frost, Y. Hayashi, and C. V. Thompson, *MRS Symp. Proc.* **317**, 485(1994)
94. Y. Gao, S. A. Dregia, and P. G. Shewmon, *Acta Metall.* **37**, 1627 (1989)
95. Y. Gao, S. A. Dregia, and P. G. Shewmon, *Acta Metall.* **37**, 3165 (1989)
96. W. A. Johnson, and R. F. Mehl, *Trans. Am. Inst. Min. Engrs* **135**, 416 (1939)
97. J. Gupta, J. M. E. Harper, J. L. Mauer IV, P. G. Blauner, and D. A. Smith, *Appl. Phys. Lett.* **61**, 653 (1992)
98. D. L. Barr, L. R. Harriott, and W. L. Brown, *J. Vac. Sci. Technol.* **B 10**, 3120 (1992)
99. B. D. Cullity, *Elements of X-Ray Diffraction* (Addison-Wesley, Reading MA 1978), pp. 297-316
100. L. G. Schultz, *J. Appl. Phys.* **20**, 1030 (1949)
101. D. Josell, and F. Spaepen, *Acta Metal. Mater.* **41**, 3017 (1993)
102. M. S. Daw, and M. I. Baskes, *Phys. Rev. B* **29**, 6443 (1984)
103. S. M. Foiles, M. I. Baskes, and M. S. Daw, *Phys. Rev. B* **33**, 7983 (1986)
104. D. Josell, and F. Spaepen, *Acta Metal. Mater.* **41**, 3007 (1993)
105. M. C. Quintana, and J. L. Sacedon, *Thin Solid Films* **14**, 149 (1972)
106. S. Mader, R. Feder, and P. Chaudhari, *Thin Solid Films* **14**, 63 (1972)
107. *Thermal Expansion - Metallic Elements and Alloys*, Thermophysical Properties of Matter (IFI/Plenum, New York), Vol. 12.
108. *Thermal Expansion - Nonmetallic Solids*, Thermophysical Properties of Matter (IFI/Plenum, New York), Vol. 13.
109. P. D. Bristowe, unpublished research
110. unknown reference
111. J. W. Cahn, and F. Larché, *Acta Metall.* **30**, 51 (1982)

112. J.W. Cahn, Interfacial Segregation, Proceedings of 1977 ASM Seminar (ASM, Metal Park OH), p. 1
113. J. E. Palmer, M.S. Thesis, MIT Dept. Elect. Eng. (1985)
114. W. Mendelhall, D. D. Wackerly, and R. L. Scheaffer, Mathematical Statistics with Applications (Duxbury Press, Belmont CA 1990), pp. 335, 761
115. H. Jaeger, P. D. Mercer, and R.G. Sherwood, Surf. Sci. **13**, 349 (1969)
116. Y. Liu, Ph. D. Thesis, MIT Dept. Mat. Sci. and Eng. (1991)
117. E. Jiran, Ph. D. Thesis, MIT Dept. Mat. Sci. and Eng. (1990)
118. C. Y. Shih, C. L. Bauer, and J. O. Artman, J. Appl. Phys. **64**, 5428 (1988)
119. H. Windischmann, CRC Crit. Rev. Sol. St. Mat. Sci. **17**, 547 (1992)
120. H. P. Longworth, and C. V. Thompson, J. Appl. Phys. **69**, 3929 (1991)
121. C. S. Smith, Trans. AIME **175**, 15 (1948)
121. E. M. Zielinski, R. P. Vinci, and J. C. Bravman, to appear in Appl. Phys Lett.
122. F. Y. Génin, J. Appl. Phys. **77**, 5130 (1995)
124. A. M. Brown, and M. F. Ashby, Acta Metall. **28**, 1085 (1980)
125. C. V. Thompson, Ann. Rev. Mater. Sci. **20**, 245 (1990)
126. F. B. Hildebrand, Advanced Calculus for Applications (Prentice Hall, New Jersey 1976), p. 357
127. B. W. Kernigham, and D. M. Ritchie, The C Programming Language (Prentice Hall, Englewoods Cliffs NJ 1988)

THESIS PROCESSING SLIP

FIXED FIELD: ill. _____ name _____

index _____ biblio _____

► COPIES Archives Aero Dewey Eng Hum
Lindgren Music Rotch Science

TITLE VARIES: ► _____

NAME VARIES: ► _____

IMPRINT. (COPYRIGHT) _____

► COLLATION: 266 & (2 vols. for Science copy)

► ADD. DEGREE: _____ ► DEPT.: _____

SUPERVISORS: _____

NOTES:

cat'r:

date:

► DEPT: Mat Sci & E page: 541

► YEAR: 1995 ► DEGREE: Ph.D.

► NAME: CAREL, Roland